Optimization of halide perovskite thin films by sequential physical vapour deposition for solar cell applications

By

Juvet Nche Fru

Submitted in partial fulfilment of the requirements
for the degree

Doctor of Philosophy (PhD) in Physics

in the
Faculty of Natural and Agricultural Sciences
Department of Physics
University of Pretoria

Supervisor: Prof M.M. Diale
Co-supervisor: Dr N. Nombona

Declaration

I, JUVET NCHE FRU, declare that the thesis, which I now submit for the degree, Doctor of Philosophy (PhD) in Physics at the University of Pretoria, is my work and has not been submitted previously by me for a degree at this or any other institution. All sources or materials have been duly cited in the text, and a list of references provided at the end of every chapter. Parts of this thesis have been published in the list of journals provided in the appendix.

Signature………………………………

Date…………………………………….

Student number: 17218072

© 2020 University of Pretoria

Abstract

In this thesis, we have developed a reproducible, safe, and scalable sequential thermal vapour deposition (STVD) method for the growth of quality 3D halide perovskite (HaP) thin films. High-quality methylammonium lead tri-bromide ($MAPbBr_3$), methylammonium lead tri-iodide ($MAPbI_3$), and methylammonium lead bromide-iodide ($MAPb(I_{1-x}Br_x)_3$) thin films have been optimised using the STVD technique. The structural, optical, morphological, and electrical properties were tuned by varying the thicknesses of the organic (MAI, MABr) and inorganic (PbI_2, $PbBr_2$) precursor thin films and post-annealing times of the HaP. X-ray diffractograms confirmed the cubic $MAPbBr_3$ structure with the $Pm\bar{3}m$ space group, tetragonal $MAPbI_3$ crystal structure with I4/mcm space group, and the tetragonal $MAPbI_3$ structure being transformed to cubic $MAPbBr_3$ system as $MAPb(I_{1-x}Br_x)_3$ (x=0.89-0.95) forms. UV-Vis spectra revealed broad absorption bands with a redshift in absorption onset from 540 to 550 nm for $MAPbBr_3$ and 750 to 780 nm for $MAPbI_3$ as the thickness of respective organic precursors increased from 300 to 500 nm. The bandgap of $MAPb(I_{1-x}Br_x)_3$ decreased from 2.21 to 2.14 eV as the thicknesses of MABr precursors increased from 300 to 500 nm. The crystallisation of the HaP started within the chamber, and prolonged post-annealing times exceeding 10 min caused the transformation of $MAPbI_3$ to PbI_2. Scanning Electron Micrographs show pin-hole-free and densely packed grains with an average size that increases as thicknesses increase. The charge carrier mobility increases while trap density decreases as the thickness of organic precursors increased. Besides, the thesis investigated the growth and stability of thin $MAPbBr_3$ films at metal/$MAPbBr_3$ interfaces. We studied the structure, morphology, and stability of the optimised $MAPbBr_3$ perovskite on aluminium (Al), tin (Sn), silver (Ag), gold-zinc (Au-Zn) and gold (Au) electrodes, immediately and 60 days later. FE-SEM images show an average grain size that increased linearly with the work function from 294 nm for Al to 850 nm for Au. The $MAPbBr_3$ grains remain glued to Sn, Ag, Au-Zn but delaminate quickly on Al. X-ray analysis of $MAPbBr_3$ reveals variable crystallographic texturing for various metals and loss in intensity of prominent peaks at different rates over time. We found that the best thicknesses of 100 nm PbI_2 and 500 nm MAI, and 100 nm $PbBr_2$ and 500 nm MABr are needed for the preparation of quality $MAPbI_3$ and $MAPbBr_3$ thin films for solar cells, respectively. Quality thin $MAPb(I_{0.11}Br_{0.89})_3$ film is formed by inter-diffusion and halide exchange processes when optimised $MAPbBr_3$ is grown on optimised $MAPbI_3$ as a bottom layer. Al speeds up the degradation of $MAPbBr_3$ at Al/$MAPbBr_3$ while $MAPbBr_3$ is relatively stable at Au-Zn/$MAPbBr_3$ interfaces.

List of abbreviations

AM	Air mass
BC	Back contact
BTL	Both-transport layer
CB	Conduction band
CTL	Charge transport layer
ETL	Electron transport layer
FTO	Fluorine-doped tin oxide
GB	Grain boundary
HaP	Halide perovskites
HaP-SCs	Halide perovskite solar cells
HTL	Hole transport layer
HOMO	Highest occupied molecular orbital
ITO	Indium-doped tin oxide
LUMO	Lowest unoccupied molecular orbital
VB	Valence band
LED	Light-emitting diode
MABr	Methylammonium bromide
$MAPbBr_3$	Methylammonium lead tribromide
MAI	Methylammonium iodide
$MAPbI_3$	Methylammonium lead tri-iodide
$MAPb(I_{1-x}Br_x)_3$	Methylammonium lead iodide-bromide
PCE	Power conversion efficiency
PV	Photovoltaic
SCLC	Space charge limited current
SPVD	Sequential physical vapour deposition
STVD	Sequential thermal vapour deposition
TWy	Terawatt year
TCO	Transparent conducting oxide

Dedication

To my lovely wife Doureen N. Anye and my daughter Chiara N. Fru for their sacrifices, love, care, and prayers

&

To my parents; Mr Nche Thomas Chi and Mme Feng Patricia Nche, for giving me a good moral and educational foundation

&

To my lovely late grandmother Mami Frida Azah for endless sacrifices that saw me through my bachelor's degree programme

&

To my siblings; Bih Shella Nche, Lum Lisette Nche, Awah Lilian Nche, Swirri Melvis Nche, Azah Miriel Nche and Chi Kluvette Nche for their love and prayer

Acknowledgement

I thank the almighty God for wisdom, knowledge, understanding, safety, and health during the entire period of this study.

I wish to express my deepest gratitude to *Prof M. Diale,* my supervisor, for accepting to supervise me with no prior experimental background and for transforming me from a poor scientific writer to an excellent independent writer. Your motivations, challenging tasks and care were a fuel in my research engine. I would particularly like to thank *Dr N. Nombona,* my co-supervisor, for her invaluable assistance and inspiration to change from a solution deposition technique to this novel vapour deposition method. I thank *Prof C.C. Theron*, Head of Physics Department, for his support. To all the members in the Clean and Green Energy Research group at the University of Pretoria, I wish to show my gratitude to you all for encouragement and friendship that countered the most challenging days and moments, *Mr M. Legodi* for guiding me through the electrical characterisation techniques. I thank *Dr Alex Paradzah* and *Dr Vitalis C. Anye* for patiently proofreading my manuscripts before submissions and for guiding me through my first publication process. I thank our collaborators in the Department of Chemistry at the University of Pretoria for UV-Vis absorption and XRD measurements. Sincere thanks to all the workers in the Laboratory for Microscopy and Microanalysis for their help.

My heartfelt appreciation goes to my family and friends outside the University of Pretoria for your love, care and motivations that allowed me to continue after the demolition of my property back home in Douala, Cameroon. I am indebted to my lovely wife, *Doureen N. Anye Espe Fru*, for the immense sacrifice of allowing me to travel and pursue this dream while she was pregnant with our beautiful daughter, *Chiara N. Fru*. I would like to show my greatest appreciation to my parents for their sacrifice, encouragement, and motivation.

My sincere gratitude to The World Academy of Science (TWAS) and the National Research Foundation (NRF) in South Africa, for making this golden opportunity possible. NRF grant no N0115/115463 of the SARChI for support and the University of Pretoria for provision of an enabling environment to play in research.

Table of Contents

List of Figures

List of Tables

1 INTRODUCTION

1.1 Global energy consumption, challenges, and outlook

Over 85% of the energy used in the World today comes from burning non-renewable fossil fuels which include coal, natural gas and oil [1,2]. The persistent rise in fossil fuel consumption due to a growing global population, industrialisation, consumerism and changing lifestyles, increases the emission of carbon dioxide (CO_2) and other greenhouse gases to the environment. The CO_2 emissions cause adverse environmental impacts such as the rise in average global temperature, ozone depletion and acid rain. For these reasons, most policy experts and scientists are advocating for the replacement of fossil fuels as a route to reduce CO_2 emissions [3]. The first crucial international treaty to curb greenhouse gas emissions was the Kyoto Protocol, signed by 192 countries in 1997 and enforced in 2005 [4]. Then came the Paris agreement, signed by 195 countries in 2015. The Paris agreement was a further step to foster international climate cooperation. It was aimed at limiting the global average air temperature rise to values far below 2°C before the end of the century, thus reducing the effects of climate change [5]. Three years after the Paris agreement, the percentage of CO_2 emissions instead increased as opposed to the first drop in the preceding years. Future projections suggest that the rate of increase will continue unless drastic measures are taken to enforce the Paris resolutions globally [3].

Another pending problem is the projected depletion of the non-renewable resources by the start of the next century. *Figure 1.1.1* shows the estimated amount of energy consumed on Earth in 2015, the total amount of renewable energies supplied every year and available non-renewable energy reserves in 2015, adapted from Perez and Perez [6]. Every year, the Earth receives 23,000 Terawatt year (TWy) of solar energy as shown, far more significant than all the other renewable energy resources shown in *Figure 1.1.1 (b)*. However, only 18.5 TWy was consumed globally in the year 2015 (*Figure 1.1.1 (a)*). The total amount of non-renewable energy reserves as of 2015 was 1560 TWy, as shown in *Figure 1.1.1 (c)*. If the status quo of 85% fossil fuel dependence is maintained and 14.72 TWy of non-renewable consumed yearly, then these resources will fully deplete in the next 105 years (the year 2120). Shifting from the depleting fossil fuels to renewable and green energies will save the future from energy depletion and the pending frequent natural disasters. These inexhaustible and clean energy resources include wind, biomass, tidal, geothermal, wave and solar amongst others, which can all be traced back to the sun.

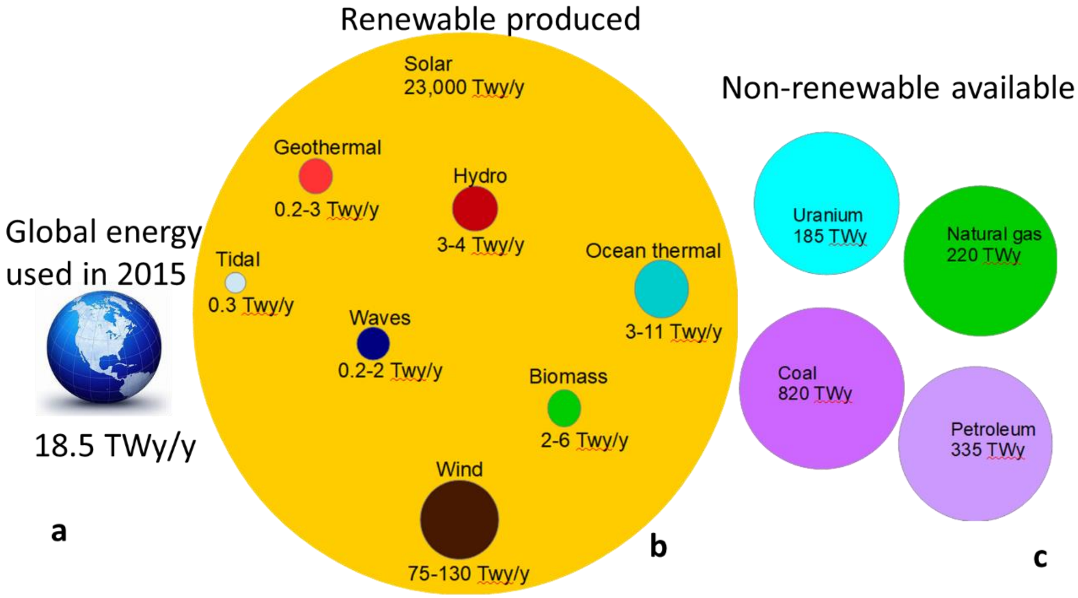

Figure 1.1.1 (a) Global energy consumed in 2015, (b) Renewable energy resources supplied yearly, (c) Non-renewable energy reserves in 2015.

Despite the massive potential of solar energy shown in *Figure 1.1.1 (b)*, only 8.76% of the World's electricity generation comes from solar, as shown in *Figure 1.1.2*. Besides, solar energy forms only 0.7% of the global energy consumed annually [2]. These point towards one direction; that most of the vast solar power potential is not exploited and could be due to high-cost and low efficiencies of commercially available technologies, including silicon [7]. The emerging photovoltaic (PV) technologies are not, however, fully developed for commercialisation further to reduce the cost and increase the performance of solar cells [8]. Perovskite solar cell is a low-cost and the fastest emerging PV technology, in terms of the rapid rise in power conversion efficiency (PCE) in a brief period [9,10]. This technology makes use of halide perovskites (HaP) absorbers. The HaP absorbers have unique optical properties, including the ability to capture a wide range of wavelengths in the visible solar spectrum.

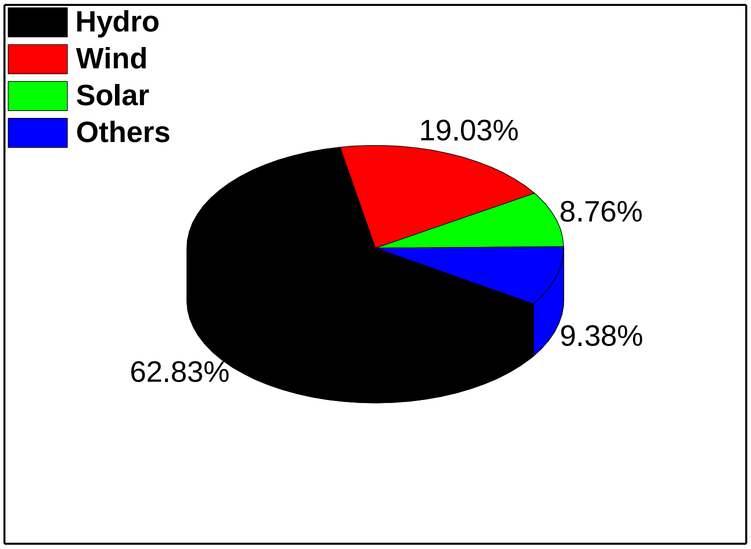

Figure 1.1.2 World's renewable energy generation in 2018 [7]

1.2 The reference solar spectra for solar cell characterisation

Scientists and manufacturers around the World characterise solar cells for various applications using different standard reference solar spectra. A solar spectrum is the range of wavelengths radiation generated by the surface of the sun, which is at a temperature of 5800 K. The sun's spectrum measured on Earth is slightly different from the original generated black body radiation. On average, the intensity of sunlight incident on the Earth's outer atmosphere is 1367 Wm^{-2} while the value at sea level is about 1000 Wm^{-2}. Attenuation, due to the scattering of blue light and absorption of red light by water droplets, carbon dioxide, and oxygen as the sunlight propagates through the Earth's atmosphere causes a decrease in intensity. Thus, the Sun's spectrum depends on the time of day and location on Earth.

Consequently, the standard reference spectra have been defined to enable solar cell manufacturers and laboratories to compare results. These spectra are given in terms Air Mass (AM) coefficients, that represent the direct optical path length from the sun through the Earth's atmosphere compared to the vertical path length in terms of the zenith angle. Air mass zero (AM0) is the standardised solar spectrum outside the Earth's atmosphere when the sun has not passed through the atmosphere. Solar cells for space applications are characterised using AM0, with an intensity of 1336.1 Wm^{-2}. The spectrum produced when the sun goes perpendicularly through the atmosphere (at 0° from the vertical reference path) is called AM1. The AM1 standard is useful for solar cells in equatorial and tropical regions. Flat-panel solar cell research for terrestrial applications makes use of Air Mass 1.5 Global (AM1.5G), with zenith angle of 48.19° and intensity 1000 Wm^{-2}. Solar concentrators are characterized using air mass 1.5 direct spectra (AM1.5D), with an intensity of 900 Wm^{-2}. *Figure 1.2.1* shows that the intensity of the sun is maximum in the visible region of the electromagnetic spectrum. Semiconductors with band gaps in the visible region are suitable materials for the active layer of solar cells. For a semiconductor of bandgap E_g, as shown in *Figure 1.2.1*, radiations with wavelengths to the right of E_g cannot be absorbed because energy is smaller than the bandgap.

In contrast, radiations with wavelengths to the left E_g are absorbed, and the excess energy lost as heat during relaxation or thermalisation. This thesis focused on organic-inorganic perovskites, which are excellent light absorbers due to high absorption coefficients and facile tuneable direct bandgap. The bandgap of these materials can be tuned to capture the whole visible spectrum.

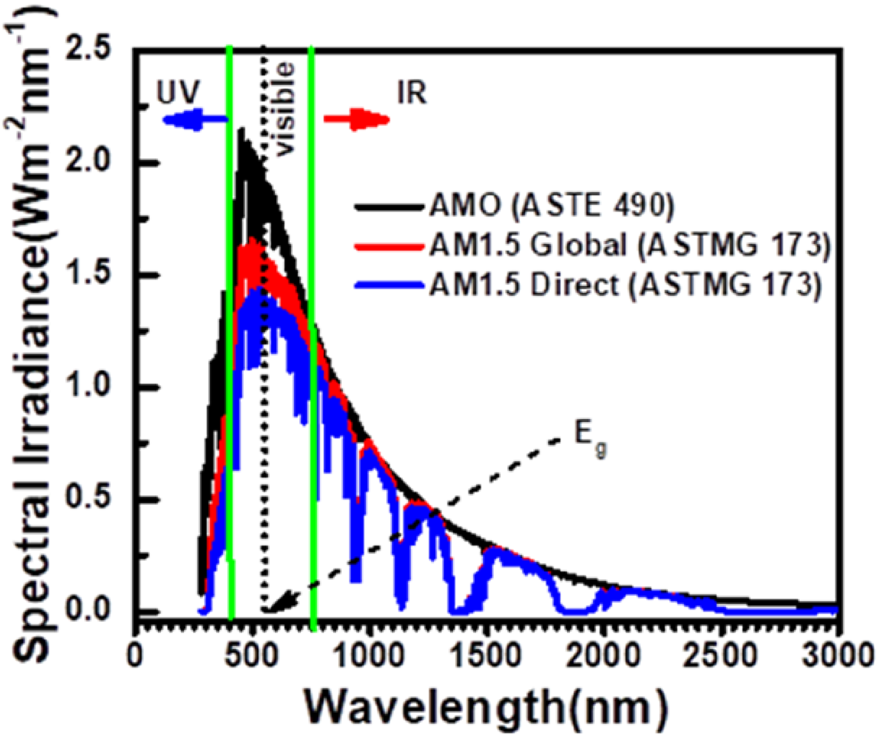

Figure 1.2.1: Spectral irradiance vs. wavelength

1.3 Evolution and generations of solar cells

The invention of the first solar cell came 44 years after the discovery of the photovoltaic effect by Antoine-César Becquerel while he was working with two solid metal electrodes inside an electrolyte solution. In 1883, the American inventor, Charles Fritts, created a high cost ($100 each) selenium based photovoltaic (PV) with 1.0% power conversion efficiency (PCE) [12]. Fritts fabricated solar cells by coating an ultra-thin layer of gold on selenium semiconductor wafers. The cells were first installed on rooftops in 1884 but were not very useful for power conversion because of the high cost. The Bell Laboratory launched the first practical silicon wafer p-n junction solar cell with PCE of 4.0% in 1954. This first practical silicon solar cells laid the foundation for the development of many commercial PV cells today. The first-generation solar cells, characterised by high cost per watt (greater than 1$/W) and low efficiency [7], were mostly used in Earth-orbiting satellites. However, their efficiencies have improved over the years with single-junction crystalline silicon solar cell having record PCE of 25.8%. In 1976, David Carlson and Christopher Wronski fabricated the first amorphous silicon thin-film photovoltaic with p-i-n architecture and PCE of 2.4%. This first amorphous silicon thin-film solar cell was the genesis of second-generation solar cells, characterized by low cost per watt (between 0.5$/W and 1$/W), but limited by lower efficiency [7]. Thin-film solar cells using copper sulphide/cadmium sulphide were the first second-generation solar cells to exceed 10% PCE. Presently, the record efficiencies of other second-generation thin-film solar cells are far greater than 10%. These include copper indium gallium selenide (CIGS) with record PCE of 22.6%, thin-film gallium arsenide (GaAs) with 28.8% record, cadmium telluride (CdTe) with 22.1% record and amorphous silicon (a-Si: H) with 14.0% record [13]. The third-generation solar cells are the emerging technologies including nanocrystalline, polymer, dye-sensitised, concentrated and perovskite solar cells, currently not well advanced commercially [14]. They have a meagre cost per watt (far less than $0.5/W) and show promisingly high efficiencies, with the potential to reach the Schockley-Queiser limit for single-carrier devices [7]. HaP absorbers were first discovered by MØLLER in 1958 [15], and 51 years later, *Kojima and co-workers* [16] applied it as a solid-state visible light sensitiser in solar cells. Since then, the PCE has risen rapidly from 3.8% in 2009 [16] to 25.2% in 2019 [17], making it the fastest emerging technology and a hotspot in the solar cell research society over 25,000 peer-reviewed articles to date. Also, it is estimated that the cost of perovskite solar panels will range from 0.1 to $0.2/W, which is very low because the materials used to make perovskite widely available and inexpensive to synthesise using low-cost flexible low cost processing methods.

1.4 Context and problem definition

Despite the remarkable progress in laboratory PCE of HaP solar cells, researches must address the pending challenges before eventual large-scale fabrication in the industry [18–20]. Some of these challenges include insufficient knowledge and conflicting interpretation of fundamental observations [18,19,21], the toxicity of lead and commonly used solvents [20,22], light-induced phase segregation in large bandgap mixed halide perovskites [23,24], poor long term environmental and operational stability of perovskites thin film and devices [25,26], poor laboratory-to-laboratory reproducibility [22], scalable manufacturing of large-area perovskite solar cells and durability of devices and modules [20]. The stability and efficiency of solar cells are highly dependent on the quality of the halide perovskites absorber, determined by the method and conditions of deposition. For a quick transition from laboratory to industrial scale, safe and scalable deposition methods need to be developed for quality large area perovskites thin films. Several scalable deposition methods have been explored for large area thin film deposition including spay-coating, doctor blade coating, screen printing [27], slot-die coating, gravure printing, ink-jet and printing vacuum/vapour assisted deposition [28,29]. The commonly used solvents in the solution deposition methods are toxic, skin penetrating and carcinogenic [20]. Thus, the development of scalable greener deposition techniques, including scalable solution methods using less hazardous solvents [20,22] and precise vacuum methods, is much needed for the transition from laboratory-scale to industrial-scale. Complete vacuum methods for HaP solar cell manufacturing are eco-friendly, very safe (toxic-solvent free), convenient, and easily scalable. Vacuum deposited HaP thin films have high qualities and stability. To date, most of the developed vacuum techniques, including co-evaporation methods, control film stoichiometry by checking the rate of deposition. However, the rate of deposition of the HaP organic precursors. This is due to the presence of impurities in the organic precursors such as methylammonium dihydrogen phosphide (MAH_2PO_3) and methylammonium hypophosphite (MAH_2PO_2) in methylammonium iodide (MAI). The concentrations of these impurities vary from one batch to another and during deposition [30].

For these reasons, techniques involving rate monitoring are not reproducible. The solution to this problem may be to perfect the stoichiometry of the thin film by checking the thicknesses of the precursors instead of the rates. The STVD technique is a physical vapour deposition (PVD) method which involves the optimisation of the stoichiometry by precisely monitoring the thickness of the precursor thin films using a crystal monitor. This guarantees laboratory-to-laboratory reproducibility of quality HaP thin films.

1.5 Aim and objectives

This thesis aims to develop and perfect the growth of halide perovskites thin films by a sequential physical vapour deposition method. The goals are:

i. Optimise the structural, optical, morphological, and electrical properties sequential physical vapour deposited methylammonium lead tri-iodide ($MAPbI_3$).
ii. Optimise the structural, optical, morphological, and electrical properties sequential physical vapour deposited methylammonium lead tribromide ($MAPbBr_3$).
iii. Optimise the structural, optical, morphological, and electrical properties of sequential physical vapour deposited $MAPbBr_3$ to on $MAPbI_3$ seed layer for form thin $MAPb(I_{1-x}Br_x)_3$ film.
iv. Fabricate transport layer-free solar cells and study their electrical properties in the dark and under illumination.
v. Study the stability of $MAPbBr_3$ thin at different metal/$MAPbBr_3$ interfaces.

1.6 Outline of the thesis

This thesis is divided into the following five (5) chapters.

Chapter 1 presents the background and motivation, context, and problem definition, aim and goal, and the outline of the thesis.

Chapter 2 reports the required literature in the thesis, including an overview of the structures and classes of HaP and related solar cell architectures. The chapter describes the principles of nucleation, growth, and vacuum thermal deposition of thin HaP films and operation of HaP solar cells.

Chapter 3 gives a detail description of the experimental methods, including the sequential physical deposition of methylammonium lead tri-iodide, methylammonium lead tri-bromide and methylammonium lead iodide-bromide thin films. It describes the X-ray diffraction, scanning electron microscopy, UV-Vis spectroscopy and electrical characterisation techniques.

Chapter 4 presents and discusses the results obtained from the sequential physical vapour deposition of methylammonium lead tri-iodide, methylammonium lead tri-bromide and methylammonium lead iodide-bromide thin films. Also, the effect of metal/$MAPbBr_3$ interfaces on the degradation of $MAPbBr_3$ perovskite is presented.

Chapter 5 concludes this thesis and presents perspectives for future work.

References

[1] M. Anaya, G. Lozano, M.E. Calvo, H. Miguez, ABX_3 perovskite for tandem solar cells, Joule. 1 (2017) 769–793. doi.org/10.1016/j.joule.2017.09.017.

[2] https://www.climatedepot.com/2017/06/21/reality-check-85-of-global-energy-consumption-based-on-fossil-fuels (accessed March 30, 2020).

[3] R.B. Jackson, P. Friedlingstein, R.M. Andrew, J.G. Canadell, C. Le Quéré, G.P. Peters, Persistent fossil fuel growth threatens the Paris Agreement and planetary health Persistent fossil fuel growth threaten the Paris Agreement and planetary health, 14 (2019) 121001. doi.org/10.1088/1748-9326/ab57b3.

[4] United Nations, Kyoto Protocol to the United Nations framework, Rev. Eur. Community Int. Environ. 7 (1998) 214-217.

[5] R. Falkner, The Paris agreement and the new logic of international climate politics, Int. Aff. 92 (2016) 1107–1125. doi.org/10.1111/1468-2346.12708.

[6] R. Perez, M. Perez, A fundamental look at supply-side energy reserves for the planet, Natural Gas 2 (2015) 215.

[7] G. Conibeeer, Third-generation photovoltaics, Mater. Today. 10 (2007) 42–50. doi:10.1016/S1369-7021(07)70278-X.

[8] https://ourworldindata.org/grapher/solar-pv-prices-vs-cumulative-capacity (accessed March 30, 2020).

[9] NREL, NREL efficiency chart, (15130).

[10] D.B. Straus, S. Guo, A.M. Abeykoon, R.J. Cava, Understanding the instability of the halide perovskite $CsPbI_3$ through temperature-dependent structural analysis, Adv. Mater. 32 (2020) 1–8. doi:10.1002/adma.202001069.

[11] https://ourworldindata.org/grapher/modern-renewable-energy-consumption (accessed March 30, 2020).

[12] C.E. Fritts, ART. LII.--On a new form of selenium cell, and some electrical discoveries made by its use, Am. J. Sci. 26 (1883) 465.

[13] B.J. Bruijnaers, Lead halide perovskite solar cells, Eindhoven University of Technology, 2018. https://research.tue.nl/nl/publications/lead-halide-perovskite-solar-cells.

[14] S. Sharma, K.K. Jain, A. Sharma, Solar Cells : In research and applications — A review, Mater. Sci. Appl. 6 (2015) 1145–1155. doi:10.4236/msa.2015.612113.

[15] C.K. MØLLER, Crystal structure and photoconductivity of cæsium plumbohalides., Nat. 182 (1958) 1436-1436. doi:org/10.1038/1821436a0.

[16] A. Kojima, K. Teshima, Y. Shirai, T. Miyasaka, Organometal halide perovskite visible-light sensitizers for photovoltaic cells, J. Am. Chem. Soc. 131 (2009) 6050–6051. doi:10.1021/ja809598r.

[17] https://www.nrel.gov/pv/cell-efficiency.html (accessed March 31, 2020).

[18] H. Chen, S. Xiang, W. Li, H. Liu, L. Zhu, S. Yang, Inorganic perovskite solar sells : A rapidly growing field, 6 (2018) 1–23. doi:10.1002/solr.201700188.

[19] L. Caliò, J. Follana-Berná, S. Kazim, M. Madsen, H.G. Rubahn, Á. Sastre-Santos, S. Ahmad, Sustainable energy & fuels, 1 (2017) 2071-2077. doi:10.1039/C7SE00367F.

[20] D.H. Kim, J.B. Whaitaker, Z. Li, M.F.A.M. van Hest, K. Zhu, Outlook and challenges of perovskite solar cells toward terawatt-scale photovoltaic module technology, Joule. 2 (2018) 1437–1451. doi.org/10.1016/j.joule.2018.05.011.

[21] L. Chen, F. De Angelis, S. Jin, Y.-K. Sun, P. V. Kamat, Energy research outlook. What to Look for in 2018, ACS Energy Lett. 3 (2018) 261–263. doi:10.1021/acsenergylett.7b01187.

[22] R. Swartwout, M.T. Hoerantner, V. Bulovi, Scalable deposition methods for large-area Production of perovskite thin films, Energy & Enviro. Mater., 2 (2019) 119–145. doi:10.1002/eem2.12043.

[23] E.L. Unger, Roadmap and roadblocks for the bandgap tunability of metal halide perovskite, J. Mater. Chem. A, 5 (2017) 11401–11409. doi:10.1039/c7ta00404d.

[24] K.A. Bush, K. Frohna, R. Prasanna, R.E. Beal, T. Leijtens, S.A. Swifter, M.D. Mcgehee, Compositional engineering for efficient wide-bandgap perovskite with improved stability to photoinduced phase segregation, ACS Energy Lett., 3 (2018) 428-435. doi:10.1021/acsenergylett.7b01255.

[25] Q. Fu, X. Tang, B. Huang, T. Hu, L. Tan, L. Chen, Y. Chen, Recent progress on the long-term stability of perovskite solar cells, Adv. Sci. 1700387 (2018). doi:10.1002/advs.201700387.

[26] X. Zhang, Strain control for halide perovskites, Matter. 2 (2020) 294–296. doi:10.1016/j.matt.2020.01.010.

[27] B.A. Kamino, B. Paviet-salomon, S. Moon, N. Badel, J. Levrat, G. Christmann, A. Walter, A. Faes, L. Ding, J.J.D. Leon, A. Paracchino, M. Despeisse, C. Ballif, S. Nicolay, Low-temperature screen-printed metallization for the scale-up of two-terminal perovskite − silicon tandems, ACS Appl. Energy Mater. 2 (2019) 3815-3821. doi:10.1021/acsaem.9b00502.

[28] C. Liu, Y.-B. Cheng, Z. Ge, Understanding of perovskite crystal growth and film formation in scalable deposition processes, Chem. Soc. Rev. 49 (2020) 1653–1687. doi:10.1039/c9cs00711c.

[29] Y.Y. Kim, T. Yang, R. Suhonen, M. Välimäki, T. Maaninen, Gravure-printed flexible perovskite solar cells : toward roll-to-roll manufacturing, Adv. Sci. 6 (2019) 1802094 doi:10.1002/advs.201802094.

[30] J. Borchert, I. Levchuk, L.C. Snoek, M.U. Rothmann, R. Haver, H.J. Snaith, C.J. Brabec, L.M. Herz, M.B. Johnston, Impurity tracking enables enhanced control and reproducibility of hybrid perovskite vapour deposition, ACS Appl. Mater. Interfaces. 11 (2019) 28851–28857. doi.org/10.1021/acsami.9b07619.

2 HaP for solar cells

2.1 Introduction

The chapter presents an overview of the structures and classes of halide perovskites (HaP) and related solar cell architectures. It outlines various methods of growing thin HaP films and describes the principles of nucleation, growth, and vacuum thermal deposition (VTD) of thin HaP films. Besides, it provides details of charge carrier generation, transport, recombination, and extraction mechanisms in HaP solar cells are provided.

2.2 Classification of HaP

2.2.1 Chemical formula and crystal structure

The perovskite structure is a compound of the form, AMX_3, after the crystallographic structure of calcium titanium oxide ($CaTiO_3$). $CaTiO_3$ is the first material of this kind discovered and given the name perovskite, after the Russian mineralogist, Lev Alekseevich Perovski. In the AMX_3 form for HaP, A stands for a monovalent cation such as caesium (Cs^+), methylammonium ($CH_3NH_3^+$, MA) and formamidinium ($H_2NCHNH_2^+$, FA), M represents a divalent cation such as lead (Pb^{2+}) and tin (Sn^{2+}) and X is a halide anion such as bromide (Br^-), iodide (I^-) and chloride (Cl^-). HaP also have mixtures of the different A-cations, M-cations and/or X-anions. The cubic perovskite crystal structure has M-cation in the 6-fold coordination position, enclosed by a corner-linked octahedron of X-anions, called MX_6 octahedral framework, and A-cations in the 12-fold coordination positions as shown in *Figure 2.2.1 (a).* The size of the A-cation is larger than that of the M-cation, large enough to fit into the 12-fold coordinated voids of the MX_6 octahedral inorganic framework, to keep the cubic symmetry, as shown in *Figure 2.2.1 (b).* HaP can reversibly transition between cubic, tetragonal and orthorhombic crystal structures at different temperatures [1].

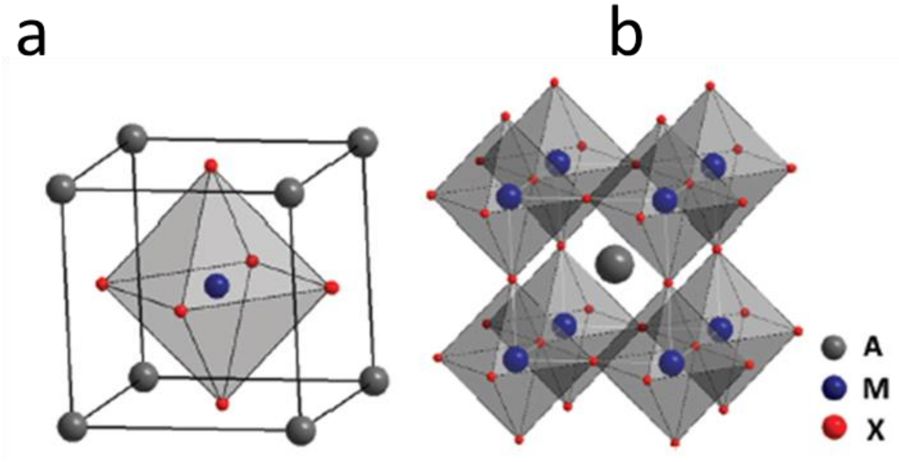

Figure 2.2.1: Crystal structure of cubic HaP with general formula AMX_3 [2].

2.2.2 Dimensional classification of HaP

The dimensionality of HaP crystals has great influence on their chemical, electrical and optical properties [3]. It depends on the size of the A-cation and that of the voids created by the MX_6 octahedral framework. HaP can be broadly classified into three dimensional (3D), two-dimensional (2D), quasi-2D, one-dimensional (1D) and zero-dimensional (0D) structures based on geometry [3,4] as shown in *Figure 2.2.2*. The 3D structures have cuboid-like, coral-like, opal-like and maze-like morphologies [5]. The 2D HaP have layered structures that are similar to the Ruddlesden-Popper (RP) phases [6], consisting of nanoplatelet (nanosheet) perovskite that is separated by large spacer cations. The RP phase has a general formula $A_{n-1}L_2M_nX_{3n+1}$. In this form, A is a small size monovalent cation (Cs^+, MA^+), L corresponds to a large size aromatic or aliphatic alkylammonium spacer cation including phenyl-ethyl ammonium (PEA^+) and butylammonium (BA^+), M is a transition metal cation (such as Pb^{2+} and Sn^{2+}), X stands for a halide anion (such as I^-, Br^-, Cl^-) and the integer n represents the number of metal halide octahedral $[MX_6]^{4-}$ layers between the two L-cations, determined by careful control of stoichiometry [4]. The 2D perovskites have strong quantum confinement effects and large bandgaps [5]. In solar cells, 2D perovskites have been applied as primary light harvesters [7], capping layers [8], passivation layers [9] and 2D/3D interfacial layers [10]. The 1D perovskites are nanowires and nanorods having a hexagonal phase used as light trapping medium and antireflection coating, and mechanical properties superior to their 3D thin-film counterparts [3,5]. 0D perovskites are quantum dots having very high photoluminescence quantum yields (approaching unity). They can be tuned to emit light in the entire visible spectrum by changing the size (quantum confinement effect) and composition [11]. Besides, they have high extinction coefficients and multiple excitons generated in well-designed quantum dot HaP solar cells, responsible for a significant increase in solar cell photo conversion efficiency (PCE).

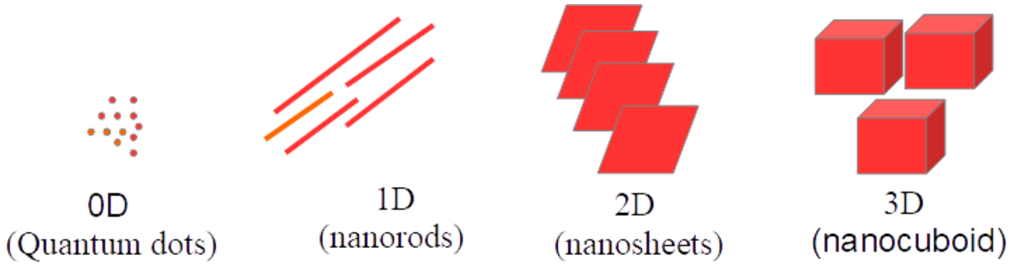

Figure 2.2.2: Dimensionality of HaP

2.2.3 Goldschmidt's tolerance factor and the dimensional stability of HaP

The ideal cubic symmetry of the 3D HaP structure is usually distorted in practice. Possible distortions include the M-cation displacement from its central position and tilting of the MX_6 octahedron, depending on the sizes of the A-cation and M-cation. The degree of distortion is determined by the Goldschmidt's tolerance factor (t) given by *Equation 2.1*,

$$t = \frac{\sqrt{2}}{2} \frac{(R_A + R_X)}{(R_M + R_X)} \quad \text{Equation 2.1}$$

where R_A is the ionic radius of A-cation, R_M is the ionic radius of M-cation, R_X is the ionic radius of X-anion. It can also predict whether a combination of anion and cation will form a stable HaP structure. For ideal cubic symmetry, the ionic size requirement for stability is quite stringent, and the A-cation and M-cation adjust their equilibrium bond distances to the X-anions, without distortion of the unit cell, such that $t = 1$. The tolerance factor ranges from 0.8 to 1.0 for practical HaP because the cubic symmetry is distorted slightly to accommodate a wide range of cations and anions. For instance, the MX_6 octahedron may distort by tilting to reduce the coordination number from 12, so that a smaller sized A-cation can be accommodated, thereby decreasing t. Also, t is reduced by displacement of an undersized M-cation inside the MX_6 octahedron that enables stable bonding and leads to ferroelectricity.

Generally, before any perovskite is formed, the stable MX_6 octahedral framework must first be produced. The MX_6 octahedral framework is stable when the octahedral factor, a ratio of R_M to R_X, ranges from 0.41 to 0.89 [11,12]. When this condition is satisfied, the dimensionality of the HaP structure is then determined by the size of the A-cations. Three-dimensional (3D) perovskite structures are formed when the size of the A-cation is such that it can fit into the MX_6 octahedral voids. This occurs for values of t ranging from 0.8 to 1. For $t = 1$, the ideal cubic symmetry is obtained. However, for values of t in 0.8 to 0.99 range, the MX_6 octahedral is slightly tilted to stabilise the perovskite structure. The tilting bends the "soft" M–X–M bond angle, resulting in the shortening of the A–X bond length without affecting the MX_6 octahedral framework. This shortening of A–X bond length causes a reduction in coordination number and improvement in the bonding of the A-cation, leading to stabilisation [12]. Layered HaP is formed when the size of the A-cation too large to fit into the voids. In this case, the value of t is more significant than 1.0. Non-perovskite structures form when t is less than 0.8.

2.3 Preparation of thin HaP films

2.3.1 Deposition methods: types and classes

Perovskite devices are easy to make using versatile and low-cost thin-film deposition methods, including doctor blade [13], spin coating [14], slot die casting [15], physical vapour deposition [16], spray coating [17], ink-jet printing [18], screen printing [19,20], pulsed laser deposition [21], dip coating [22], electrode-position [23] and gravure printing [24]. We can broadly group these techniques into the solution and vapour methods. The solution techniques include doctor blade, spin coating, slot die casting, and spray coating ink-jet printing, screen printing, dip coating, electrode-position, and gravure printing. They all start with the creation of a wet film, using some mechanical means, subsequently dried at a temperature lower than 100°C [25]. Most of the solution-based methods are fast deposition processes with a low capital requirement, but, their running cost is high due to stringent quality control requirements, solvent treatment and handling of toxic solvents [25]. The most widely used solution-based method is spin coating. It has produced very high PCE solar cells, however, about 90% of the solution being deposited is wasted and the method only works well for substrate areas less than 1.0 cm^2 [25]. In one-step solution coating methods, the perovskite ink (solution of precursors in suitable solvent (s)) is first prepared before the thin film deposition in a single step [26]. In contrast, for two-step solution coating methods, a solution of the inorganic lead or tin halide precursor is first deposited followed by the organic or caesium halide precursor solution to form the perovskite. For instance, in the formation of $MAPbI_3$ using a two-step method, the PbI_2 thin film is first deposited, then MAI. The deposited PbI_2 thin film forms the PbI_6 octahedral framework containing voids into which MAI intercalate, leading to the formation of $MAPbI_3$ [27].

Vapour methods, on the other hand, are solvent-free techniques with high capital expenditure and slow throughputs. Some advantages of these methods include easy control of the deposition environment, leading to high laboratory-to-laboratory reproducibility at no additional cost from treatment and recycling of solvents and quality control of the precursor inks [25]. Typically, vapour deposition methods include physical vapour deposition (PVD), atomic layer deposition (ALD), sputter deposition and chemical vapour deposition (CVD) are widely used in solar cell manufacturing industries to date [25]. PVD involves the conversion of material from solid-state through vapour phase to thin film condensed phase under vacuum. If the energy for the sublimation of the material is heat, then the method is known as vacuum thermal deposition (VTD). VTD is the cheapest vapour method and has been applied to deposit HaP in different ways including co-evaporation (typically single source or dual source), flash evaporation and sequential evaporation. Single source co-evaporation involves the vaporisation of precursors that are mixed inside a single crucible while dual-source co-evaporation involves the simultaneous deposition of precursors from separate crucibles. Both co-evaporation approaches for the deposit of HaP perfect the stoichiometry by controlling the rate of deposition, which is usually not stable due to the light molecular weight of the vapours. The random collisions of the vapour molecules with the tiny amount of air molecules inside the vacuum chamber decreases their mean free paths and cause fluctuations in the rate of deposition [28]. Likewise, for sequential thermal vacuum deposition (STVD), the precursors are placed in separate crucibles and deposited independently, one layer on another. Sometimes, the layers are made to alternate many times to perfect the stoichiometry. Usually, the inorganic lead halide precursor is first deposited, then the organic layer is used to convert it to perovskite through inter-diffusion and recrystallization. STVD enables precise control of thickness (measured by a crystal monitor), environment and morphology, thus is reproducible, since a quartz crystal monitor can accurately check the consistency. However, STVD has been rarely exploited for the synthesis of HaP. Partial vapour deposition method, also known as vapour-assisted deposition (VAD), is a sequential deposition method where the organic lead halide layer is deposited using any solution method and organic layer deposited using any of the vapour methods. *Sheng and co-workers* reported the preparation of $MAPbBr_3$ thin films by VAD [29]. Their approach consisted of the deposition of a solution of $PbBr_2$ by spin coating followed by treatment of the deposited film with MABr vapour at 150˚C for 10 min. They achieved films with long carrier diffusion length exceeding 1.0 μm and perovskite solar cell with PCE of 8.7% and V_{oc} of 1.45 V. Presently, chemical vapour deposition (CVD) is the only vapour method that has been used for the preparation of $MAPbBr_3$. *Leyden and co-workers* [30] synthesized $MAPbBr_3$ by CVD for light-emitting diode and achieved luminescence of 560 cd/m^2. PVD has the potential to improve stability by enhancing the stoichiometry and quality of the thin HaP films and can be applied to a variety of substrates [31]. *Jung and co-workers* synthesized lead-free methylammonium tin tri-iodide ($MASnI_3$) by both STVD and co-evaporation [32]. They realized that the sequential physical vapour deposited films were more efficient than co-evaporated ones.

2.3.2 The principle of STVD of thin HaP films

Five fundamental steps engage in the synthesis by SVTD, including sublimation (evaporation), transportation, condensation, interdiffusion and recrystallisation, in that order. Heat energy is supplied to a crucible holding the precursor by some means. The energy causes bonds to break, and atoms (clusters of atoms or molecules) dislodge from the surface of the material at a suitable temperature (above the melting point) and appreciable vapour pressure in the chamber. All materials experience outgassing (leaking of gas from the material) within a vacuum when heated initially, resulting in the first rise in pressure of chamber before the sublimation starts. The rate of evaporation depends on the vapour pressure of the target material at a given temperature. High vacuum conditions are needed for faster sublimation, to prevent oxidation, reduce the density of contaminant and to increase the mean free path of the evaporated materials [25]. The mean free path of gas at a pressure of 10^{-5} Torr is 8.0 m and is known as the Knudsen number. The evaporated atoms are transported through a vacuum by the pressure gradient between the hot source and the colder substrate's surface along straight lines (without collisions). The vapour condenses into a thin film on the substrate because it is at a lower temperature.

For a pure HaP grown by STVD, a thin film of lead halide (PbX_2) precursor is first deposited to form the PbX_6 octahedral framework having voids. The organic halide precursor (MAX) is then deposited on the PbX_2 thin film. The heat produced within the chamber causes interdiffusion of the two layers, resulting in the filling of the voids and next recrystallisation of $MAPbX_3$. Interdiffusion can be prevented by lowing the temperature of the substrate to 0°C. *Patel and co-workers* showed that inter-diffusion and reaction during vapour deposition could be stopped by lowering the temperature of the substrate to 0°C before the deposit of MAI on the PbI_2 [33].

2.3.3 Nucleation and grain growth in vapour deposited thin HaP films

The fundamental kinetic mechanisms involved during the formation of polycrystalline thin films are nucleation, growth and coalescence [34]. Grain growth is a process through which the average grain size of a purely crystalline material increases by the motion of grain boundaries. It can also lead to the evolution of intermediate crystallographic orientations (textures), resulting in possibilities of tailoring the electronic, mechanical and chemical properties [35,36]. For HaP in the vapour phase, it follows the Volmer-Weber growth mode [25]. In this mode, small molecular clusters nucleate directly on the substrate surface because the molecules bound more strongly to each other than to the substrate. The impinged groups then merge to form a continuous thin film. The driving force for the crystal growth process is the chamber pressure, substrate temperature and substrate-material surface properties. High temperatures increase high angle grain boundary mobility, which favours grain growth.

On the other hand, the presence of particles/solutes inhibits grain growth by pinning the grains. Another factor that inhibits grain growth is the presence of highly textured films having many low angle grain boundaries with low energies that reduce driving the force for grain growth. Finally, the texture resulting from grain growth depends on the film thickness, deposition temperature, grain growth temperature, thermal expansion coefficients of film and substrates and mechanical properties of the film [34].

There are two categories of grain growth phenomena: normal and abnormal grain growth, as shown in *Figure 2.3.1.* Normal grain growth is a continuous process in which the microstructure coarsens uniformly, resulting in monomodal grain size (typically smaller than film thickness) distribution in which the form is independent of time. On the other hand, abnormal or secondary recrystallization grain growth is a discontinuous process in which specific energetically favoured grain (grains with high boundary energy and mobility, favourable texture and fewer second-phase particles) in a matrix of smaller monomodal grains overgrow and consume the smaller grains, resulting in bimodal grain size distribution which is time-dependent. The abnormal grains can grow and impinge unto other irregular grains, which may again result in a monomodal grain size distribution.

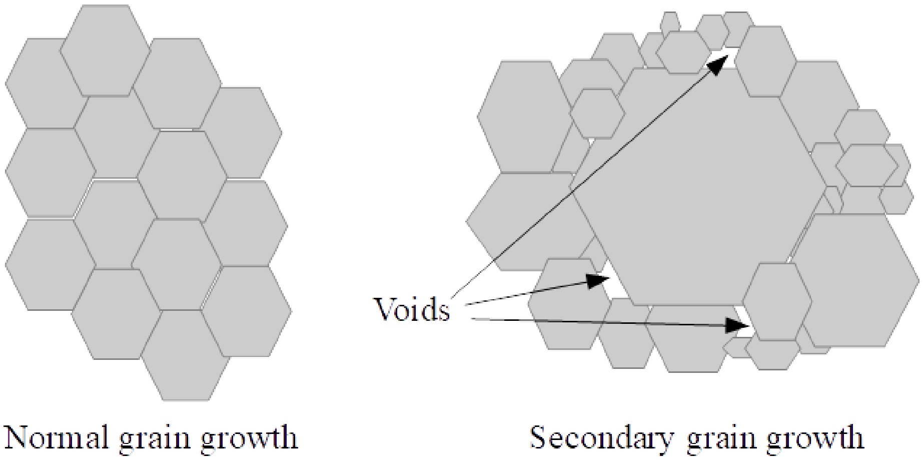

Figure 2.3.1: Schematic diagrams of normal and abnormal grain growth

2.4 Perovskite solar cell architectures

HaP solar cells can be grouped into four classes depending on the presence or absence of the charge transport layer(s) (CTL). These classes include conventional HaP solar cells, with and without electron transport layer (ETL) and hole transport layer (HTL) as shown in *Figure 2.4.1* [37]. Perovskite solar cells with at least a transport layer explored to date can be further grouped under inverted planar [38], planar [39] and mesoporous architectures [40]. The ETLs are materials with high electron mobility and affinity while HTLs have high hole mobility and affinity. This means ETL allows the passage of electrons and stop holes and vice versa. *Pitchaiya and co-workers* presented an extensive review of HTL and ETL materials applied in perovskite solar cells [41]. Generally, the main ideas behind fabricating solar cells without charge transport layers is to reduce cost, improve stability and simplify the architecture. This is feasible because HaP light absorbers can also serve as both ETL and HTL, due to their high extinction coefficients, high charge carrier mobility, carrier diffusion lengths and long carrier lifetimes [37,42].

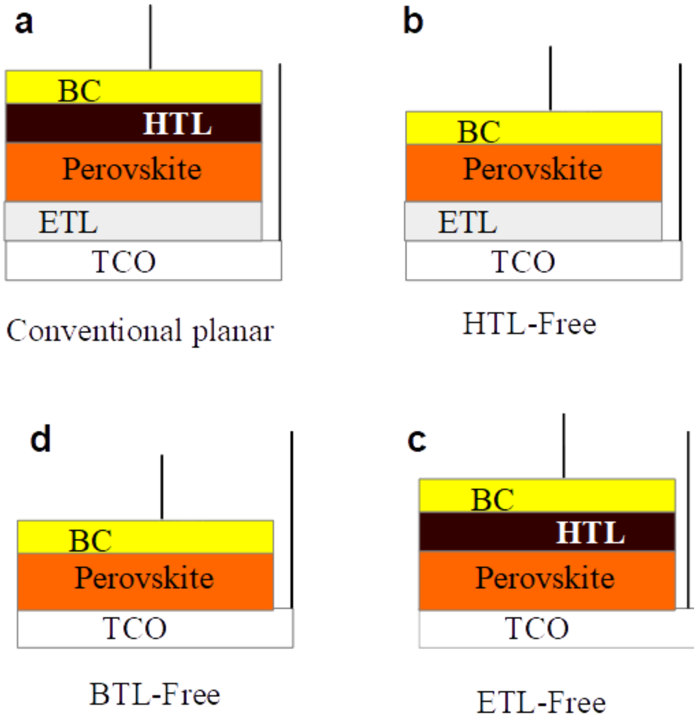

Figure 2.4.1: Schematic diagrams of perovskite solar cell architectures, (a) Conventional perovskite solar cell, (b) HTL-free perovskite solar cell, (c) ETL-free perovskite solar cell, (d) BTL-free perovskite solar cell.

2.4.1 Conventional HaP solar cells

Figure 2.4.2 shows the schematics of conventional HaP solar cells. The conventional HaP solar cells are those with both the ETL and HTL layers. These solar cells have produced the highest efficiencies to date. For the conventional inverted (p-i-n) planar solar cells, the HaP is deposited on the HTL, and the ETL on the HaP, to have a Glass/TCO/HTL/HaP/ETL/BC architecture as shown in *Figure 2.4.2 (a)*. In addition to excellent charge transport properties, the HTL must be transparent to allow light to pass through to the HaP and the ETL must require low annealing temperatures (typically, < 120°C), to avoid thermal decomposition of the HaP [25]. Some materials used as HTLs in HaP-SCs include poly(3,4-ethylene dioxythiophene): polystyrene sulfonate (PEDOT:PSS) [43], doped nickel oxide (NiO_x) [44], Nickel Phthalocyanine (NiPc), polytriarylamine (PTAA), copper(I)iodide (CuI) [45], copper(I)oxide (Cu_2O) [46], copper(II)oxide (CuO) [46] and reduced graphene oxide (r-GO)/PTAA bilayer [41]. The fullerenes are commonly used as the ETLs in inverted perovskite solar cells because of the suitable band alignment and excellent electrical conductivity. However, due to their high cost, low open-circuit voltages (typically due to interfacial defects) and poor photochemical and thermal stabilities, solar cells using fullerenes have increased interest in developing novel ETLs. N-type conjugated polymers, based on bithiophene imide and thienylthiazole imide, are possible substitutions for the fullerenes by *Chen and co-workers*, producing solar cells with high PCE (20.89%) and stability due to their high hydrophobicity and mobile ion blocking capability [47].

Likewise, the conventional planer (n-i-p) perovskite solar cells have the Glass/TCO/ETL/HaP/HTL/BC architecture, as shown in *Figure 2.4.2 (b)*. The ETLs must be transparent, and HTLs processed at low temperature in this architecture. Candidate materials used as ETLs in the past include zinc oxide (ZnO), tin oxide (SnO_2) [48], tin oxide-potassium chloride composite (SnO_2-KCl) [49], niobium doped tin oxide (Nb-SnO_2) [48] and tungsten oxide (WO_x) [50], to mention but a few. Possible candidates for HTLs include PEDOT:PSS, 2,2',7,7'-tetrakis (N,N-di-p-methoxyphenylamine)-9,9'-spirobifluorene (spiro-MeOTAD) [41,51], graphene oxide(GO)/PEDOT:PSS hybrid bilayer, GO/spiro-MeOTAD hybrid, tungsten trioxide(WO_3)/spiro-MeOTAD hybrid [52] and more. The most widely used spiro-MeOTAD has many issues, including high cost, the need for additives to improve conductivity, acceleration of degradation and hysteresis, and the presence of pinhole defects [51].

Mesoscopic conventional HaP solar cells are characterized by the presence of mesoporous layer (typically TiO_2 and Al_2O_3 nanoparticles) as shown in *Figure 2.4.2 (c).* The mesoporous layer functions as the ETL and scaffold of the HaP layer. Typical mesoporous layers include nanoparticles of semiconductors such as titanium dioxide (TiO_2), lithium doped titanium dioxide (Li-TiO_2) [53], ZnO [54], $BaSnO_3$ [55], $BaTiO_3$/TiO_2 bilayer, $NiTiO_3$, and insulators like Al_2O_3 and ZrO_2. TiO_2 is widely used in mesoscopic solar cells; however, it has low electron mobility; therefore, needs doping to improve the efficiency of a solar cell.

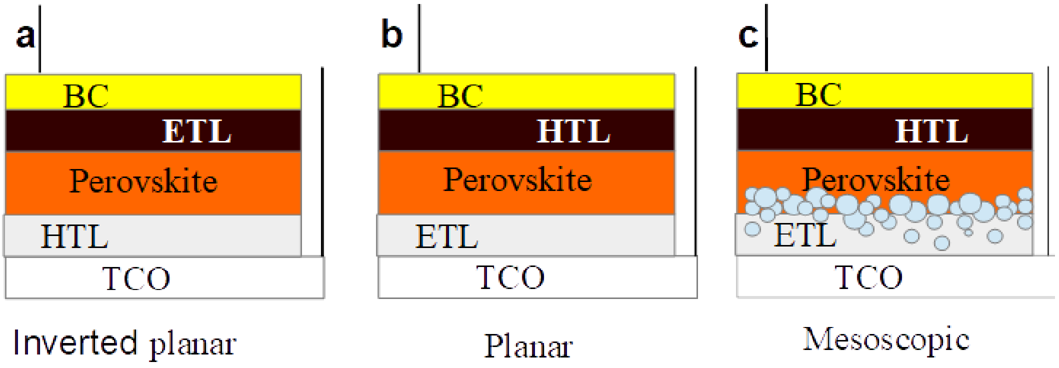

Figure 2.4.2: Schematic diagrams of conventional perovskite solar cells, (a) Inverted solar cell, (b) Planar solar cell, and (c) Mesoscopic solar cell.

2.4.2 ETL-free solar cells

Figure 2.4.3 is the schematic diagrams of ETL-free solar cell architecture. These solar cells may have the inverted (*Figure 2.4.3 (a)*) or the planar (*Figure 2.4.3 (b)*) configurations [37], where transparent conducting oxide (TCO) includes fluorine-doped tin oxide (FTO) or indium-doped tin oxide (ITO) and the back contacts (BCs) includes Au, Al, C and more. These solar cells have shown higher PCEs, compared to the conventional perovskite solar cells. Surface modification of FTO has improved the efficiency and stability of ETL-free solar cells significantly. *Huang and co-workers* studied the effect of FTO surface modification using tetramethylammonium hydroxide (TMAH) in glass/FTO–TMAH/HaP/spiro-OMeTAD/Au solar cell [56]. They obtained surprisingly high PCE of 20.1% and reduced hysteresis, attributed to defect passivation at the FTO/HaP interface and in the perovskite layer by TMA^+ ions. *Cheng and co-workers* modified the surface of FTO using hydroxyl ethyl functionalized imidazolium iodide (BIPH-II). They saw a rise in PCE from 9.01 to 17.31% for glass/FTO–BIPH-II/perovskite/spiro-OMeTAD/Au solar cells [57]. Another idea realization of ETL-free perovskite solar cell is the fabrication of p-n heterojunction devices with TCO/HaP(n-type)/HTL(p-type)/BC configuration. *Cui and co-workers* synthesised n-type self-doped $MAPbI_3$ by low-temperature annealing in the 100-150 temperature range and used it in an FTO/$MAPbI_3$(n-type)/spiro-OMeTAD /Au solar cell [58]. They obtained an impressive 15.69% PCE that was maintained over 21 days, showing long term stability.

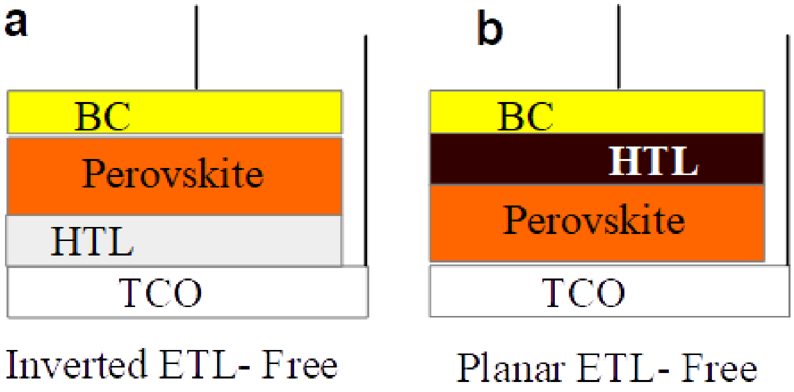

Figure 2.4.3: Schematic diagrams of ETL-free solar cell architecture, (a) Inverted ETL-free solar cell. (b) Planar ETL-free solar cell.

2.4.3 HTL-free solar cells

Figure 2.4.4 shows the schematic diagrams of HTL-free solar cell architectures including the inverted (*Figure 2.4.4 (a)*), planar (*Figure 2.4.4 (b)*) and mesoscopic (*Figure 2.4.4 (c)*) architectures. Most literature on mesoscopic TCO/ETL/HaP/BC uses c-TiO_2 and m-TiO_2 as ETL and Au and C as rear contacts [37]. In contrast, the inverted TCO/HaP/ETL/BC configurations generally use the fullerenes as ETLs and have shown efficiencies exceeding 20% [59]. There are reports on the use of other ETLs, including ZnO, m-TiO_2/m-ZrO_2 bilayer, m-TiO_2/m-Al_2O_3 bilayer and more [37]. *Wang and co-workers* fabricated an all-inorganic HTL-free solar cell, with FTO/ZnO/$CsPbIBr_2$/C configuration, and saw a PCE of 7.60% which decreased by only 10% after 624 hours, under 10% humidity and room temperature [60]. *Wu and co-workers* improved the PCE of ITO/$MAPbI_3$/ETL/Cu inverted HTL-free solar cell from 11.0 to 20.2% by doping $MAPbI_3$ with 2,3,5,6-tetrafluoro-7,7,8,8-tetracyanoquinodimethane (F4TCNQ) molecule [61]. The F4TCNQ molecule improved the PCE by increasing the conductivity of $MAPbI_3$ and its electronic contact with the ITO.

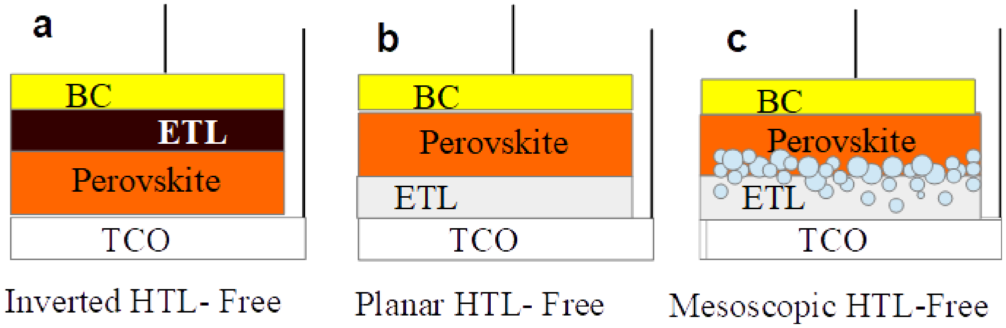

Figure 2.4.4: Schematic diagrams of HTL-free solar cell architecture, (a) Inverted HTL-free solar cell, (b) Planar HTL-free solar cell, (c) Mesoscopic HTL-free solar cell.

2.4.4 BTL-free solar cells

BTL-free HaP solar cells have the most straightforward architectures, without ETLs and HTLs, as shown in *Figure 2.4.5*. They have promising potential to reduce the overall cost to less than half that of conventional perovskite solar cells [37]. TCO/HaP/BC gives the general configuration of these solar cells. The pioneering work on BTL-free solar cells was done by *Chen and co-workers*, in which they fabricated an ITO/$CsSnI_3$(p-type)/Au Schottky solar cell with PCE of 0.9% [62]. This extremely low PCE was due to high series and low shunt resistance. They suggested different ways to improve the performance of such solar cells, including reducing the sheet resistance of ITO, growing of high-quality $CsSnI_3$ thin films and forming a p-n heterojunction with $CsSnI_3$ using a suitable n-type absorber. A more efficient, simplified FTO/$CsPbBr_3$/C solar cell with a PCE of 2.35% was later reported by *Duan and co-workers* [63]. They showed that interfacial modification using graphene quantum dots (GQDs) and $CsPbIBr_2$ quantum dots (PQDs), shown in the FTO/GQDs/$CsPbBr_3$/C and FTO/GQDs/$CsPbBr_3$/PQDs/C configurations, improved the PCEs from 2.35 to 3.19 and 4.10% respectively. The presence of grain boundaries in HaP absorber has been proven to reduce the PCE and V_{oc} of BTL-free solar cells significantly. *Peng and co-workers* showed that ITO/$MAPbBr_3$(polycrystalline)/Au had PCE of 0.056% and V_{oc} of 0.29 V while ITO/$MAPbBr_3$(monocrystalline)/Au had PCE of 5.49% and V_{oc} of 1.25V [64]. The performance improvement was due to the absence of grain boundaries (typical accumulation sites for defects) in monocrystalline $MAPbBr_3$.

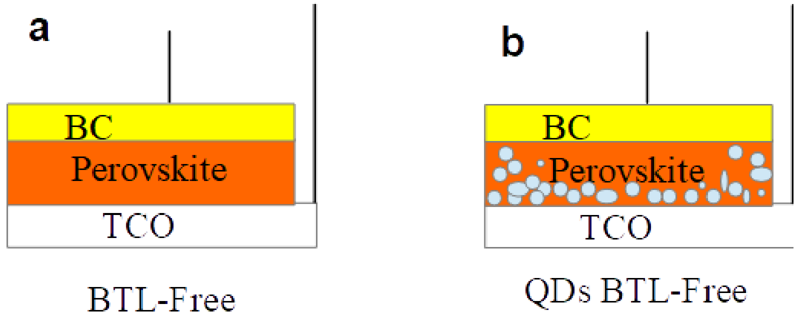

Figure 2.4.5: Schematic diagrams of BTL-free solar cell architecture, (a) Planar BTL-free solar cell, (b) QDs BTL-free solar cell.

2.5 The general working principle of HaP solar cells

The working principle of solar cells is based on a physical and chemical occurrence called the photovoltaic effect, the production of current and voltage in a material when exposed to light. The mechanisms involved in converting light energy to electrical energy in solar cells include generation, transport, recombination, and extraction of charge carriers. These mechanisms limit the PCE of solar cells; that is, they determine the critical photovoltaic parameters such as V_{oc}, short-circuit current density (J_{sc}), and fill factor (FF). Knowledge of the mechanisms from different photovoltaic technologies does not directly apply to perovskite PV, and their complete understanding is not fully set up for HaP solar cells. Comprehensive scientific knowledge of the fundamental mechanisms must address the roadblocks to commercialisation and push PCEs towards the Schockley-Queisser. We will examine up to date knowledge of charge carrier generation, transport, recombination, and extraction in perovskite solar cells in the following sub-sections.

2.5.1 Charge carrier generation

Charge carrier generation is the first mechanism amongst the working principles of solar cells and is determined by the light absorption properties and exciton binding energy of the active layer. HaP absorbers have unique light absorption properties compared with the materials for other technologies, including relatively high absorption coefficients, direct and tuneable bandgaps, and sharp absorption onsets [65,66]. The high absorption coefficients (typically greater than 10^4 cm^{-1}) and direct bandgap allow for the use of ultrathin active layers (typically in the 300-600 nm range) to absorb a wide range of wavelengths in the visible spectrum [65]. The ultrathin absorbers mean short charge transport paths leading to a reduction in energetic losses due to recombination processes, thus high V_{oc}. The sharp absorption onsets (purely exponential) with low Urbach energies (typically less than 15 meV), attributed to well-ordered microstructures and no deep level states, enable high V_{oc} [65,66]. Besides, a sharp absorption edge means little sub-bandgap absorption due to a few deep level states [66]. Also, the flexibility of tuning the bandgap to capture a large section of the visible spectrum by merely changing the composition is an added advantage for light absorption. With regards to the low exciton binding energies of HaP, mostly free charge carriers dominate following light absorption, with very few low binding energy excitons (weakly bound electron-hole pairs) [67]. This is attributed to the direct generation of free carriers and/or the rapid dissociation of the low energy excitons within the absorber. Therefore, unlike the other emerging technologies, the use of interfaces in perovskite solar cells is mainly for selective charge collection and not exciton dissociation [67]. The presence of some interfaces introduces defects that cause recombination and decrease open voltage. The relative amount of exciton and free charge carriers have been shown to depend on crystallite size.

Figure 2.5.1 is a schematic diagram of the optical generation mechanisms in HaP solar cells. Light with photon energy less than the bandgap is transparent to the perovskite absorber, as shown in *Figure 2.5.1 (a)*. When the energy of the incident photon is greater than the bandgap, the light is absorbed, following its interaction with an electron deep in the valence band, as shown in *Figure 2.5.1 (b).* This causes electronic transitions to energy levels deep in the conduction band while leaving holes in a valence band. Some of the generated electrons remain coupled with associated holes and are known as excitons. The energy needed to dissociate excitons in HaP is deficient, leading to more free carriers than excitons following an excitation. Furthermore, photons with energy equal to the bandgap are absorbed by electrons at the top of the valence band to move the conduction band minimum, as shown in *Figure 2.5.1 (c).*

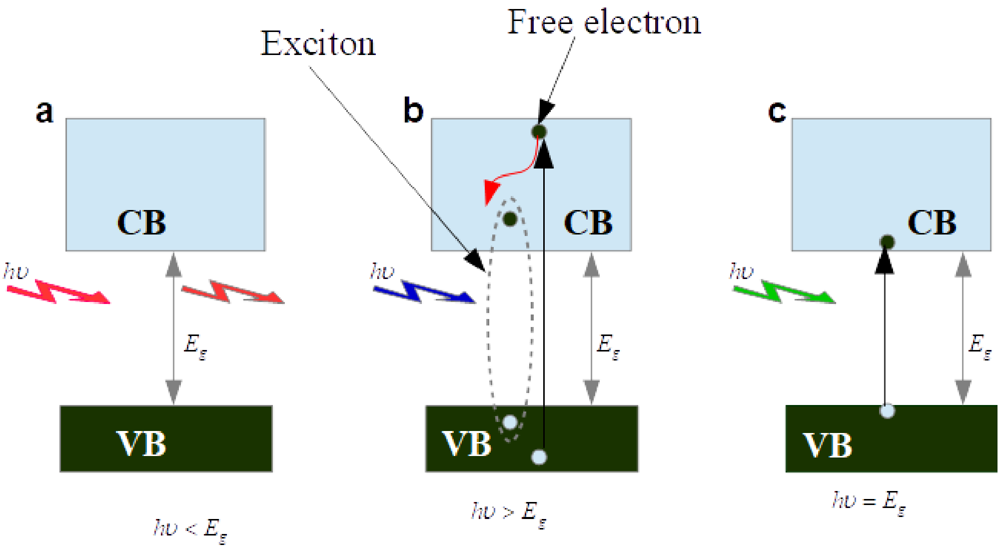

Figure 2.5.1: Schematic diagram showing optical charge carrier generation in HaP, (a) Energy of incident photon less than bandgap, (b) Energy of incident photon greater than bandgap, (c) Energy of incident photon equals bandgap.

2.5.2 Charge carrier transport

Charge carrier transport is the selective movement of electrons and holes to the two contacts of a solar cell, under the action of forces due to an electric field (drift) and concentration gradient (diffusion). The effectiveness of this motion is characterised by carrier diffusion length (L), carrier lifetime (τ), and carrier mobility (μ) of the absorber. These properties are related as shown in *Equation 2.2*,

$$L = \sqrt{D\tau} \qquad \text{Equation 2.2}$$

where D is the diffusion coefficient and is related to μ by *Equation 2.3*,

$$D = {}^{\mu q}\!\big/_{k_B T} \qquad \text{Equation 2.3}$$

where k_B is the Boltzmann constant, T is the absolute temperature, and q is the elementary charge. The carrier lifetime and diffusion length show material quality for conventional semiconductors and greatly determine the performance of solar cells. The carrier mobility is the main parameter that determines the diffusion length, as seen in *Equation 2.3.* The diffusion length is the average distance travelled between the generation of charge carriers and recombination. For charge carriers to be transported successfully to each interface, the perovskite material must have high mobility and long carrier lifetime and diffusion length.

HaP are low-cost and solution-processed semiconductors with excellent charge transport properties, including long diffusion lengths (exceeding 5.0 μm) long carrier lifetimes (exceeding 1.0 μs) for both single crystals and polycrystalline thin films [68–70]. The diffusion lengths and carrier lifetimes depend on several factors, including the method of processing, the composition of the HaP, method of measurement, crystallinity, to name a few [69,71,72]. The diffusion length for single monocrystalline perovskite material is greater than that for polycrystalline material of the same composition [69,72]. This shows that the presence of grain boundaries in HaP reduce the diffusion length. Previously, some literature claimed that hole diffusion length was more significant than electron diffusion length in $MAPbI_3$ [73,74], suggesting the electrons are trapped species following excitation while holes are the diffusion species.

On the contrary, other reports claimed that electron diffusion length in $CsPbI_3$ and $MAPbI_{3-x}Cl_x$ is greater than the hole diffusion length [73,75]. A more import result saw that electron and hole diffusion lengths $MAPbI_3$ are almost balanced though that of electrons is slightly greater, consistent with the larger effective mass for hole [76]. This parity in diffusion lengths of both carriers is essential for efficient extraction of both charge carriers.

Despite the extensive characterisation of diffusion lengths and lifetimes for different HaP, the origin of the surprisingly high values stays a subject for scientific discussion. Generally, the long non-radiative carrier lifetimes are as a result of slow transfer of electronic energy into vibrational (phonon) energy due to low trap densities, weak electron-phonon coupling or the need to release many phonons in an electronic transition [77]. Long radiative carrier lifetimes in HaP have been attributed to high defect formation energies [78], presence of uncharged ferroelectric domains [79] and large polaron (polarization cloud greater than atomic spacing) shielding [80]. Another explanation of the long carrier lifetimes is the fact that HaP have low phonon energies which makes them sensitive only to defects in the middle of the bandgaps, which are few in most cases [77].

2.5.3 Charge carrier recombination

Recombination is a charge carrier annihilation process which involves a transition of an electron from its metastable state in the conduction band to re-occupy the electron-hole state in the valence band. Generally, three recombination mechanisms occur in all semiconductors, including band-to-band recombination, trap-assisted recombination, or Shockley-Read-Hall (SRH) recombination, and Auger recombination, as shown in *Figure 2.5.2*. All these mechanisms are also present in HaP solar cells, with trap aided recombination dominating [81]. Regarding band-to-band recombination (*Figure 2.5.2 (a)*), an electron from the conduction band recombines directly with a hole in the valence band releasing a weakly absorbed photon in the process. The photon is said to be weakly absorbed because its energy is equal to the bandgap of the semiconductor and it can exit the semiconductor as is the case in light-emitting diodes (LEDs). Most published literature have considered HaP to have a direct bandgap, which is a requirement for efficient band-to-band recombination. On the other hand, trap-assisted-recombination takes place in semiconductors having mid-gap states or deep level traps. It is a two-step process through a deep-level defect in the bandgap, known as a recombination centre. An electron is first captured by an electron trap, then a hole moves to the same state and recombines with the electron before it can be thermally re-emitted to the conduction band, as shown in *Figure 2.5.2 (b).* Auger recombination is a three-particle non-radiative process including an electron-electron-hole (e-e-h) and a hole-hole-electron (h-h-e) process. In an e-e-h process, an electron first collides and gives its energy to a second electron, pushing it high into the conduction band, as shown in *Figure 2.5.2 (c).* Then the second electron gradually gives off energy as a phonon and relaxes back to the conduction band edge. Auger recombination is the dominant mechanism in $MAPbI_3$ at high carrier concentration and is due to large spin-orbit coupling that distorts the PbI_6 octahedral framework [82]. Suitable halide substitution and strain engineering can suppress Auger recombination. Recombination in HaP solar cells can occur in different regions, including the bulk perovskite layer, perovskite/HTL and perovskite/ETL interfaces, and HTL/ELT shunt paths.

Radiative band-to-band, non-radiative SRH and non-radiative Auger are recombination processes in the bulk of the perovskite absorber of a solar cell. Band-to-band and SRH recombination can be monomolecular or bimolecular. Monomolecular recombination is a first-order process (that is, the rate of recombination is proportional to minority carrier density) in which the rate is dependent on the concentration of one charge carrier species only and the half-life is independent of the carrier concentration (constant) [83]. It can be due to the presence of many electrons or holes, or in a highly doped semiconductor. On the other hand, bimolecular recombination is a second-order process (that is, the recombination rate is proportional to the product of both electron and hole carrier densities) in which the charge densities of both electrons and holes vary considerably. Also, the half-life depends on the carrier concentration. For instance, the recombination via a trap centre that accepts both electrons and holes, that is, the charge carriers find each other. The high PCEs of 3D HaP solar cells is partly attributed to the fact that the free electron-hole bimolecular radiative recombination process is slow; however, this limits the efficiencies of 3D HaP LEDs [83]. Both the monomolecular and bi-molecular mechanisms can co-occur in the bulk of some HaP. For instance, *Milot and co-workers* saw monomolecular recombination processes in FASnI$_3$ and attributed it to the unintended relatively high p-doping of density 5.0 x 10^{17} cm^{-3} [84]. Also, they showed that the monomolecular radiative recombination was active even at very low carrier densities. Furthermore, they proved that FASnI$_3$ also shows strong bimolecular radiative recombination. In Pb-based perovskite that exhibit nonradiative monomolecular recombination rates, SRH tends to be the dominant process at low charge carrier densities.

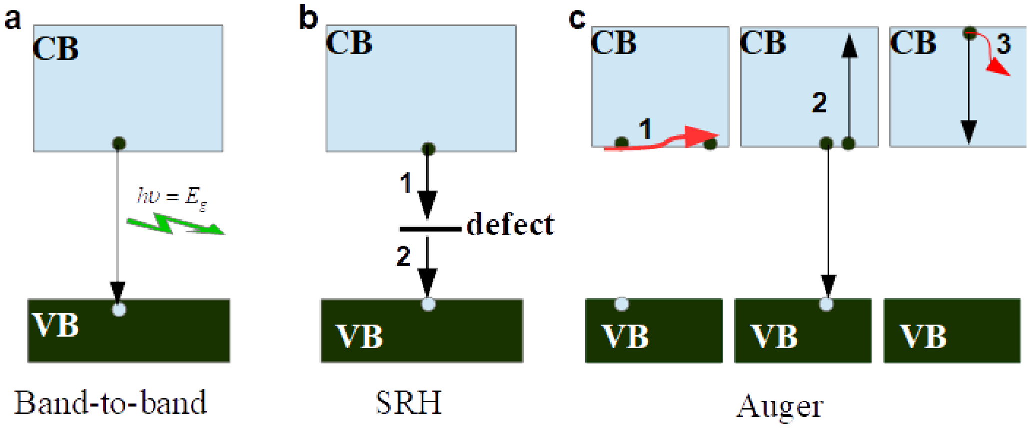

Figure 2.5.2: Schematic diagrams showing various recombination mechanisms, (a) Radiative band-to-band recombination, (b) Non-radiative SRH recombination, (c) Non-radiative Auger recombination.

Figure 2.5.3 shows a schematic diagram of charge injection (continuous lines 4 and 5), interfacial recombination (dashed lines 1 and 2) and shunt recombination (dotted line 3) processes in perovskite solar cells. Recombination at CTL/perovskite interface means an electron injected into an ETL (line 5) recombines with a hole in the perovskite(line 2) or a hole injected into the HTL (line 4) recombines with an electron in the perovskite layer (line 1). This could be due to an imperfect CTL/perovskite band alignment, a low carrier mobility CTL, defects at the CTL/perovskite interface and ion migration [85].

Large interface energy differences cause severe interfacial charge recombination losses that limit PCE [86]. An optimum CTL/perovskite band mismatch of 0.2 eV has been shown to cause efficient charge injection and minimum interfacial recombination losses [87]. An HTL mobility exceeding 10^{-4} cm^2/V s is required for high PCE [88]. *Shekar and co-workers* showed that nonradiative trap-assisted recombination at CTL/perovskite interfaces dominate those at grain boundaries, suggesting performance improvement should be focused on passivation of traps at interfaces [89]. Interestingly, interfacial recombination can be suppressed by introducing a suitable thin insulating interlayer between the CTL and perovskite. These interface modifiers that are deposited on perovskite are expected to passivate the perovskite surface and GB defects, ensure suitable band alignment, and prevent moisture ingress into the perovskite. Some examples of modifiers that reduced HaP/spiro-MeOTAD interface recombination include PTAA, P3HT, Al_2O_3, GO and more, summarized in a review article published by *Chen and co-workers* [85].

As mentioned earlier, charge carrier recombination also occurs through shunt paths (line 3) due to incomplete surface coverage and the presence of pinholes/voids on the perovskite that results in direct contact between the ETL and HTL. This charge loss process depends on the device architecture and perovskite surface morphology only. Earlier efforts on addressing this problem were focused on improving the methods of thin-film deposition to produce quality films, with full surface coverage and no pinholes. *Liu and co-workers* introduced the transition from nanostructured to efficient planar heterojunction devices [16]. They showed that solar cells fabricated by solution deposition of $CH_3NH_3PbI_{3-x}Cl_x$ on TiO_2 compact layer were less efficient (PCE of 8.6% and V_{oc} of 0.84 V) than solar cells from vapour deposited $CH_3NH_3PbI_{3-x}Cl_x$ (PCE of 15.4% and V_{oc} of 1.07 V). This was attributed to the inadequate film coverage of the solution deposited films that created recombination shunt paths that reduced the V_{oc} and PCE. Recently, *Zhu and co-workers* discovered that pinholes in one-step solution-processed 700 nm thick $CsPbIBr_2$ did not form destructive shutting paths [90].

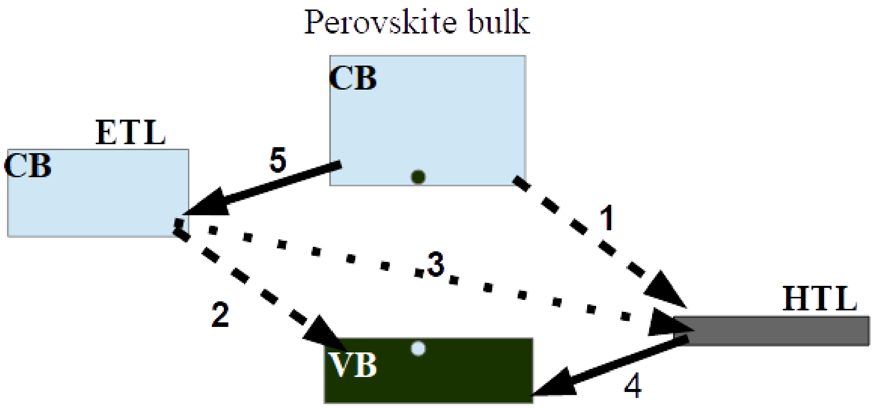

Figure 2.5.3: Schematic diagram of interfacial recombination pathways.

2.5.4 Charge carrier extraction

Following charge carrier generation and transportation towards the interfaces, charges that succeed to arrive at the interfaces (without recombination in the bulk) need to be extracted selectively, with minimal losses in V_{oc}, J_{sc} and FF. An ideal interfacial/selective layer must offer meagre series resistance, not absorb light, select only one type of carrier, have good mobility, and have good band alignment with the perovskite as shown in *Figure 2.5.4*. Previously, CTLs were thought to perform two essential functions, namely, selective carrier injection and exciton dissociation. This meant that high-efficiency solar cells must have both ETL and HTL. However, the paradigm changed when high efficiencies (exceeding 20%) were obtained from HTL-free, and ETL-free and BTL-free solar are presently being fabricated. The new school of thought says a CTL only functions to selectively inject charges and conduct the injected charges to the electrodes where they are extracted to the external circuit. Besides, the electric field in the perovskite layer, for charge separation, was thought to be due to the energy difference between Fermi levels of the HTL and ETL, assuming the electrodes make ohmic contacts with the CTLs.

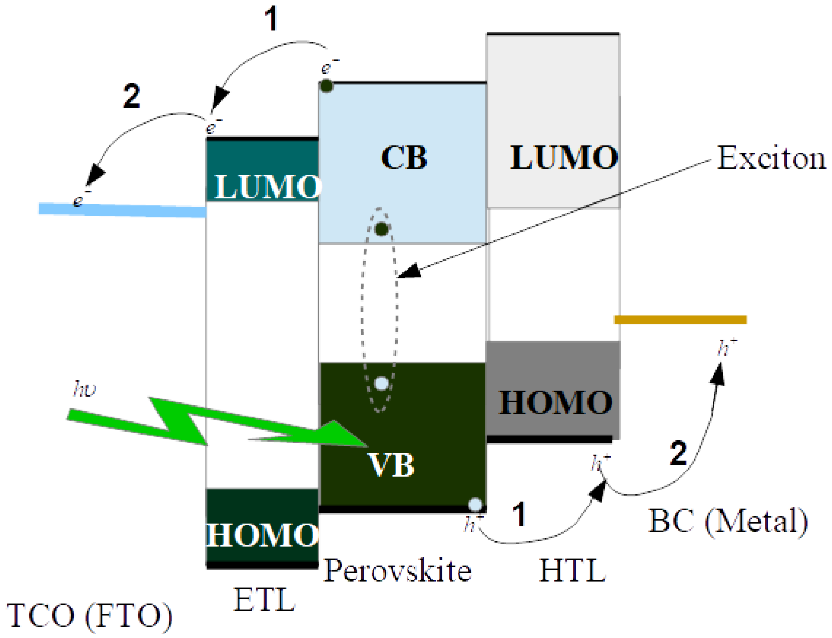

Figure 2.5.4: Schematic diagram of general band alignments and charge carrier extraction of perovskite solar cells.

2.5.5 Band alignment and working principle of BTL-free and HTL-free solar cells

Figure 2.5.5 illustrates the schematic diagrams of band alignments, including the conduction and valence band potentials for FTO/$MAPbI_3$/Au, FTO/$MAPbBr_3$/Au and FTO/$MAPb(I_{1-x}Br_x)_3$/Au BTL-free solar cells. When the light of wavelength greater or equal to the band of the HaP absorber falls on a BTL-free solar cell, it is absorber and weakly bound excitons generated. The generated excitons dissociate within the bulk of the HaP. The free electrons are injected directly into the FTO while the holes are injected into the Au electrodes. The extracted electrons move through the external circuit, dissipate some energy across the load, and finally recombine with holes electrodes.

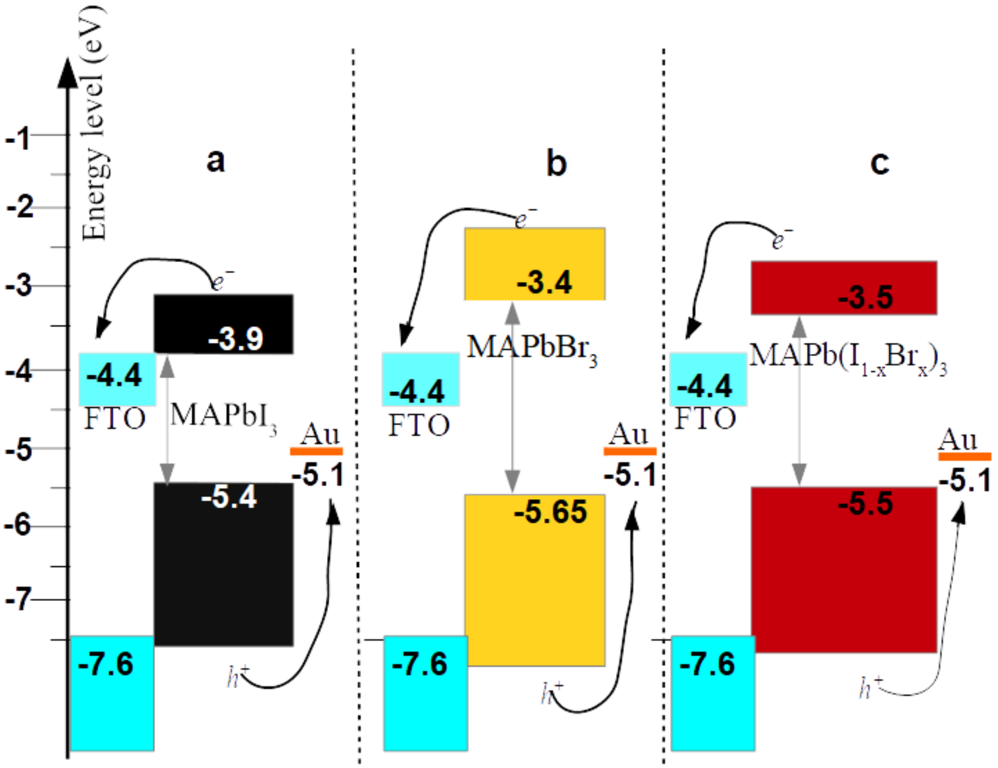

Figure 2.5.5: Schematic diagrams showing band alignments, conduction and valence potentials and charge extraction the fabricated BTL-free solar cells, (a) FTO/$MAPbI_3$/Au solar cell. (b) FTO/$MAPbBr_3$/Au solar cell, (c) FTO/$MAPb(I_{1-x}Br_x)_3$/Au solar cell.

Figure 2.5.6 shows the schematic diagrams of band alignments of FTO/c-TiO_2/m-TiO_2/$MAPbI_3$/Au, FTO/c-TiO_2/m-TiO_2/$MAPbBr_3$/Au and FTO/c-TiO_2/m-TiO_2/$MAPb(I_{0.11}Br_{0.89})_3$/Au HTL-free solar cells, including conduction and valence band potentials.

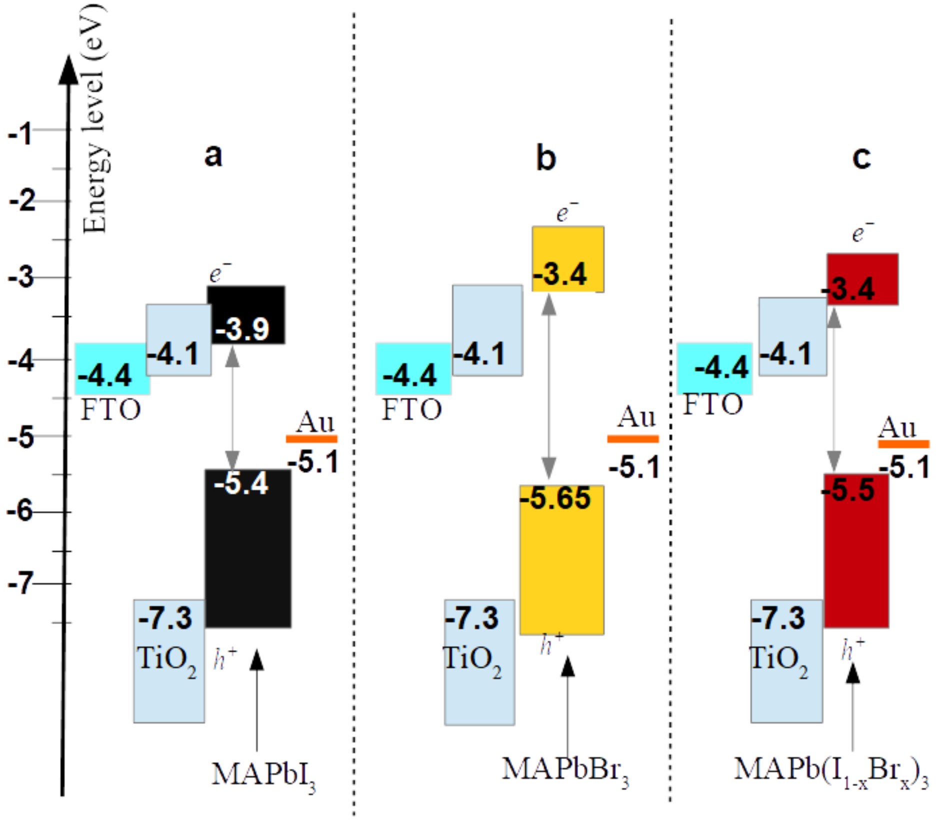

Figure 2.5.6: Schematic diagrams of the band alignments of the fabricated BTL-free solar cells, showing conduction and valence band potentials, (a) FTO/TiO_2/$MAPbI_3$/Au solar cell, (b) FTO/TiO_2/$MAPbBr_3$/Au solar cell, (c) FTO/TiO_2/$MAPb(I_{1-x}Br_x)_3$/Au solar cell.

2.6 Interaction of HaP with metal electrodes

One primary source of instability is caused by the reaction of the HaP with metal electrodes when in direct or indirect contact. Indirect contact occurs when the metal diffuses through the hole and electron transport layers into the active layer of the device or when the halide ions diffuse out of the active layer to the electrode. For instance, corrosion of silver (Ag) electrode due to the reaction with diffused hydrogen iodide (HI), produced during the decomposition of methylammonium lead tri-iodide ($MAPbI_3$) absorber of an encapsulated solar cell, has been shown to speed up the degradation of $MAPbI_3$ [91]. *Wang and co-workers* showed that $MAPbI_3$ reacted rapidly with Ag electrodes, and the reaction was driven by diffused iodide (I^-) ions which caused corrosion of the electrode [92]. Similarly, metal electrodes can diffuse into the HaP active layer through the hole transport layer or electron transport layer, leading to degradation of the perovskite[93,94]. Metal electrodes make direct contact with HaP in the following examples. In simple configurations such as Schottky diodes, BTL-free solar cells, resistive switching devices, and photodetectors involve the deposition of perovskite directly on the metal substrates [95,96]. Also, electrodes are deposited directly on perovskite in hole-conduction-layer-free solar cells [97].

2.7 Tuning the bandgap of HaP

One of the most attractive attributes of thin HaP films is bandgap tunability. This can be achieved by changing the geometry through compositional substitution of the A, B, and X sites. Substitutions of A-site cation alter bandgap by uniform lattice expansion or contraction and tilting of BX_6 octahedral [98]. *Castelli and co-workers* demonstrated that changing the A-site cation from FA through MA to Cs increases the bandgap of the HaP [99]. Likewise, *Prasanna and co-workers* showed that partial replacement of FA with Cs in lead-based perovskite increases the bandgap due to octahedral tilting whereas partial the same partial substitution for tin-based perovskite caused a decrease in bandgap due to isotropic contraction [98]. Uniform lattice contraction raises the energy of the valence band maximum more than that of the conduction band minimum leading to a decrease in the bandgap. The use of large A-site cations (such as DA) form 2D layered perovskite with larger bandgaps than the 3D perovskites. Increasing the size of the group 14 B-site cation (Ge to Sn to Pb) causes a decrease in the bandgap and an increase in chemical and divalent stabilities. Abnormally small bandgaps, less than 1.20 eV, applicable to bottom absorbers in all perovskite tandem cells, have been obtained by mixing Pb and Sn cations [100]. Changes in X-site anions is the most effective way of tuning the bandgaps of HaP. In this case, the difference in bandgap correlates with the change in the electronic states of the anions from 3p through 4p to 5p for Cl, Br and I, respectively. The bandgap changes from 1.55 eV to 3.00 eV as the X-site anions $MAPbX_3$ is changed from I through Br to Cl. Mixing Br and I produce significant changes in the bandgap, capable of covering the entire visible range [101], because of their comparable ionic sizes. Likewise, mixing Cl and I does not lead to noticeable changes in bandgap due to the massive difference in ionic radius. The empirical relationship between the bandgap of the $MAPb(I_{1-x}Br_x)_3$ alloy and that of its $MAPbI_3$ and $MAPbBr_3$ components shown in *Equation 2.4* [101,102],

$$E_g[MAPb(I_{1-x}Br_x)_3] = E_g[MAPbI_3] + \{E_g[MAPbBr_3] - E_g[MAPbI_3] - b\}x + bx^2 \qquad \text{Equation 2.4}$$

where x is the Br mole-ratio, E_g the bandgap, and b is the bowing parameter that accounts for the curvature of bandgap energies with halide composition.

2.8 Defects in HaP

Defects are lattice distortions including structural and chemical inhomogeneities introduced during processing; either intentionally or unintentionally. They have effects on optical, electrical, magnetic, thermal, and mechanical properties. In this section, we will focus on nature, classification, properties, origins, characterisation methods, effects, and mitigations of defects in HaP materials.

2.8.1 Nature and classes of defects in HaP

Defects can be broadly classified as intrinsic or extrinsic. Intrinsic (structural) flaws exist within the crystal lattice of any pure material. On the other hand, extrinsic defects involve those created by foreign species in the crystal lattice. Like in any other semiconductor material, these defects in HaP can be classified based on dimensionality into zero-dimensional (0D), one-dimensional (1D), two-dimensional (2D) and three-dimensional (3D) as displayed *Figure 2.8.1.* The formation of intrinsic defects requires an amount of energy known as the activation or activation energy. Most studies involving the 0D defects have been done computationally by first-principle calculations. However, reviews on the higher dimensional defects have been conducted via computational and experimental methods.

0D defects, also known as microscopic point defects, are defects that occur at or around a single lattice point. They include vacancies, interstitials, Schottky defects, Frenkel defects and ant-sites, as shown in *Figure 2.8.1.* Vacancies are empty positions in a crystal lattice that is typically occupied by a native species. Physically, the formation energy of a vacancy includes the net energy needed in breaking bonds within the bulk, reforming bonds at the surface and restructuring of the lattice. Self-interstitials can be regarded as the reverse of vacancies. These defects occur when an atom or an ion is moved from the surface to a normally unoccupied position (interstitial site) in the bulk crystal lattice. Interstitial sites are usually smaller, and the formation energy energies of these defects usually more significant than for vacancies. By nature, an interstitial and vacancy can form simultaneously if a species is moved from a lattice site to a nearby interstitial location resulting in vacancy/interstitial pair called Frenkel defect. Frenkel pairs occur in ionic lattices where there are large size differences between anions and cations. Smaller energies must form Frenkel pairs than isolated vacancies and interstitial defects. Similarly, vacancies can occur in pairs known as Schottky defects. Schottky defects are neutral paired defects formed when a cation and an anion are simultaneously moved from the bulk of a crystal to its surface, leading to a positive and negative vacancy couple. Other paired defects include anti-sites in which two nearby species exchange positions within a crystal lattice. Examples of points defects in the widely studied $MAPbI_3$ include native defects such as positive iodine vacancies (I_V^+), negative iodine vacancies (I_V^-), neutral iodine vacancies (I_V), negative lead vacancies (Pb_V^{-2}), positive lead interstitial (Pb_i^{2+}), iodide interstitials (I_i), positive methylammonium interstitials (MA_i^+), negative methylammonium vacancy (MA_V^-) and impurities such as Au interstitials [103–105]. *Yang and co-workers* showed that the bulk I_V^+ have low formation energies, low diffusion barriers and fast hopping rates, making them primarily responsible ionic conductivity in $MAPbI_3$ [103]. They also showed that the diffusion barrier and formation energy of gold (Au) interstitial impurities in $MAPbI_3$ are low, leading to possible diffusion of Au into $MAPbI_3$ devices with Au/$MAPbI_3$ interfaces are biased. Meanwhile, defects such as Pb_V^{-2}, Pb_i^{2+} and MA_V^+ have very high activation energies, implying that their formation may require very high temperatures or strong irradiation conditions to form, thus not likely to participate in the defects [105]. Cation substitutions such as MA_{Pb} and Pb_{MA} and substitution anti-sites including MA_I, Pb_I, I_{MA} and I_{Pb} are also present in $MAPbI_3$ [106,107]. The nature of Schottky defects and Frenkel type defects have also been studied in HaP. *Dewinggih and co-workers* showed that iodine vacancy/interstitial (I_V^+/I_V^-) Frenkel-pair trapping centres are abundant in $MAPbI_3$ and are annihilated under illumination conditions which increases photoluminescence quantum efficiency [108]. *Kim and co-workers* showed that the formation energies of Schottky defects (neutral vacancy pairs) such as PbI_2 and MAI in $MAPbI_3$ are relatively low. [109]. Fortunately, these defects are not trap-states that can reduce carrier lifetime. A Schottky couple in HaP has very low formation energies and originates from halide vacancy coupling with the metal vacancies [105].

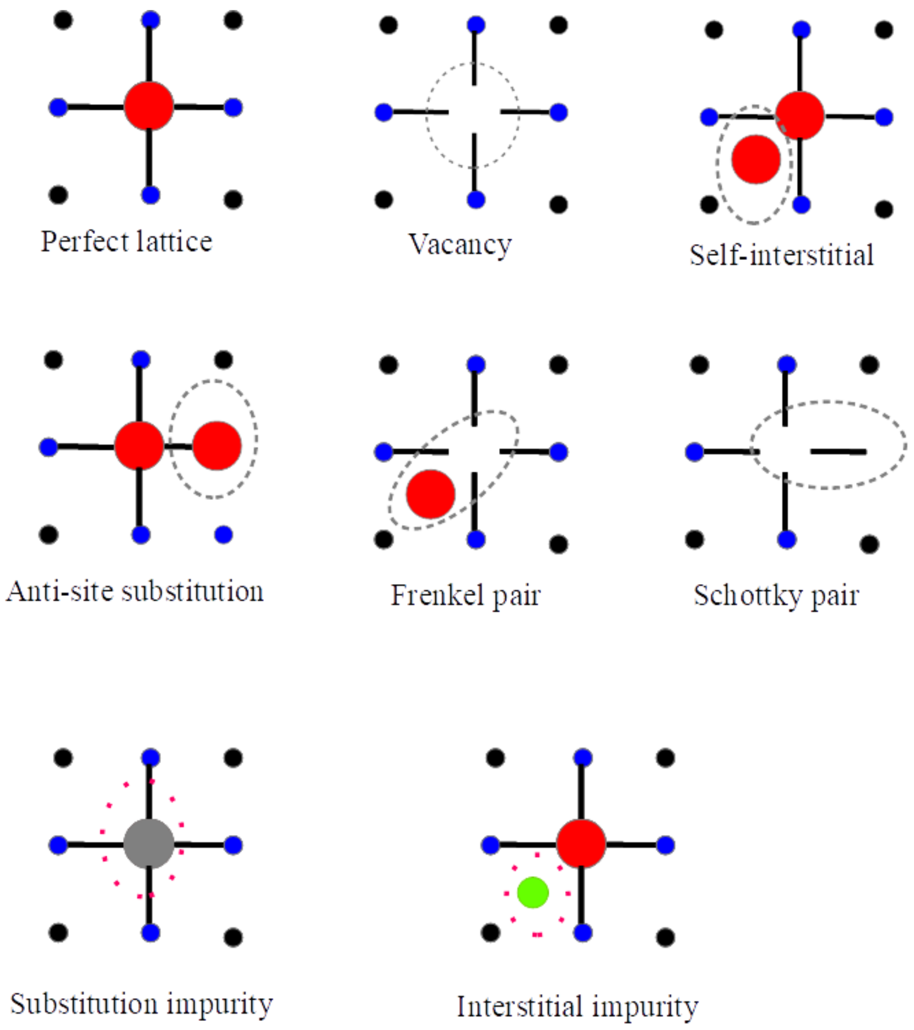

Figure 2.8.1: Schematic diagrams of intrinsic (dashed lines) and extrinsic (pink dots) point (0D) defects [122]

1D defects, also known as line defects, are due misalignment of ions and the presence of vacancies along a line. The two types of dislocations; edge and screw dislocations are typical examples of line defects. Dislocations determine the mechanical and electronic properties of semiconductors. Edge dislocation arises when lines of ions are missing from a naturally perfect array of ions. It can be visualized as an extra half-plane of ions ending inside in crystal and causing the adjacent planes to bend symmetrically at the edge of this half-plane. Screw dislocations, on the other hand, is due to a line misalignment that shifts a block of ions gradually upwards or downwards. Dislocations are characterized by the Burger’s vector, which perpendicular to dislocation line for edge dislocation and parallel to the line for screw dislocation. Dislocation density, ρ, is related to the crystallite size, D, by Williamson and Smallman formula [110] given by *Equation 2.5*,

$$\rho = \frac{n}{D^2} \qquad \text{Equation 2.5}$$

where n equals unity for minimum dislocation density, like in conventional semiconductors, dislocation density (number of dislocation lines per unit area) has adverse effects on carrier lifetimes, diffusion lengths and photoluminescence quantum efficiencies of HaP. By controlling the dislocation density using a remote epitaxy approach involving the growth HaP on polar graphene-coated substrates, *Jiang and co-workers* showed that carrier lifetime in HaP is enhanced by reducing dislocation density [111].

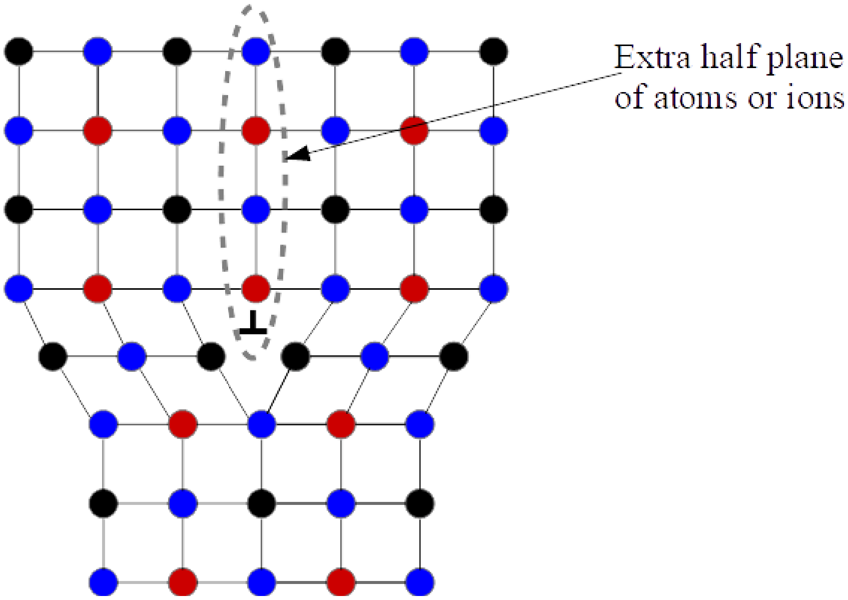

Figure 2.8.2: Edge dislocation along an axis perpendicular to the page.

2D defects are planar defects and include grain boundaries (GBs), surfaces or perovskite/transport layer interfaces, stacking faults and twin boundaries. GBs are interfaces between two grains in polycrystalline materials, as shown in *Figure 2.8.3 (a).* In HaP, GBs are sources of high defect densities, trap accumulation sites, infiltration sites for water vapour and fast pathways for ion migration due to reduced steric hindrance [112]. GBs serve as trapping centres for charge carriers leading to non-radiative recombination that reduces carrier life-time and also causing hysteresis in the current-voltage characteristic [113]. *DeQuilettes and co-workers* [114] measured the photoluminescence intensities and carrier lifetimes from different grains and grain boundaries of the same $MAPbI_3$ thin film. They concluded that grain boundaries are dimmers and show the fastest nonradiative recombination. The surfaces of HaP are also defective, as shown in *Figure 2.8.3 (b).* They contain a large number of charged defects [115] including iodine vacancies [116], X-terminating surfaces with nonstoichiometric compositions and improper bonding; (110)-X_2 halide surfaces with a large number of broken bonds [117,118]), and Pb dangling bonds [118]. SRH recombination at interfaces with the transport layers is the dominant loss mechanism in perovskite solar cells [89]. With regards to stacking faults, they occur in crystals characterized by a periodic sequence of atomic planes due to an interruption in the typical regular arrangement. *Song and co-workers* showed that $MAPbI_3$ phases with I/Pb ratios ranging from 3.2 to 3.5 form stacked perovskite sheets with a large amount of stacking faults whereas thin films with I/Pb ratios ranging from 2.9 to 3.1 form the conventional 3D perovskite with few stacking faults (alpha phase) [119]. First-principles studies of electronic properties of {111} twin boundaries in mixed HaP containing FA, Cs, Br and I revealed that twin boundaries in these perovskites are nucleation sites for I-rich and Cs-rich formation, which are hole traps and can cause electron-hole recombination leading loss in V_{oc} [120]. Direct imaging using TEM has revealed twin boundaries in a $MAPbI_3$ thin film range from 100-300 nm wide with twin boundaries parallel to $\{112\}_t$ [121]. By varying the anti-solvent during deposition, *Tan and co-workers* were able to change the defect density of the (111) twin boundary for $Cs_{0.05}FA_{0.81}MA_{0.14}PbI_{2.55}Br_{0.45}$ mixed perovskite to establish the relationship with PCE [122].

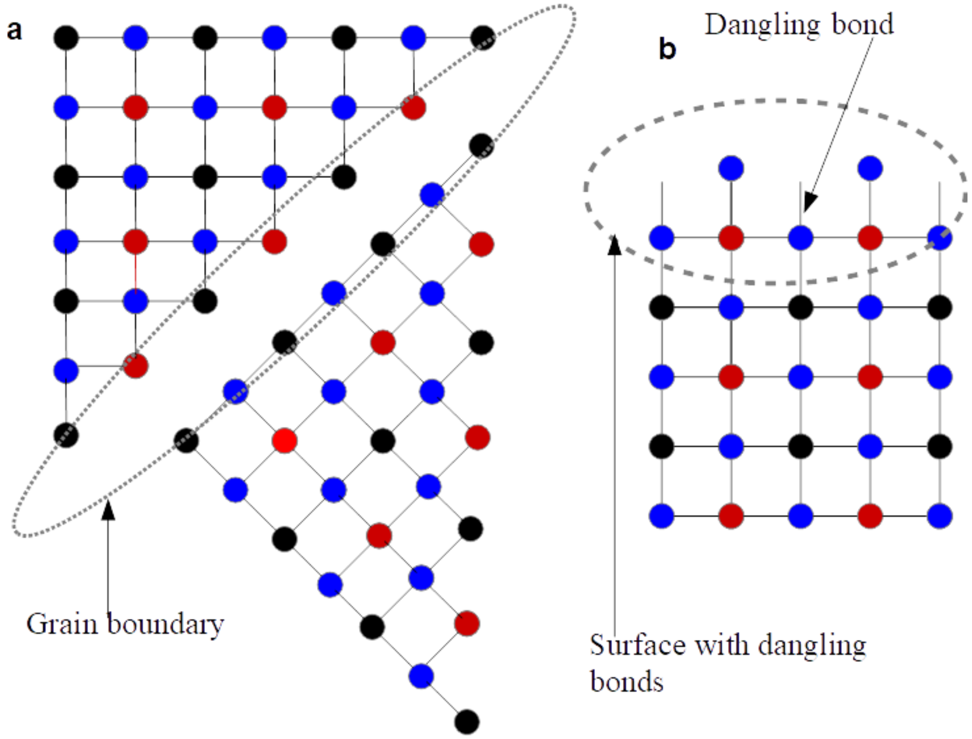

Figure 2.8.3: Schematic diagram showing grain boundaries and surface defects (dangling bonds) in HaP.

3D defects, also known as volume or spatial defects, are macroscopic defects including cracks, voids, or pinholes (clusters of vacancies), and precipitates (groups of impurities) formed by a concentration of lower-dimensional defects. Voids can be regarded as a coalition of vacancies, as shown in *Figure 2.8.4 (a).* Cracks (*Figure 2.8.4b*) can form quickly on HaP thin films during processing and under the application of bending-tensile stress due to the brittle nature. *Yadavalli and co-workers* saw random grain boundary micro-cracks after processing of $MAPbI_3$ and $FAPbI_3$ thin films. Also, they showed that macro through-thickness cracks, introduced by bending-tension, could be healed simply by mechanical and time-dependent thermal treatments [123]. Mechanically, the cracks were healed by bending-compression stress followed by fattening and thermally, by annealing at 100℃ for 5 min or 80℃ for 10 min. The presence of voids in HaP thin films is inevitable, and their effects on solar cells efficiency are detrimental. The density of voids on the surface of a HaP thin-film depends on the preparations methods [124,125]. *Li and co-workers* showed that $MAPbI_3$ films produced by two-step dipping under static growth conditions had more pinholes than those grown under dynamic dipping conditions (stirring MAI solution with PbI_2 substrate) [125]. Seo and co-workers reported a direct observation of voids and fiend-assisted void passivation in HaP films on FTO using electron beam induced current (EBIC) technique. They showed that the voids were trapping centres for electrons and holes and could be passivated by materials with bandgaps higher than that of the HaP. The material causes a change in the band structure of the HaP, leading to the creation of an electric field near the void that prevents charge carrier trapping, reducing recombination and improving efficiency [126]. Besides, the voids caused the delamination of the perovskite thin film by weakening the adhesion force between the film and the substrate. To the best of my knowledge, no studies on precipitates in HaP have been reported in the literature.

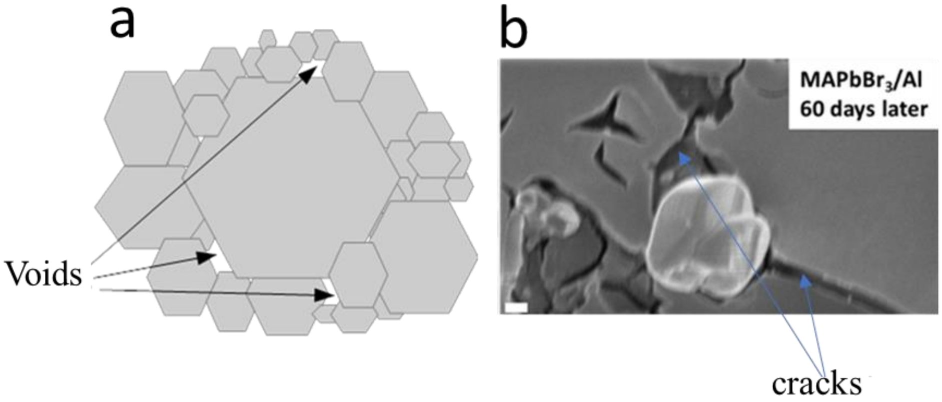

Figure 2.8.4: 3D defects (a) Schematic diagram of voids (pinholes), (b) SEM micrograph showing cracks of Al substrate having $MAPbBr_3$ grains.

2.8.2 The role of defects on HaP

There are so many conflicting reports about the role of defects on the performance of solar cells and other optoelectronic devices. Some reports say that defects have adverse effects on performance while other literature, for the same defects, claim they have positive influences. Also, understanding the role of defects in devices is very difficult because the intrinsic ‘soft’ nature of HaP may lead to variable (time-dependent) defect density [105]. This dynamic defect density may be due to the ease of creating and destroying charge trap states by external stimuli [105].

Elemental Freckle defects like I, Pb and CH_3NH_3 vacancies serve as dopants in $MAPbI_3$ [109]. This explains self-doping property in $MAPbI_3$. That is, the ability to change from p-type through intrinsic to n-type semiconductor only by changing concentration or processing temperature. GBs serve as significant charge dissociation centres and photocurrent transduction pathways rather than recombination centres [127]. Effective charge separation and collection photogenerated charges in $MAPbI_3$ thin films for $MAPbI_3$/FTO/TiO_2/FTO heterojunction structures [128]. They showed that the mid-gap and shallow defect states in $MAPbI_3$ do not accelerate electron-hole recombination, and the I_i instead suppressed it by a factor of 2 [129]. They proved that photogenerated carriers only couple with low-frequency phonons (from a weak coupling between inorganic and organic lattice) and the coupling between electron and hole states are soft, explaining the defect tolerance in HaP.

Hole trapping by iodide interstitials reduces free carrier losses $MAPbI_3$ which partly explains their defect tolerance nature [130]. The presence of air-induced shallow defects increases the photoluminescence intensity of $MAPbBr_3$ single crystal in the air compared to that it vacuum[131]. Surface defects or grain boundaries serve as trapping centres for charge carriers. These grain boundaries accelerate nonradiative recombination, reduces carrier lifetime and causes hysteresis in the current-voltage characteristic [113]. Defects induce local changes in crystal phase transition temperatures in metal HaP[132]. The presence of defects reduces the electrical conductivity of $MAPbBr_3$ single crystals [131]. I_i produces mid-gap states in $MAPbI_3$ that rapidly trap charge carriers, thus reducing carrier density and accelerating nonradiative electron-hole recombination [133]. *Qiao and co-workers* obtained contrary results after considering the coupling effect with low-frequency phonons using ab initio nonadiabatic molecular dynamics. Pinholes in HaP thin films cause direct contact between the ETL and the HTL, leading to leakage current and voltage losses [134].

2.8.3 Traps in HaP

Traps are defect states with energy level within the bandgap of a semiconductor. Charged carriers can be held in charge traps either permanently or temporally depending on the depth of the energy level. Charge traps with energy levels close the valence or conduction bands are called shallow traps. Charge carriers held in shallow traps can be emitted after some time before they recombine with the opposite charge carrier that may later be captured by the same trap. Deep traps, on the other hand, have energy around the middle of the bandgap and are called mid-gap states. Charge carriers captured by mid-gap may not be re-emitted before they recombine the opposite charge carriers, thus are called recombination centres. Traps are electrically charged when empty but neutral when filled with photogenerated charge carriers [104].

Despite the many reports on the defect tolerance in HaP, numerous theoretical and experimental studies still reveal the presence of traps with different characteristics [135]. Properties related to traps include trap density, energy level, capture cross-section and chemical nature. The trap density depends on composition, crystallinity, position on the surface of grains and the depth in grains. Based on the position on the surface, *DeQuilettes and co-workers* showed that trap density is higher at the grain boundaries than at the centre of the grains, and varies from grain to grain in HaP thin films [114]. Likewise, *Ni and co-worker* investigated the dependence of defect density on the depth and showed that the density of surface traps in $MAPbI_3$ single crystals is higher than in the bulk [136]. They also saw that charge density at the interfaces in polycrystalline thin films is more significant than in the interior of the films.

Furthermore, looking at crystallinity, they showed that trap density at the interior of thin films is greater than in the bulk of single crystals. In line with composition, *Ni and co-workers* saw that the trap density of $MAPbBr_3$ single crystal (3.0×10^{10} cm^{-3}) was greater than that of $MAPbI_3$ single crystals (1.4×10^{10} cm^{-3}), with the same growth conditions. Generally, HaP have very low trap densities contrary to what is expected from low temperature and cheap solution-processed materials [137]. The low density of traps is attributed to defect tolerance [138,139]. Like many other semiconductors, defects in HaP can be grouped into shallow and deep traps based on their energy level within bandgap as shown in

Figure 2.8.5. Frist-principle calculations have revealed that the dominant intrinsic defects in $MAPbI_3$ are shallow levels [140,141]. This partial supply explanation of the long electron-hole diffusion length and high V_{oc} of $MAPbI_3$ solar cells. The probability of forming deep traps increase as one moves from I through Br to Cl due increase in the bandgap. *Kim and co-workers* observed that deep level straps are formed due to the bonding states between dangling Pb and X and shorter Pb–X bond lengths and wider bandgaps increase the possibility [141]. *Jin and co-workers* claim that point defects in $MAPbI_3$ are expected to produce only shallow traps [106], even though, I_i and its complexes with MA_V have been reported to induce deep level by Du [142]. Experimental evidence of deep level traps has also been reported in $MAPbI_3$. *Heo and co-workers* identified deep levels with energies at E_1 (0.62 eV), E_2 (0.75 eV) and E_2 (0.76 eV) using deep level transient spectroscopy [137]. Co-workers Likewise, *Legodi and co-workers* identified two dominant shallow defects in $MAPbBr_3$ single crystals with energies at 0.17 eV and 0.20 eV from the conduction band edge [143]. The chemical nature of traps determines the type of carrier they capture. Traps that capture electrons are known electron traps (*Figure 2.8.5(a)*) while those that capture holes are known as hole traps (*Figure 2.8.5(b)*). Deep level traps, shown in *Figure 2.8.5(c),* can capture both. Another unique property associated with defects is the reversible disappearance of defects in vacuum leading to the improved electrical conductivity of HaP in a vacuum than in air [131].

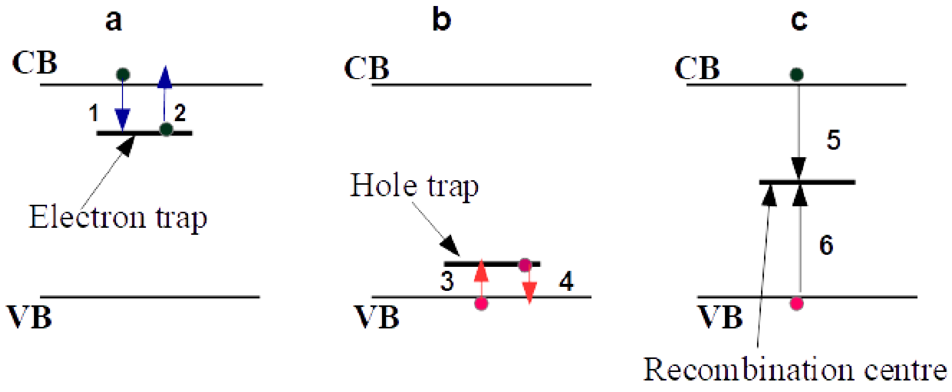

Figure 2.8.5: Schematic diagrams of nature of trap states in HaP, (a) Shallow electron trap state, (b) Shallow hole trap state, (c) Deep level trap state (recombination centre).

2.8.4 Ways of Mitigating defects

It has been shown that recombination centres limiting charge carrier lifetimes in HaP are preferentially located close to the surface rather than in the bulk of the crystal [144]. Most attempts to mitigate these surface defects involve using different additives that will either improve film morphology by increasing the grain size to reduce the number of grain boundaries or cause surface passivation [145]. *Figure 2.8.6 (a, b)* is the schematic diagrams of defective and passivates surfaces. Grain boundaries serve as perfect sites for surface traps and also offer opposition to the flow of charge carriers [145]. The effect of grain boundaries on a lifetime of charge carriers has been reduced by passivation of the perovskite surface with Lewis acid additives like 1,2-ethanedithiol [144] and Lewis base additives [70]. They suggested that the Lewis bases donate electrons to surface traps, thus preventing them from capturing charge carriers while the Lewis acids donate protons, as shown in *Figure 2.8.6 (b).* Surface treatment by post-deposition of a variety of Lewis bases (electron-donating molecules) and surface ligands passivates surface defects, thereby reducing non-radiative recombination. The presence of excess PbI_2 between grain boundaries also has a passivation effect [146]. The addition of an optimum amount of potassium iodide (KI) in triple cations $(Cs_{0.06}FA_{0.79}MA_{0.15})Pb(I_{0.85}Br_{0.15})_3$ perovskite reduces non-radiative losses and photoinduced halide ion migration by passivation the perovskite film and interfaces [147]. This is achieved by the excess iodide from KI compensating for any halide vacancies (trap states). At the same time, potassium ion selectively depletes bromide from crystal, thereby reducing trap states that results from bromide rich perovskite. The formation of benign (potassium-rich, halide-sequestering species) from excess halides at the grain boundaries and interfaces, immobilizes halide ion migration. The addition of a strong electron acceptor of 2,3,5,6-tetrafluoro7,7,8,8-tetracyanoquinodimethane (F4TCNQ) into perovskite functional layer, fills grain boundaries, thus reducing metallic lead defects and iodide vacancies significantly [148]. Excess MAI intrinsically passivates the surface of $MAPbI_3$ films leading to reduced surface recombination velocity and improved total carrier lifetime [149]. Additives such as sulfonated carbon nanotubes [145], Lewis bases like urea and thurea [150] and Lewis acid−base adduct (for example, PbI_2 adduct with O-donor DMSO is excellent for improving grain size in $MAPbI_3$ and PbI_2 adduct with S-donor thiourea is excellent for $FAPbI_3$) [151] mitigate defects by producing larger grains with fewer grain boundaries. Addition of sulfonated carbon nanotubes also passivates perovskite by filling grain boundaries [145]. Other Lewis bases such as thiophene and pyridine passivate the perovskite surface by donating an electron to under-coordinated Pb atoms present in the crystal [70]. Fullerenes (PCBM) deposited on the top of the perovskite have a passivation effect which reduces photocurrent hysteresis and trap density [152]. Defects in perovskite solar cells can be healed by light and humidity of a certain amount [153]. The effect of combining light and atmospheric treatments increases the internal luminescence quantum efficiencies of polycrystalline perovskite films from 1% to 89%, with carrier lifetimes of 32 µs and diffusion lengths of 77 µm, which are comparable with results from low defect density perovskite single crystals [153]. The substitution of iodine with chlorine in $MAPbI_3$ improves on morphology and reduces bulk trap density [74]. Defects in HaP can be annihilated by creating a vacuum [131]. *Qiao and co-workers* showed that alkalis metals mitigate I_i defects in two ways: by increasing its formation energy thus reducing concentration, and binding strongly to them thereby eliminating mid-gap states that act as traps for electrons and holes, thereby increasing carrier density and extending the carrier lifetimes significantly [133]. *Fang and co-workers* showed that the 4-fluorophenylmethylammonium-trifluoroacetate additive passivates both uncoordinated the lead and halide ions in mixed-cation mixed-HaP, $FA_{0.33}Cs_{0.67}Pb(I_{0.7}Br_{0.3})_3$ [154]. This is possible because the trifluoroacetate anion binds with lead cation and the 4-fluorophenylmethylammonium cations with the halide ion. This dual passivation suppressed hysteresis, halide segregation and ion migration leading to an improvement in the operational lifetime of light-emitting diodes from 1.0 to 14.0 h.

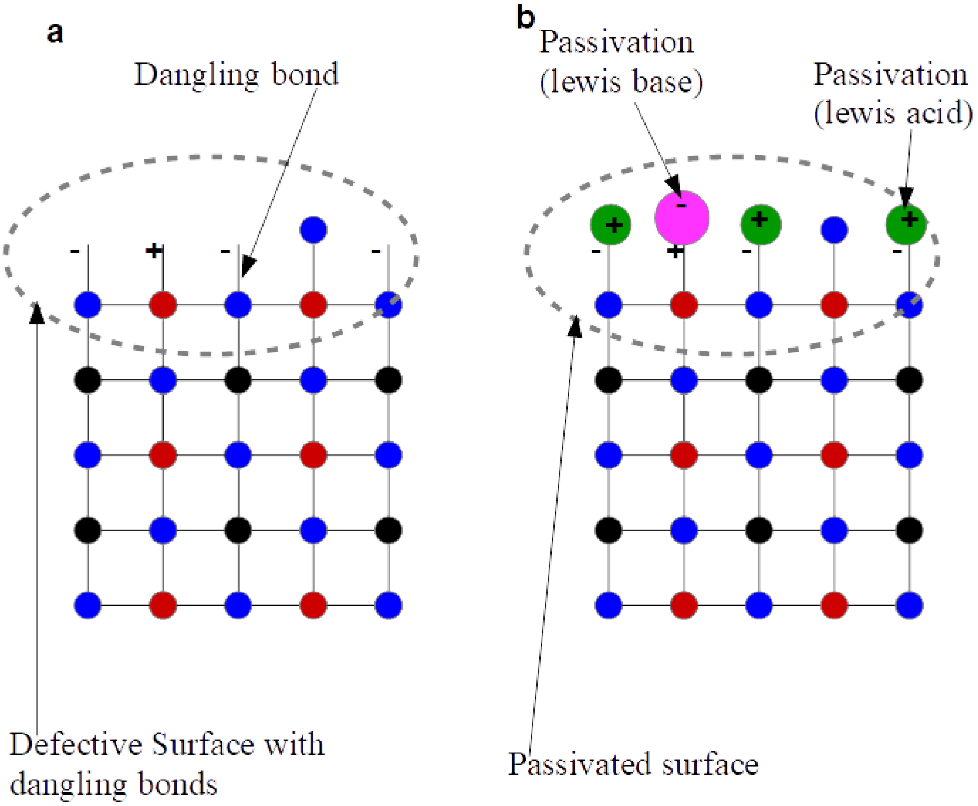

Figure 2.8.6: Schematic diagram showing defective and passivates surfaces.

2.8.5 Characterisation of trap density in HaP by space charge limited current (SCLC) theory

Characterisation of defects involves determining the trap density, energy level, capture cross-section and nature or type of defects in a material. Bulk defects in HaP have so far been characterised using the following methods; space charge limited current (SCLC), thermal admittance spectroscopy (TAS), thermal stimulated current (TSC), steady-state photoluminescence spectroscopy (SSPLS), deep level transient spectroscopy (DLTS), current deep level transient spectroscopy (I-DLTS), transient resolved photo-luminescence (TR-PL) and kelvin probe force microscope (KPFM). The working principle, advantages and disadvantages of the methods above were reviewed intensively by *Ran and co-workers* in 2018 [135]. Though it was very challenging to characterise surface defects, transient refection pump-probe (TRPP) technique has been successfully employed to measure the surface transport properties like diffusion coefficient and surface recombination velocity (SRV) [149].

SCLC trap density and mobility measurements involve a simple analysis of the current (*I*)-voltage (*V*) characteristics of single-carrier devices, which consist of an insulator/semiconductor sandwiched between two selective ohmic contacts. These devices have the same architecture as those used in solar cells and diodes as opposed to other methods which involve the use of either very thick devices (time-of-flight method) or lateral structures with lateral charge transports (field-effect-transistor mobility measurements) [155]. A semi-log plot of the dark *I-V* data for forward and reversed bias is first plotted to verify the nature of the contacts. If the curve is symmetric then it confirms that the contacts are ohmic hence SCLC theory may be valid. The trap density and mobility then determined from the double-log *I-V* curves. This was achieved by performing a linear fit at different parts of the graphs to determine the exponent of the general power-law given by *Equation 2.6* [156],

$$I = kV^{m}$$

Equation 2.6

where *k* is a constant and *m* the exponent, corresponding to the slope of the double-log *I-V* curve and determines the transport mechanism. *m* ~ 1 at low voltages contacts and the bulk conduction mechanism are ohmic[157], and the conductivity of the system depends on both mobility and equilibrium carrier concentration [158]. In this case, the thermally generated free charge carrier density is greater than the injected carrier density, and current is driven by the drifting of mobile charge carriers that are intrinsically present in the material [156]. This is true for metals and highly doped semiconductors where the relationship between the current density (*J*), majority carrier concentration (*n*), majority carrier mobility (μ_p), charge (*q*), thickness/length (*L*), and applied voltage (*V*) is given by *Equation 2.7,*

$$J = q\mu_p n \frac{V}{L}$$

Equation 2.7

The equation does not describe conduction in the linear regime for intrinsic and lowly doped semiconductors. The conduction for such materials has been shown to depend on both drift and diffusion of charge carriers due to space charges. The relationship between *J, q,* μ_p*, V, L,* the relative permittivity of material (ε_r) and permittivity of free space (ε_0) in this case is given by *Equation 2.8* [157],

$$J = 4\pi^2 \frac{K_B T}{q} \mu_p \varepsilon_0 \varepsilon_r \frac{V}{L^3}$$ Equation 2.8

where $\mu_p K_B T/q$ is the Einstein-Smoluchowski diffusion coefficient, and T is the absolute temperature. At a specific voltage known as the cross-over voltage, V_x, there is a transition from the linear regime to trap-free square law (m =2). At V_x, the density of the thermally generated charge carrier equals the density of injected charge carriers. The region in which $m = 2$ is called the space charge limited current (SCLC) region. Current density in this region only depends on carrier mobility and no more on equilibrium carrier concentration and is dominated by injected carriers from the contacts [158]. In this circumstance, the relationship between J, L, ε_r, ε_0, μ_p and V follows the Mott-Gurney law given by *Equation 2.9,*

$$J = \frac{9}{8} \varepsilon_o \varepsilon_r \mu_p \frac{V^2}{L^3}$$ Equation 2.9

The derivation of Mott-Gurney law assumes the following: only one type of charge carrier is present, the electric field at injecting electrode is zero, the current is not limited by traps, the magnitude of permittivity and carrier mobility is constant, and material has no intrinsic conductor but charges are injected from one electrode and collected from the other. However, practical semiconductors have traps, and the Mott-Gurney law is changed to accommodate them.

In the presence of shallow traps, the cross over occurs when the injected trap density doubles the thermally generated trap density, and m is slightly more significant than two [159]. For semiconductors with deep level traps, a very steep region exits on double-log I-V plot, with a slope that is far more significant than two [158]. The cross-over voltage in the presence of traps is also known as the charge filled voltage limit, V_{TFL}. In this case, localized trap-states are supplied as the voltage is increased up to V_{TFL}, after which there is a transition from ohms law to trap-free square rule. The modified Mott-Gurney law [160] is then applied to calculate the carrier mobility, is given in *Equation* 2.10,

$$J = \frac{9}{8}\varepsilon_o \varepsilon_r \theta \mu_p \frac{V^2}{d^3}$$ Equation 2.10

where θ is the trap factor, the ratio of free charge carriers to the sum of free and trapped charged carriers. This equation is used to calculate μ_p in the presence of traps that are found at discrete levels above the valence band. The N_t is calculated using *Equation 2.11* [161],

$$V_{TFL} = qN_t \frac{d^2}{2\varepsilon_o \varepsilon_r}$$ Equation 2.11

where N_t is trap density, *d* is film thickness, ε_r is equal to 25.5 for $MAPbBr_3$ [161].

2.9 Mott-Schottky (M-S) theory on HaP

M-S analysis is a well-established experimental technique to determine the charge carrier density (N_d) and the built-in voltage (V_{bi}) from *C-V* measurements. It is widely applied in conventional semiconductor devices with p-n and semiconductor/metal junctions, which have a fixed depletion or space charge region. The junction (depletion) capacitance per unit area C_{dl} is given by *Equation 2.12,*

$$\frac{1}{C_{dl}{}^2} = \frac{2\varepsilon_o \varepsilon_r}{qN_d}(V_{bi} - V)$$ Equation 2.12

Where N_d is the doping density of the donor and V_{bi} is the built-in voltage. M-S plot is a graph of C_{dl}^{-2} vs. *V* from which the N_d is obtained from the gradient of the linear part and V_{bi} is the intercept obtained after extrapolation of the linear component to the voltage axis as shown in *Figure 2.9.1.* The linear region with negative slope exists on the plot under particular condition incorporating the requirement that there are no electrons/holes in the space charge region and there is a homogenous distribution of the space charges [162,163].

The M-S plot for HaP solar cells differ from that of conventional semiconductor solar cells like silicon, as shown in *Figure 2.9.1* [164]. The M-S plot for silicon solar cells, having a fixed depletion layer, shows an extended linear part with a negative slope, as shown in *Figure 2.9.1 (a).* In such solar cells, only one capacitance type, the depletion capacitance, exists in the capacitance-voltage spectrum. The capacitance spectrum for perovskite solar cells consist of three distinct regions associated with different mechanisms: a constant (geometric) capacitance, a depletion capacitance and an exponential capacitance region [165]. *Figure 2.9.1 (b)* shows the M-S plot for our fabricated FTO/c-TiO_2/m-TiO_2/$MAPb(I_{0.11}Br_{0.89})_3$/Au HTL-free solar cells, showing the three distinct regions in the -0.5 to 2.0 V range. The constant geometric capacitance region, having capacitance per unit area, C_g, occurs for negative bias and zero bias and is due to the polarisability of the perovskite. It shows that the $MAPb(I_{0.11}Br_{0.89})_3$ is fully depleted for applied voltages in this range; that is, the width of the depletion layer is more significant than its geometric thickness [166]. Following this region, is a depletion capacitance region ranging from 0 to 0.2 V, with capacitance per unit area given by C_{dl}, standing for the linear region with a negative slope that can be extrapolated as shown to obtain V_{bi} as shown in *Figure 2.9.1.* As the biasing voltage is made more positive towards the V_{bi}, there is a deviation from the linear dependence on M-S plot as the capacitance tends to increase exponentially. The exponential capacitance, also known as the diffusion capacitance [167], has previously been attributed to the charged ions accumulation occurring at the TiO_2/perovskite and perovskite/Au interfaces [162,165]. For other semiconductors, *Bera and co-workers* attributed an exponential increase in capacitance with an increasing negative bias to the accumulation of electrons, a constant capacitance to depletion region, and exponential growth at a forward bias to the accumulation of holes [168]. Other reasons for the constant capacitance may include the presence of injection barriers [169] and accumulation of space charges at the interfaces [162,165,167,170], which may be due to low level of doping, intrinsic nature of the perovskite and the presence mobile ions [162].

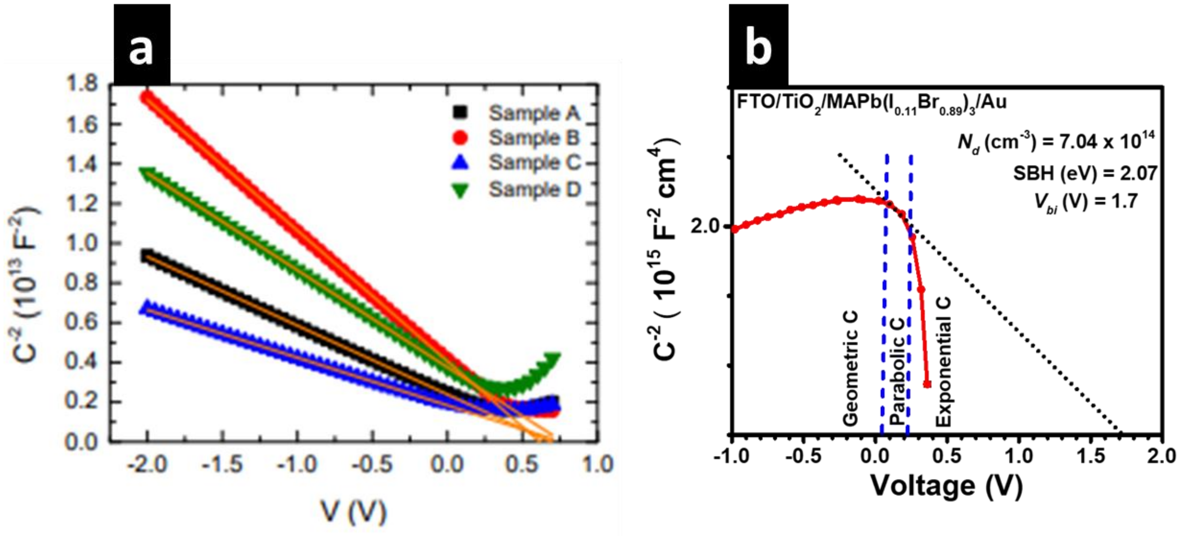

Figure 2.9.1: (a) Mott-Schottky plot for high-efficiency silicon solar cells from the literature [164], *(b) Mott-Schottky plot for FTO/c-TiO_2/m-TiO_2/$MAPb(I_{0.11}Br_{0.89})_3$/Au HTL-free solar cell.*

References

[1] S. Thomson, Observing phase transitions in a halide perovskite using temperature-dependent photoluminescence spectroscopy, Edinburgh Instruments, (2018) AN_P45.

[2] X. Liu, W. Zhao, H. Cui, Y. Xie, Y. Wang, T. Xu, F. Huang, Correction : organic-inorganic halide perovskite-based solar cells – revolutionary progress, Inorg Chem Front. 2 (2015) 584-584. doi:10.1039/c5qi90015h.

[3] T. Qiu, Y. Hu, F. Xu, Z. Yan, F. Bai, G. Jia, Recent advances in one-dimensional halide perovskite for optoelectronic applications, Nanoscale 10 (2018) 20963–20989. doi:10.1039/c8nr05862h.

[4] E. Shi, B. p. F. Gao, Yao, Akriti, A.H. Coffey, L. Dou, Two-dimensional halide perovskite nanomaterials and heterostructures, Chem. Soc. Rev. 47 (2018) 6001–6446. doi:10.1039/c7cs00886d.

[5] C. Zhang, D. Kuang, W. Wu, A review of diverse halide perovskite morphologies for efficient optoelectronic applications, 1900662 (2019) 1–30. doi:10.1002/smtd.201900662.

[6] S.N. Ruddlesden, P. Popper, The compound $Sr_3Ti_2O_7$ and its structure, Acta Cryst. 11 (1958) 54–55. doi.org/10.1107/S0365110X58000128.

[7] D.H. Cao, C.C. Stoumpos, O.K. Farha, J.T. Hupp, K.G. Mercouri, 2D homologous perovskite as light-absorbing materials for solar cell applications, J. Am. Chem. Soc. 2 (2015). doi:10.1021/jacs.5b03796.

[8] P. Chen, Y. Bai, S. Wang, M. Lyu, J. Yun, L. Wang, In situ growth of 2D perovskite capping layer for stable and efficient perovskite solar cells, 1706923 (2018) 1–10. doi:10.1002/adfm.201706923.

[9] Q. Jiang, Y. Zhao, X. Zhang, X. Yang, Y. Chen, Z. Chu, Q. Ye, X. Li, Z. Yin, J. You, Surface passivation of perovskite film for efficient solar cells, Nat. Photonics. 13 (2019) 460–466. doi:10.1038/s41566-019-0398-2.

[10] T. Niu, J. Lu, X. Jia, Z. Xu, M. Tang, D. Barrit, N. Yuan, J. Ding, X. Zhang, Y. Fan, T. Luo, Y. Zhang, D. Smilgies, Z. Liu, A. Amassian, S. Jin, K. Zhao, S. Liu, Interfacial engineering at the 2D/3D heterojunction for high-performance perovskite Solar Cells, Nano Lett. 19 (2019) 7181–7190. doi:10.1021/acs.nanolett.9b02781.

[11] Y. Li, J. Feng, H. Sun, Perovskite quantum dots for light-emitting devices, Nanoscale 11 (2019) 19119–19139. doi:10.1039/c9nr06191f.

[12] R.J. Sutton, Towards stable perovskite materials for photovoltaics, University of Oxford, 2018.

[13] Y. Deng, E. Peng, Y. Shao, Z. Xiao, Q. Dong, J. Huang, Environmental science trihalide perovskite solar cells with doctor-bladed, Energy Environ. Sci. 8 (2015). doi:10.1039/C4EE03907F.

[14] P. Docampo, J.M. Ball, M. Darwich, G.E. Eperon, H.J. Snaith, polymer substrates, Nat. Commun. 4 (2013) 1–6. doi:10.1038/ncomms3761.

[15] R. Patidar, D. Burkitt, K. Hooper, D. Richards, T. Watson, Slot-die coating of perovskite solar cells : An overview, Mater. Today Commun. 22 (2020) 100808. doi:10.1016/j.mtcomm.2019.100808.

[16] M. Liu, M.B. Johnston, H.J. Snaith, Efficient planar heterojunction perovskite solar cells by vapour deposition., Nature. 501 (2013) 395–8. doi:10.1038/nature12509.

[17] A.T. Barrows, A.J. Pearson, C.K. Kwak, A.D. Dunbar, A.R. Buckley, D.G. Lidzey, Efficient planar heterojunction mixed-halide perovskite solar cells deposited via spray-deposition, Energy & Environmental Science, 7 (2014) 2944-2950. doi:10.1039/C4EE01546K.

[18] Z. Wei, H. Chen, K. Yan, S. Yang, Inkjet printing and instant chemical transformation of a CH_3 NH_3PbI_3/nanocarbon electrode and interface for planar perovskite Solar cells, Angewandte

Chemie International Edition, 53 (2014) 1–6. doi:10.1002/anie.201408638.

[19] H. Wang, W. Yao, Q. Tian, M. Li, B. Tian, L. Liu, Z. Wu, Printable monodisperse all-inorganic perovskite quantum dots : synthesis and banknotes protection applications, Adv. Mater. Tech. 3 (2018) 1800150. doi:10.1002/admt.201800150.

[20] B.A. Kamino, B. Paviet-salomon, S. Moon, N. Badel, J. Levrat, G. Christmann, A. Walter, A. Faes, L. Ding, J.J.D. Leon, A. Paracchino, M. Despeisse, C. Ballif, S. Nicolay, Low-temperature screen-printed metallization for the scale-up of two-terminal perovskite − silicon tandems, ACS Appl. Energy Mater. 2. (2019) 3815-3821. doi:10.1021/acsaem.9b00502.

[21] Y. Liang, Y. Yao, X. Zhang, W. Hsu, Y. Gong, J. Shin, D. Eric, M. Dagenais, I. Takeuchi, Y. Liang, Y. Yao, X. Zhang, W. Hsu, Fabrication of organic-inorganic perovskite thin films for planar solar cells via pulsed laser deposition, AIP Adv. 6 (2016) 015001.doi:10.1063/1.4939621.

[22] H. Liao, P. Guo, C. Hsu, M. Lin, B. Wang, L. Zeng, W. Huang, C. Myae, M. Soe, W. Su, M.J. Bedzyk, M.R. Wasielewski, A. Facchetti, R.P.H. Chang, M.G. Kanatzidis, T.J. Marks, Enhanced efficiency of hot-cast large-area planar perovskite solar cells/modules having controlled chloride incorporation, Adv. Energy Mater. 7 (2017) 1601660. doi:10.1002/aenm.201601660.

[23] U.A. Charles, M.A. Ibrahim, Electrodeposition of organic-inorganic tri-HaP solar cell, J. Power Sources. 378 (2018) 717–731. doi:10.1016/j.jpowsour.2017.12.075.

[24] Y.Y. Kim, T. Yang, R. Suhonen, M. Välimäki, T. Maaninen, Gravure-printed flexible perovskite solar cells : toward roll-to-roll manufacturing, Adv. Science 6 (2019) 1802094. doi:10.1002/advs.201802094.

[25] R. Swartwout, M.T. Hoerantner, V. Bulovi, Scalable deposition methods for large-area production of perovskite thin films, Energy & Environ. Mater. 2 (2019) 119–145. doi:10.1002/eem2.12043.

[26] A. Kojima, K. Teshima, Y. Shirai, T. Miyasaka, Organometal halide perovskite as visible-light sensitizers for photovoltaic, J. Am. Chem. Soc., 131 (2009) 6050–6051. doi.org/10.1021/ja809598r.

[27] H. Wei, Y. Tang, B. Feng, H. You, Importance of PbI_2 morphology in two-step deposition of $CH_3NH_3PbI_3$ for high-performance perovskite solar cells, Chin. Phys. B, 26 (2017) 128801. doi:10.1088/1674-1056/26/12/128801.

[28] P. Pistor, J. Borchert, W. Fränzel, R. Csuk, R. Scheer, Monitoring the phase formation of co-evaporated lead halide perovskite thin films by in situ x-ray diffraction, J. Phys. Chem. Lett. 5 (2014) 3308–3312. doi:10.1021/jz5017312.

[29] R. Sheng, A. Ho-baillie, S. Huang, S. Chen, X. Wen, X. Hao, M.A. Green, Methylammonium lead bromide perovskite-based solar cells by vapour-assisted deposition, J. Phys. Chem. C, 119 (2015) 3545-3549. doi:10.1021/jp512936z.

[30] M.R. Leyden, L. Meng, Y. Jiang, L.K. Ono, L. Qiu, E.J. Juarez-perez, C. Qin, C. Adachi, Y. Qi, Methylammonium lead bromide perovskite light-emitting diodes by chemical vapor deposition, J. Phys. Chem. Lett. 8 (2017) 3193-3198. doi:10.1021/acs.jpclett.7b01093.

[31] L.K. Ono, M.R. Leyden, S. Wang, Y. Qi, Organometal halide perovskite thin films and solar cells by vapor deposition, J. Mater. Chem. A. 4 (2016) 6693–6713. doi:10.1039/c5ta08963h.

[32] M.C. Jung, S.R. Raga, Y. Qi, Properties and solar cell applications of Pb-free perovskite films formed by vapor deposition, RSC Adv. 6 (2016) 2819–2825. doi:10.1039/c5ra21291j.

[33] J.B. Patel, R.L. Milot, A.D. Wright, L.M. Herz, M.B. Johnston, Formation dynamics of $CH_3NH_3PbI_3$ perovskite following two-step layer deposition, J. Phys. Chem. Lett. 7 (2016) 96-102.doi:10.1021/acs.jpclett.5b02495.

[34] C. V. Thompson, Structure evolution during processing of polycrystalline films, Annual Review Mater. Sci. 30 (2000) 159-190. doi.org/10.1146/annurev.matsci.30.1.159.

[35] V.Y. Novikov, Abnormal grain growth in thin films not caused by decreased energy of their free surface, Mater. Lett. 65 (2011) 2618–2620. doi:10.1016/j.matlet.2011.05.096.

[36] C. V Thompson, Grain growth in thin films, Annu. Rev. Mater. Sci. 20 (2003) 245–268. doi:10.1146/annurev.ms.20.080190.001333.

[37] J.F. Liao, W.Q. Wu, Y. Jiang, J.X. Zhong, L. Wang, D.B. Kuang, Understanding of carrier dynamics, heterojunction merits and device physics: towards designing efficient carrier transport layer-free perovskite solar cells, Chem Soc Rev, 49 (2020) 354-381. doi:10.1039/c8cs01012a.

[38] L. Meng, J. You, T. Guo, Y. Yang, Recent advances in the inverted planar structure of perovskite solar cells, Acc. Chem. Res. 49 (2016) 155-165. doi:10.1021/acs.accounts.5b00404.

[39] P. Docampo, J. Ball, M. Darwich, G. Eperon, J. snaith, Efficient organometal trihalide perovskite planar-heterojunction solar cells on flexible polymer substrates, Nat Commun. 4 (2013) 1-6. doi.org/10.1038/ncomms3761.

[40] F. Giordano, A. Abate, J. Pablo, C. Baena, M. Saliba, T. Matsui, S.H. Im, S.M. Zakeeruddin, M.K. Nazeeruddin, A. Hagfeldt, M. Graetzel, Enhanced electronic properties in mesoporous TiO2 via lithium doping for high-efficiency perovskite solar cells, Nat. Commun. 7 (2016) 1–6. doi:10.1038/ncomms10379.

[41] S. Pitchaiya, M. Natarajan, A review on the classification of organic/inorganic/carbonaceous hole-transporting materials for perovskite solar cell application, Arab. J. Chem. 13 (2020) 2526–2557. doi:10.1016/j.arabjc.2018.06.006.

[42] D. Zhou, T. Zhou, Y. Tian, X. Zhu, Y. Tu, Perovskite-based solar cells:materials, methods, and future perspectives, J. Nanomater. 2018 (2018). doi.org/10.1155/2018/8148072.

[43] W. Li, N. Cheng, Y. Cao, Z. Zhao, Z. Xiao, W. Zi, Boost the performance of inverted perovskite solar cells with PEDOT : PSS/Graphene quantum dots composite hole transporting layer, Org. Electron. 78 (2020) 105575. doi:10.1016/j.orgel.2019.105575.

[44] P. Chen, S. Yang, Potassium-doped nickel oxide as the hole transport layer for efficient and stable inverted perovskite solar cells, ACS Appl. Energy Mater. 2 (2019) 6705-6713. doi:10.1021/acsaem.9b01200.

[45] H. Wang, Z. Yu, J. Lai, X. Song, X. Yang, One plus one greater than two: high-performance inverted planar perovskite solar cells based on, J. Mater. Chem. A, 6 (2018) 21435–21444. doi:10.1039/c8ta07332e.

[46] C. Zuo, L. Ding, Solution-processed Cu_2O and CuO as hole transport materials for efficient perovskite solar cells, Small, 11 (2015) 5528–5532. doi:10.1002/smll.201501330.

[47] W. Chen, Y. Shi, Y. Wang, X. Feng, A.B. Djurišić, H.Y. Woo, X. Guo, Z. He, N-type conjugated polymer as efficient electron transport layer for planar inverted perovskite solar cells with a power conversion efficiency of 20.86%, Nano Energy. 68 (2019) 104363. doi:10.1016/j.nanoen.2019.104363.

[48] X. Ren, D. Yang, Z. Yang, J. Feng, X. Zhu, J. Niu, Y. Liu, W. Zhao, S.F. Liu, Solution-processed Nb:SnO_2 electron transport layer for efficient planar perovskite solar cells, Appl. Mater. Interfaces. 9 (2017) 2421-2429. doi:10.1021/acsami.6b13362.

[49] P. Zhu, S. Gu, X. Luo, Y. Gao, S. Li, J. Zhu, H. Tan, Simultaneous contact and grain-boundary passivation in planar perovskite solar cells using SnO_2-KCl composite electron transport layer, Adv. Energy Mater., 10 (2020) 1903083. doi:10.1002/aenm.201903083.

[50] C. Chen, Y. Jiang, Y. Wu, J. Guo, X. Kong, X. Wu, Y. Li, D. Zheng, S. Wu, S. Wu, X. Gao, S. Wu, X. Gao, X. Gao, Q. Wang, G. Zhou, Y. Chen, K. Kempa, J. Gao, Low-temperature processed WOx as electron transfer layer for planar perovskite solar cells exceeding 20% efficiency Cong,

Sol. RRL. 4 (2020) 1900499. doi:doi.org/10.1002/solr.201900499.

[51] Z. Hawash, L.K. Ono, Y. Qi, Recent advances in spiro-MeOTAD Hole transport material and its applications in organic-inorganic halide perovskite solar cells, 1700623 Adv. Mater. Interfaces 5 (2018) 1700623. doi:10.1002/admi.201700623.

[52] G. Kim, G. Kang, K. Choi, H. Choi, T. Park, solution-processable inorganic-organic double-layered hole transport layer for highly stable planar perovskite solar cells, Adv. Energy Mater. 8 (2018) 1801386. doi:10.1002/aenm.201801386.

[53] F. Giordano, A. Abate, J. Pablo, C. Baena, M. Saliba, T. Matsui, S.H. Im, S.M. Zakeeruddin, M.K. Nazeeruddin, A. Hagfeldt, M. Graetzel, Enhanced electronic properties in mesoporous TiO_2 via lithium doping for high-efficiency perovskite solar cells, Nat. Commun. 7 (2016) 1–6. doi:10.1038/ncomms10379.

[54] J. Luo, Y. Wang, Q. Zhang, Progress in perovskite solar cells based on ZnO nanostructures, Sol. Energy. 163 (2018) 289–306. doi:10.1016/j.solener.2018.01.035.

[55] L. Zhu, Z. Shao, J. Ye, X. Zhang, X. Pan, S. Dai, Mesoporous $BaSnO_3$ layer-based perovskite solar cells, 3 (2016) 970–973. doi:10.1039/c5cc08156d.

[56] C. Huang, P. Lin, N. Fu, C. Liu, B. Xu, K. Sun, D. Wang, X. Zeng, S. Ke, Facile fabrication of highly efficient ETL-free perovskite solar cells with 20% efficiency by defect passivation and interface engineering, 55 (2019) 2777–2780. doi:10.1039/c9cc00312f.

[57] A.H. Cheng, Y. Li, M. Zhang, K. Zhao, Z. Wang, Self-assembled ionic liquid for highly efficient electron transport layer free perovskite solar cells, ChemSusChem. 13 (2020) 2779-2785. doi:10.1002/cssc.202000342.

[58] P. Cui, D. Wei, J. Ji, D. Song, Y. Li, X. Liu, J. Huang, T. Wang, J. You, M. Li, Highly efficient electron-selective layer free perovskite solar cells by constructing effective p–n heterojunction, Sol. RRL. 1 (2017) 1600027. doi:10.1002/solr.201600027.

[59] Z. Zhou, S. Pang, Highly efficient inverted hole-transport-layer-free perovskite solar cells, J. Mater. Chem. A. 8 (2020) 503–512. doi:10.1039/c9ta10694d.

[60] C. Wang, J. Zhang, L. Jiang, L. Gong, H. Xie, Y. Gao, H. He, Z. Fang, J. Fan, Z. Chao, planar solar cells with ZnO as electron-transporting materials, J. Alloys Compd. 817 (2019) 152768. doi:10.1016/j.jallcom.2019.152768.

[61] W.Q. Wu, Q. Wang, Y. Fang, Y. Shao, S. Tang, Y. Deng, H. Lu, Y. Liu, T. Li, Z. Yang, A. Gruverman, J. Huang, Molecular doping enabled scalable blading of efficient hole-transport-layer-free perovskite solar cells, Nat. Commun. 9 (2018) 1–8. doi:10.1038/s41467-018-04028-8.

[62] Z. Chen, J.J. Wang, Y. Ren, C. Yu, K. Shum, Schottky solar cells based on $CsSnI_3$ thin-films, Appl. Phys. Lett. 101 (2014) 093901. doi.org/10.1063/1.4748888.

[63] J. Duan, Y. Zhao, B. He, Q. Tang, Simplified perovskite solar cell with 4.1% efficiency employing inorganic $CsPbBr_3$ as Light Absorber, Small. 14 (2018) 1704443. doi:10.1002/smll.201704443.

[64] W. Peng, L. Wang, B. Murali, K. Ho, A. Bera, N. Cho, C. Kang, V.M. Burlakov, J. Pan, L. Sinatra, C. Ma, W. Xu, D. Shi, E. Alarousu, A. Goriely, J. He, O.F. Mohammed, T. Wu, O.M. Bakr, Solution-grown monocrystalline hybrid perovskite films for hole-transporter-free solar cells, Adv. Mater. 28 (2016) 3383–3390. doi:10.1002/adma.201506292.

[65] F. Haug, J. Yum, C. Ballif, Organometallic halide perovskites: sharp optical absorption edge and its relation to photovoltaic performance, J. Phys. Chem. Lett. 5 (2014) 1035-1039. doi.org/10.1021/jz500279b

[66] L. Krückemeier, U. Rau, M. Stolterfoht, T. Kirchartz, How to report record open-circuit voltages in lead halide perovskite solar cells, Adv. Energy Mater. 10 (2020) 1902573.doi:10.1002/aenm.201902573.

[67] V. D'Innocenzo, G. Grancini1, M.J.P. Alcocer, A.R.S. Kandada, S.D. Stranks, M.M. Lee, G. Lanzani, A.P. Henry J. Snaith, Excitons versus free charges in organo-lead tri-halide perovskites, Nat. Commun. 5 (2014) 3586. doi: 10.1038/ncomms4586.

[68] D. Shi, V. Adinolfi, R. Comin, M. Yuan, E. Alarousu, A. Buin, Y. Chen, S. Hoogland, A. Rothenberger, K. Katsiev, Y. Losovyj, X. Zhang, P.A. Dowben, O.F. Mohammed, E.H. Sargent, O.M. Bakr, Low trap-state density and long carrier diffusion in organolead tri-halide perovskite single crystals, Science 347 (2015) 519–522. doi: 10.1126/science.aaa2725.

[69] X. Zhu, V. Podzorov, Extended carrier lifetimes and diffusion in hybrid perovskites revealed by Hall effect and photoconductivity measurements, Nature Commun. 7 (2016) 1-9. doi:10.1038/ncomms12253.

[70] N.K. Noel, A. Abate, S.D. Stranks, E. Parrott, V. Burlakov, A. Goriely, H.J. Snaith, Enhanced photoluminescence and solar cell performance via Lewis base passivation of organic-inorganic lead halide perovskites, ACS Nano 8 (2014) 9815-9821.doi:10.1021/nn5036476.

[71] S. Passivation, G.W.P. Adhyaksa, L.W. Veldhuizen, Y. Kuang, S. Brittman, R.E.I. Schropp, E.C. Garnett, Carrier diffusion lengths in hybrid perovskites: processing, composition, aging, and surface passivation effects, Chem. Mater. 28 (2016) 5259-5263. doi:10.1021/acs.chemmater.6b00466.

[72] B. Wu, Y. Zhou, G. Xing, Q. Xu, H.F. Garces, A. Solanki, Long minority-carrier diffusion length and low surface-recombination velocity in inorganic lead-free $CsSnI_3$ perovskite crystal for solar cells, Adv. Funct. Mater. 27 (2017): 1604818. doi:10.1002/adfm.201604818.

[73] E. Edri, S. Kirmayer, A. Henning, S. Mukhopadhyay, K. Gartsman, Y. Rosenwaks, G. Hodes, D. Cahen, Why lead methylammonium tri-iodide perovskite-based solar cells require a mesoporous electron-transporting scaffold (but Not Necessarily a Hole Conductor), Nano Lett., 14 (2014) 1000–1004. doi.org/10.1021/nl404454h

[74] F. Xie, H. Su, J. Mao, K.S. Wong, W.C.H. Choy, Evolution of diffusion length and trap state induced by chloride in perovskite solar cell, J. Phys. Chem. C, 120 (2016) 21248-21253. doi:10.1021/acs.jpcc.6b06914.

[75] B. Li, Y. Zhang, L. Fu, T. Yu, S. Zhou, L. Zhang, L. Yin, Surface passivation engineering strategy to fully-inorganic cubic $CsPbI_3$ perovskite for high-performance solar cells, Nat. Commun. 9 (2018) 1–8. doi:10.1038/s41467-018-03169-0.

[76] G. Xing, N. Mathews, S. Sun, S.S. Lim, Y.M. Lam, M. Graetzel, S. Mhaisalkar, T.C. Sum, Long-range balanced electron-and hole-transport lengths in organic-inorganic $CH_3NH_3PbI_3$, Science, 342 (2013) 344-347. doi: 10.1126/science.1243167.

[77] T. Kirchartz, T. Markvart, U. Rau, D.A. Egger, Impact of small phonon energies on the charge-carrier lifetimes in metal-halide perovskite, J. Phys. Chem. 9 (2018) 939-946. doi:10.1021/acs.jpclett.7b03414.

[78] E. Alarousu, A.M. El-zohry, J. Yin, A.A. Zhumekenov, C. Yang, E. Elhabshi, I. Gereige, A. Alsaggaf, A. V Malko, O.M. Bakr, O.F. Mohammed, Ultralong radiative states in hybrid perovskite crystals: compositions for sub-millimetre diffusion lengths, J. Phys. Chem. Lett. 8 (2017) 4386-4390. doi:10.1021/acs.jpclett.7b01922.

[79] A.M. Rappe, Ferroelectric domain wall induced band-gap reduction and charge separation in organometal halide perovskites, J. Phys. Chem. Lett. 6 (2015) 693-699. doi:10.1021/jz502666j.

[80] H. Zhu, K. Miyata, Y. Fu, J. Wang, P.P. Joshi, Screening in crystalline liquids protects energetic carriers in hybrid perovskites, Science, 353 (2016) 1409-1413. doi: 10.1126/science.aaf9570.

[81] X. Zhang, J. Shen, C.G. Van De Walle, First-principles simulation of carrier recombination mechanisms in halide perovskites, Adv. Energy Mater. 1902830 (2019) 1–20.

doi:10.1002/aenm.201902830.

[82] J. Shen, X. Zhang, S. Das, E. Kioupakis, C.G. Van De Walle, Unexpectedly Strong Auger Recombination in halide perovskites, Adv. Energy Mater. 1801027 (2018) 1–7. doi:10.1002/aenm.201801027.

[83] G. Xing, B. Wu, X. Wu, M. Li, B. Du, Q. Wei, J. Guo, E.K.L. Yeow, T.C. Sum, W. Huang, Transcending the slow bimolecular recombination in lead- halide perovskite for electroluminescence, Nat. Commun. 8 (2017) 14558. doi:10.1038/ncomms14558.

[84] R.L. Milot, G.E. Eperon, T. Green, H.J. Snaith, M.B. Johnston, L.M. Herz, Radiative monomolecular recombination boosts amplified spontaneous emission in $HC(NH_2)_2SnI_3$ perovskite films, J. Phys. Chem. Lett., 7 (2016) 4178-4184. doi:10.1021/acs.jpclett.6b02030.

[85] J. Chen, N. Park, Causes and solutions of recombination in perovskite solar cells, Adv. Mater. 1803019 (2019) 1–56. doi:10.1002/adma.201803019.

[86] J. Ding, J. Duan, C. Guoc, Q. Tang, Toward charge extraction in all-inorganic perovskite solar cells by interfacial engineering, J. Mater. Chem. A. 6 (2018) 21999–22004. doi:10.1039/c8ta02522c.

[87] J. Yang, Y. Luo, Q. Bao, Y. Li, J. Tang, Recent advances in energetics and stability of metal halide perovskite for optoelectronic applications, Adv. Mater. 1801351 (2019) 1–25. doi:10.1002/admi.201801351.

[88] A. Alnuaimi, I. Almansouri, A. Nayfeh, Effect of mobility and band structure of hole transport layer in planar heterojunction perovskite solar cells using 2D TCAD simulation, J. Comput. Electron. 15 (2016) 1110–1118. doi:10.1007/s10825-016-0850-1.

[89] T.S. Sherkar, C. Momblona, A. Jorge, M. Sessolo, H.J. Bolink, L.J.A. Koster, Recombination in perovskite solar cells: Significance of grain boundaries, interface traps, and defect ions, ACS Energy Lett. 2 (2017) 1214–1222. doi:10.1021/acsenergylett.7b00236.

[90] W. Zhu, Z. Zhang, W. Chai, D. Chen, H. Xi, J. Chang, J. Zhang, C. Zhang, Y. Hao, Benign pinholes in $CsPbIBr_2$ absorber film enable efficient carbon-based, all-inorganic perovskite solar cells, ACS Appl. Energy Mater. 2 (2019) 5254–5262. doi:10.1021/acsaem.9b00944.

[91] Y. Han, S. Meyer, Y. Dkhissi, K. Weber, J.M. Pringle, U. Bach, L. Spiccia, Y.-B. Cheng, Degradation observations of encapsulated planar $CH_3NH_3PbI_3$ perovskite solar cells at high temperatures and humidity, J. Mater. Chem. A. 3 (2015) 8139–8147. doi:10.1039/C5TA00358J.

[92] J. Wang, X. Chen, F. Jiang, Q. Luo, L. Zhang, M. Tan, M. Xie, Y. Li, Y. Zhou, W. Su, Y. Li, C. Ma, Electrochemical corrosion of Ag electrode in the silver grid electrode-based flexible perovskite solar cells and the suppression method, Solar RRL, 1800118 (2018) 1–10. doi:10.1002/solr.201800118.

[93] W. Ming, D. Yang, T. Li, L. Zhang, M.H. Du, Formation and diffusion of metal impurities in perovskite solar cell material $CH_3NH_3PbI_3$: implications on solar cell degradation and choice of an electrode, Adv. Sci. 5 (2018) 1700662. doi:10.1002/advs.201700662.

[94] L. Zhao, R.A. Kerner, Z. Xiao, Y. Lisa, K.M. Lee, J. Schwartz, B.P. Rand, B.P. Rand, Redox chemistry dominates the degradation and decomposition of metal halide perovskite optoelectronic devices redox chemistry dominates the degradation and decomposition of metal halide perovskite optoelectronic devices, ACS Energy Lett. 1 (2016) 595-602. doi:10.1021/acsenergylett.6b00320.

[95] B. Li, W. Hui, X. Ran, Y. Xia, F. Xia, L. Chao, Y. Chen, W. Huang, Memory devices and artificial synapses, J. Mater. Chem. C, 7 (2019) 7476–7493. doi:10.1039/c9tc02233c.

[96] K. Kang, H. Ahn, Y. Song, W. Lee, J. Kim, Y. Kim, D. Yoo, T. Lee, High-performance solution-processed organo-metal halide perovskite unipolar resistive memory devices in a cross-bar array structure, Adv. Mater. 1804841 (2019) 1–9. doi:10.1002/adma.201804841.

[97] J.A.S.K.K. Shaat, H.M.N. Shurrab, A.I. Abelilah, L.A. Al, K.N. Al, Perovskite solar cells free of hole transport layer, J. Sol-Gel Sci. Technol. 90 (2019) 443–449. doi:10.1007/s10971-019-04957-w.

[98] R. Prasanna, A. Gold-parker, T. Leijtens, B. Conings, A. Babayigit, H. Boyen, M.F. Toney, M.D. Mcgehee, Bandgap tuning via lattice contraction and octahedral tilting in perovskite materials for photovoltaics, MULTIPLE SCLEROSIS JOURNAL, 22 (2017). doi:10.1021/jacs.7b04981.

[99] I.E. Castelli, J.M. García-lastra, K.S. Thygesen, K.W. Jacobsen, Bandgap calculations and trends of organometal halide perovskite, APL Mater., 2 (2014) 081514. doi:10.1063/1.4893495.

[100] W. Liao, D. Zhao, Y. Yu, N. Shrestha, K. Ghimire, C.R. Grice, C. Wang, Y. Xiao, A.J. Cimaroli, R.J. Ellingson, N.J. Podraza, K. Zhu, R. Xiong, Y. Yan, Fabrication of efficient low-bandgap perovskite solar cells by combining formamidinium tin iodide with methylammonium lead iodide, J. Am. Chem. Soc. 138 (2016) 12360-12363. doi:10.1021/jacs.6b08337.

[101] Y. Zhang, Y. Liu, Y. Li, Towards optimised optoelectronic applications, J. Mater. Chem. C., 4 (2016) 9172-9178. doi:10.1039/C6TC03592B.

[102] J.H. Noh, S.H. Im, J.H. Heo, T.N. Mandal, S. Il Seok, Chemical management for colourful, efficient, and stable inorganic−organic hybrid nanostructured solar cells, Nano lett. 13 (2013) 1764-1769. doi.org/10.1021/nl400349b

[103] D. Yang, W. Ming, H. Shi, L. Zhang, M.-H. Du, Fast diffusion of native defects and impurities in perovskite solar cell material $CH_3NH_3PbI_3$, Chem. Mater., 28 (2016) 4349–4357. doi.org/10.1021/acs.chemmater.6b01348

[104] T.S. Sherkar, C. Momblona, A. Jorge, M. Sessolo, H.J. Bolink, L.J.A. Koster, Recombination in perovskite solar cells: the significance of grain boundaries, interface traps, and defect ions, ACS Energy Lett., 2 (2017) 1214–1222. doi.org/10.1021/acsenergylett.7b00236

[105] S.G. Motti, D. Meggiolaro, S. Martani, R. Sorrentino, A.J. Barker, F. De Angelis, A. Petrozza, Defect activity in lead halide perovskites, Adv. Mater. 31 (2019) 1901183. doi:10.1002/adma.201901183.

[106] H. Jin, E. Debroye, M. Keshavarz, I.G. Scheblykin, M.B.J. Roeffaers, J.A. Steele, It ' s a trap ! On the nature of localised states and charge trapping in lead halide perovskites, Mater. Horiz., 7 (2020) 397–410. doi:10.1039/c9mh00500e.

[107] W.S. Yang, B. Park, E.H. Jung, N.J. Jeon, Iodide management in formamidinium-lead-halide – based perovskite layers for efficient solar cells, Sci. 1379 (2017) 1376–1379. doi: 10.1126/science.aan2301

[108] T. Dewinggih, Shobih, L. Muliani, Herman, R. Hidayat, The temperature effect on the working characteristics of solar cells based on organometal halide perovskite crystals the temperature effect on the working characteristics of solar cells based on organometal halide perovskite crystals, J. Phys. Conf. Ser. 877 (2017). doi :10.1088/1742-6596/877/1/012043.

[109] J. Kim, S. Lee, J.H. Lee, K. Hong, The role of intrinsic defects in methylammonium lead iodide, J. Phys. Chem. Lett. 5 (2014) 1312-1317. doi.org/10.1021/jz500370k.

[110] G.K. Williamson, R.E. Smallman, III. Dislocation densities in some annealed and cold-worked metals from measurements on the X-ray Debye-Scherrer spectrum, Philos. Mag. 1 (1956) 34–46. doi:10.1080/14786435608238074.

[111] J. Jiang, X. Sun, X. Chen, B. Wang, Z. Chen, Y. Hu, Y. Guo, L. Zhang, Y. Ma, L. Gao, F. Zheng, L. Jin, M. Chen, Z. Ma, Y. Zhou, N.P. Padture, K. Beach, H. Terrones, Y. Shi, D. Gall, T. Lu, E. Wertz, J. Feng, J. Shi, Carrier lifetime enhancement in halide perovskites via remote epitaxy, Nat. Commun. (2019) 1–12. doi:10.1038/s41467-019-12056-1.

[112] Y. Shao, Y. Fang, T. Li, Q. Wang, Q. Dong, Y. Deng, Y. Yuan, H. Wei, M. Wang, A. Gruverman,

J. Shield, J. Huang, Grain boundary dominated ion migration in polycrystalline organic-inorganic halide perovskite films, Energy Environ. Sci. 9 (2016) 1752-1759 .doi:10.1039/c6ee00413j.

[113] H. Uratani, K. Yamashita, Charge carrier trapping at surface defects of perovskite solar cell absorbers : A First-Principles Study, J. Phys. Chem. Lett. 8 (2017) 742-746. doi:10.1021/acs.jpclett.7b00055.

[114] D.W. DeQuilettes, S.M. Vorpahl, S.D. Stranks, H. Nagaoka, G.E. Eperon, M.E. Ziffer, H.J. Snaith, D.S. Ginger, Impact of microstructure on local carrier lifetime in perovskite solar cells, 348 (2015).

[115] M. Zhang, Q. Chen, R. Xue, Y. Zhan, C. Wang, J. Lai, J. Yang, H. Lin, J. Yao, Y. Li, L. Chen, Y. Li, Reconfiguration of interfacial energy band structure for high-performance inverted structure perovskite solar cells, Nat. Commun. 10 (2019) 1–9. doi:10.1038/s41467-019-12613-8.

[116] W. Wu, P.N. Rudd, Z. Ni, C.H. Van Brackle, H. Wei, Q. Wang, B.R. Ecker, Y. Gao, J. Huang, Reducing surface halide deficiency for efficient and stable iodide- based perovskite solar cells, J. Am. Chem. Soc. 142 (2020) 3989-3996. doi:10.1021/jacs.9b13418.

[117] D. Jain, S. Chaube, P. Khullar, S.G. Srinivasan, B. Rai, Bulk and surface DFT investigations of inorganic halide perovskite screened using machine learning and materials property databases, Phys. Chem. Chem. Phys. 21. (2019) 19423–19436. doi:10.1039/c9cp03240a.

[118] W. Kong, T. Ding, G. Bi, H. Wu, hybrid lead–halide perovskite, Phys. Chem. Chem. Phys., 18 (2016) 12626–12632. doi:10.1039/c6cp00325g.

[119] Z. Song, S.C. Watthage, A.B. Phillips, B.L. Tompkins, R.J. Ellingson, M.J. Heben, Impact of processing temperature and composition on the formation of methylammonium lead iodide perovskites, Chem Mater., 27 (2015) 4612-4619. doi:10.1021/acs.chemmater.5b01017.

[120] K.P. Mckenna, Electronic properties of {111} twin boundaries in a mixed-ion lead halide perovskite solar absorber, ACS Energy Lett. 3 (2018) 2663-2668. doi:10.1021/acsenergylett.8b01700.

[121] M.U. Rothmann, W. Li, Y. Zhu, U. Bach, L. Spiccia, J. Etheridge, Y.B. Cheng, Direct observation of intrinsic twin domains in, Nat. Commun. 8 (2017) 6–13. doi:10.1038/ncomms14547.

[122] C.S. Tan, Y. Hou, M.I. Saidaminov, A. Proppe, Y.S. Huang, Y. Zhao, M. Wei, G. Walters, Z. Wang, Y. Zhao, P. Todorovic, S.O. Kelley, L.J. Chen, E.H. Sargent, Heterogeneous supersaturation in mixed perovskites, Adv. Sci. 7 (2020) 1903166. doi:10.1002/advs.201903166.

[123] S.K. Yadavalli, Z. Dai, H. Zhou, Y. Zhou, N.P. Padture, Acta materialia facile healing of cracks in organic À inorganic halide perovskite thin films, 187 (2020) 112–121. doi.org/10.1016/j.actamat.2020.01.040.

[124] B. Li, J. Tian, L. Guo, C. Fei, T. Shen, X. Qu, G. Cao, Dynamic growth of pinhole-free conformal $CH_3NH_3PbI_3$ film for perovskite solar cells, ACS Appl. Mater. Interfaces 8 (2016) 4684-4690.doi:10.1021/acsami.5b11679.

[125] S. Chaudhary, S. Kumar, C. Mohan, S. Negi, Materials science in semiconductor processing enhanced performance of perovskite photodetectors fabricated by two-step spin coating approach, Mater. Sci. Semicond. Process. 109 (2020) 104916. doi:10.1016/j.mssp.2020.104916.

[126] G. Seo, D. Lee, S. Heo, M. Seol, Y. Lee, K. Kim, S.H. Kim, J. Lee, D. Lee, J. Lee, D.W. Kwak, D. Lee, H.Y. Cho, J. Park, T.K. Ahn, M.K. Nazeeruddin, Microscopic analysis of inherent void passivation in perovskite solar cells, ACS Energy Lett. 2 (2017) 1705-1710. doi:10.1021/acsenergylett.7b00484.

[127] J. Li, Q. Ge, J. Hu, D. Wang, L. Wan, Microscopic investigation of grain boundaries in organolead halide perovskite solar cells, ACS Appl. Mater. Interfaces 7 (2015) 28518-28523. doi:10.1021/acsami.5b09801.

[128] J.S. Yun, A. Ho-baillie, S. Huang, S.H. Woo, Y. Heo, J. Seidel, F. Huang, Y. Cheng, M.A. Green,

Benefit of grain boundaries in organic-inorganic halide planar perovskite solar cells, J. Phys. Chem. Lett. 6 (2015) 875-880.doi:10.1021/acs.jpclett.5b00182.

[129] W. Chu, Q. Zheng, O. V Prezhdo, J. Zhao, W.A. Saidi, Low-frequency lattice phonons in halide perovskite explain high defect tolerance toward electron-hole recombination, Sci. Adv. 6 (2020) eaaw7453. doi: 10.1126/sciadv.aaw7453.

[130] W. Li, J. Liu, F. Bai, H. Zhang, O. V Prezhdo, Hole trapping by iodine interstitial defects, ACS Energy Lett. 2 (2017) 1270-1278. doi:10.1021/acsenergylett.7b00183.

[131] H. Zhang, Y. Liu, H. Lu, W. Deng, K. Yang, Z. Deng, Reversible air-induced optical and electrical modulation of methylammonium lead bromide ($MAPbBr_3$) single crystals, Appl. Phys. Lett. 111 (2017) 103904. doi:10.1063/1.5001843.

[132] A. Dobrovolsky, A. Merdasa, E.L. Unger, A. Yartsev, I.G. Scheblykin, Transition temperature in metal-halide perovskites, Nat. Commun. 8 (2017) 1-8. doi:10.1038/s41467-017-00058-w.

[133] L. Qiao, W. Fang, R. Long, Forschungsartikel Extending Carrier Lifetimes in Lead halide perovskite with alkali metals by passivating and eliminating halide interstitial defects, Angew. Chem., 59 (2020) 4684-4690. doi:10.1002/ange.201911615.

[134] Y. Rong, Y. Hu, A. Mei, H. Tan, M.I. Saidaminov, S. Il Seok, M.D. Mcgehee, E.H. Sargent, H. Han, Challenges for commercializing perovskite solar cells, Sci. 361 (2018) 6408. doi:10.1126/science.aat8235.

[135] C. Ran, J. Xu, W. Gao, C. Huang, S. Dou, Defects in metal triiodide perovskite materials towards high-performance solar cells: origin, impact, characterization, and engineering, Chem Soc Rev, 47 (2018) 4581-4610. doi:10.1039/c7cs00868f.

[136] Z. Ni, C. Bao, Y. Liu, Q. Jiang, W. Wu, S. Chen, X. Dai, Resolving spatial and energetic distributions of trap states in metal halide perovskite solar cells, Sci. 1358 (2020) 1352–1358. doi: 10.1126/science.aba0893

[137] S. Heo, G. Seo, Y. Lee, D. Lee, M. Seol, J. Lee, J.-B. Park, K. Kim, D.-J. Yun, Y.S. Kim, J.K. Shin, T.K. Ahn, M.K. Nazeeruddin, Deep level trapped defect analysis in $CH_3NH_3PbI_3$ perovskite solar cells by deep level transient spectroscopy, Energy Environ. Sci. 10 (2017) 1128–1133. doi:10.1039/C7EE00303J.

[138] J. Kang, L. Wang, High defect tolerance in lead halide perovskite, J. Phys. Chem. Lett. 8 (2017) 489-493 .doi:10.1021/acs.jpclett.6b02800.

[139] D. Meggiolaro, S.G. Motti, E. Mosconi, A.J. Barker, J. Ball, A. Riccardo, F. Deschler, A. Petrozza, F. De Angelis, Environmental science of lead-halide perovskite, Energy Environ. Sci. 11 (2018) 702–713. doi:10.1039/C8EE00124C.

[140] W.J. Yin, T. Shi, Y. Yan, Unusual defect physics in $CH_3NH_3PbI_3$ perovskite solar cell absorber, Appl. Phys. Lett. 104 (2014) 143101. doi:10.1063/1.4864778.

[141] J. Kim, C. Chung, K. Hong, defects from the intrinsic defects of lead tri-halide, Phys. Chem. Chem. Phys. 18 (2016) 27143-27147. doi:10.1039/c6cp02886a.

[142] M. Du, Density functional calculations of native defects in $CH_3NH_3PbI_3$: Effects of Spin−Orbit coupling and self-interaction error, J. Phys. Chem. Lett. 6 (2015) 1461-1466. doi:10.1021/acs.jpclett.5b00199.

[143] J.W. Rosenberg, M.J. Legodi, Y. Rakita, D. Cahen, M. Diale, Laplace current deep level transient spectroscopy measurements of defect states in methylammonium lead bromide single crystals, J. Appl. Phys. 122 (2017) 145701. doi:10.1063/1.4995970.

[144] R.J. Stewart, C. Grieco, A. V Larsen, J.J. Maier, J.B. Asbury, Approaching bulk carrier dynamics in organo-halide perovskite nanocrystalline films by surface passivation, J. Phys. Chem. Lett. 7 (2016) 1148-1153. doi:10.1021/acs.jpclett.6b00366.

[145] Y. Zhang, L. Tan, Q. Fu, L. Chen, T. Ji, Y. Chen, perovskite by sulfonate-carbon nanotube, Chem. Commun. 52 (2016) 5674-5677. doi:10.1039/C6CC00268D.

[146] Q. Chen, H. Zhou, T. Song, S. Luo, Z. Hong, H. Duan, L. Dou, Y. Liu, Y. Yang, Controllable self-induced passivation of hybrid lead iodide perovskite toward high-performance solar cells, Nano Lett. 14 (2014) 4158-4163. doi.org/10.1021/nl501838y.

[147] M. Abdi-jalebi, Z. Andaji-garmaroudi, S. Cacovich, C. Stavrakas, B. Philippe, E.M. Hutter, A.J. Pearson, S. Lilliu, T.J. Savenije, J.M. Richter, M. Alsari, P. Edward, H. Rensmo, G. Divitini, C. Ducati, R.H. Friend, S.D. Stranks, halide perovskite with potassium passivation, Nat. Publ. Gr. 555 (2018) 497–501. doi:10.1038/nature25989.

[148] C. Liu, Z. Huang, X. Hu, X. Meng, L. Huang, J. Xiong, Grain boundary modification via F4TCNQ to reduce defects of perovskite solar cells with excellent device performance, ACS Appl. Mater. Interfaces. 10 (2018) 1909-1916. doi:10.1021/acsami.7b15031.

[149] Y. Yang, M. Yang, D.T. Moore, Y. Yan, E.M. Miller, K. Zhu, M.C. Beard, Lead iodide perovskite films, ACS Appl. Mater. Interfaces 10 (2018) 1909-1916. doi.org/10.1021/acsami.9b07149.

[150] C. Hsieh, Y. Liao, Y. Lin, C. Chen, C. Tsai, E.W. Diau, S. Chuang, Low-temperature, simple and efficient preparation of perovskite solar cells using Lewis bases urea and thiourea as additives: stimulating large grain, RSC Adv. 8 (2018) 19610-19615. doi:10.1039/c8ra03175d.

[151] J. Lee, H. Kim, N. Park, Lewis Acid−Base Adduct Approach for High-Efficiency Perovskite Solar Cells, Acc Chem Res. 49 (2016) 311-319. doi:10.1021/acs.accounts.5b00440.

[152] Y. Shao, Z. Xiao, C. Bi, Y. Yuan, J. Huang, Origin and elimination of photocurrent hysteresis by fullerene passivation in $CH_3NH_3PbI_3$ planar heterojunction solar cells, Nat. Commun. 5 (2014) 5784. doi:10.1038/ncomms6784.

[153] R. Brenes, A. Osherov, T.J. Savenije, S.D. Stranks, R. Brenes, D. Guo, A. Osherov, N.K. Noel, C. Eames, E.M. Hutter, S.K. Pathak, F. Niroui, R.H. Friend, M.S. Islam, H.J. Snaith, V. Bulovi, Metal halide perovskite polycrystalline films exhibiting properties of single crystals metal halide perovskite polycrystalline films exhibiting properties of single crystals, Joule 1 (2017) 155-167. doi:10.1016/j.joule.2017.08.006.

[154] Z. Fang, W. Chen, Y. Shi, J. Zhao, S. Chu, J. Zhang, Dual passivation of perovskite defects for light-emitting diodes with external quantum efficiency exceeding 20%, Adv. Funct. Mater. 30 (2020) 1909754. doi:10.1002/adfm.201909754.

[155] J.A. Röhr, D. Moia, S.A. Haque, T. Kirchartz, J. Nelson, Exploring the Validity and Limitations of the Mott-Gurney Law for Charge-Carrier Mobility Determination of Semiconducting Thin-Films, J. Phys. Condens. Matter. 30 (2018) 105901. doi.org/10.1088/1361-648X/aaabad.

[156] A. Hajibadali, M.B. Nejad, G. Farzi, Schottky diodes based on polyaniline / multi-walled carbon nanotube composites, Braz. J. Phys. 45 (2015) 394-398. doi:10.1007/s13538-015-0334-y.

[157] J.A. Röhr, T. Kirchartz, J. Nelson, On the correct interpretation of the low voltage regime in intrinsic single-carrier devices, J. Phys. Condens. Matter. 29 (2017) 205901. doi.org/10.1088/1361-648X/aa66cc.

[158] T. Kirchartz, Influence of diffusion on space-charge-limited current measurements in organic semiconductors, Beilstein J. Nanotechnol. 4 (2013) 180–188. doi:10.3762/bjnano.4.18.

[159] P. Ca, I. Chakraborty, N. Panwar, A. Khanna, U. Ganguly, Space Charge Limited Current with Self-heating in $Pr_{0.7}Ca_{0.3}MnO_3$ based RRAM, arXiv:1605.08755

[160] S.A. Moiz, M.M. Ahmed, K.S. Karimov, Estimation of electrical parameters of OD organic semiconductor diode from measured I-V characteristics, ETRI J. 27 (2005) 319–324. doi:10.4218/etrij.05.0104.0100.

[161] M.I. Saidaminov, A.L. Abdelhady, B. Murali, E. Alarousu, V.M. Burlakov, W. Peng, I. Dursun,

L. Wang, Y. He, G. MacUlan, A. Goriely, T. Wu, O.F. Mohammed, O.M. Bakr, High-quality bulk hybrid perovskite single crystals within minutes by inverse temperature crystallization, Nat. Commun. 6 (2015) 1–6. doi:10.1038/ncomms8586.

[162] M. Fischer, K. Tvingstedt, A. Baumann, V. Dyakonov, Doping Profile in Planar Hybrid Perovskite Solar Cells identifying Mobile Ions, (2018). doi:10.1021/acsaem.8b01119.

[163] W. Shockley, The Theory of p-n junctions in semiconductors and p-n junction transistors, Bell Syst. Tech. J. 28 (1948) 435–489. doi.org/10.1002/j.1538-7305.1949.tb03645.x.

[164] A.F. Braña, E. Forniés, N. López, B.J. García, High-Efficiency Si Solar Cells Characterization Using Impedance Spectroscopy Analysis High-Efficiency Si Solar Cells Characterization Using Impedance Spectroscopy Analysis, J. Phys. Conf. Ser. 647 (2015) 012069. doi:10.1088/1742-6596/647/1/012069.

[165] O. Almora, C. Aranda, E. Mas-marzá, G. Garcia-belmonte, On Mott-Schottky analysis interpretation of capacitance measurements in organometal perovskite solar cells On Mott-Schottky analysis interpretation of capacitance measurements in organometal perovskite solar cells, AIP Pub. 109 (2016) 173903. doi:10.1063/1.4966127.

[166] I.M. Dharmadasa, Y. Rahaq, A.A. Ojo, T.I. Alanazi, Perovskite solar cells: a deep analysis using current-voltage and capacitance-voltage techniques, J. Mater. Sci. Mater. Electron. 30 (2019) 1227–1235. doi:10.1007/s10854-018-0390-5.

[167] S. S. Hegedus, W.N. Shafarman, Thin-film solar cells: device measurements and analysis, Prog Photovolt Res Appl., 176 (2004) 155–176. doi:10.1002/pip.518.

[168] B. Bera, A. Chakraborty, T. Kar, P. Leuaa, M. Neergat, Density of States, Carrier concentration, and flat band potential derived from electrochemical impedance measurements of N-doped carbon and their influence on electrocatalysis of oxygen reduction reaction, J. Phys. Chem. C. 121 (2017) 20850–20856. doi:10.1021/acs.jpcc.7b06735.

[169] P. Yadav, D. Prochowicz, M. Saliba, P.P. Boix, S.M. Zakeeruddin, M. Grätzel, Interfacial kinetics of efficient perovskite solar cells, Crystals 7 (2017) 252. doi:10.3390/cryst7080252.

[170] H. Lee, C. Lee, Influence of electrical traps on the current density degradation of inverted perovskite solar cells. Mater. 12 (2019) 1644. doi.org/10.3390/ma12101644.

3 Experimental

3.1 Introduction

The chapter starts by listing the materials used for growing the HaP thin films and for the fabrication of solar cells in this work. This is followed by an outline of the method of cleaning fluorine-doped tin oxide (FTO) substrates. It presents detailed descriptions of the sequential thermal vapour deposition of methylammonium lead tri-iodide ($MAPbI_3$), methylammonium lead tri-bromide ($MAPbBr_3$) and methylammonium lead iodide-bromide ($MAPb(I_{1-x}Br_x)_3$). A brief description of the UV-Vis spectroscopy, X-ray diffraction and scanning electron microscopy techniques presented. The fabrication technique of FTO/$MAPbI_3$/Au, FTO/$MAPbBr_3$/Au and FTO/$MAPb(I_{1-x}Br_x)_3$/Au, FTO/TiO_2/$MAPbI_3$/Au and FTO/TiO_2/$MAPb(I_{1-x}Br_x)_3$/Au devices for the electrical characterisation of the respective perovskite materials are described. Finally, the current-voltage (*I*-*V*) and capacitance-voltage (*C*-*V*) measurement procedures of the devices under dark and illumination conditions are presented.

3.2 Materials

All precursors and solvents used in this work were bought from Sigma-Aldrich and are listed in *Table 3.2.1*. The MAI solution (0.42 M in 2-propanol) was dried in a rotary evaporator to obtain a powder while the other chemicals were used as received.

Table 3.2.1 Precursors and solvents, including their purities and concentrations.

Materials	**Purity/concentration**
Methylammonium bromide powder (MABr)	98%
Methylammonium iodide powder (MAI)	98%
Methylammonium iodide solution (MAI)	0.42 M
Lead(II)iodide powder (PbI_2)	99.9%
Lead(II)bromide powder ($PbBr_2$)	99.9%
Titanium diisopropoxide bis(acetylacetonate)	75 wt. % in isopropanol
1-butanol	≥ 99.4%
Ethyl cellulose	48.0-49.5% (w/w) ethoxyl basis
Ethanol	95.0%
Titanium (IV) oxide (TiO_2) nano-powder	99.5%
Gold	99.997%
terpineol	≥ 96.0%, FG

3.3 The procedures for cleaning the substrates and vacuum chamber

The FTO (0.7 Ω cm) and glass substrates were first trimmed using a diamond cutter and then cleaned sequentially in acetone, isopropanol, and deionised water under ultrasonication (50 Hz, 100 W) for 10 min to remove oils, grease, and particle contaminations. The cleaned substrates were dried by blowing with a pressurised stream of pure nitrogen gas. Before the depositions, the chamber was cleaned using a solution of extran diluted with deionized water (volume ratio 1:4). The cleaning of the substrates and chamber reduce the effects of residual contaminants.

3.4 Preparation of HaP thin films using the sequential thermal vapour deposition method

3.4.1 Preparation of methylammonium Lead tri-iodide using the STVD technique

Figure 3.4.1 is the schematics for the STVD of $MAPbI_3$.The formation of the $MAPbI_3$ thin films was optimised on microscope glass substrates. The substrates were trimmed and cleaned as earlier described. MAI powder was obtained by drying MAI solution (0.42 M in 2-propanol) using a rotary evaporator while PbI_2 powder was used as received. The powders were placed in separate boron nitride crucibles C1 and C2, with PbI_2 in C1 and C2 holding MAI. The two crucibles were inserted into two heating coils in the evaporation chamber. The rings were connected to the power supply in a circuit with two switches S1 and S2, as shown in *Figure 3.4.1.* Air was pumped from the evaporation chamber until a pressure of 1.0×10^{-4} mbar was reached. The film thickness and substrate temperature were kept under check using a quartz crystal monitor and a thermocouple placed at the same level as the substrate. The crystal monitor was calibrated for PbI_2 thickness measurement by setting density to 6.16 g cm^{-3} and Z-factor to 1.10. Also, MAI film thickness was monitored by selecting the density to 1.20 g cm^{-3} and Z-factor to 2.70. PbI_2 was deposited when S2 was opened, and S1 closed while MAI was deposited when S2 was closed, and S1 unlocked. When the desired film thickness was reached, the shutter was closed, and the current gradually reduced to zero. The stoichiometry of $MAPbI_3$ was optimised by varying the thicknesses of PbI_2 and MAI. The crystallization of $MAPbI_3$ was accomplished by annealing the compound film at 100℃ for 10 min in an air-heated oven. The films using PbI_2 (99.9 %), and MAI powder from 0.42 M in 2-propanol are called SPL1**.** Finally, the experiment was repeated using PbI_2

(99.9 %), and MAI (98%) with MAI thickness maintained at 500 nm while annealing time was varied from 0 to 60 min. The samples formed from PbI_2 (99.9 %) and MAI (98%) are called SPL2

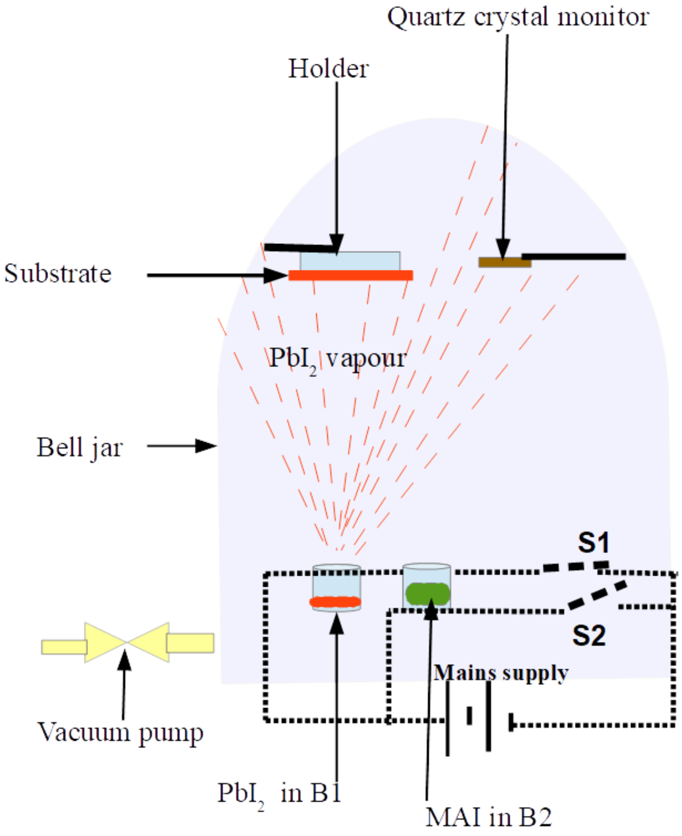

Figure 3.4.1: Schematic diagram for STVD of $MAPbI_3$*.*

3.4.2 Preparation of methylammonium lead tri-bromide using the STVD technique

Figure 3.4.2 is the schematic diagram for STVD of $MAPbBr_3$. The formation of $MAPbBr_3$ thin films was optimised on FTO substrates. The substrates were trimmed a cleaned as previously described. $PbBr_2$ and MABr were placed in two separate boron nitride crucibles B1 and B2, with $PbBr_2$ in B1 and MABr in B2. The crucibles were inserted into two heating coils in the evaporation chamber. The coils are connected to the power supply in the circuit containing two switches S1 and S2. Air is pumped from the chamber until a pressure of 2.0 x 10^{-5} mbar is reached. The film thickness and substrate temperature are checked by a quartz crystal monitor and thermocouple placed at the same level as the substrate. The crystal monitor was calibrated for $PbBr_2$ thickness measurement by setting the density to 6.66 g cm^{-3} and Z-factor to 1.15. Also, MABr film thickness was monitored by selecting the density to 1.30 g cm^{-3} and

Z-factor to 2.81. When the desired film thickness is reached, the shutter is closed, and the current gradually reduced to zero. $PbBr_2$ is deposited when S2 is opened and S1 closed while MABr is deposited when S2 is closed and S1 unlocked. The stoichiometry of $MAPbBr_3$ is optimised by varying the thicknesses of $PbBr_2$ and MABr. The crystallization of $MAPbBr_3$ was accomplished by annealing the compound film at 100°C for 10 min in an air-heated oven. Finally, the experiment is repeated on glass as a substrate and for the 500 nm thick MABr sample with the annealing time varied from 0 to 60 min.

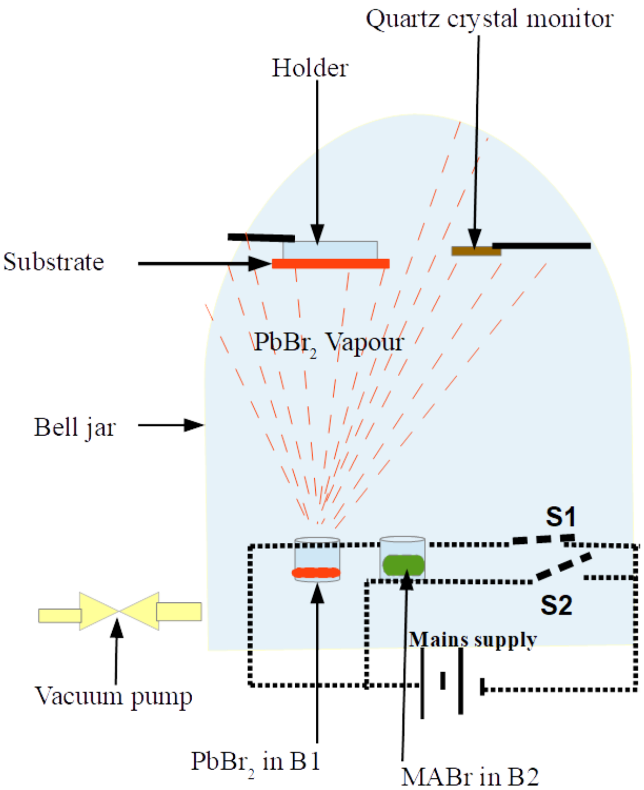

Figure 3.4.2: Schematic diagram for STVD of $MAPbBr_3$.

3.4.3 Synthesis of methylammonium lead iodide-bromide perovskite using the STVD technique.

Figure 3.4.3 illustrates the experimental process of growing thin $MAPb(I_{1-x}Br_x)_3$ alloy film using the STVD technique. PbI_2 (99.9 %) and MAI (98%) powders were placed in two separate cylindrical boron nitride boats B1 and B2 and inserted into individual heating coils inside the evaporation chamber. The rings were connected to the power source, as shown in *Figure 3.4.3 (a)*. The evaporation chamber was then evacuated to a pressure of 2.0 x 10^{-5} mbar before deposition. However, the pressure increases slightly when sublimation starts and decreases again to the initial pressure during the deposition process. An inbuilt quartz crystal monitor, placed at the same level as the substrate inside the chamber, was used to monitor the thickness of thin films during the deposition process. The crystal monitor was calibrated for PbI_2 thickness measurement by setting the density to 6.16 g cm^{-3}, and Z-factor to 1.10 and MAI film thickness was monitored by setting the density to 1.20 g cm^{-3} and Z-factor to 2.70. 100 nm of PbI_2 was first deposited, followed by the deposition of 500 nm MAI to form $MAPbI_3$. The heat generated from the heating the crucibles raised the temperature of the substrates to 140°C during the deposition of PbI_2 and 95°C during the deposition of MAI. Post deposition annealing of the $MAPbI_3$ thin film was done in the air inside an oven heated at 100°C for 10 min. After the annealing, the prepared $MAPbI_3$ is loaded into the chamber, with boats B1 and B2 now containing $PbBr_2$ and MABr, respectively, as shown in *Figure 3.4.3 (b).* The thickness of $PBBr_2$ was kept constant at 100 nm while that of MABr was varied from 300 to 500 nm, in steps of 100. The heat generated from the heating the crucibles raised the temperature of the substrates to 140°C during the deposition of $PbBr_2$ and 95°C during the deposition of MABr.

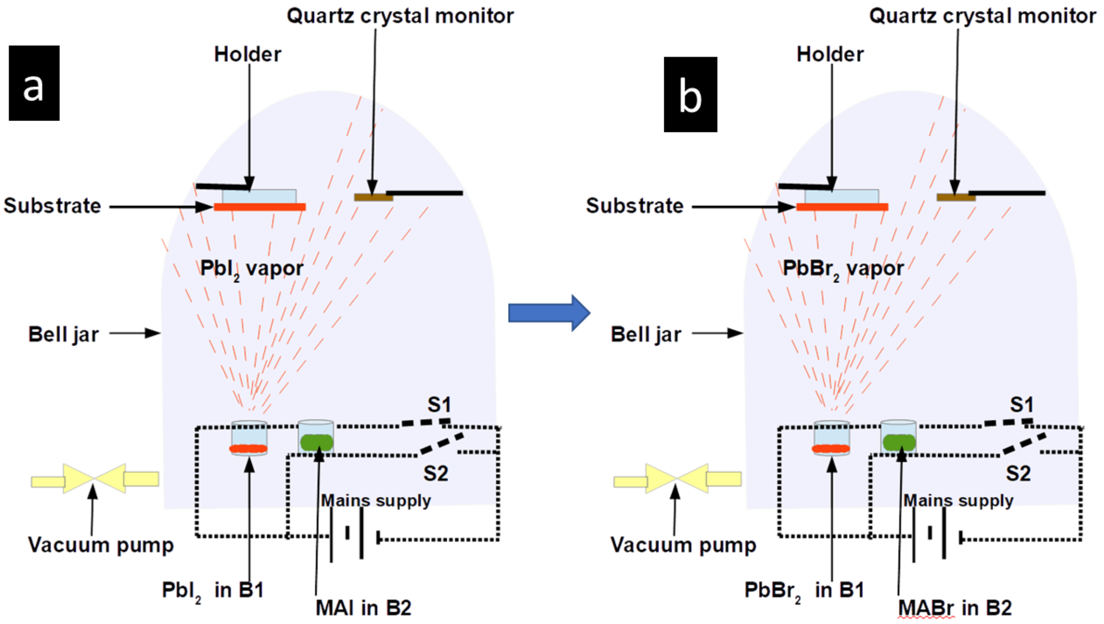

Figure 3.4.3: Schematic diagram of the process of preparing thin $MAPb(I_{1-x}Br_x)_3$ films by STVD

3.5 Preparing of titanium (IV) compact layer (c-TiO_2) and mesoscopic layer (m-TiO_2)

The precursor solution for the deposition of TiO_2 compact (c-TiO_2) layer was prepared by mixing 0.55 ml of titanium diisopropoxide bis(acetylacetonate) and 5 ml of 1-butanol to give 0.3 M TiO_x solution. The c-TiO_2 layer was deposited by spin-coating the 0.3 M TiO_x solution on FTO at 3000 rpm for 30 s. The film was dried in an oven at 125℃ for 5 min. The experiment is repeated once before annealing in a furnace at 500℃ for 30 min to produce a compact-TiO_2 layer. TiO_2 paste was prepared by dissolving 1.2 g of TiO_2 nanoparticles in 10 ml of ethanol, 4 ml of terpineol and 10 % ethyl cellulose (0.6 g ethyl cellulose in 10 ml of ethanol). The mixture was stirred overnight at room temperature. The paste was spin-coated at 3000 rpm for 30 s and dried at 125℃ for 5 min before sintering at 500℃ for 30 min to form the mesoporous-TiO_2 (m-TiO2) layer. The $MAPb(I_{1-x}Br_x)_3$ thin alloy film was grown on the as described in *section 3.4.3.*

3.6 Device fabrication

Figure 3.6.1 shows the fabrication of the simple FTO/$MAPbBr_3$/Au device. The device was fabricated to find the trap density and charge carrier mobility using space charge limited current theory. Regarding the FTO/$MAPbI_3$/Au device, 15 x 10 mm FTO substrate is trimmed and cleaned by sonication as described before. One edge of the conducting side of the cleaned substrate is covered with heat-resistant tape, followed by rapid deposition of $MAPbI_3$ by STVD as described earlier. The device is completed by thermal vapour deposition of 100 nm thick gold electrode through a shadow mask. The FTO/$MAPbI_3$/Au device is fabricated after the same procedure, except that $MAPbI_3$ is deposited in place of $MAPbBr_3$.

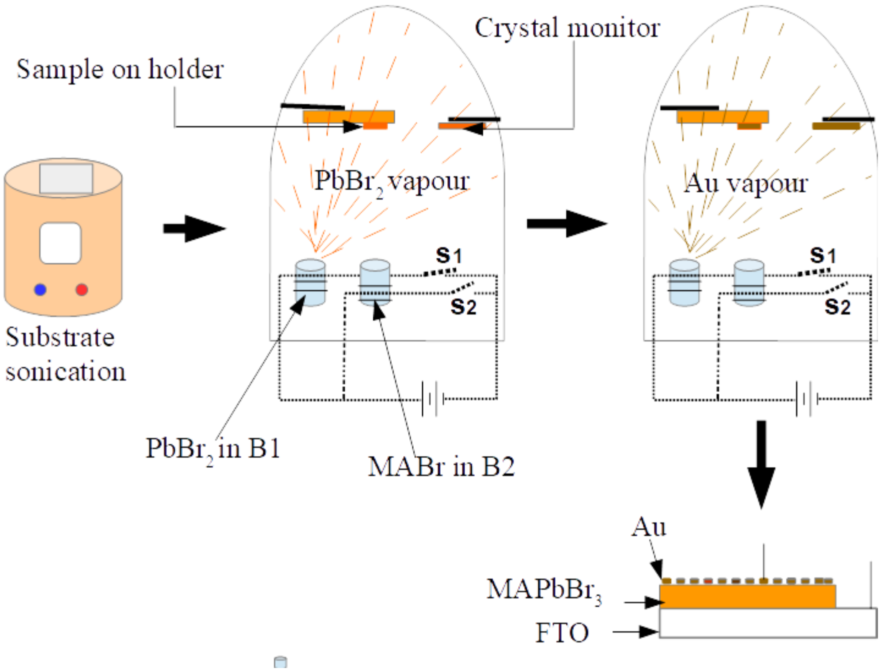

Figure 3.6.1: Schematic diagrams for fabrication FTO/MAPbBr$_3$/Au BTL-free solar cells.

We fabricated FTO/c-TiO$_2$/m-TiO$_2$/perovskite/Au devices, as shown in *Figure 3.6.2*. The c-TiO2, m-TiO$_2$ and perovskite {including MAPbI$_3$, MAPbBr$_3$ and MAPb(I$_{1-x}$Br$_x$)$_3$} were grown as described previously. The devices were then completed by depositing 100 nm of Au electrodes through a circular shadow mask.

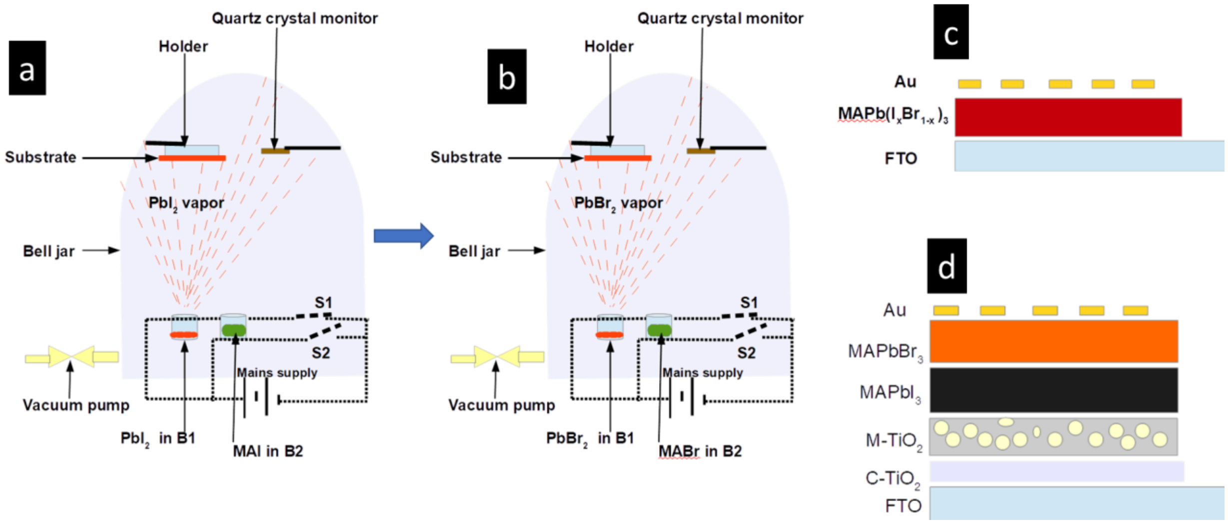

Figure 3.6.2: Schematic diagram for the fabrication of FTO/MAPb(I$_{1-x}$Br$_x$)$_3$/Au and FTO/c-TiO$_2$/m-TiO$_2$/ MAPb(I$_{1-x}$Br$_x$)$_3$/Au solar cells.

3.7 Thin-film characterization

3.7.1 Optical absorption spectrum by UV-Vis spectrometer

Figure 3.7.1 shows a simplified schematic diagram of the optical absorption spectrum measurement process using UV-Vis spectrometer. The optical absorption spectra (*Figure 3.7.2 (a)*) of the films were measured by CARY 100 BIO UV-Vis spectrometer with a wavelength of incident light ranging from 200 to 800 nm. Light from the source is split into two beams by a monochromator; one passes through the sample and the other through a reference. The intensity of the light passing through the sample (I) is compared to the intensity of the light passing through the reference (I_o), equal to intensity before light passes through the sample. The ratio (I/I_o) is called transmittance (%T), which is related to absorbance, A, by *Equation 3.1*,

$$A = -\log(I/I_o) \qquad \text{Equation 3.1}$$

The absorption coefficient, α , is a material property of the thin film related to the absorbance as shown by *Equation 3.2*,

$$\alpha = 2.303\, A/t \qquad \text{Equation 3.2}$$

where t is the thickness of the thin film.

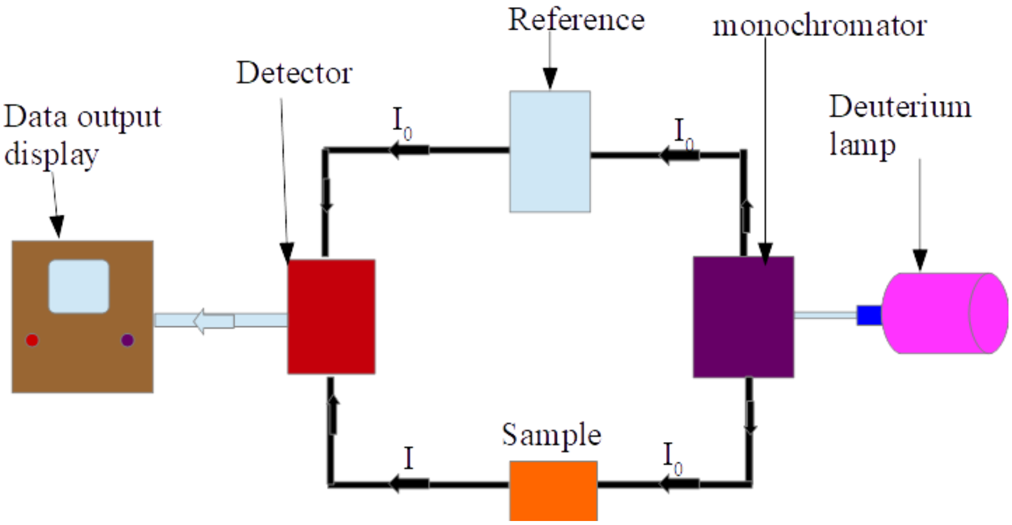

Figure 3.7.1: Schematic diagram of the optical absorption measurement process using UV-Vis spectrometer.

One approach to determine bandgap is by using a Tauc-plot (*Figure 3.7.2 (b)*) obtained from the Mott and Davis formula given by *Equation 3.3* [1],

$$(\alpha h\upsilon)^{1/n} = A(h\upsilon - E_g) \qquad \text{Equation 3.3}$$

where E_g is bandgap, and A is a proportionality constant, where α is the absorption coefficient, h is the Plank constant; n equals 1/2, 2, 3/2, and 3 for direct allowed, indirect allowed, direct forbidden, and indirect forbidden transitions, respectively. The Tauc plot for direct bandgap materials is a plot of the square of the product of the absorption coefficient and photon energy against photon energy. The bandgap is the intercept on the energy axis of an extrapolation of the linear part of the graph, as shown in *Figure 3.7.2 (b)*. Another method used in this thesis is the relationship between the energy of a photon and wavelength in quantum mechanics illustrated by *Equation 3.4*,

$$E_g(eV) = \frac{1240}{\lambda(nm)}$$ Equation 3.4

where E_g (eV) is the bandgap and λ (nm) is the wavelength of the photon at the onset of absorption shown in *Figure 3.7.2 (a).*

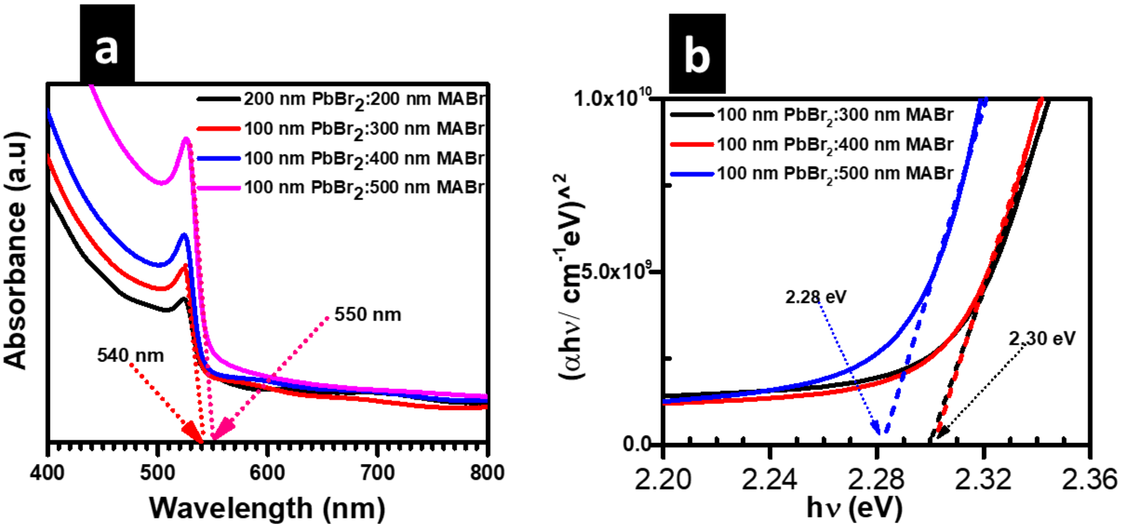

Figure 3.7.2: (a) The optical absorption spectra of MAPbBr₃ for various thicknesses of PbBr₂ and MABr, (b) Direct bandgap Tauc's plot from the optical absorption spectra of MAPbBr₃ for various thicknesses of PbBr₂ and MABr.

3.7.2 Structural characterisation by X-ray diffraction

X-ray diffraction (XRD) is a rapid non-destructive technique used for phase identification and atomic spacing calculation of crystalline thin films and powders. The phase(s) in the sample is found by comparing the diffractograms of the measured spectral pattern against known references in a search/match procedure. The schematic diagram for the XRD set up is shown in *Figure 3.7.3.* Our thin films were assessed by the Bruker D2-Phaser X-ray diffractometer using Cu Kα radiation with λ equals 1.5405 Å. 2θ was varied from 10 to 50° in steps of 0.05. A collimated monochromatic beam of X-rays from the cathode source was directed at a rotating crystalline sample on the sample mount. Upon interacting with the sample, the beam was diffracted by the crystal planes within the thin film according to Bragg's law (*Equation 3.5*). The diffractograms were also used to determine the crystallite size, micro-strain, lattice constant and dislocation density.

$$n\lambda = 2d\sin\theta \qquad \text{Equation 3.5}$$

where $n = 1$, θ is the Bragg's diffraction angle, λ is the wavelength and d is the spacing between the planes of atoms. In a 2θ diffraction scan, the angle between the incident and the diffraction beams 2θ is varied within a set range and diffractograms recorded. The lattice constant of the cubic $MAPbBr_3$ and $MAPb(I_{1-x}Br_x)_3$ crystals were calculated using *Equation 3.6,*

$$a = d\left(h^2 + k^2 + l^2\right)^{\frac{1}{2}} \qquad \text{Equation 3.6}$$

where a is the lattice constant and *(hkl)* are the miller indices. Similarly, the lattice constant of the tetragonal $MAPbI_3$ unit cell was calculated using *Equation 3.7,*

$$\frac{1}{d^2} = \frac{h^2 + k^2}{a^2} + \frac{l^2}{c^2} \qquad \text{Equation 3.7}$$

where a and c are the lattice constants. Line broadening of diffractograms is determined by three principal effects, including instrumental, crystallite size and micro-strains [2,3]. We used the Williamson-Hall (W-H) plot to quantify their contributions of crystallite size and micro-strain to line broadening [4] and ignored the effect due to the instrument since it is systematic. Relationship between them is given by Williamson and Hall's formula shown in *Equation 3.8,*

$$FWHM\cos\theta = \frac{K\lambda}{D} + 4\varepsilon\sin\theta \qquad \text{Equation 3.8}$$

where *FWHM* is the full width at half maximum determined from a Gaussian fit of peaks, D is the crystallite size, ε is the micro-strain and K is the Scherer constant which is determined by the crystallite shape and is considered as 0.94 for spherical crystallites with cubic symmetry. The slope of the W-H plot corresponds to the micro-strain, and the crystallite size equals a constant multiplied by the reciprocal of the intercept shown in *Figure 3.7.4*. W-H analysis is best when large crystallites and thick films are involved. Dislocation density, ρ, is related to the crystallite size by Williamson and Smallman's formula [5] given by *Equation 3.9*,

$$\rho = \frac{n}{D^2} \qquad \text{Equation 3.9}$$

where n equals unity for minimum dislocation density.

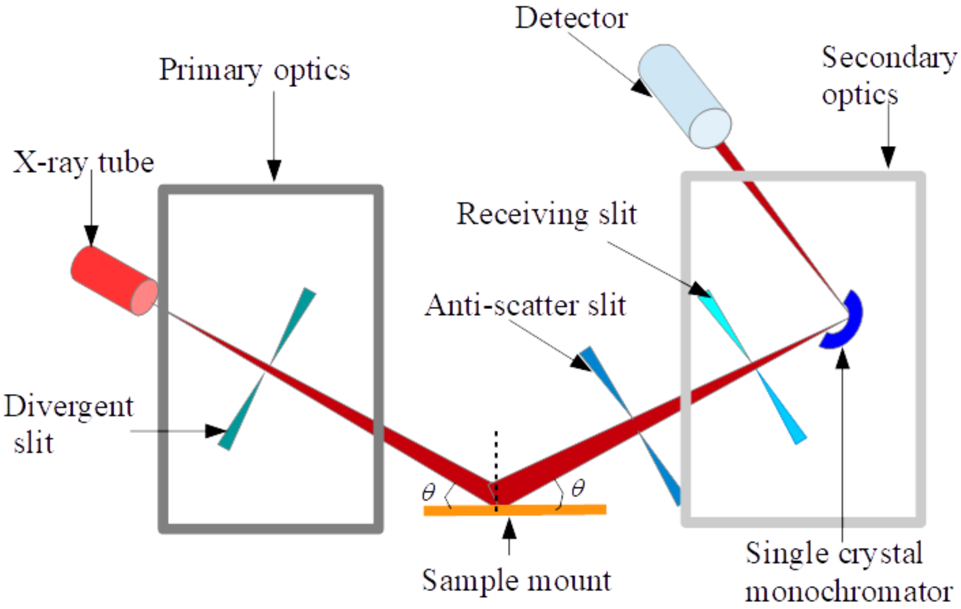

Figure 3.7.3: Schematic diagram of XRD measurement process using Bruker D2-Phaser X-ray diffractometer.

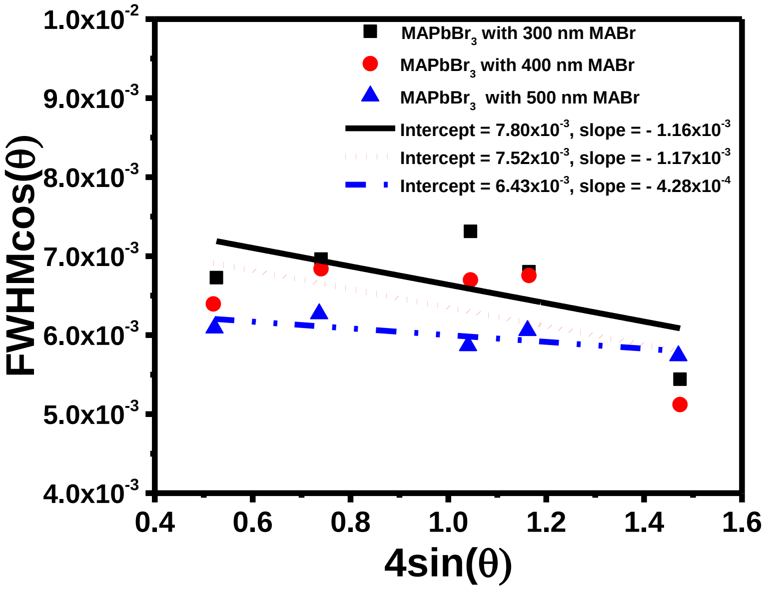

Figure 3.7.4: W-H plot of $MAPbBr_3$ *thin film for various thicknesses of MABr.*

3.7.3 Morphological characterization by scanning electron microscopy

Scanning electron microscopy (SEM) is a destructive surface imaging technique involving the use of a beam of fast-moving electrons to scan the surface of a specimen to produce a magnified 3D morphology and composition. SEM can image objects down to 10 nm size. A beam of electrons from an electron gun is accelerated through vacuum towards the anode. The first electromagnetic coil from the top brings the beam to a precise focus, and the next electromagnet moves the electron (e) beam from side to side to scan across the surface being viewed. The electrons hitting the surface are reflected, and the scattered electrons are registered by the detector and information transformed into a picture.

We determined the morphology of out thin films by the Field Emission Scanning Electron Microscope (FE-SEM, Zeiss Crossbeam 540). The samples were coated with gold to make them conducting before the analysis. Grain size analysis was done on the FE-SEM micrographs following the American Standard for Testing Materials (ASTM) using Average Grain Intercept (AGI) with the help of Image J Software.

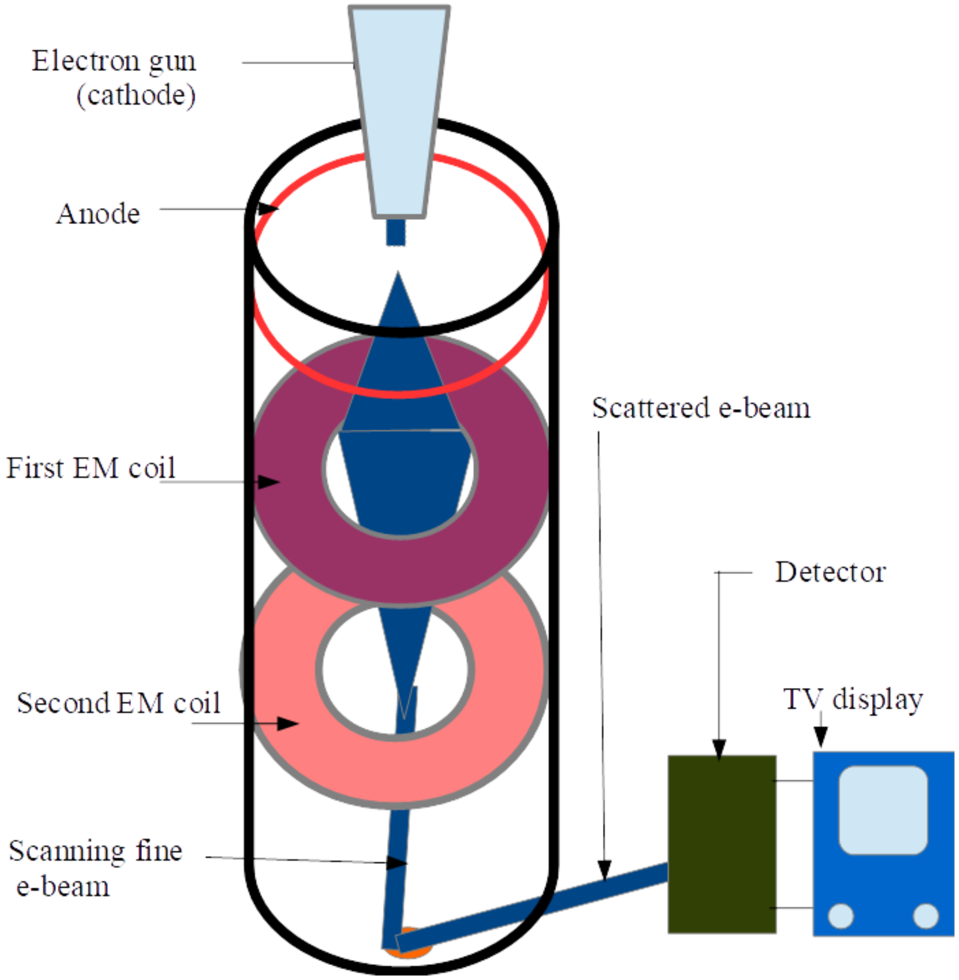

Figure 3.7.5: Schematic diagram of the SEM measurement process using FE-SEM Zeiss Crossbeam 540.

3.8 Device characterisation

3.8.1 Light current-voltage measurements

Current-voltage (*I*-*V*) measurements under standard illumination conditions at room temperature, were performed using a system comprising a solar simulator (Oriel LCS-100^{TM} Small Area So11A Series, Oriel Cornerstone, Newport), a source measure unit (SMU) (Key-sight B2912-A), a programmable voltage supply (Keithley 230) and computer with LabVIEW Software shown in *Figure 3.8.1*. The solar simulator consists of build-in Xenon Arc Lamp (100 W), mirror and an AM1.5 filter. Before the start of the experiment, the irradiance intensity of the simulator is calibrated using a standard cell (Oriel, model

91150V) that is connected to a thermocouple. Light *I-V* measurements were performed under solar output conditions of 1000 W/m^2 at 25°C and AM1.5 G reference spectral filtering. The lamp was switched automatically using the LabVIEW Software to take the light measurements at once after the dark measures were completed.

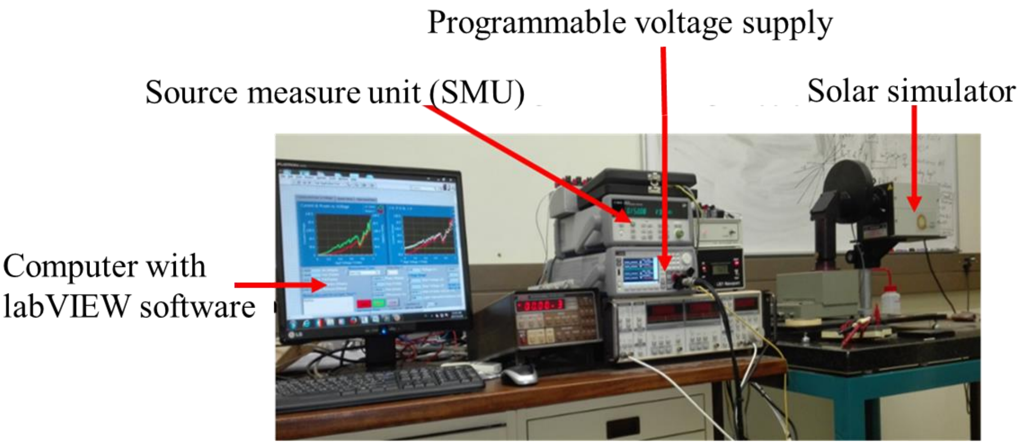

Figure 3.8.1: An automatic set-up for I-V measurements under dark and standard illumination conditions.

3.8.2 Dark current-voltage measurements

Figure 3.8.2 shows an automatic set-up for dark *I-V* measurements. In use, the device is placed on the sample stage inside the opaque Faraday cage and separate probes connected to its front and back contacts. The light microscope ensures good contact is made with the samples and the Faraday cage to create darkness and minimize electrical noise on the sample when it is closed. The Hewlett Packard pA/DC voltage 4140B source meter, which measures current down to 10^{-15} A with 0.5% accuracy, is used to source *V* and measure the resulting *I*. The meter is controlled automatically using software installed in the computer, which also displays estimated data. The *I-V* measurements were then used for SCLC analysis to calculate the carrier mobility and trap density.

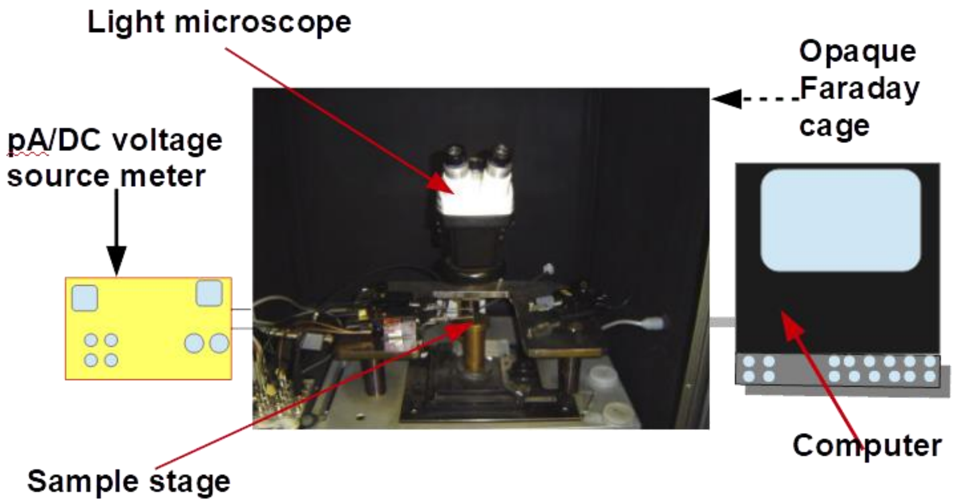

Figure 3.8.2: An automatic set-up for dark I-V and C-V Measurements.

3.8.3 Dark capacitance-voltage measurement

Figure 3.8.2 is also used for automatic *C-V* measurements under dark conditions. A 4192A LF Impedance Analyser with measurement frequency ranging from 5 Hz to 13 MHz, was used for the *C-V* measurement. The measurements were conducted at a constant frequency of 1 MHz so that the defects within the device should not respond to electric field variations [6]. The measured values were then used for Mott-Schottky analysis to determine doping density, built-in voltage, and presence of charge accumulation during device operation.

References

[1] E.A. Davis, N.F. Mott, Conduction in non-crystalline systems V. Conductivity, optical absorption and photoconductivity in amorphous semiconductors, Philos. Mag. 22 (1970) 903–922. doi:10.1080/14786437008221061.

[2] P.M. Shafi, A.C. Bose, Impact of crystalline defects and size on X-ray line broadening : A phenomenological approach for tetragonal SnO2 nanocrystals Impact of crystalline defects and size on X-ray line broadening : A phenomenological approach for tetragonal, AIP Adv. 5 (2015) 057137. doi:10.1063/1.4921452.

[3] A.R. Bushroa, R.G. Rahbari, H.H. Masjuki, M.R. Muhamad, Approximation of crystallite size and microstrain via XRD line broadening analysis in TiSiN thin films, Vaccum. 86 (2012) 1107–1112. doi:10.1016/j.vacuum.2011.10.011.

[4] G.K. Williamson, W.H. Hall, X-ray line broadening from filed aluminium and wolframL'elargissement des raies de rayons x obtenues des limailles d'aluminium et de tungsteneDie verbreiterung der roentgeninterferenzlinien von aluminium- und wolframspaenen, Acta Metall. 1 (1953) 22–31. doi:https://doi.org/10.1016/0001-6160(53)90006-6.

[5] G.K. Williamson, R.E. Smallman, III. Dislocation densities in some annealed and cold-worked metals from measurements on the X-ray Debye-Scherrer spectrum, Philos. Mag. 1 (1956) 34–46. doi:10.1080/14786435608238074.

[6] I.M. Dharmadasa, Y. Rahaq, A.A. Ojo, T.I. Alanazi, Perovskite solar cells: a deep analysis using current-voltage and capacitance-voltage techniques, J. Mater. Sci. Mater. Electron. 30 (2019) 1227–1235. doi:10.1007/s10854-018-0390-5.

4 Results and discussion

4.1 Sequential thermal deposition of methylammonium lead tri-bromide

4.1.1 Introduction

In this section, the results from the preparation of methylammonium lead tri-bromide ($MAPbBr_3$) using sequential thermal vapour deposition (STVD) of lead(II)bromide ($PbBr_2$) and methylammonium bromide (MABr) single layers are presented and discussed. The structural, morphological, optical, and electrical properties of the thin $MAPbBr_3$ films are optimised by varying $PbBr_2$ and MABr thicknesses and annealing time. XRD spectra show the cubic $MAPbBr_3$ crystal structure having the $Pm\overline{3}m$ space group. UV-Vis spectra show a shift in absorption onset from 540 to 550 nm as the thickness of MABr was increased from 300 to 500 nm, and an optimum bandgap of 2.28 eV. Scanning electron micrographs show large pinhole-free densely packed grains with an increase in average grain size from 217 to 302 nm as the thickness of MABr increases from 300 to 500 nm. Dark current-voltage characteristics of Au/$MAPbBr_3$/FTO devices reveal an ohmic conduction behaviour at low voltages and trap-space charge limited current at high voltages. The charge carrier mobility increases from 1.89×10^{-2} to 1.08×10^{-1} cm^2 V^{-1} s^{-1}, while the trap density decreases from 1.89 x 1016 to 1.40 x 1016 cm^{-3} as the thickness of MABr is increased from 300 to 500 nm.

4.1.2 Structural properties of methylammonium lead tri-bromide

Figure 4.1.1 ***(a)*** presents the diffractograms of thin 3D $MAPbBr_3$ films grown for various MABr thicknesses on FTO. Peaks corresponding to FTO were seen on the diffractograms and were referenced using JCPDS number 41-1445. It is observed that the other Bragg peaks on all patterns are sharp, showing good crystallinity. Besides, the 2θ diffraction directions occur at 14.95˚, 21.14˚, 23.88 ˚, 26.54˚, 30.13˚, 33.73˚, 37.67˚, 43.12˚, 45.86˚ and 48.47˚, which agrees closely with the works of literature for single crystals of cubic $MAPbBr_3$ having $Pm\overline{3}m$ space group [1–3]. The various diffraction directions are matched to the (100), (110), (111), (200), (210), (211), (220), (300), and (310) diffraction planes, respectively. Notably, the extra peak at 23.88˚, which does not occur on the patterns for single crystals, was initially indexed to $PbBr_2$ by JCPDS card file number 31-0679 and supported by the XRD spectrum of $PbBr_2$ powder *Figure 4.1.2 (a).* But its intensity is seen to increase, in the same sense as for all the other peaks of $MAPbBr_3$ single crystal, upon increasing the annealing time and thickness of MABr as shown in *Figure 4.1.1 (a).* The increase in the intensity of diffraction planes with the thickness of MABr could be due to a rise in the number of carbon, hydrogen and bromine atoms at the Wyckoff positions of the space group, resulting in high structure factor and consequently the high-intensity peaks. Also, it could be due to an increase in the orientation of planes in given directions as MABr thickness was increased, which increased the multiplicity factor and so peak intensities. Still, in line with the different peak, we saw that increasing the annealing time for the 500 nm thick MABr thin film, reduced both the intensity of the extra peak and that of the prominent (100) peak for $MAPbBr_3$ as shown in *Figure 4.1.2 (a).* Furthermore, the intensity of the principal (100) plane and the extra peak at 23.88˚ showed the same variations with the increase in annealing time. This similarity in response to changing annealing time and thickness of MABr by the peaks corresponding to $MAPbBr_3$ and the extra peak points to the fact that the different peak may be one of the characteristic peaks of $MAPbBr_3$ polycrystalline thin film on FTO and glass substrates. It is known that crystallographic texturing of thin polycrystalline films depends on many factors, including the substrate type, deposition method and growth conditions. Regarding the variation in the intensity of the (100) peak with annealing time, it was observed to decrease as annealing time was increased. This inverse correlation shows that prolonged post-deposition annealing causes a loss in crystallinity of the $MAPbBr_3$ thin film. Besides, *Figure 4.1.2 (a)* illustrates that the crystallization of $MAPbBr_3$ started inside the deposition chamber since the as-deposited film displays the cubic crystal structure of $MAPbBr_3$. The crystallisation within the chamber is so because the temperature of the substrate was 95℃ during the evaporation of the MABr on $PbBr_2$. This temperature is close to the annealing temperature (100℃) for $MAPbBr_3$ in the literature [4]. Thus, the thermal energy generated during the evaporation process was enough to cause diffusion of MABr into the voids in the $PbBr_2$ octahedral framework, leading to the formation of $MAPbBr_3$. Therefore, when post-annealing 100, only a short time (less than 10 min) is recommended to enhance crystallization while preserving good crystallinity.

Figure 3.7.4 shows the W-H plot was used to quantify the contributions crystallite size and micro-strain to line broadening [5]. First, it is seen that the slopes were negative, which could be due to several factors including compressive stress, stacking faults and line broadening not caused by strain. However, the effect of micro-strain could not be ignored. Micro-strain may originate from the thermal annealing and in minimization of the interface, surface, and grain boundary energies during grain growth. It is known that compressive stresses are always found in films grown by thermal vapour deposition because the technique involves particle bombardment on the substrate [6]. The magnitude of the compressive micro-strain was seen to decrease as the thickness of MABr increased, as shown in *Figure 4.1.2 (b).* The size of micro-strain is known to be proportional to the degree of lattice distortion, which is measured from the change in a lattice constant from its bulk value. *Figure 4.1.1 (b)* shows the variation of lattice constants of $MAPbBr_3$ thin film with MABr thickness. It was seen that the lattice constant increased proportionately with the thickness of MABr. Also, the lattice constant (5.9300(2) Å) of high-purity bulk $MAPbBr_3$ by *Tisdale and co-workers* [3], which agrees closely with that of the 500 nm thick film (5.9240 Å), indicating that the unit cell was least distorted when the thickness of MABr was 500 nm. Lattice distortions maybe because of temperature differences (thermal expansion) and chemical differences (impurities). Therefore, $MAPbBr_3$ films having 500 nm thick MABr may have the least chemical differences (strain) due to the smallest ionic radii differences of its constituents, implying high purity. In the same light, we can deduce that the phase purity increased with increase in MABr thickness. Next, the crystallite sizes of $MAPbBr_3$ thin films were calculated for different MABr thicknesses and the results displayed in *Figure 4.1.1 (c).* It was seen that the crystallite size increases with an increase in MABr thickness, like lattice constant. The increase in both average crystallite size and lattice constant with the thickness of MABr could due to decrease in size of compressive micro-strain, which could be responsible for the redshift in absorption onset that has caused the reduction in the bandgap, vide infra.

Figure 4.1.1 (d) is the variation of dislocation density with the thickness of MABr. The dislocation density is observed to decrease from 2.891 x 10^{11} to 1.973 x 10^{11} cm^{-2} as the thickness of MABr was increased. By performing analytic studies, *Hyder and Wilkov* [7] showed the effect of dislocation density affects the V_{oc}, I_{sc}, PCE and minority carrier lifetime of indium gallium nitride (InGaN)-based multi-junction solar cells. Similarly, the $MAPbBr_3$ thin film having 500 nm thick MABr and smallest dislocation density may lead to high-performance solar cells.

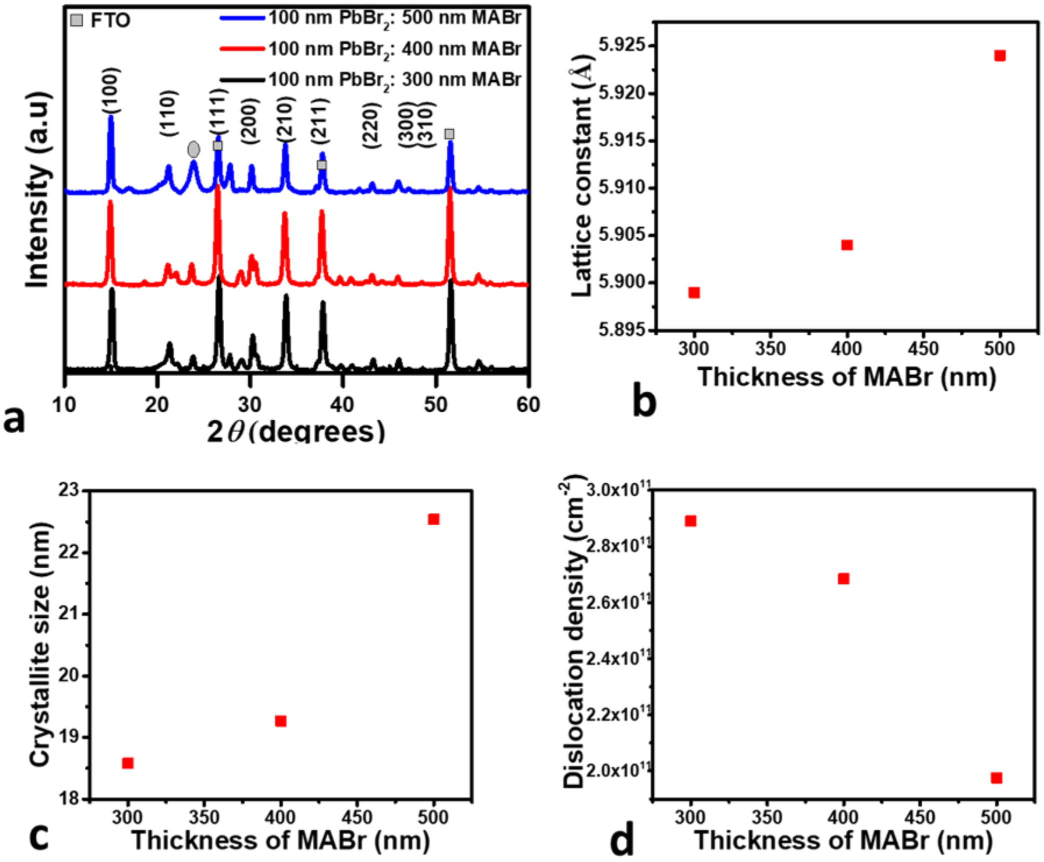

Figure 4.1.1: (a) XRD patterns of $MAPbBr_3$ for various thickness of MABr, (b) Change in lattice constant of $MAPbBr_3$ vs. thickness of MABr, (c) Change in crystallite size of $MAPbBr_3$ thin films vs. thickness of MABr, (d) Dislocation density of $MAPbBr_3$ thin film vs. thickness of MABr.

Finally, *Figure 4.1.2 (c, d)* show the diffractograms for the thin films with an equal thickness of $PbBr_2$ and MABr and films with $PbBr_2$ to MABr ratios greater than one. It was seen that characteristic peaks for $MAPbBr_3$ were missing for $PbBr_2$ to MABr ratio greater than one, saying that the perovskite is not formed under such conditions. Similarly, equal $PbBr_2$ and MABr thicknesses do not lead to the formation of pure $MAPbBr_3$ thin films. This is aimed at investigating the possibility of growing $MAPbBr_3$ thin film for the equal thickness of $PbBr_2$ and MABr, and for the thickness of $PbBr_2$ greater than that of MABr. This explains why our focus on perfecting the synthesis of $MAPbBr_3$ included only the variation of MABr thickness while that of $PbBr_2$ was kept constant.

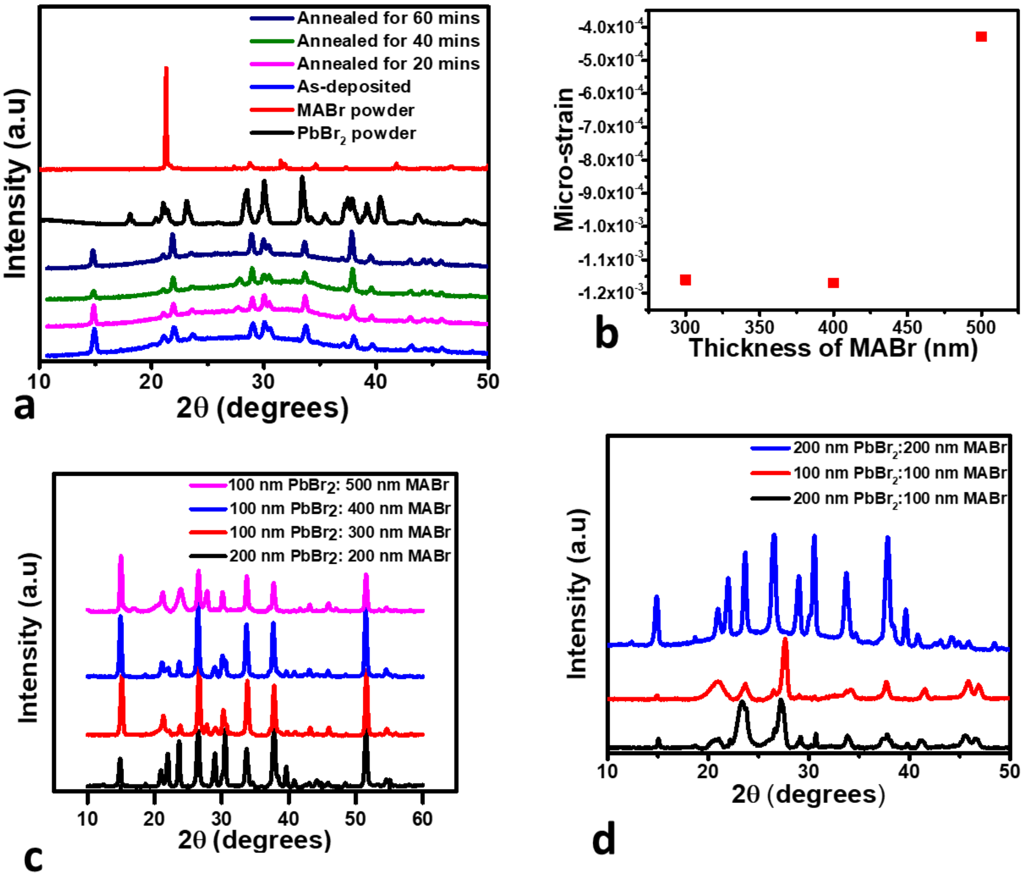

Figure 4.1.2: (a) Diffractograms of MAPbBr$_3$ thin film for varying annealing times, (b) Micro-strain of MAPbBr$_3$ thin films vs. thickness of MABr, (c) Diffractograms including films with an equal thickness of PbBr$_2$ and MABr (d) Diffractograms including films with a thickness of PbBr$_2$ greater than that of MABr.

4.1.3 Optical properties of methylammonium lead tri-bromide

Figure 4.1.3 (a) illustrates the UV-Vis absorption spectra of thin MAPbBr$_3$ films for various thicknesses. A broad absorption band was seen between 400 and 550 nm, in agreement with the literature [8]. Also, there is a redshift in absorption onset from 540 to 550 nm as the MABr thickness increased from 400 to 500 nm, corresponding to a decrease in the bandgap. *Figure 4.1.3 (b)* shows the Tauc plot from which the bandgap was determined. We observed that the bandgap decreases from 2.30 to 2.28 eV as the thickness of MABr from 300 to 500 nm. The decrease in the bandgap was attributed to the increase in crystallite size as the thickness was increased, vide infra, consistent with a previous study of copper iodide (CuI) thin film [9,10]. The narrowing of the bandgap may reduce the possibility of forming mid-gap states that may decrease the charge carrier lifetime of solar cells [11]. *Figure 4.1.3 (c)* shows the relationship between bandgap and lattice constant. It was seen that the bandgap decreases as the lattice constant increases. Thus agrees closely with previous reports for other cubic semiconductors in the literature [12]. For instance, *Dalven* [12] showed by empirical calculations that the band gaps of cubic semiconductors are inversely proportional to the square of the lattice constant. This is because the increase in lattice constant means the inter-atomic distance increased, which implies force binding the valence electrons and parent atoms decreased, therefore less energy required to free them for conduction. *Figure 4.1.3 (d)* shows that the net $MAPbBr_3$ film thickness is directly proportional to the thickness of MABr, as expected. However, it is less than the sum of the thicknesses of $PbBr_2$ and MABr, possibly due to bond formation.

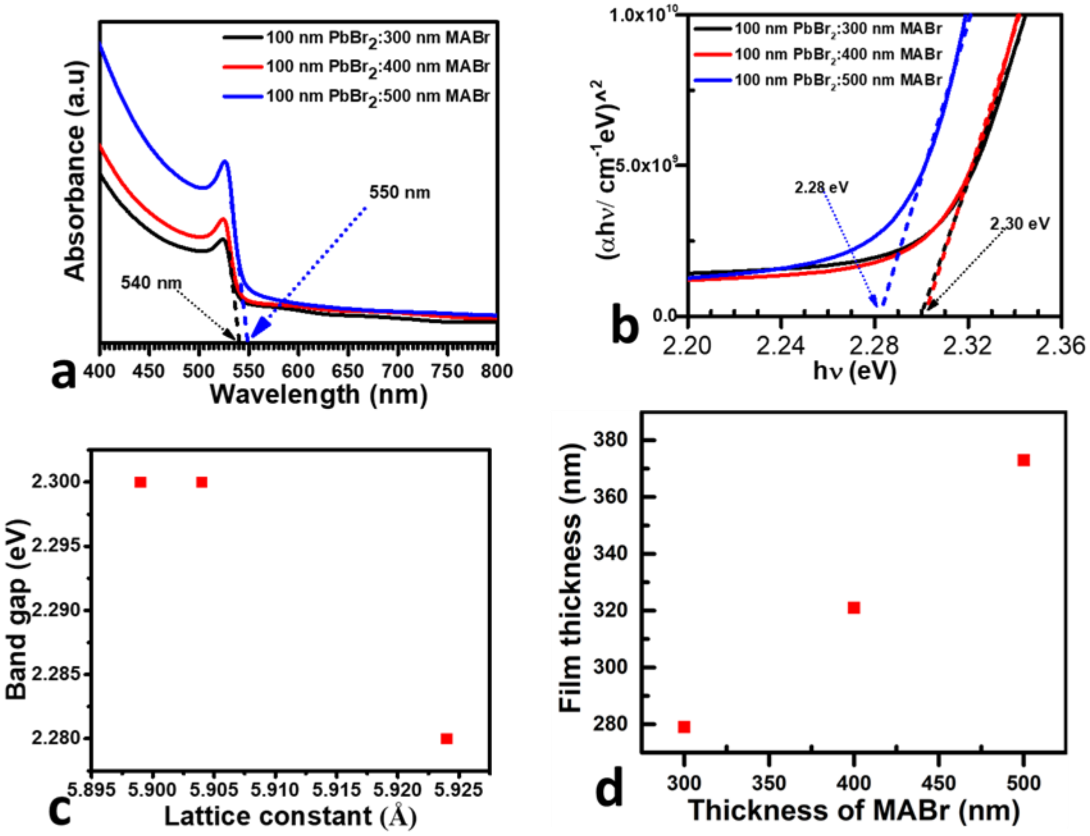

Figure 4.1.3: (a) UV-Vis absorption spectra of $MAPbBr_3$ for various thickness of MABr, (b) Direct bandgap Tauc-plot of $MAPbBr_3$ for different MABr thickness, (c) Bandgap of $MAPbBr_3$ for various thickness of MABr, (d) The film thickness of $MAPbBr_3$ vs. thickness of MABr.

The experiments were repeated on the glass as substrate by while varying thickness, and by changing annealing time for 500 nm thick MABr, and results displayed in *Figure 4.1.4.* We obtained the same onset of absorption, as shown in *Figure 4.1.4 (a),* indicating similar bandgaps. This suggests that the new method is reproducible. Also, we observed that the annealing the bandgap did not change upon increasing annealing time. This is consistent with previous reports by *Bi and co-workers* in the literature [13]. However, the absorbance increases slightly with an increase in annealing time. Furthermore, the bandgap of the as-deposited thin film is equal to those of thin films that were annealed at 100℃ in air for various times, confirming that the heat energy produced in the chamber was enough to activate inter-diffusion and reaction to make $MAPbBr_3$ as mentioned above. The results for changing thickness in glass substrate shown in *Figure 4.1.4 (b)* similar to that of changing the thickness on FTO shown in *Figure 4.1.4 (a),* further confirming reproducibility.

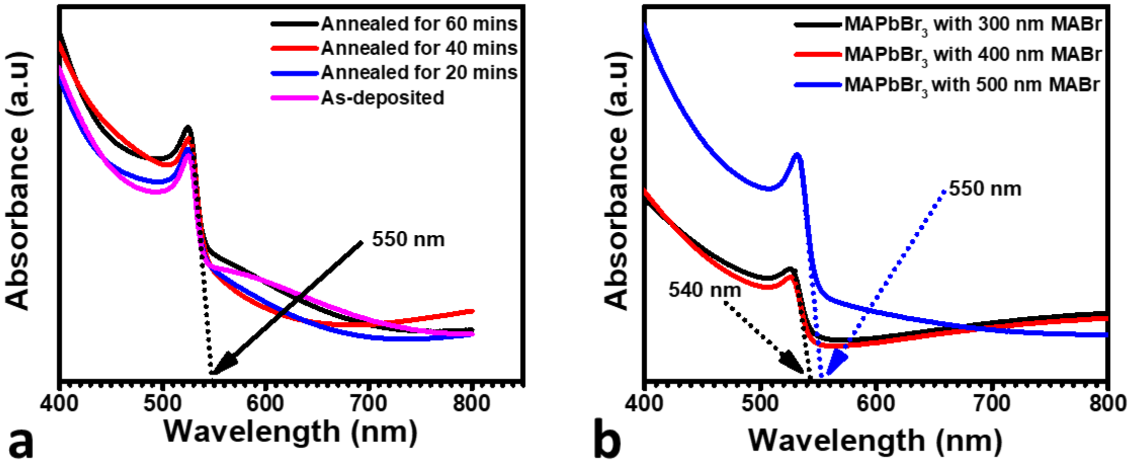

Figure 4.1.4: (a) UV-Vis spectra of $MAPbBr_3$ including 500 nm thick MABr annealed at different times, (b) UV-Vis spectra of $MAPbBr_3$ for various thicknesses of MABr synthesized on glass.

4.1.4 Morphological properties of methylammonium lead tri-bromide

Figure 4.1.5 stands for the surface morphology of $MAPbBr_3$ thin films for different MABr thickness and the relationship between average grain size and thickness of MABr. It was seen that the substrates were entirely covered with pin-hole-free densely packed and bimodal distributed grains, as shown in *Figure 4.1.5 (a-c).* The dense nature of the grains is vital for solar cell applications to minimize photo-current leakage and to avoid recombination through shunt paths [14,15]. *Eperon et co-workers*

[14] demonstrated that HaP thin films having full substrate coverage showed the highest photo-current and resulted in high PCE. The bimodal size distribution and variable orientation showed that the tin films were polycrystalline [16]. This polycrystallinity agrees closely with the diffractograms having sharp peaks with several reflection planes, vide infra. The differences in grain sizes and orientations arise during grain growth in thin polycrystalline films because of the competition in minimizing free surface, interface, grain boundary and strain energies [16,17]. Additionally, the bimodal size distraction is evidence of an abnormal grain growth mechanism during film formation.

Figure 4.1.5 (d) shows that the average grain size increases from 217 to 302 nm as the thickness of MABr increased from 300 to 500 nm. This is consistent with other reports for polycrystalline thin films grown by thermal vapour deposition. For instance, *Dammers and Radelaar* [18] showed that the average size of vapour-deposited grains is proportional to the square root of the film thickness. We think that the increase in average grain size with the thickness of MABr may be due to the decrease for $PbBr_2$ residue as it reacts with the MABr. This cause the formation of larger $MAPbBr_3$ grains leading to the increase in the average grain size. Besides, the increase in average grain size may be due to a decrease in dislocation density which reduces abnormality in grain growth during thermal annealing [17]. This increase in average grain size with thickness points to the fact that films containing 100 nm $PbBr_2$ and 500 nm MABr have the smallest number of grain boundaries and trap sites. This will cause the least electron scattering and nonradiative recombination during charge transport in solar cells.

In comparison, the average crystallite size obtained from W-H analysis *(Figure 4.1.1 (c))* is ten times smaller than the average grain size shown in *Figure 4.1.5 (d)*. This could be because the grains of polycrystalline thin films consist of two or more crystallites that coalesced in grain growth. This difference between grain size and crystallite size has also been seen for other semiconductors. For instance, *Garg and co-workers* [19] showed that the grain size of CsI is the same as its crystallite size for thicknesses less than 4 nm. However, for film thicknesses greater than 4 nm, the difference between grain and crystallite size increased because the crystallites moved and merged to form bigger grains during the grain growth.

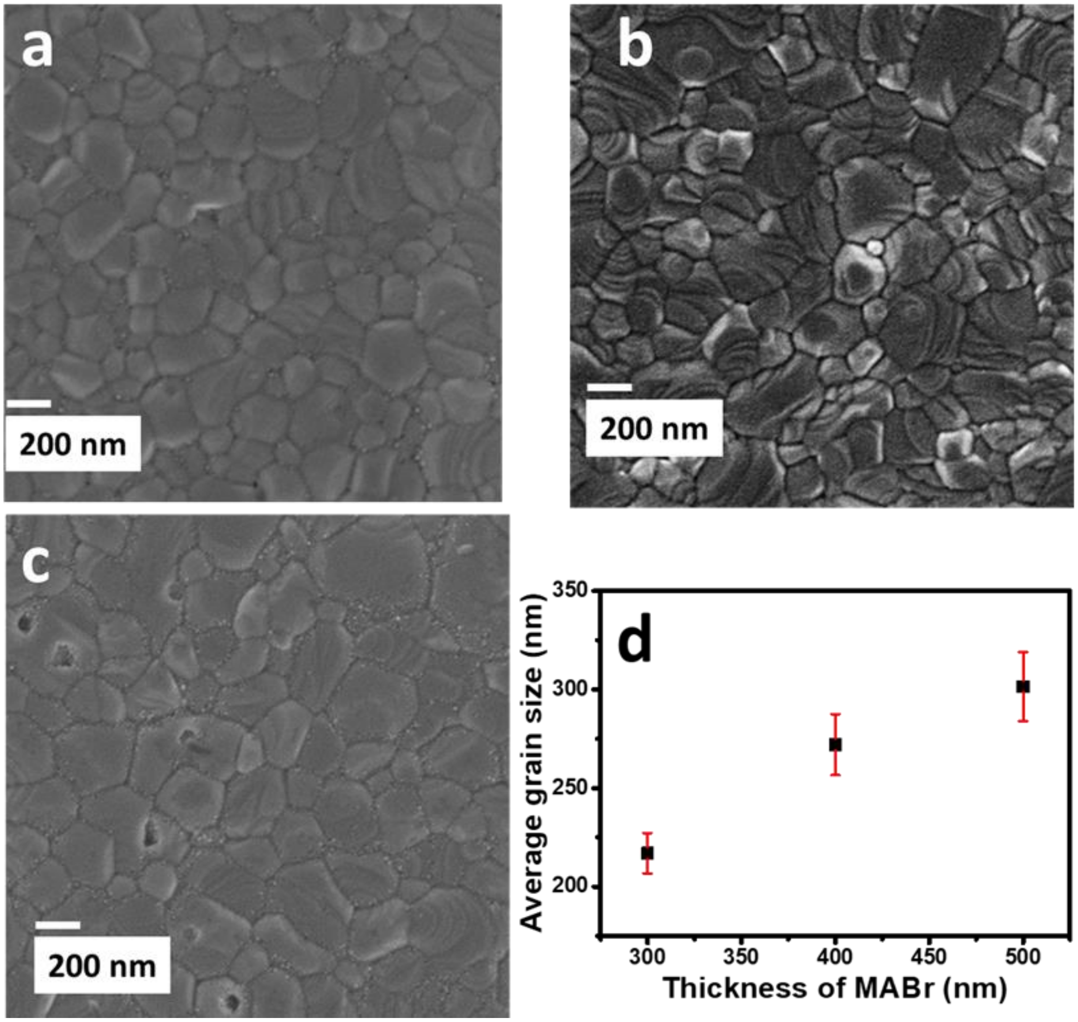

Figure 4.1.5: FE-SEM micrographs of $MAPbBr_3$ for various thickness, (a) 100 nm $PbBr_2$:300 nm MABr, (b) 100 nm $PbBr_2$:400 nm MABr, (c) 100 nm $PbBr_2$:500 nm MABr, (d) Average grain size vs. thickness of MABr.

4.1.5 Electrical properties of methylammonium lead tri-bromide

4.1.5.1 Dark current-voltage analyses of Au/$MAPbBr_3$/FTO devices

Figure 4.1.6 presents the dark current-voltage (*I-V*) study of the Au/$MAPbBr_3$/FTO devices for different thickness of MABr, from which the trap density and carrier mobility were calculated. In *Figure 4.1.6 (a)*, a weak-linear *I-V* relationship is observed for the solar cell with 300 nm MABr and a quadratic relationship as the thickness is increased from 400 to 500 nm. Similar associations have been obtained for zero-bias Schottky detectors [20] and zero-bias Pt/$MAPbBr_3$/Au Schottky diode [21]. Furthermore, the near symmetric semi-log *I-V* plots shown in *Figure 4.1.6 (b),* shows the presence of a slightly rectifying contact [22]. The $MAPbBr_3$/Au is expected to be ohmic because Au has a high work function of 5.1 eV [23] and forms an ohmic contact with p-type semiconductors. $MAPbBr_3$ is p-type with a work function of 4.6 eV [24]. This may be due to the small barrier height, which corresponds to the difference between the work functions of Au and $MAPbBr_3$. The ohmic contact eases electrons injection from the electrode into the bulk of $MAPbBr_3$ thin film of the solar cell. The quality of the ohmic contact was determined by calculating the specific contact resistivity of the devices. *Figure 4.1.6 (d)* shows that relationship between the specific contact resistivity of the devices and the thickness of MABr of the thin film. It was seen to increase with an increase in MABr thickness, showing a decrease in the level of doping [25]. This shows that the $MAPbBr_3$ thin films were self-doped, and their level of doping decreased as MABr thickness was increased. Also, the apparent slight rectification observed for devices having the 400 and 500 nm MABr thick films could be due to the formation of a small potential barrier at the p-n junction between FTO (n-type) and $MAPbBr_3$ (p-type).

Figure 4.1.6 (c) shows the double-log *I-V* curves from which the trap density and carrier mobility were calculated using space charge limited current (SCLC) theory. Two distinct regions were seen on the graphs corresponding to the ohmic and shallow trap SCLC conduction mechanisms. Only the Ohmic mechanism (m ~ 1 for all sections of the curve) was seen for the solar cell having 300 nm thick MABr. Whereas, solar cells having $MAPbBr_3$ thin films with 400 and 500 nm MABr demonstrated the ohmic behaviour for voltage in the 0–0.2 V range and shallow trap SCLC bulk transport mechanism for voltages in the 0.7–1.0 V range. No section of the curves had a steep slope confirming that only shallow traps are present in the $MAPbBr_3$, which is consistent with very sharp absorption onset, vide infra. It was seen that the trap density, N_t, decreased from 1.89×10^{16} to 1.40×10^{16} cm^{-3} as thickness increased from 400 to 500 nm. This is in line with the variation of dislocation density with MABr thickness, vide infra. Notably, the values obtained were only an order of magnitude higher than values for quality $MAPbBr_3$ single crystals calculated by *Wenger and co-workers* [26], which gave rise long diffusion lengths (in microns). *Wenger and co-workers* measured the N_t for single crystal $MAPbBr_3$ and thin films using light transmission spectroscopy, ellipsometry, spatially resolved and time-resolved photoluminescence spectroscopy and achieved 1.22×10^{15} and 7.0×10^{16} cm^{-3} respectively. Furthermore, the trap densities had the same order of magnitude as those obtained for HaP in high-efficiency solar cells. For instance, *Yang and co-workers* got a trap density of 1.22×10^{16} cm^{-3} for $MAPbI_3$ perovskite which resulted in solar cells with 19.62% PCE [27]. Finally, the carrier mobility, μ_p, was calculated also calculated from *Figure* 4.1.6 *(c)* using the modified Mott-Gurney model [28]. The values are ranging from 1.89 x 10^{-2} to 1.08 x 10^{-1} cm^2 V^{-1} s^{-1} for 400 and 500 nm MABr thick samples, respectively. It is important to note that the calculated values are within the range for inorganic semiconductors (10^{-4} - 10^3 cm^2 V^{-1} s^{-1}) [29], however, are two orders of magnitude lower than values single crystals calculated using the SCLC method [30]. *Saidaminov and co-workers* calculated μ_p for high quality $MAPbBr_3$ single crystals that were grown by the inverse temperature crystallization and obtained 24 cm^2 V^{-1} s^{-1} [30], which is only two orders magnitude higher. *Chen and co-workers* got 0.9, 5.6 and 54.6 cm^2 V^{-1} s^{-1} after the respective first, second and third crystallization of bulk $MAPbBr_3$, synthesized by the inverse temperature crystallization method [31]. They attributed the increase in carrier mobility after repeated crystallization to be due to the formation of voids by surface states that favoured the movement of electrons. The lower μ_p obtained for our polycrystalline thin films when compared with the single crystals may be due to the presence of ionized impurities at grain boundaries which scatter charge carriers, thus reducing their mobilities. Moreover, the μ_p was seen to increase proportionally with MABr thickness. This increase in μ_p may be due to the increase in grain size, which inevitably caused a decrease in grain boundaries and trap density.

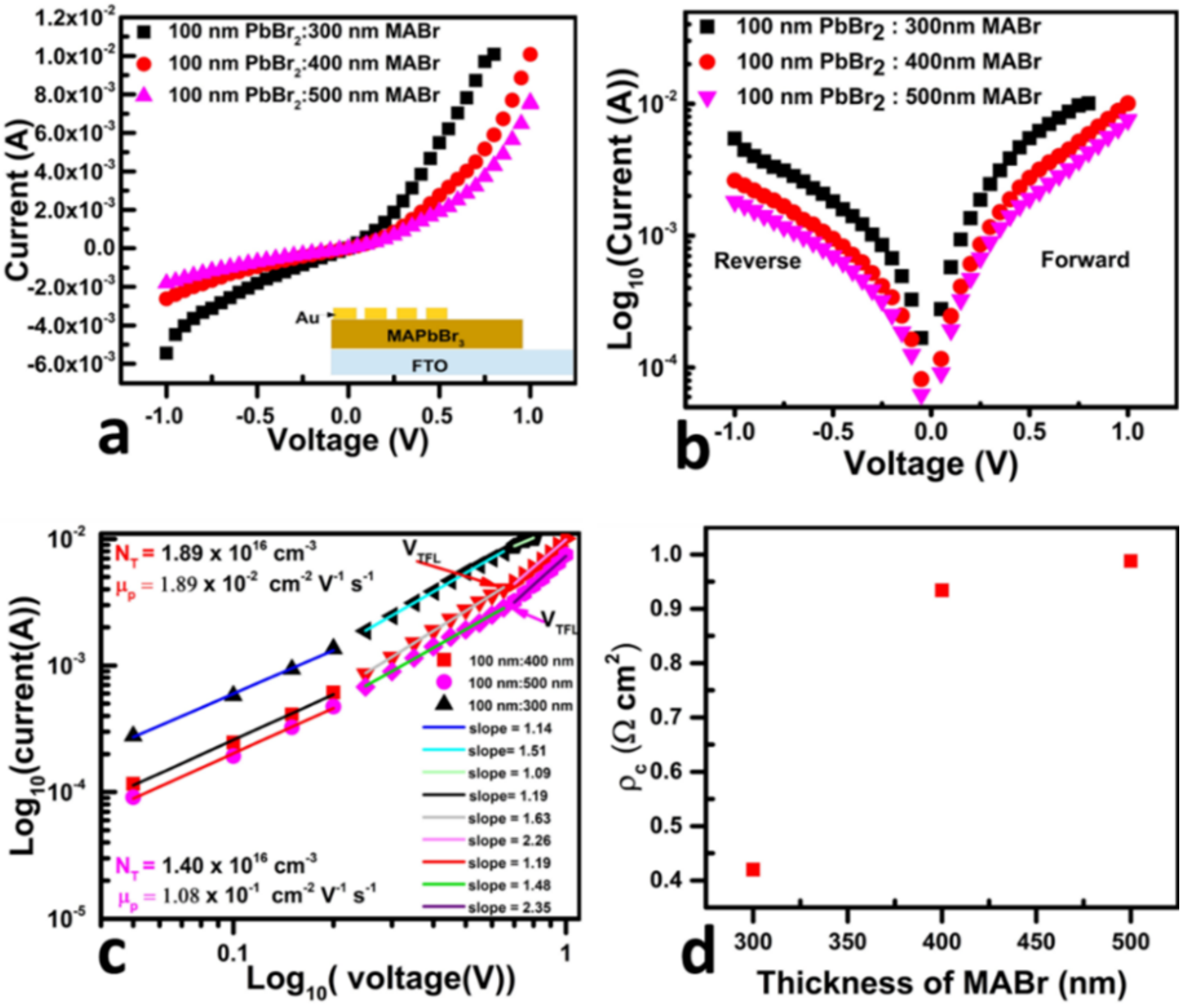

Figure 4.1.6: Electrical characterisation of FTO/MAPbBr$_3$/Au, (a) I-V characteristic, (b) Semi-log I-V characteristics, (c) Double log I-V characteristics, (d) The specific resistivity of Au/MAPbBr3/FTO vs. thickness of MABr.

4.2 Sequential thermal vapour deposition of methylammonium lead tri-iodide

4.2.1 Introduction

In this section, we discuss the results of thin 3D MAPbI$_3$ film prepared by STVD of single layers of PbI$_2$ and MAI. The phase purity of the thin MAPbI$_3$ films is optimised by varying the thicknesses of the MAI and PbI$_2$ and post-annealing time. The crystal structure, surface morphology and UV-Vis absorption spectrum depend significantly on the thickness of MAI and post-annealing time. X-ray diffractograms confirmed the tetragonal crystal structure of $MAPbI_3$ with I4/mcm space group and transformation of PbI_2-deficient $MAPbI_3$ to PbI_2-rich $MAPbI_3$ upon increasing annealing time. UV-Vis optical spectra reveal a redshift in the onset of absorption from 750 to 780 nm as the MAI thickness increases and a slight blue shift as the annealing time increases. Field emission scanning electron microscopy micrographs show densely packed polycrystalline grains with minor pinholes and full coverage. Also, we fabricated simplified BTL-free FTO/$MAPbI_3$/Au devices and analysed their current density-voltage (*J-V*) characteristics under dark and illumination conditions, to know the electrical behaviour of the thin $MAPbI_3$ films. The *J-V* characteristics under illumination reveal that the photogenerated current decreases with an increase in annealing time. Space charge limited current analysis of dark current *J-V* curves shows that PbI_2-deficient $MAPbI_3$ has higher mobility than PbI_2-rich $MAPbI_{3,}$ and trap density increases with annealing time. The thin $MAPbI_3$ films prepared using PbI_2 (99.9 %) and MAI (0.42 M in 2-propanol) were called SPL1 while the thin $MAPbI_3$ films grown using PbI_2 (99.9 %) and MAI (98%) were called SPL2.

4.2.2 Structural properties

4.2.2.1 Structural properties of $MAPbI_3$ for various MAI thickness

Figure 4.2.1 (a) is the diffractograms of the prepared SPL1 thin films for various thicknesses of MAI. All the diffraction directions show sharp peaks specifying good crystallinity. The structure was matched to the tetragonal crystal system of $MAPbI_{3,}$ having the I4/mcm space group, consistent with the literature [30,32–34]. The extra (001) diffraction direction was attributed to the PbI_2 residue, in conformity with JCPDS card number 07-0235. Also, the intensity of the extra peak was seen to decrease as MAI was increased from 300 to 500 nm, showing that the purity of $MAPbI_3$ increases with the MAI thickness. It was observed that the intensities of (110) and (220) directions increased with MAI thickness, writing down an increase in crystallinity of $MAPbI_3$. This may be due to a rise in the number of the required carbon, hydrogen, and iodine atoms at the Wyckoff positions in the crystal lattice that increased the structure factor and peak intensity. Another reason could be the increase in the number of reflection planes as MAI was added, which increases the multiplicity factor since each layer of added atoms contributes to the resultant intensity of a peak. In comparison, it was seen that the ratio of PbI_2 to MAI thickness that gave SPL1 films is different from the results by *Miguel and co-workers* [35], who used an automated STVD method. This disparity could be due to the difference in the deposition parameters and conditions used.

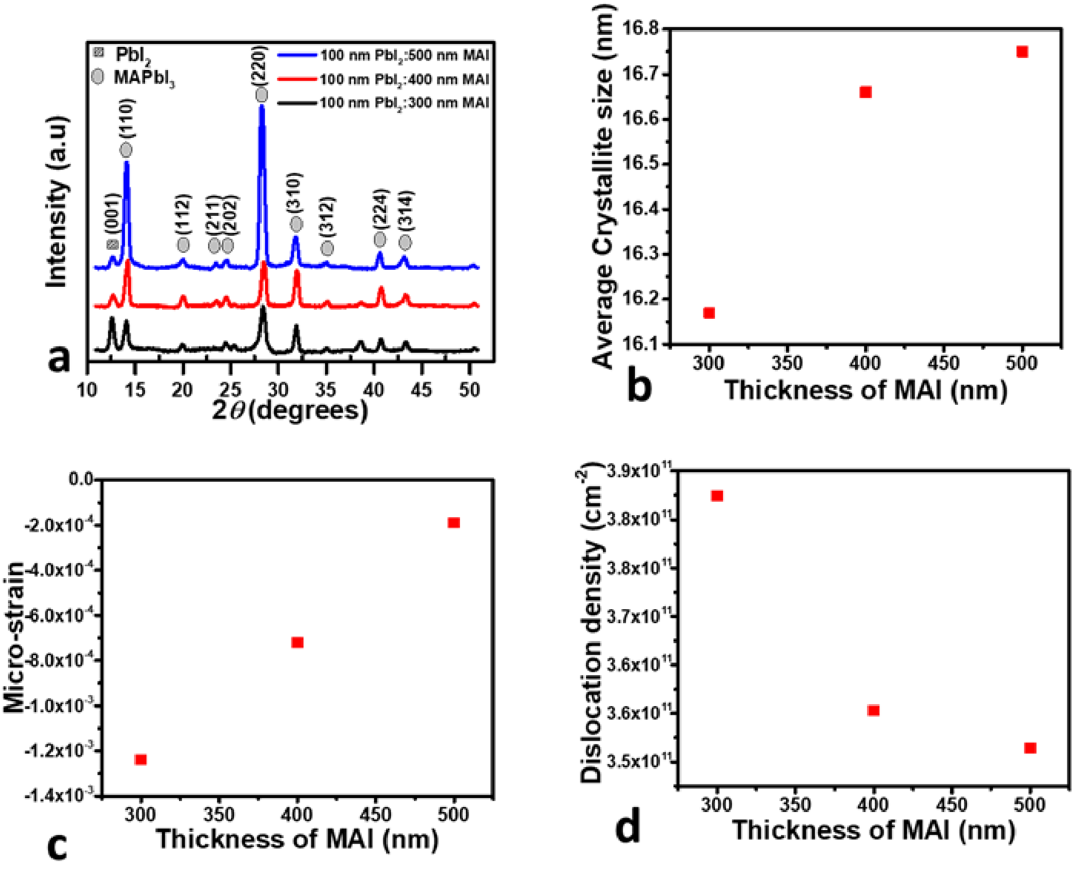

Figure 4.2.1: (a) XRD Pattern of SPL1 thin film, (b) Micro-strain of the SPL1 thin film vs. thickness of MAI, (c) Crystallite size of the SPL1 thin film vs. thickness of MAI, (d) Dislocation density of SPL1 thin film vs. thickness of MAI.

The average crystallite size and micro-strain for the SPL1 films were calculated from W-H plot and shown in *Figure 4.2.1 (b, c).* It was seen that the micros-strains were negative and decreased in size as the thickness of MAI is increased. The negative size shows that the strains are compressive. *Zhao and co-workers* [36] observed that hole extraction at the perovskite/HTL interface was enhanced by the fattening of the valence band when micro-strain was decreased, and carrier mobility increased when the micro-strain was wholly removed. Also, *Jones and co-workers* [37] saw that micro-strain enhanced defect concentration in $MAPbI_3$ films and promoted non-radiative recombination. Thus, the decrease in micro-strain may cause low defect density and non-radiative recombination. *Figure 4.2.1(d)* shows how the dislocations density of the SPL1 films vary with MAI thickness. It was seen that the dislocation density was inversely proportional to the thickness and has also been shown to reduce the PCE of perovskite solar cells. *Haque and co-workers* [38] calculated the dislocation density of solution-processed $CsPbI_3$ solar cells and saw the best PCE for cells with the lowest density had. Therefore, the 500 nm thick MAI thin film, with the lowest dislocation density, may give high performing solar cells. It is important to remark that, these analyses of micro-strain, crystallite size and dislocation density were performed without considering the peaks corresponding to PbI_2 residue on the diffractograms. However, when the peaks for PbI_2 were considered, it was seen that PbI_2-rich films had lower dislocation densities than PbI_2-deficient ($MAPbI_3$-pure) films.

Regarding optimisation, *Figure 4.2.2* includes diffractions spectra of the SPL1 films for 50 nm PbI_2:350 nm MAI and 300 PbI_2:100 nm MAI. Notably, the characteristic (110) and (220) directions, showing the formation $MAPbI_{3,}$ were absent on the diffractograms. This means $MAPbI_3$ was not formed when the thickness of PbI_2 was greater than that of MAI, and when the thickness of PbI_2 was less than 100 nm. However, when the thickness of PbI_2 is kept at 100 nm and that of MAI at 300 nm, all the characteristic peaks for $MAPbI_3$ appeared. It was for this reason that we decided to continue the optimisation process by keeping the thickness of PbI_2 at 100 nm and increase that of MAI from 300 to 500 nm, to reduce the amount of residue that was seen.

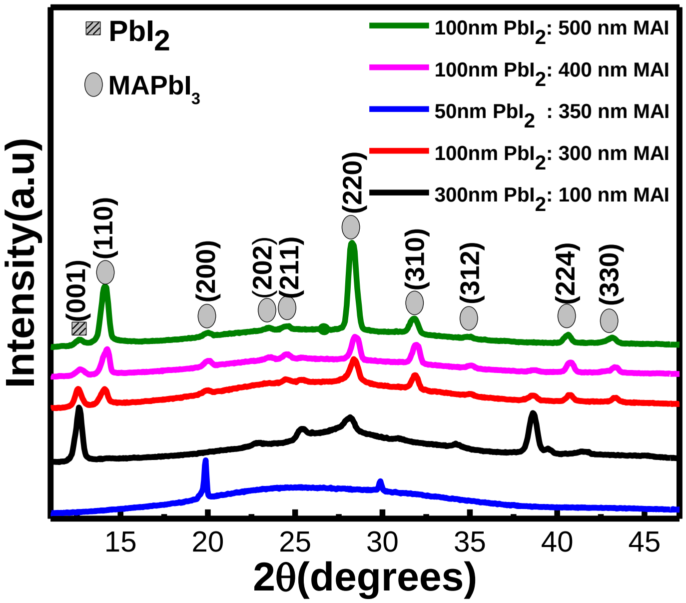

Figure 4.2.2: X-ray diffractograms showing films with a ratio of PbI_2 *to MAI greater than one and films with a ratio of* PbI_2 *to MAI less than one.*

Table 4.2.1 shows the change in lattice constants and unit cell volume of the SPL1 thin films as the thickness MAI was increased. It was seen that the dimensions of the unit cells increase continuously along the *c*-axis. However, increasing the thickness of MAI from 300 to 400 nm caused the unit cell to contract along the *a*-axis and elongates along the *c*-axis, and as the thickness was increased beyond 400 nm, there was elongation on both axes. These changes caused the unit cell volume to decrease from 300 to 400 nm thickness before increasing again. These non-linear changes in lattice constants may be caused by the presence of PbI_2 residue; the peaks corresponding to PbI_2 were not excluded during the calculations.

Table 4.2.1: Variation of lattice constants and unit cell volume of SPL1 thin film with thickness of MAI.

The thickness of MAI (nm)	**Lattice constant, *a*, (Å)**	**Lattice constant, *b* (Å)**	**Lattice constant, *c* (Å)**	**Unit cell volume, *V* ($Å^3$)**
300	8.881	8.881	12.479	984.246
400	8.860	8.860	12.508	981.873
500	8.902	8.902	12.542	993.898

4.2.2.2 Structural properties of $MAPbI_3$ thin films for various annealing time

Figure 4.2.3 includes the structural analyses of the SPL2 thin films for different annealing times. The diffractograms have sharp peaks, showing good crystallinity, and a strong dependence on annealing time, as shown in *Figure 4.1.3 (a).* In comparison, the crystal structures are tetragonal with I4/mcm space, like the results for SPL1 thin films, vide infra. The as-deposited thin film showed a pure $MAPbI_3$ phase *(Figure 4.1.3 (a)),* showing crystallisation of the film started during the deposition process within the chamber. This could be possible because the temperature of the substrate (95°C) was within the range of annealing temperatures for $MAPbI_3$. Thus MAI could diffuse into the voids in the PbI_6 octahedral framework and recrystallize to form $MAPbI_3$. It has been shown that the annealing temperature for the recrystallization of $MAPbI_3$ is in a 90-105°C range [39]. The temperature of the substrate during deposition vapour deposition of MAI on PbI_2 determines whether inter-diffusion will take place. *Patel and co-workers* demonstrated that inter-diffusion and reaction during thermal vapour deposition of MAI could be prevented by the initial lowering of the substrate temperature to 0°C [40]. However, they saw that interdiffusion and reaction were possible under vacuum at room temperature as $MAPbI_3$ was formed, but the reaction was incomplete as MAI residue was seen in the film. The reaction ran to completion upon exposure to humid air at 21°C since moisture exposure increased the mobility of MAI. Also, they saw that longer annealing times improved the crystallinity and absorbance continuously. This claim contradicted what was seen after prolonged annealing of our samples. No apparent change in the peak intensity (crystallinity) and no PbI_2 residue were seen on the diffractograms, after the first 20 min of annealing. However, a very intense (001) PbI_2 peak was seen after annealing for 40 min, showing that long annealing time may cause a transformation of $MAPbI_3$ to PbI_2, consistent with previous results [41]. As annealing continued, the intensity of the PbI_2 peak decreased as the time was increased from 40 to 60 min, showing a possible reaction between the transformed PbI_2 and MAI to form $MAPbI_3$ again. The observation was supported by other reports in the literature. *Chen and co-workers* [41] showed that increasing annealing time beyond that needed just to complete the formation of $MAPbI_3$ leads to the release of PbI_2, which passivates the grain boundaries, thus improving electrical properties and performance. *Park and co-workers* [42] demonstrated that PbI_2 residues are formed during the annealing step of the reaction rather than the initial stages.

Figure 4.2.3 (b) shows the variation of average crystallite size for the SPL2 thin films with annealing time. The average crystallite size was seen to decrease slightly after 20 min of annealing, increased drastically between 20 to 40 min and then reduced again beyond 40 min. The trend correlates well with the variation of the intensity of the (001) PbI_2 peak as annealing time was increased, vide infra. Interestingly, it was realized that the crystallite size was largest after 40 min of annealing when the PbI_2 peak is most intense. Thus, these fluctuations of the average crystallite size with an increase in annealing time could be due to the phase transformation occurring in the sample. Also, the presence of PbI_2 residue in $MAPbI_3$ thin films may result in the average crystallite sizes. *Figure 4.1.3 (c)* shows how the micro-strain for the SPL2 thin films with annealing time. It was seen that the micro-strain varied from a first large negative (compressive) micro-strain that gradually relaxed after 20 min and to a significant positive (tensile) strain after 40 min, then back to compressive strain as after 60 min. The change from compressive strain to tensile and back could be attributed to the reversible seen transformation between PbI_2 to $MAPbI_3$.The tensile nature of the micro-strain after 40 min may have caused the large crystallite size, in the presence of a large proportion of PbI_2 from the transformation of $MAPbI_3$. Now, we look at what other others have reported on how $MAPbI_3$ having PbI_2 residue affects the performance of devices. It was realized the presence of PbI_2 residue produced both positive and negative effects. *Jacobsson and co-workers* [43] showed that $MAPbI_3$ thin films that were deficient in PbI_2 had a high crystalline quality and made solar cells with high V_{oc}. However, they had MAI at the grain boundaries, which perturbed charge transport and led to low performance. But solar cells with PbI_2-rich films showed the highest performance. *Kwon and co-workers* [44], on the other hand, demonstrated that pure $MAPbI_3$ (without

PbI$_2$ residue) has high photon absorption and long carrier lifetime, which leads to more photogenerated current and high PCE.

Figure 4.2.3 (d) shows the variation of dislocation density for the SPL2 thin films with annealing time. It was seen that the dislocation density increased slightly during the first 20 min, then decreases drastically between 20 and 40 min before growing again. The irregular variations in dislocation could also be due to the reversible transformation between the PbI$_2$ and MAPbI$_3$ phases as the annealing time was increased. Remarkably, the smallest dislocation density was seen after 40 min of annealing, when the transformed PbI$_2$ was highest. This points out that the dislocation density is lower for PbI$_2$-rich MAPbI$_3$ films than PbI$_2$ short films.

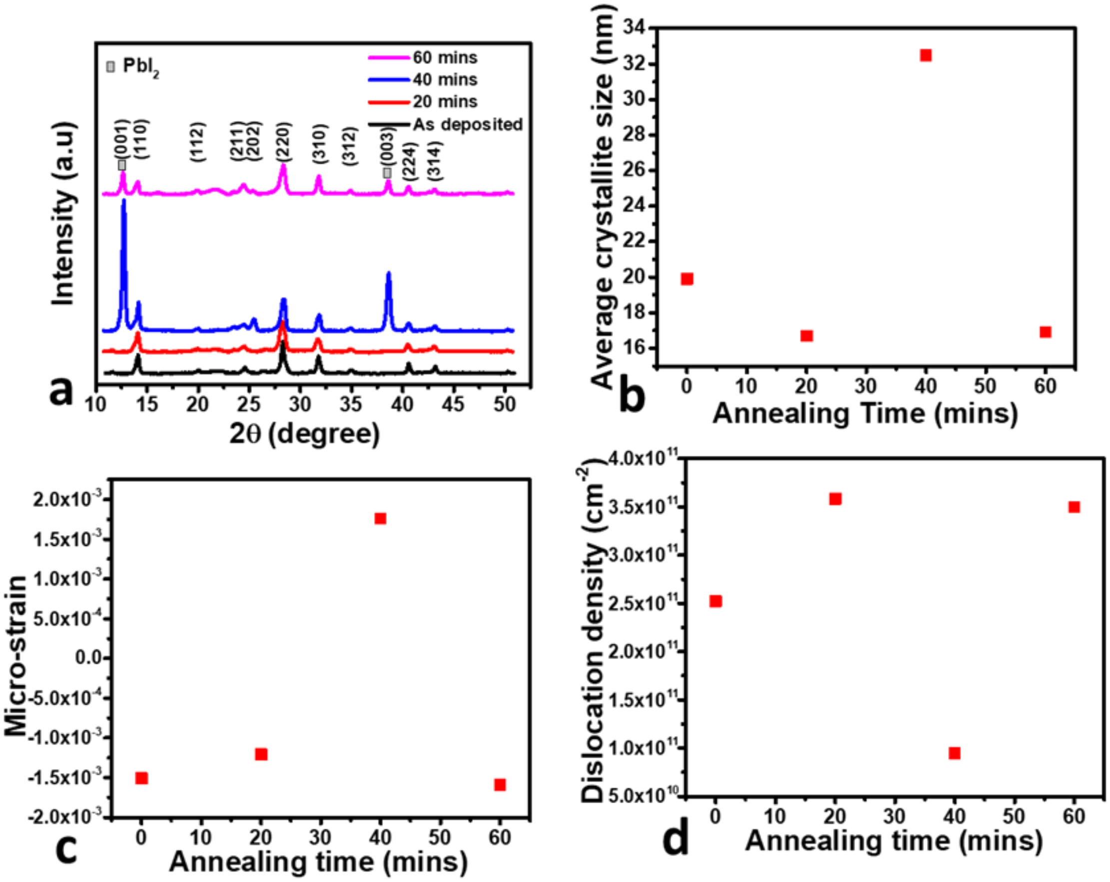

Figure 4.2.3: Structural analysis of SPL2 thin film having 400 nm thick MAI for various annealing times, (a) XRD diffractograms of SPL2 thin film for different annealing times, (b) Average crystallite size of SPL2 for various annealing times, (c) Micro-strain of SPL2 thin film vs. annealing time, (d) Dislocation density of MAPbI$_3$ for different annealing times.

Table 4.2.2 illustrates how the lattice constants, unit cell volumes and grain sizes of SPL2 depend on annealing time. It was seen that the change in unit cell volume with annealing time was irregular. The irregular change could be attributed to thermal expansion [45] and the reversible phase transformations from $MAPbI_3$ to PbI_2 (*Figure 4.2.3 (a)*), consistent with reports by *Chen and co-workers* [41]. As can be observed in *Figure 4.2.3 (a)* and *Table 4.2.2*, the as-deposited film is deficient of PbI_2 and lattice constants *a* and *c* equals 8.905 and 12.526 Å respectively. The lattice constants increase after 20 min of annealing, leading to an increase in *V* cell, which may be due to thermal expansion during annealing. However, increasing the annealing time from 20 to 40 min leads to decrease in *V* and the sudden appearance of a very intense PbI_2 peak. This may be because the effect of phase transformation from $MAPbI_3$ to PbI_2 dominating that of thermal expansion and leading to a decrease in the decrease in *V*. Increasing time to 60 min reduces the intensity of the PbI_2 peak and there is a slight increase in *V* possibly due to thermal expansion.

Table 4.2.2: Variation of lattice constants, unit cell volume and grain size of SPL2 thin film for various annealing times

Annealing time (min)	**Lattice constant, *a* (Å)**	**Lattice constant, *b* (Å)**	**Lattice constant, *c* (Å)**	**Unit cell volume, *V* ($Å^3$)**	**Average grain size (nm)**
0	8.905	8.905	12.526	993.230	501.56± 36.47
20	8.924	8.924	12.553	999.693	413.07± 57.12
40	8.897	8.897	12.556	993.890	264.31±32.78
60	8.907	8.907	12.549	995.571	206.46±20.85

4.2.3 Optical properties of $MAPbI_3$

4.2.3.1 UV-Vis absorption of $MAPbI_3$ for various MAI thickness

Figure 4.2.4 (a) shows the UV-Vis absorption spectra of SPL1 thin films for various MAI thicknesses. Every spectrum exhibited an extended absorption band in the 500 to 400 nm wavelength range, in good agreement with the literature [46]. Besides, there was a redshift in absorption onset as the thickness of MAI was increased, translating to a decrease in direct bandgap from 1.66 to 1.60 eV and indirect bandgap from 1.65 to 1.59 eV as displayed in *Figure 4.2.4 (d)*. This downsizes in bandgap could be because of the gain in average crystallite size and tensile microstrain [47]. *M. Ozta* [47] saw that the energy bandgap of indium phosphide (InP) thin film was inversely related to the grain size and micro-strain. In the same light, *D. Innocenzo and co-workers* [48] investigated the connection between the morphology and luminescence properties of HaP and demonstrated that optical bandgap reduced with increment in crystallite size resulting to longer charge carrier lifetimes. Furthermore, reduction in the bandgap, towards the 1.40 eV, is useful to improve the PCE of the single-junction perovskite solar cells, following Shockley-Queisser theory [49,50]. Equally, the decrement in bandgap lowers the possibility of developing mid-gap trap states (recombination centres) in $MAPbI_3$, which may shorten carrier lifetimes [11].

Figure 4.2.4 (b, c) illustrate the direct and indirect bandgap Tauc-plots, respectively that were employed to measure the bandgaps. Either case showed perfect fits, indicating that the $MAPbI_3$ exhibits both direct and indirect bandgap properties, known as the Rashba effect [51]. *Etienne and co-workers* [52] showed that the Rashba effect in HaP originate from splitting and shifting of the conduction band minimum in the momentum-space due to spin-orbit coupling. This has also been confirmed to enhance charge carrier lifetimes in HaP [53].

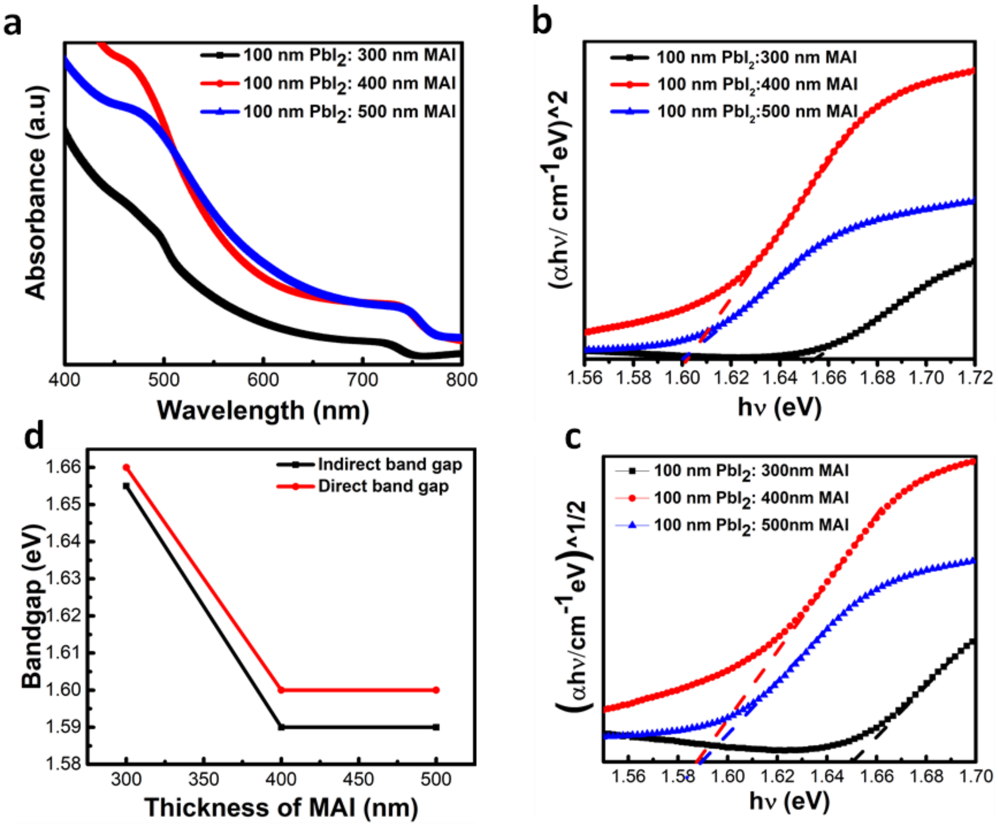

Figure 4.2.4: (a) UV-Vis absorption spectra of thin SPL1 films for various thickness of MAI, (b) Direct bandgap Tauc-plot of $MAPbI_3$ for various MAI thickness, (c) Indirect bandgap Tauc-plot of $MAPbI_3$ for different MAI thickness, (d) Bandgap of thin SPL1 films different MAI thickness.

4.2.3.2 UV-Vis absorption of $MAPbI_3$ for varying annealing time

Figure 4.2.5 (a, b) respectively depict the UV-Vis absorption spectra and direct bandgap Tauc-plots of the thin SPL2 films, for different annealing times. All the spectra show an onset of absorption close to 780 nm, attributed to the formation of $MAPbI_3$. *Figure 4.2.5 (c)* shows that the direct bandgap, from the Tauc-plot, increases proportionately with the increase in annealing time. The uniform rise in bandgap with annealing time can be attributed to the decrease in average grain size, as shown in *Figure 4.2.5 (d),* which agrees with the literature [54]. The increase in bandgap with annealing time could also be due to the presence of PbI_2 from the transformation of $MAPbI_3$ as the annealing time was increased, with absorption onset at 515 nm (large bandgap) [55,56]. Increase in annealing time affects the absorbance differently in various regions of the visible spectrum. The absorbance of the as-deposited thin film, which is deficient in PbI_2, is highest in the 500-800 nm range, while the absorbance of the film annealed after 40 min is lowest in the same range. This indicates that the PbI_2-deficient $MAPbI_3$ then-films absorb more in the 500-800 nm range (visible spectrum) than then PbI_2-rich thin-films, and this is consistent with previous reports by [44,56]. *Kwon and co-workers* [44] proved that $MAPbI_3$ with excess PbI_2 has a lower absorbance than that of pure $MAPbI_3$. Similarly, *Abdelmageed and co-workers* [56] showed that the intensity of visible light absorption decreased as more PbI_2 was produced from the degradation of $MAPbI_3$. *Figure 4.2.5 (b)* shows that the square of the product of absorption coefficient and energy decreases as annealing time increases. This implies that the absorption coefficient decreases with an increase in annealing time and could be due to the presence of more PbI_2 in the thin SPL2 film, from the transformation of $MAPbI_3$ as the annealing time is increased.

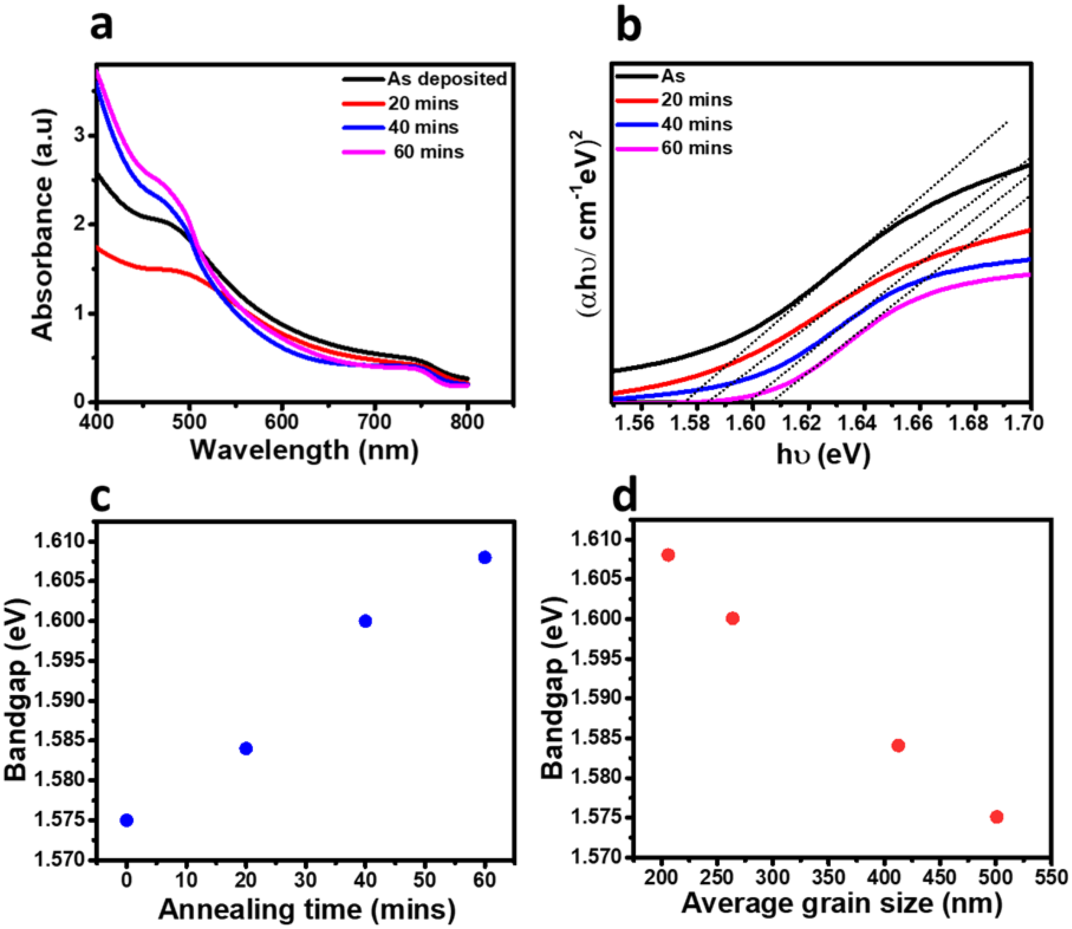

Figure 4.2.5: (a) UV-Vis absorption spectra of thin SPL2 films for different annealing times, (b) Direct bandgap Tauc-plot of SPL2 for different annealing times, (c) Bandgap of thin SPL2 films vs. annealing time,(d) Bandgap of thin SPL2 films vs. average grain size.

4.2.4 Morphological properties of methylammonium lead tri-iodide

4.2.4.1 Surface morphology analysis of $MAPbI_3$ for various MAI thicknesses

Figure 4.2.6 depicts the surface morphology of the prepared SPL1 thin films for distinct MAI thicknesses. The thin films in *Figure 4.2.6 (a, b)* were grown by depositing 300 and 400 nm of MAI, respectively. It was seen that the grains were densely packed, randomly oriented, and fully covered the substrate. The compact nature and full coverage of the grains are useful for solar cells since photo-current leakage and recombination through shunt paths (vide infra) will be minimized, leading to an increase in open-circuit voltage and fill factor [57,58]. Also, the sizes and orientations of the grains were seen to vary, showing that the films are polycrystalline. The average grain size was seen to increase from 150 to 180 nm as the thickness of MAI was increased from 300 to 400 nm. The grain size was not computed for the 500 nm MAI thick, thin-film because the grains were not visible, as seen in *Figure 4.2.6 (c)* and were presumed to be covered by the excess MAI. However, one could assume that the average grain size increased proportionately with MAI thickness. The increase in grain size will inevitably result in fewer grain boundaries leading to reduced electron scattering and trap density [59]. The reduction in trap density, by passivation, has been shown to improve V_{oc} and stability of perovskite solar cells by *Liu and co-workers* [60]. Therefore, we deduce that the reduction in grain boundaries will also lead to an increase in stability.

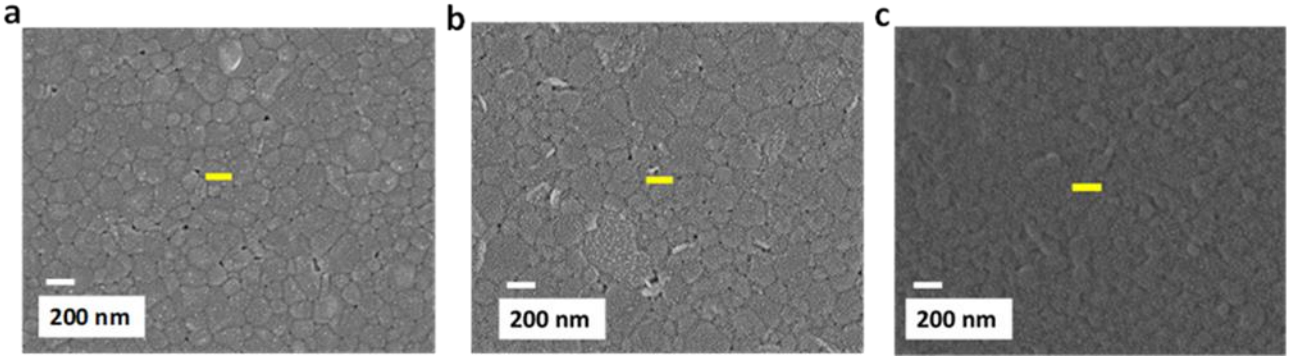

Figure 4.2.6: The FE-SEM images of SPL1 thin film for various thickness of MAI, (a) Having 100 nm PbI_2 and 300 nm MAI thickness ratio, (b) Having 100 nm PbI_2 and 400 nm MAI thickness ratio.,(c) Having 100 nm PbI_2 and 500 nm MAI thickness ratio.

4.2.4.2 Surface morphology analysis of $MAPbI_3$ for increasing annealing time

Figure 4.2.7 shows the FE-SEM micrographs of thin SPL2 films annealed in air at 100℃ for various times. The thin films display densely packed and randomly oriented pin-hole-free grains which thoroughly covered the substrates. The average grain size was seen to reduce with an increase in annealing time, as presented in *Table 4.2.2*. In particular, the average grain size for the as-deposited film is twice more than that of the film annealed for 40 min. The decrease in average grain size maybe because of the transformation from $MAPbI_3$ to PbI_2. *Meerholz and co-workers* [61] showed that the effect of excess PbI_2 in precursor solution includes the accumulation of excess crystalline PbI_2 at grain boundaries and the surface and the reduction in average grain size. In comparison, it was seen that the average grain size of the SPL2 films was more significant than for SPL1, for the same annealing time. The difference in the average grain sizes of the SPL2 and SPL1 thin films could be based on the difference in purity of the MAI used in the deposition. Note that the MAI powder precursor used for SPL1 is obtained by the evaporation of 2-propanol from 0.42 M solution of MAI while that sued for SPL2 is of MAI 98 % purity used as received.

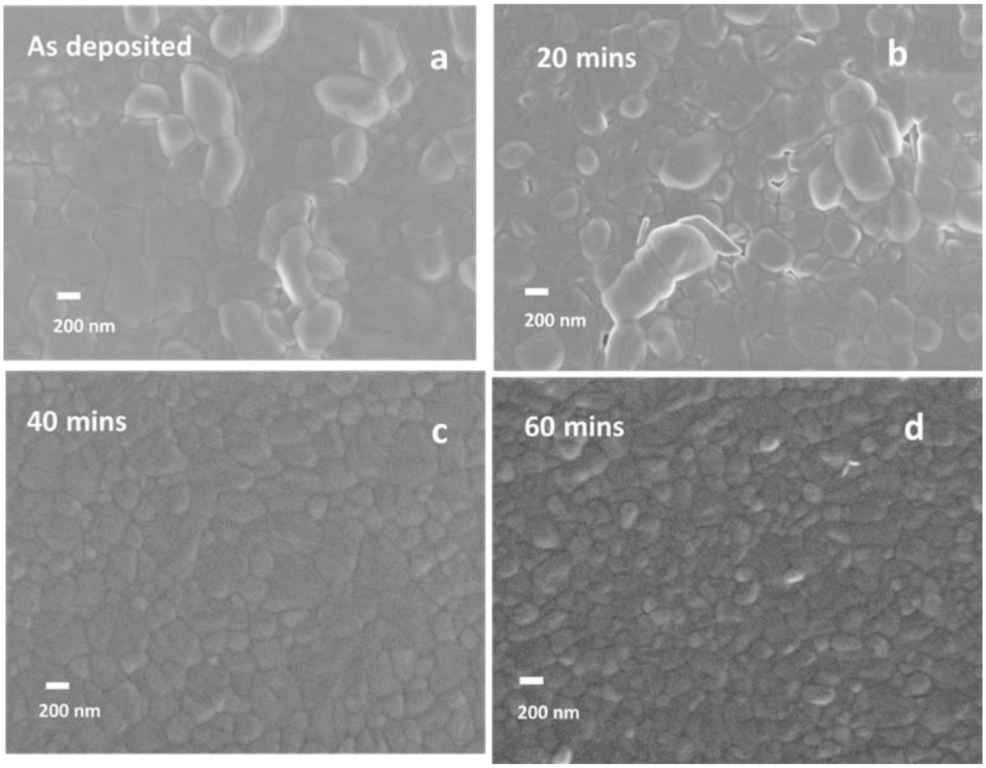

Figure 4.2.7: FE-SEM micrographs of SPL2 thin films for various annealing times, (a) Micrograph of as-deposited sample, (b) Micrograph of SPL2 thin film annealed for 20 min, (c) Micrograph of SPL2 thin film annealed for 40 min, (d) Micrograph of SPL2 film annealed for 60 min.

4.2.5 Electrical properties of methylammonium lead tri-iodide

Figure 4.2.8 presents the current density-voltage *(J-V)* characteristics under dark and illumination conditions for different FTO/SPL2/Au devices, where SPL2 is annealed for varied times. The dark semi-log *J-V* plots are to verify the nature of the contacts and the possibility of using the space charge limited current (SCLC) theory to calculate the carrier mobility and trap density. All the curves are symmetric showing a small barrier to charge carrier injection from the electrodes (ohmic contacts) and validating the possible application of SCLC theory, following the literature [62,63]. The quality of the small injection barriers (ohmic contacts) was determined by computing the specific resistivity (ρ_c) [64], and the result is displayed in *Table 4.2.3*. It is well known that ρ_c is inversely related to the doping concentrations [25] and small values of ρ_c also reveal ohmic contacts. It was seen that the specific resistivity increased and then decreased as the annealing time was increased. In this regard, we think that prolonged annealing causes fluctuations in doping concentrations. Besides, the values of the specific resistivity are generally low, indicating good ohmic contact. This correlates well with the fact that $MAPbI_3$ is p-type and forms an ohmic contact with large work function metals like Au. *Table 4.2.3* also shows how the carrier mobility, trap density and trap factor varied with annealing time. The trap density was seen to increase with an increase in annealing time. Notably, the highest carrier mobility was obtained for the unannealed samples. This shows that prolong annealing will be detrimental to performance when the film is applied in solar cells. The *J-V* measurements under illumination conditions were performed, with the devices exposed to simulated solar light of 1000 W m^{-2} intensity. The measurements show that the current density for any given voltage under illumination conditions is higher in all the devices than the dark current density and the difference between the currents decreases with an increase in annealing time. This means that the sequential thermal vapour deposited $MAPbI_3$ can generate charge carriers when exposed to sunlight, however, the amount of photogenerated charge carriers decreases with prolong annealing time. In particular, the as deposited SPL2 film generated the highest number of carriers when in forward bias. This is consistent with the UV-Vis spectrum of the sample which has the highest absorbance in the 500-800 nm range. Generally, the differences between the current densities under light and dark conditions are small. This narrow difference could be because the electric field at the p-n junction between the FTO and SPL2 films is weak such that the charge separation is ineffective.

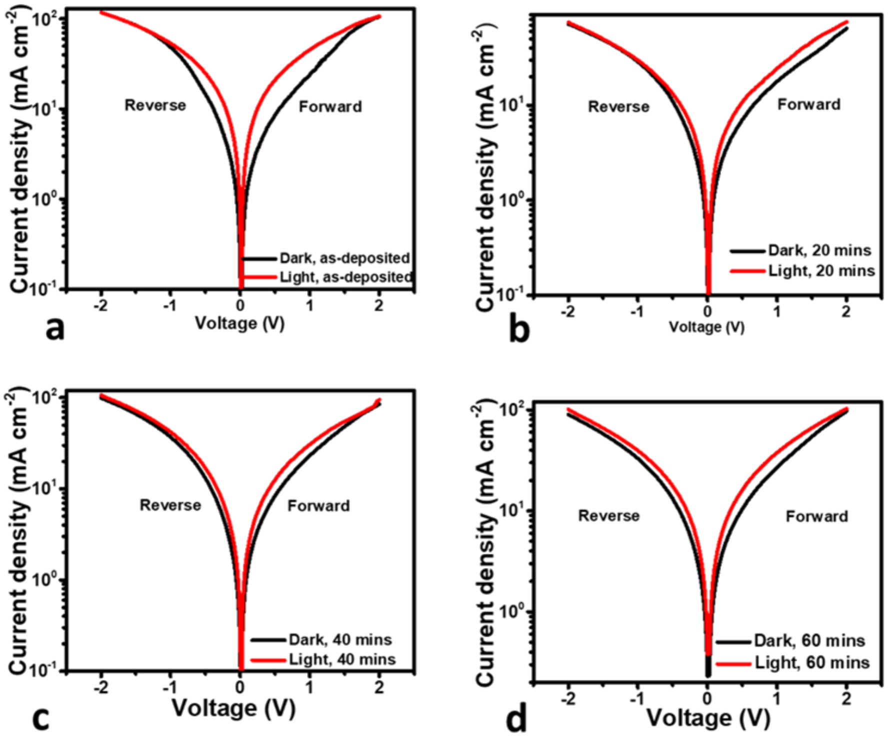

Figure 4.2.8: Semi-log J-V characteristics of FTO/SPL2/Au devices under dark and illumination, where the thin SPL2 films are annealed at different times, (a) For as-deposited SPL2 thin film, (b) SPL2 film annealed for 20 min, (c) SPL2 film annealed for 40 min, (d) SPL2 film annealed for 60 min.

Table 4.2.3: Variation of trap density, charge carrier mobility, trap factor and specific contact resistivity of SPL2 thin films with annealing time.

Annealing time (min)	Trap density (cm $^{-3}$)	Mobility (cm^2 V^{-1} s^{-1})	Trap factor	Specific contact resistivity (Ω cm^2)
0	3.25×10^{16}	1.29	0.235	0.067
20	4.22×10^{16}	0.43	0.420	0.073
40	4.51×10^{16}	0.49	0.495	0.071
60	4.55×10^{16}	0.56	0.496	0.054

4.3 Sequential thermal deposition of methylammonium lead iodide-bromide

4.3.1 Introduction

In this section, thin methylammonium lead iodide-bromide ($MAPb(I_{1-x}Br_x)_3$) films for solar cell application are grown by STVD of thin $MAPbBr_3$ film on sequential thermal vapour deposited $MAPbI_3$ bottom layer. The structural, optical, morphological, and electrical properties of the $MAPb(I_{1-x}Br_x)_3$ thin films are studied as the thickness of methylammonium bromide (MABr) in the $MAPbBr_3$ is increased from 300 to 500 nm. The X-ray diffractograms confirm that tetragonal $MAPbI_3$ is transformed into a cubic-like $MAPbBr_3$ structural phase of $MAPb(I_{1-x}Br_x)_3$ (x= 0.89-0.95) and with PbI_2 formed alongside. UV-Vis absorption spectra show that the bandgap of the thin alloy film decreases from 2.21 to 2.14 eV as the thickness of MABr is increased from 300 to 500 nm. Field emission scanning electron microscopy micrographs depicted densely packed grains that entirely covered the substrate. The average grain size increased from 150 to 320 nm as the thickness of MABr rose from 300 to 500 nm. Space charge limited current analysis of FTO/MAPb($I_{1-x}Br_x$)$_3$/Au showed high charge carrier mobilities that increased linearly with MABr thickness and low trap densities that decrease with increase in MABr thickness. Analysis of dark current density-voltage curves for FTO/c-TiO$_2$/m-TiO$_2$/MAPb($I_{0.11}Br_{0.89}$)$_3$/Au and FTO/c-TiO$_2$/m-TiO$_2$/MAPbI$_3$/Au revealed built-in high voltage of 1.6 V with charge accumulation at interfaces and 0.7 V with no charge accumulation at interfaces, respectively. This study introduces a simple way of growing mixed halide hybrid perovskite thin films for efficient hole-transport-layer-free solar cells.

4.3.2 Structural properties of methylammonium lead iodide-bromide

Figure 4.3.1 (a) illustrates the X-ray patterns of MAPbI$_3$ and MAPbBr$_3$ on glass, and MAPbBr$_3$ on MAPbI$_3$ as a bottom layer. The diffractograms of pure thin MAPbI$_3$ film shows fine peaks in several directions, corresponding to the tetragonal crystal structure with I4/mcm space group, according to the literature [30,32,33]. The diffractograms of pure MAPbBr$_3$ matches the cubic crystal structure which has $Pm\overline{3}m$ space group, according to the literature [1–3]. Now, the MAPb($I_{1-x}Br_x$)$_3$ thin alloy films diffractograms, shown in *Figure 4.3.1 (a, b),* show the presence of all the prominent peaks of cubic MAPbBr$_3$ and the (001) peak corresponding to PbI$_2$ but do not contain the principal (110) peak for tetragonal MAPbI$_3$. This points out that the tetragonal phase of MAPbI$_3$ is changed to the cubic structure of MAPbBr$_3$ as MAPb($I_{1-x}Br_x$)$_3$ alloy is formed, consistent with earlier findings [65–67]. The bromine mole ratio, *x,* was computed using an experimental equation relating the bandgaps, E_g, of the MAPb($I_{1-x}Br_x$)$_3$ thin alloy film and those of pure MAPbI$_3$ and MAPbBr$_3$, given in *Equation 4.1,*

$$E_g[MAPb(I_{1-x}Br_x)_3] = E_g[MAPbI_3] + \{E_g[MAPbBr_3] - E_g[MAPbI_3] - b\}x + bx^2 \qquad \text{Equation 4.1}$$

where *b* is the bowing parameter, *Noh and co-workers* obtained *b* as 0.33 for Br-I mixing of the MAPbI$_3$ and MAPbBr$_3$ polycrystalline films [66]. Similarly, *Zhang and co-workers* got *b* as 0.21 for Br-I mixing upon the tuning of single-crystalline MAPb($I_{1-x}Br_x$)$_3$ [68]. The small values of *b* for MAPb($I_{1-x}Br_x$)$_3$ is a sign that MAPbI$_3$ and MAPbBr$_3$ are fully miscible in solid solutions. By substituting the bandgaps (from the UV-Vis absorption analysis, vide infra) and *b* as 0.33 into *Equation 4.1,* we obtained *x* as 0.95, 0.94 and 0.89 for 300, 400 and 500 nm MABr thickness, giving MAPb($I_{0.05}Br_{0.95}$)$_3$, MAPb($I_{0.06}Br_{0.94}$)$_3$ and MAPb($I_{0.11}Br_{0.89}$)$_3$ respectively. The high value of *x,* close to 1.0, confirms the cubic crystal structure of the MAPb($I_{1-x}Br_x$)$_3$, according to earlier reports [66,68]. *Pistor and Burwig* [67] performed a detailed study on the mechanism leading to the formation of $MAPb(I_{1-x}Br_x)_3$ by exposing $MAPbI_3$ to MABr vapour and $MAPbBr_3$ to MAI vapour. They proved that it was due to reversible halide exchange at high substrate temperatures and added that it is easier to replace I with Br than Br with I because the atomic radius of Br and the formation enthalpy of $MAPbBr_3$ are smaller. Likewise, they proved that Br substitutes I when $MAPbI_3$ is open to MABr vapour while I replace Br when $MAPbBr_3$ is available to MAI vapour. Thus, the high content of Br we obtained in the thin $MAPb(I_{1-x}Br_x)_3$ alloys correlates well with the results of *Pistor and Burwig.* The existence of PbI_2 peak in the XRD spectra of the thin $MAPb(I_{1-x}Br_x)_3$ alloys, shown in *Figure 4.3.1 (a, b),* is consistent with previous results in the literature [65,69]. Note that the PbI_2 peak is not seen in the XRD spectra of $MAPbI_3$; however, it appears in the XRD pattern of $MAPb(I_{1-x}Br_x)_3$. This means that the PbI_2 was formed with the alloys and its formation may include the decomposition of $MAPbI_3$ due to prolonged annealing, and high temperatures within the chamber as the top $MAPbBr_3$ layer was prepared. We have shown previously that post-annealing of $MAPbI_3$ thin film for 40 min leads to the appearance of a sharp PbI_2 peak, which decreases in intensity upon increasing the time to 60 min because the $MAPbI_3$ is formed again. Similarly, it has been proven that annealing $MAPbI_3$ at temperatures beyond 120°C causes the decomposition of $MAPbI_3$ to PbI_2 [67]. The intensity of the PbI_2 peak reduces while that of the (100) peak increases as the thickness of MABr is increased from 400 to 500 nm. This could be due to the transformation of the available PbI_2 to $MAPb(I_{1-x}Br_x)_3$ as the MABr thickness is increased and may be due to the high temperature (140°C) of the substrate as the $PbBr_2$ was being deposited on the $MAPbI_3$ bottom layer. The exact mechanism of this transformation is not fully understood.

Figure 4.3.1 (c, d) shows how the average crystallite size and micro-strain of the thin $MAPb(I_{1-x}Br_x)_3$ alloys change with an increase in MABr thickness. The average crystallite size is observed to fall within the 28-42 nm range, in line with earlier reports in the literature [70]. Further, we observed that the average crystallite size first increased, and then decreased as the thickness increases. This collides with the variation in the intensity of the PbI_2 peak shown in *Figure 4.3.1(b).* So, the change in average crystallite size may include, among other things, the difference in the amount of PbI_2 produced with thin alloy film. *Figure 4.3.1(d)* shows the change in micro-strain of the thin $MAPb(I_{1-x}Br_x)_3$ alloy films as the thickness of MABr is increases from 300 to 500 nm. It is seen that the micro-strain decreases as the thickness of MABr increases. The increment in the thickness of MABr from 300 to 500 nm causes the Br to I ratio to switch from 24:1 to 7:1. The film having 500 nm thick MABr, with the smallest proportion of Br to I, is the least micro-strained. Hence, the micro-train of MAPb($I_{1-x}Br_x$)$_3$ reduces with a decrease in Br to I ratio.

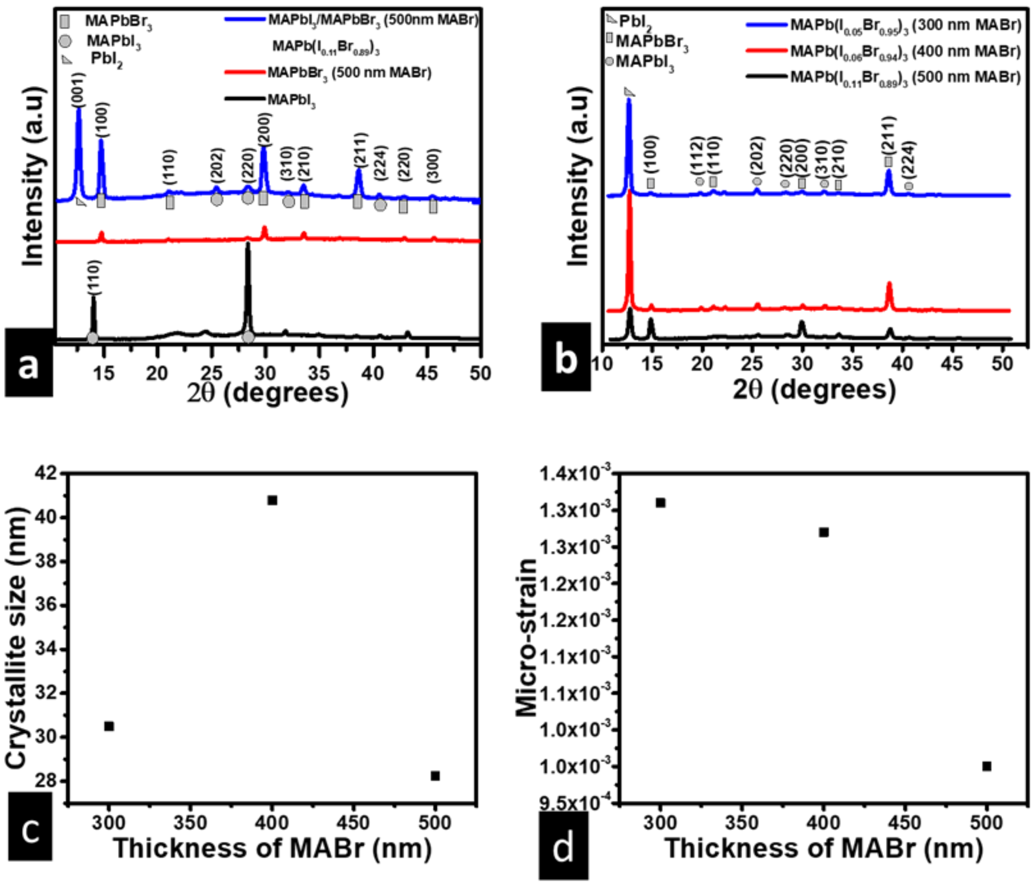

Figure 4.3.1: (a) XRD spectra of $MAPbI_3$, $MAPbBr_3$, and MAPb($I_{1-x}Br_x$)$_3$ (b) XRD spectra of MAPb($I_{1-x}Br_x$)$_3$ for various thicknesses of MABr, (c) Crystallite size of the MAPb($I_{1-x}Br_x$)$_3$ vs. thickness of MABr, (d) micro-strain of MAPb($I_{1-x}Br_x$)$_3$ vs. thickness of MABr.

4.3.3 Optical properties of methylammonium lead iodide-bromide

Figure 4.3.2 (a, b) represent the absorbance against wavelength of $MAPbI_3$, $MAPbBr_3$ and MAPb($I_{1-x}Br_x$)$_3$, where x = 0.95, 0.94 and 0.89. The onsets of absorption for $MAPbI_3$, $MAPbBr_3$ and MAPb($I_{0.11}Br_{0.89}$)$_3$ are seen at 785, 552 and 580 nm respectively, as shown in *Figure 4.3.2 (a)*, corresponding to bandgaps of 1.58, 2.25 and 2.14 eV. The bandgap of the MAPb($I_{0.11}Br_{0.89}$)$_3$ is closer in value to that of $MAPbBr_3$ than $MAPbI_3$. This collides with the fact that the MAPb($I_{0.11}Br_{0.89}$)$_3$ adopts the cubic crystal structure of $MAPbBr_3$ as exposed by the diffractograms in *Figure 4.3.1(a).* According to

Lehmann and co-workers [71], the incorporation of a tiny quantity of I does not alter the $MAPbBr_3$ crystal structure because the Br-rich compositions have stronger intermolecular forces; hence, reorientation of the cations is suppressed. Further, the absorbance of pure $MAPbI_3$ is greater than that of $MAPb(I_{1-x}Br_x)_3$ and $MAPbBr_3$, while that of $MAPb(I_{1-x}Br_x)_3$ is greater than that of pure $MAPbBr_3$. This cannot be due to thickness because the thickness of $MAPb(I_{1-x}Br_x)_3$ is greater than $MAPbI_3$. Rather, this could be due to the presence I in $MAPbI_3$ and $MAPb(I_{1-x}Br_x)_3$. The $MAPbI_3$ with a greater mole ratio of I has higher absorbance than $MAPb(I_{1-x}Br_x)_3$. Also, increasing the I mole ratio in $MAPb(I_{1-x}Br_x)_3$ causes a redshift in the onset of absorption, leading to a decrease in the optical bandgap. This decrease in bandgap maybe because the ionic radius of I is higher than that of Br leading to an expansion of the lattice [72]. *Figure 4.3.2 (b)* shows that absorbance and absorption onset of the $MAPb(I_{1-x}Br_x)_3$ depend greatly on the value of x and the thickness of MABr. It is seen that the onset of absorption increases as x decreases, leading to a linear relationship between bandgap and x as shown in *Figure 4.3.2 (c)*, consistent with previous results [65]. The linear relationship is a sign that the bandgap of $MAPb(I_{1-x}Br_x)_3$, synthesized by SPVD, can be tuned for x ranging from 0.89 to 1.0 by increasing the thickness of MABr. This is quite a small range when compared to alloying using other methods but is useful to form $MAPb(I_{1-x}Br_x)_3$ alloys with small I content which shows improved absorption than $MAPbBr_3$. One more outstanding feature in the absorption spectrum of $MAPb(I_{1-x}Br_x)_3$ shown in *Figure 4.3.2 (b)* is the sharp onset of absorption which according to *Stranks and co-workers* [73], shows low levels of energetic disorder. The lattice constants of the thin $MAPb(I_{1-x}Br_x)_3$ alloy cubic structures were computed, using the same method for cubic $MAPbBr_3$ earlier reported in the literature [74], and plotted against x as shown in *Figure 4.3.2 (d).* A negative correlation of the lattice constant with x is observed, and this agrees with the report by *Kulkarni and co-workers* [75] who used a solution sequential deposition method. Similarly, the bandgap is inversely related to the lattice constant, as shown in *Figure 4.3.2 (e).* Hence, this confirms that the decrease in bandgap as I mole ratio increases may be due to an increase in the lattice constant (lattice expansion). This is because an increase in the lattice constant causes the interatomic distance to increase, thus reducing the binding force between the valence electrons and nucleus. Consequently, the energy required to convert a bound electron to a free or conduction electron reduces.

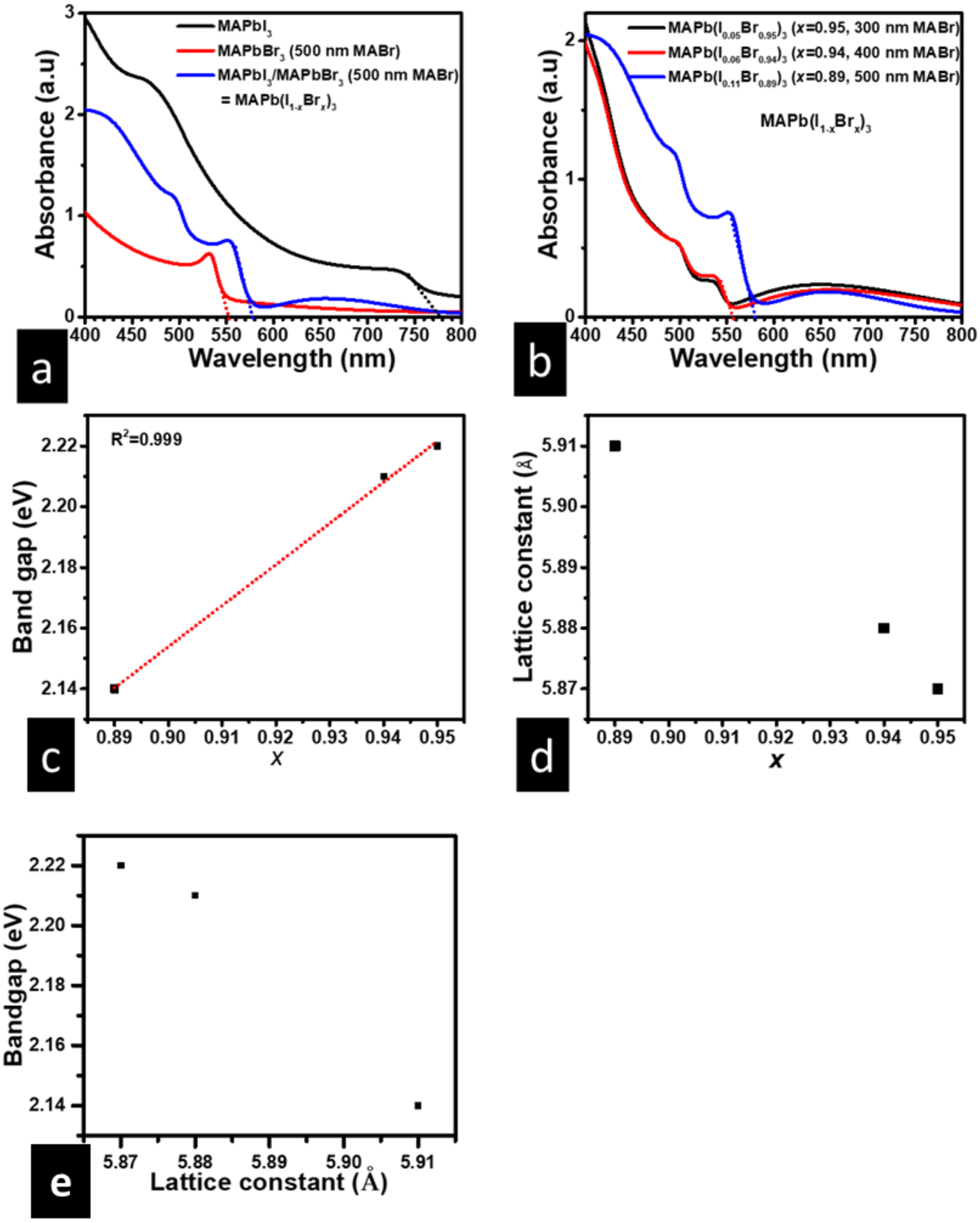

Figure 4.3.2: (a)Variation of UV-Vis absorption of the $MAPbI_3$, $MAPbBr_3$ and $MAPb(I_{1-x}Br_x)_3$ for various wavelengths, (b) Absorbance vs. wavelength of the $MAPb(I_{1-x}Br_x)_3$, (c) Bandgap vs. x of $MAPb(I_{1-x}Br_x)_3$, (d) Bandgap vs. x of $MAPb(I_{1-x}Br_x)_3$, (d) Bandgap vs. lattice constant of $MAPb(I_{1-x}Br_x)_3$.

4.3.4 Morphological properties

Figure 4.3.3 presents the FE-SEM micrographs and change of average grain size of for $MAPb(I_{1-x}Br_x)_3$ (where x = 0.95, 0.94 and 0.89) with the thickness of MABr. The films show full coverage of the substrate with densely packed and randomly oriented pinhole-free grains. It evolves from cuboidal grains plus gel-like structures, at MABr thickness of 300 nm, to one with only faceted cuboidal bimodal distributed grains, at MABr thickness of 500 nm. The faceted is characteristic of the pure $MAPbBr_3$ cubic structure in earlier reported in the literature [74]. The correlates well with the increase in the intensity of the (100) characteristic peak for cubic $MAPbBr_3$ as the thickness of MABr is increased from 300 to 500 nm. The gel-like structures seen when the MABr thickness is 300 nm ($MAPb(I_{0.05}Br_{0.95})_3$ can be linked to the rod-like structures that were seen on faceted grains solution deposited ($MAPb(I_{0.05}Br_{0.95})_3$ by *Kulkarni and co-workers* [75], and were associated with high Br content. The average grain size is seen to increase from 150 to 320 nm as the thickness of MABr increases from 300 to 500 nm. The 500 nm MABr thick, thin-film, with the most intense (100) characteristic peak corresponding to $MAPbBr_3$, has the largest average grain size. This points to the fact that the increase in average grain size could be due to a rise in the number and size of the $MAPbBr_3$ grains in the thin alloy films.

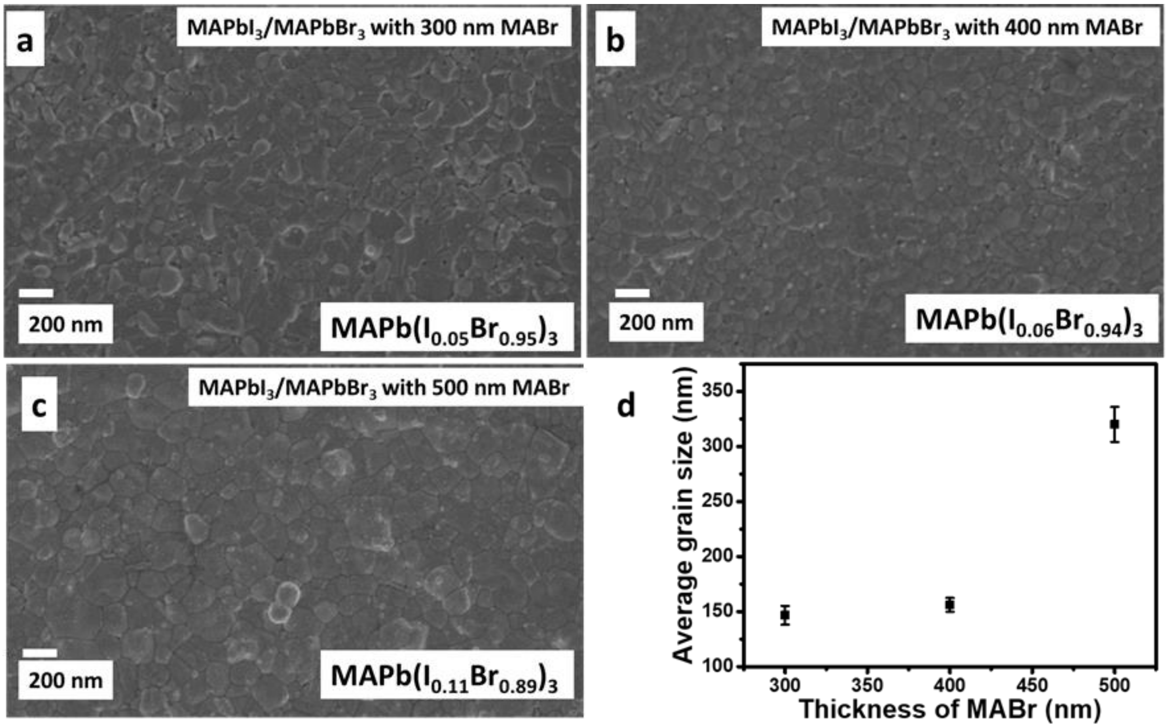

Figure 4.3.3: FE-SEM micrographs and average grain size of $MAPb(I_{1-x}Br_x)_3$ *thin films for various MABr thicknesses, (a)* $MAPb(I_{0.05}Br_{0.95})_3$ *having 300 nm of MABr, (b)* $MAPb(I_{0.06}Br_{0.94})_3$ *having 400 nm of MABr, (c)* $MAPb(I_{0.11}Br_{0.89})_3$ *having 500 nm of MABr, (d) Average grain size of* $MAPb(I_{1-x}Br_x)_3$ *thin films for various MABr thicknesses.*

4.3.5 Electrical properties

Figure 4.3.4 (a, b) are the respective semi-log and double-log plots of the dark current-voltage (*I-V*) characteristics of simple FTO/$MAPb(I_{1-x}Br_x)_3$/Au BTL-free solar cells, where $x = 0.95$, 0.94 and 0.89. The semi-log plots are slightly symmetric, a sign that the solar cells are partly rectifying. The partial rectification may be due to a p-n junction between the p-type $MAPb(I_{1-x}Br_x)_3$ and n-type FTO. The double-log plot displays two distinct parts for all values of x. These include a region with slopes ⊔ 1 for small voltages and a region with a slope greater than two at high voltages, as shown in *Figure 4.3.4 (b).* This points out that the bulk charge carrier transport mechanism of the thin $MAPb(I_{1-x}Br_x)_3$ alloy film in the FTO/$MAPb(I_{1-x}Br_x)_3$/Au device is ohmic conduction at low voltages, as reported in the literature [76,77]. It is known that the slope is two for the SCLC mechanism. However, slopes were greater than 2. This may be subject to two things; the presence of traps and the existence of a built-in voltage [77]. Since our observed forward and reverse bias semi-log *I-V* plots are symmetric, it implies that there is no built-in voltage. Thus, a slope that is greater than two is only due to the presence of traps. The trap density,

N_t, and carrier mobility, μ_p, can then be calculated using an equation relating the transition voltage and the modified Mott-Gunney law as described in the literature [28,74,77–79]. *Figure 4.3.4 (c, d)* presents the individual variations of the μ_p and N_t with the thickness of MABr. The μ_p increases linearly while N_t decreases as MABr thickness increases. Thus, the sample having 500 nm MABr has the highest μ_p. This could be due to limited charge trapping and scattering at the $MAPb(I_{0.11}Br_{0.89})_3$ surface because of the presence of only the faceted grains with large average grain size as shown in *Figure 4.3.3 (c).* This was confirmed by the observed trap density decreasing with an increase in the thickness of MABr.

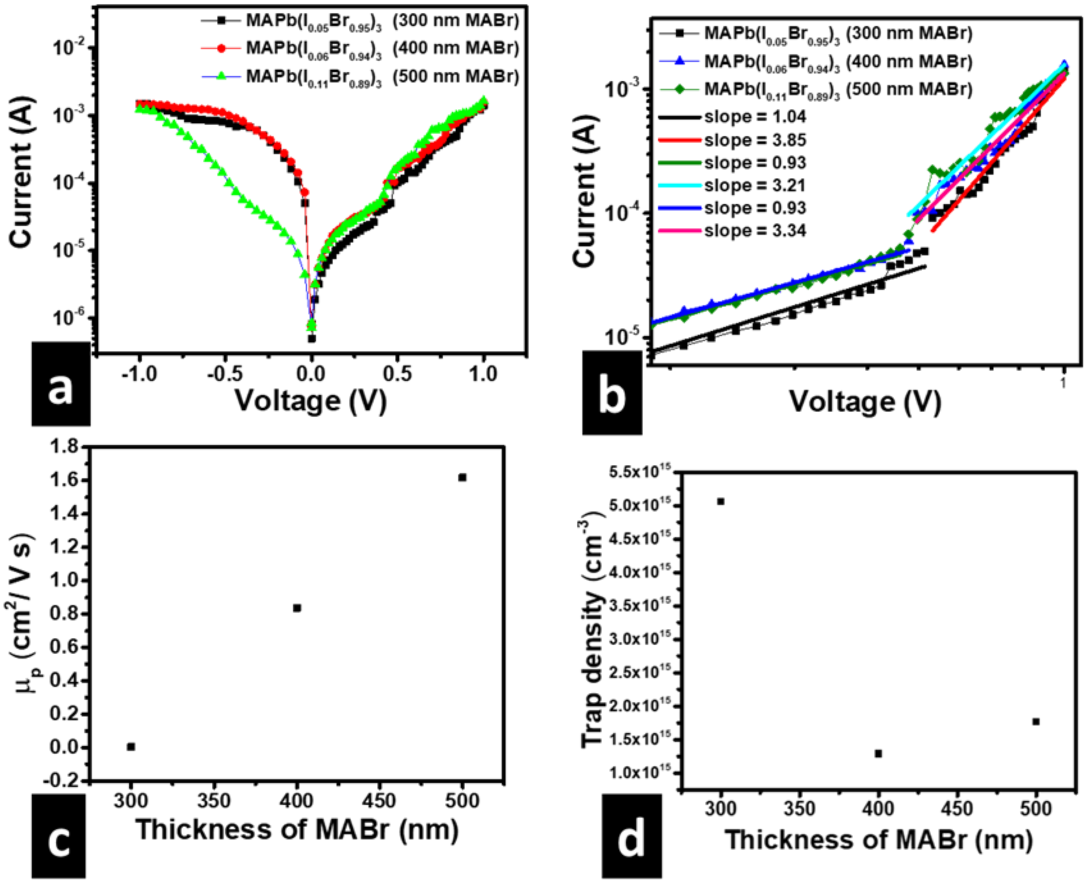

Figure 4.3.4: Dark current-voltage characteristics for FTO/ $MAPb(I_{1-x}Br_x)_3$/Au from which the mobility and trap density at are extracted, (a) Semi-log I-V characteristic, (b) Double-log I-V characteristic (c) Mobility of charge carriers vs. thickness of MABr, (d) Trap density vs. thickness of MABr.

Figure 4.3.5 (a) shows the dark current density (*J*) against bias voltage (*V*) characteristics for FTO/c-TiO_2/m-TiO_2/$MAPb(I_{0.11}Br_{0.89})_3$/Au HTL-free solar cells. The highly anti-symmetric nature of the semi-log plot in *Figure 4.3.5 (b)* confirms that the device is rectifying. Hence, there exit built-in voltage (V_{bi}) obtained by extrapolation of the exponential part of the linear *J-V* curve to the *V*-axis, as shown in *Figure 4.3.5 (a)*. It is seen that the intercept is 1.6 eV, corresponding to the V_{bi} of the FTO/c-TiO_2/m-TiO_2/$MAPb(I_{0.11}Br_{0.89})_3$/Au solar cell. Note that the FTO/c-TiO_2/m-TiO_2/$MAPb(I_{0.11}Br_{0.89})_3$/Au solar cell is more rectifying while the FTO/$MAPb(I_{0.11}Br_{0.89})_3$/Au solar cell only slightly rectifying as illustrated by *Figure 4.3.4 (a),* with no clear V_{bi}. This points out that the large rectification is due to the introduction of the c-TiO_2/m-TiO_2 layers and maybe caused by the difference in Fermi-levels between TiO_2 and $MAPb(I_{0.11}Br_{0.89})_3$, confirming the p-type character of the $MAPb(I_{0.11}Br_{0.89})_3$. The large V_{bi} at the p-n junction is fundamental for effective charge separation in solar cells leading to less recombination within the depletion layer [80,81].

According to the earlier SCLC analysis, $MAPb(I_{0.11}Br_{0.89})_3$ had the highest carrier mobility when compared to the other mixed halide thin alloy films (*Figure 4.3.4 (c)*) and the as-deposited $MAPbI_3$ containing 500 nm thick MAI had the highest carrier mobility compared to the post-annealed films (*Table 4.2.3*). In this light, FTO/c-TiO_2/m-TiO_2/$MAPbI_3$/Au was also fabricated to compare its electrical properties under dark with those of FTO/c-TiO_2/m-TiO_2/$MAPb(I_{0.11}Br_{0.89})_3$/Au, and to ascertain the effect of alloying on these properties. *Figure 4.3.5 (c, d*) shows the linear and the semi-log plots of the dark *J-V* characteristic of FTO/c-TiO_2/m-TiO_2/$MAPbI_3$/Au HTL-free solar cells. The anti-symmetric semi-log plot also says that the device is rectifying and the V_{bi} is 0.7 eV. In comparison, the V_{bi} of the mixed halide thin alloy film device is more than twice that of the pure $MAPbI_3$ device. This may imply that the level of p-type doping in $MAPb(I_{0.11}Br_{0.89})_3$ is more significant than in $MAPbI_3$, probably due to the presence of Br atoms.

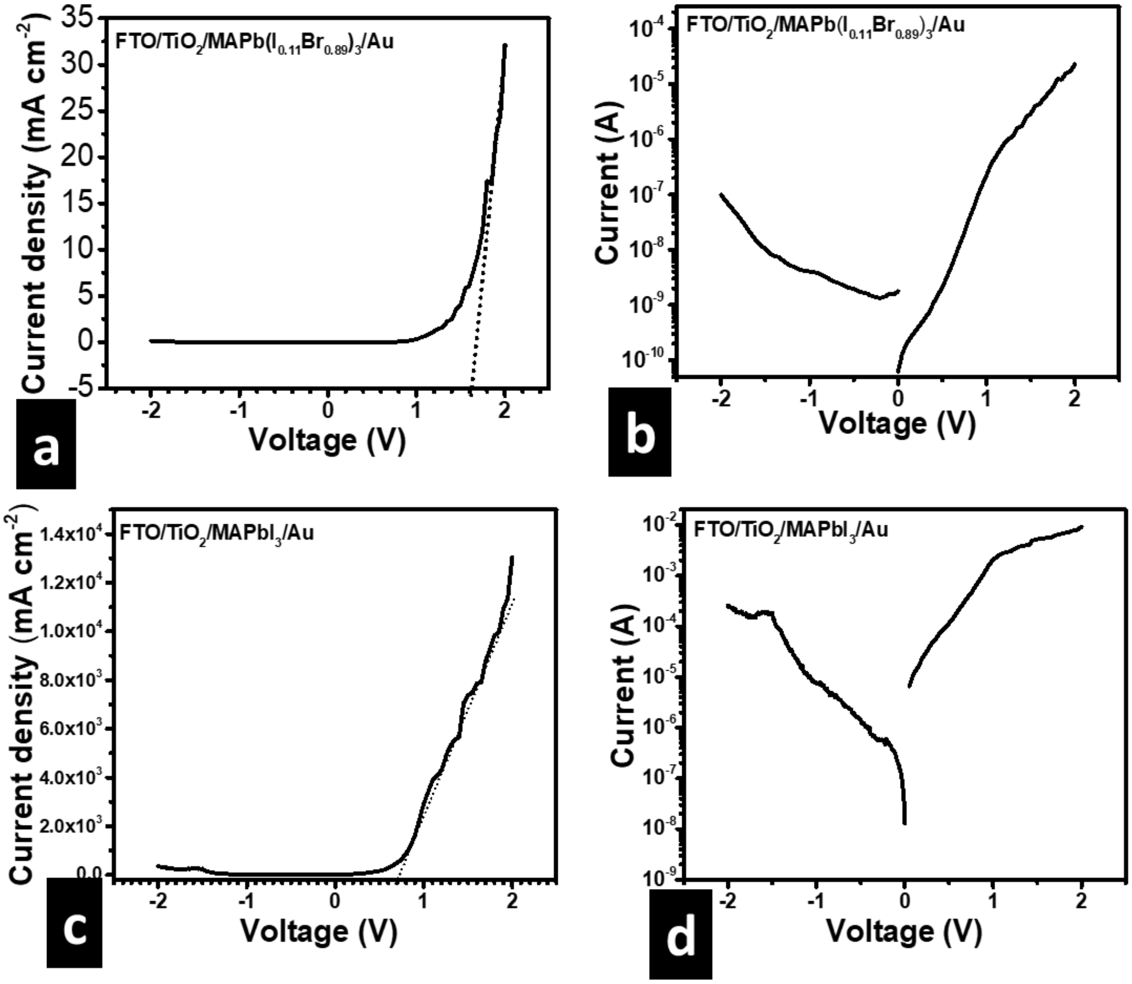

Figure 4.3.5: (a) Linear plot of dark J-V characteristic of FTO/c-TiO$_2$/m-TiO$_2$/MAPb(I$_{0.11}$Br$_{0.89}$)$_3$/Au, (b) Semi-log plot of dark J-V of FTO/c-TiO$_2$/m-TiO$_2$/MAPb(I$_{0.11}$Br$_{0.89}$)$_3$/Au, (c) Linear plot of dark J-V characteristic of FTO/c-TiO$_2$/m-TiO$_2$/MAPbI$_3$/Au, (d) Semi-log plot of dark J-V of FTO/c-TiO$_2$/m-TiO$_2$/MAPbI$_3$/Au.

Figure 4.3.6 (a, b) is the graph of capacitance per unit area (*C*) vs. bias voltage (*V*), and Mott-Schottky (M-S) plots respectively, for the FTO/c-TiO$_2$/m-TiO$_2$/MAPb(I$_{0.11}$Br$_{0.89}$)$_3$/Au solar cell. M-S plot is a well-known method to determine the charge carrier density (N_d) and V_{bi} from *C-V* measurements. It is widely applied in conventional semiconductor devices having p-n and semiconductor/metal junctions, with fixed depletion or space charge regions. For such devices, the junction capacitance per unit area, C_{dl}, is related to the *V* by *Equation 4.2,*

$$\frac{1}{C_{dl}{}^{2}}=\frac{2\varepsilon_{o}\varepsilon_{r}}{qN_{d}}(V_{bi}-V)$$ Equation 4.2

where ε_0 is the vacuum permittivity, ε_r is the dielectric constant of the donor, q is the electronic charge, N_d is the doping density of the donor. As a reminder, the M-S plot is a graph of C_{dl}^{-2} vs. V. The N_d is computed from the slope of the linear part of the graph. At the same time, the V_{bi} is calculated from the intercept resulting from the extrapolation of the linear component to the voltage-axis. For conventional semiconductors, the plot is entirely linear with a negative slope. A linear region with a negative incline exists on the plot provided there are no electrons/holes in the space charge region, and there is a homogenous distribution of the space charges [82,83]. Our results for FTO/c-TiO_2/m-TiO_2/$MAPb(I_{0.11}Br_{0.89})_3$/Au, show four distinct regions, which include an exponential increase in capacitance as the negative bias voltage increases, a constant capacitance region ranging from -0.5 to 0.0 V, a small linear dependence region ranging from 0.0 to 0.2 V and exponential growth in capacitance with voltage above 0.2 V as shown in *Figure 4.3.6 (b). Bera and co-workers* [84] had identical results for another semiconductor and attributed the exponential increase in capacitance with an increasing reverse bias to the accumulation of electrons, the constant capacitance region to depletion region and an exponential increase in capacitance at a forward bias to the accumulation of holes. Other reasons for constant capacitance may include the width of the depletion region exceeds the thickness of the perovskite absorber and thus perovskite is fully depleted, presence of injection barriers [85] and accumulation of space charges at the interfaces [81,82,86,87], which may be due to low level of doping, intrinsic nature of the perovskite and the presence mobile ions [82]. The exponential capacitance also called diffusion capacitance [87], has previously been linked to the charged ions accumulation occurring at the TiO_2/perovskite and perovskite/Au interfaces in the literature [82,86]. The existence of the other capacitances different from the depletion capacitance shows that the determination of N_d and V_{bi} from M-S plot may be invalid. This may account for the difference between the V_{bi} (1.75 eV) obtained from M-S plot and that from the dark *J-V* characteristic (1.6 eV), vide infra. *Figure 4.3.6 (c, d)* presents the *C-V* and M-S plots for FTO/c-TiO_2/m-TiO_2/$MAPbI_3$/Au solar cells, respectively. At first, the capacitance increases sharply as the sizeable negative bias is decreased and then stays nearly constant as negatives bias decreases to zero and the forward bias increased 0 to 2 V. The constant capacitance for a long range of biasing voltage may be a sign that the depletion width exceeds thickness of the perovskite absorber as earlier mentioned and no accumulation of charges at the interfaces.

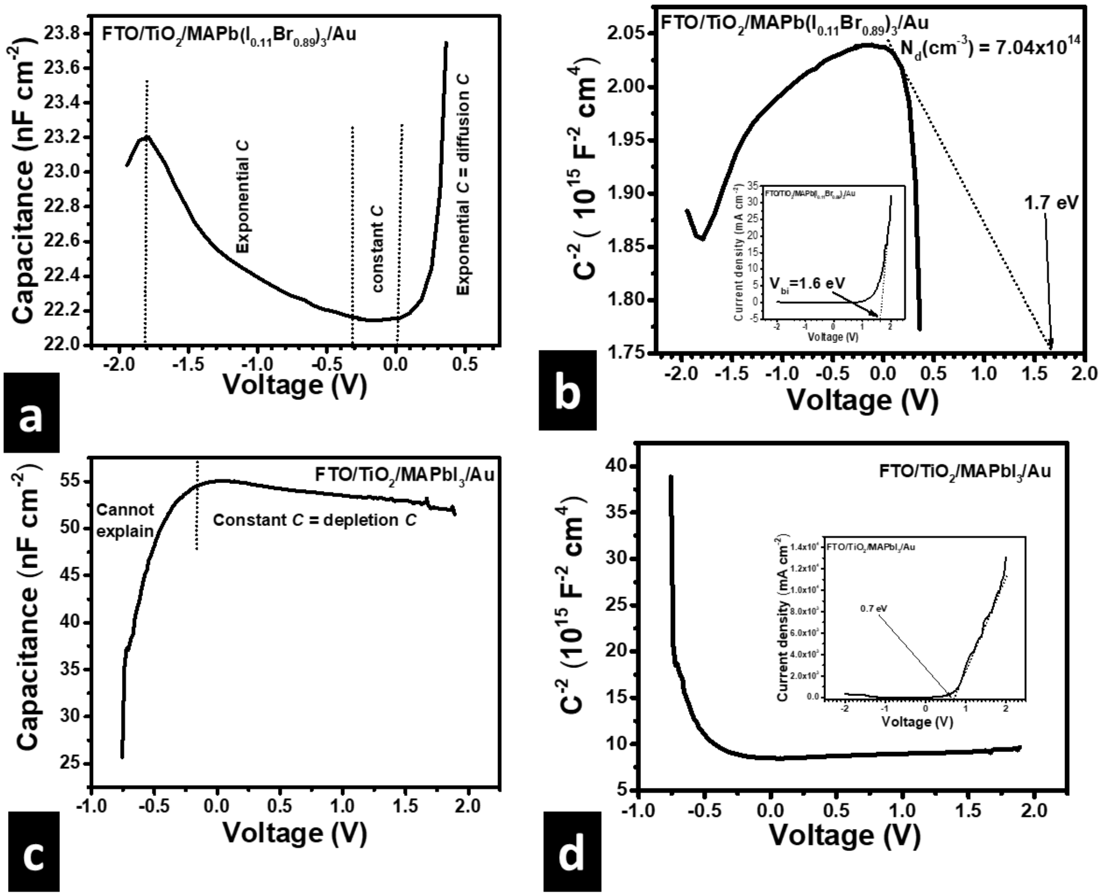

Figure 4.3.6: Dark current-voltage, capacitance-voltage and Mott-Schottky plots for FTO/c-TiO_2/m-TiO_2/ $MAPb(I_{1-x}Br_x)_3$/Au solar cell, (a) Linear plot current density vs. voltage, (b) Semi-log plot of current vs. voltage, (c) linear plot of capacitance vs. voltage, (d) Mott-Schottky plot.

4.4 Growth and degradation of thin $MAPbBr_3$ films at metal/$MAPbBr_3$ interface

4.4.1 Introduction

In this section, the structure, morphology and rate of decay of methylammonium lead tri-bromide ($MAPbBr_3$) perovskite at interfaces with aluminium (Al), tin (Sn), silver (Ag), gold-zinc (Au-Zn) and gold (Au) are studied. X-ray diffractograms showed a cubic $MAPbBr_3$ structure with $Pm\overline{3}m$ space group and different crystallographic textures for all substrates. The rate of degradation of $MAPbBr_3$ was slowest on Au-Zn and fastest on Al. The structural and morphological properties were observed for 60 days to monitor the status of degradation. FE-SEM images showed compact grains and a bimodal grain size distribution, with average grain size that increased linearly with an increase in the work function of the metal from 294 nm for Al to 850 nm for Au $MAPbBr_3$ grains remained glued to Sn, Ag, Au-Zn and Au but delaminated quickly on the Al substrate. This work proposes the choice of metal electrodes/substrates for stable optoelectronic devices and solar cells.

4.4.2 Structural properties

Figure 4.4.1 (a-e) displays the symmetrical *θ-2θ* scan diffractograms of 3D $MAPbBr_3$ thin films grown on different metal substrates, observed for an ageing time of 60 days. Also, *Figure 4.4.1(f)* shows the X-ray diffractograms of the thin 3D $MAPbBr_3$ films on glass and FTO. The as-deposited thin films on glass and FTO were used as references. The spectra of all the as-prepared thin films showed the cubic crystal structure containing the $Pm\overline{3}m$ space group, concordant with the literature [3,88]. The intensities of $MAPbBr_3$ diffraction peaks on the glass reference are observed to differ from one plot to another. This apparent difference is due to the variation in intensities of corresponding metal/$MAPbBr_3$ diffraction peaks. The graph with a less significant difference has a more observable glass/$MAPbBr_3$ peak.

Figure 4.4.2 (a-f) shows the XRD patterns of $PbBr_2$ and MABr and $MAPbBr_3$ on Al, Sn, Ag, Au-Zn, and Au, and $MAPbBr_3$ on the different metal substrates. No peaks corresponding to $PbBr_2$ and MABr residues are observed on Al, Sn, Au-Zn, and Au, indicating complete crystallization of $MAPbBr_3$. In our previous study on the optimisation of the SPVD of $MAPbBr_3$ on FTO [74,89], we showed that crystallization started inside the vacuum chamber during deposition and post-annealing in air merely completed the process. In this section, we have observed that the process depends on the nature of the substrate. The crystallization of single-phase $MAPbBr_3$ on Al, Sn and Au substrates was complete, as shown in *Figure 4.4.2 (a, b and e).* However, $PbBr_2$ and MABr residues were observed alongside $MAPbBr_3$ on Ag and Au-Zn substrates, as shown in *Figure 4.4.2 (c, e).* Besides, extra unidentified peaks were observed at 31.44˚ for $MAPbBr_3$ on Al and 40.13˚ for $MAPbBr_3$ on Au-Zn. The intensities of the extra peaks decrease after 60 days, showing that the diffraction peaks may belong to the unstable $MAPbBr_3$. However, these peaks are absent on the diffraction pattern on simulated diffraction patterns of $MAPbBr_3$ [2,90]. This could be because the $MAPbBr_3$ grew on planes specific to the nature of the substrate materials. Notably, peaks corresponding to Sn [91], Ag [92], Au [93] and FTO substrates were identified alongside those of $MAPbBr_3$, as shown illustrated by *Figure 4.4.1(b, c and e)* and *Figure 4.4.2*. This could be because the $MAPbBr_3$ films on the metals were more compact and covered the entire substrate, which limited X-ray penetration.

A highly textured $MAPbBr_3$ thin film with preferred orientation on the extra plane at 31.44˚ for and along the (200) plane on the Sn surface was observed as shown by the patterns of the as-deposited film in *Figure 4.4.1(a, b).* Generally, there were significant changes in texture from one substrate to another, as shown in *Figure 4.4.2 (f).* This variation in texture shows that the crystallographic texturing of 3D $MAPbBr_3$ thin film can be manipulated using a suitable choice of a metal substrate. The differences in the texture could be because of the peculiar ways of lessening the surface, interface and strain energy during the grain growth processes [94]. The texturing of HaP thin films influences surface recombination rate, bulk diffusion length, and so, the performance of the device. *Zhu and co-workers* [95] summarised the effects of texturing on the performance and stability of solar cells. They stated that highly textured HaP films result in solar cells with high PCEs and excellent stability.

Similarly, *Jiang and co-workers* [96] showed that texturing of HaP thin films influences bulk diffusion length and surface recombination at the contacts, and highly oriented films give better performance. *Figure 4.4.1(a-e)* shows that $MAPbBr_3$ thin-film degraded after protracted ageing under ambient conditions (room temperature and atmospheric pressure) and the rate of degradation depends on the material of the substrate. Comparing the diffractograms of the as-deposited $MAPbBr_3$ thin films with those measured after ageing for 60 days, we saw that the intensities of the pronounced peaks decreased the most on Al and the least on Au-Zn. These imply that the $MAPbBr_3$ thin-film decomposed at a rapid rate on the Al and gradual rate on the Au-Zn. The phases present after the 60 days ageing period were also checked. The results revealed that the degradation products were similar on all the substrates and were matched to $PbBr_2$ and MABr. Additionally, peaks corresponding to alumina (Al_2O_3) were also observed on the Al substrate and could be due to the reaction between Al and oxygen in the atmosphere to form the thin oxide layer of Al_2O_3.

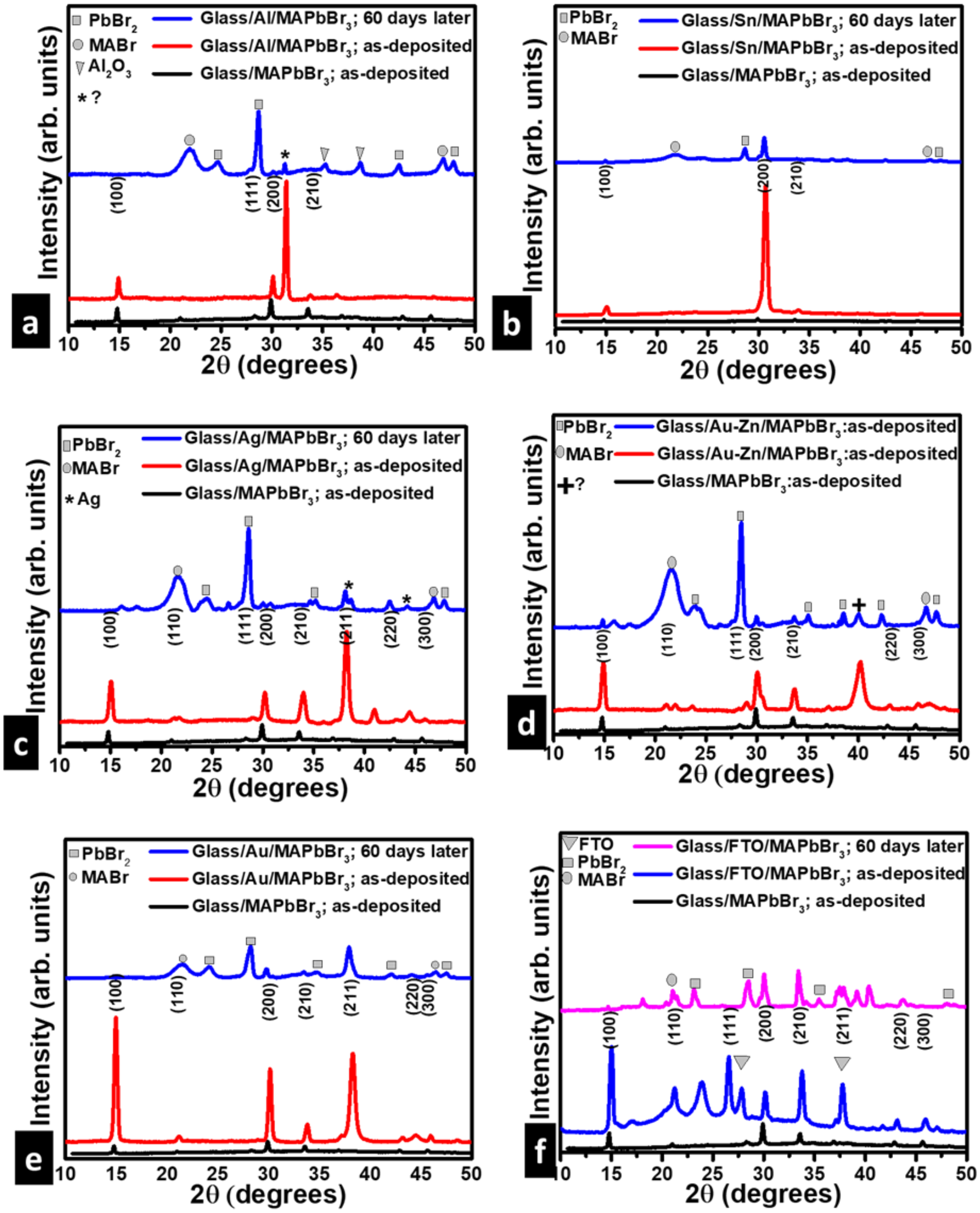

Figure 4.4.1:(a-e) X-ray diffraction patterns of $MAPbBr_3$ on glass and different metal surfaces immediately after and 60 days later (f) X-ray diffraction patterns of $MAPbBr_3$ on glass and FTO surfaces immediately and 60 days after deposition.

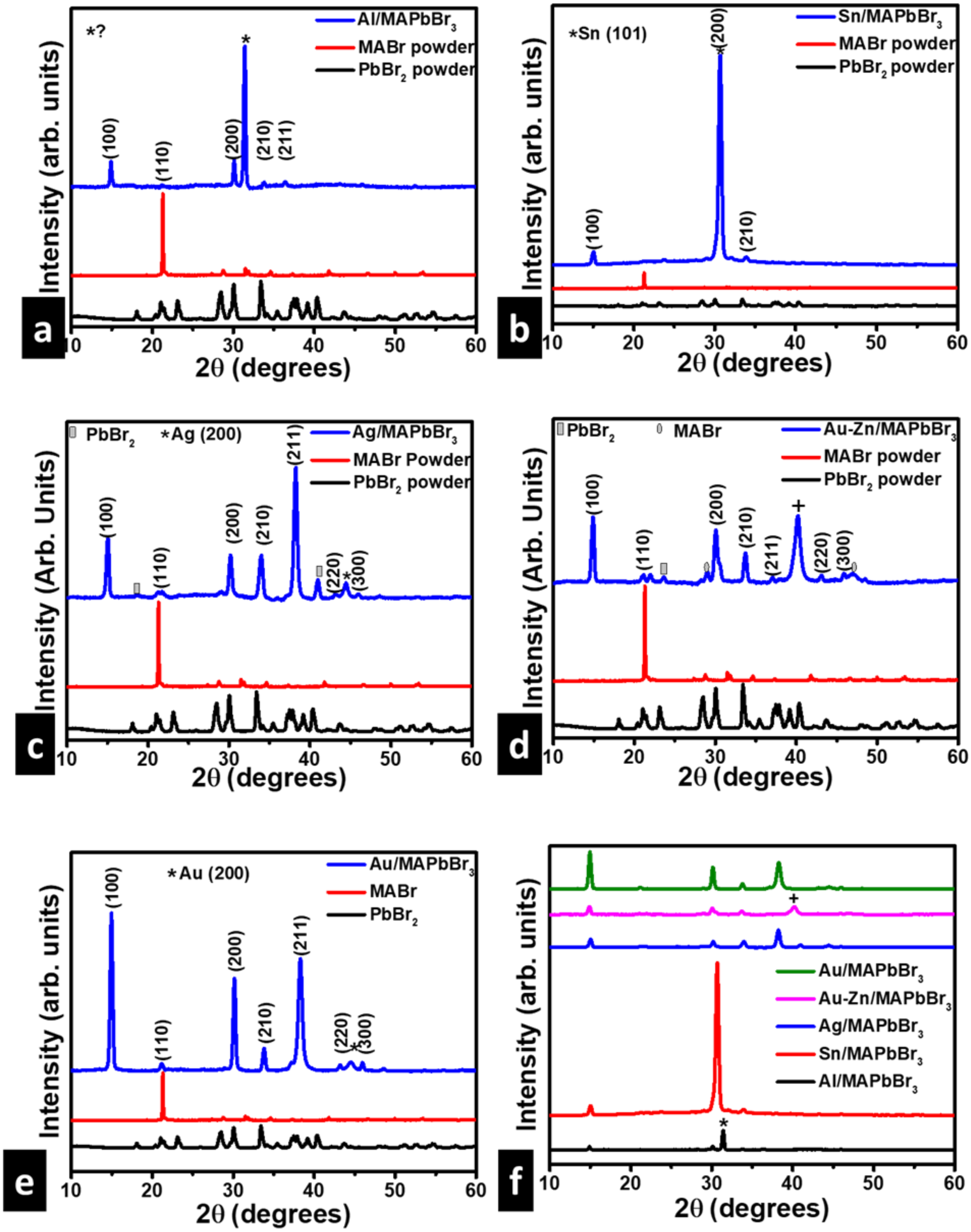

Figure 4.4.2: XRD patterns of $PbBr_2$ and MABr and $MAPbBr_3$ on Al (a), Sn (b), Ag (c), Au-Zn (d), and Au (e) and (f) $MAPbBr_3$ on the different metal substrates

Figure 4.4.3 (a) shows the variation of the lattice constant of the thin $MAPbBr_3$ films with work-functions. We observed an inverse dependence of the lattice constant on work function. Similarly, the crystallite size was observed to be inversely dependent on work function. The decrease in the crystallite size may be due to a drop in the dimensions of the unit cell since the lattice constants for $MAPbBr_3$ on Sn, Ag, Au-Zn and Au were slightly less than the natural value ($a_o = 5.93$ Å), obtained from $MAPbBr_3$ powdered sample. The difference between the observed lattice constant and the natural lattice constant could be because the films were strained to fit the substrate leading to the accumulation of strain energy. This is confirmed by *(c)*, which shows that the micro-strain increases with an increase in the work function of the metals. The increase in the micro-strain with work function correlates well with the decrease in the crystallite size and lattice constants. This implies that as crystallite sizes and lattice constant decrease, the micro-strain increased, in agreement with the literature [97–99]. *Shafi and co-workers* [98] showed that an inverse dependence exists between crystallite size and micro-strain for nanocrystalline tin oxide powders. Figure 4.4.3 (c) also shows that the micros-strains for the as-deposited thin films are positive while those for the degraded thin films are all negative. The positive values of micro-strain indicate the presence of tensile stress fields while the negative values signify compressive stress fields. The means that the degradation of HaP leads to a change of micro-strain from tensile to compressive. Micro-strain has been shown to produce both positive and negative effects on solar cell performance. *Zhu and co-workers* [100] proved that charge carrier lifetime increases as micro-strain decreases, leading to improvement in electron and hole extraction in perovskites solar cells. Similarly, *Jones and co-workers* [37] showed that micro-strain enhances structural defect accumulation and causes non-radiative recombination leading to a decrease in minority carrier lifetime. The calculated lattice constant of the film is greater than a_o. This could be due to tensile stress fields from the impingement and coalescence of growing islands leading to the very large crystallites observed in *Figure 4.4.3 (b)* [101].

On the other hand, $MAPbBr_3$ thin films prepared on Ag, Sn, Au-Zn, and Au showed lattice constants that were smaller than the a_o, probably because of smaller tensile stress fields resulting from the small crystallite sizes [102]. *Figure 4.4.3 (b)* also shows that the values of the crystallite sizes of the as-deposited $MAPbBr_3$ thin films are greater than the crystallite sizes after ageing for 60 days. This means that the crystallite size of $MAPbBr_3$ thin film decreases it decays. Figure 4.4.3 (d) illustrates that the most considerable percentage difference in crystallite size occurs for the $MAPbBr_3$ prepared on Al substrate and the least difference for $MAPbBr_3$ on Au-Zn. This supports the fact that the rate of degradation of $MAPbBr_3$ was fastest on Al and slowest on Au-Zn.

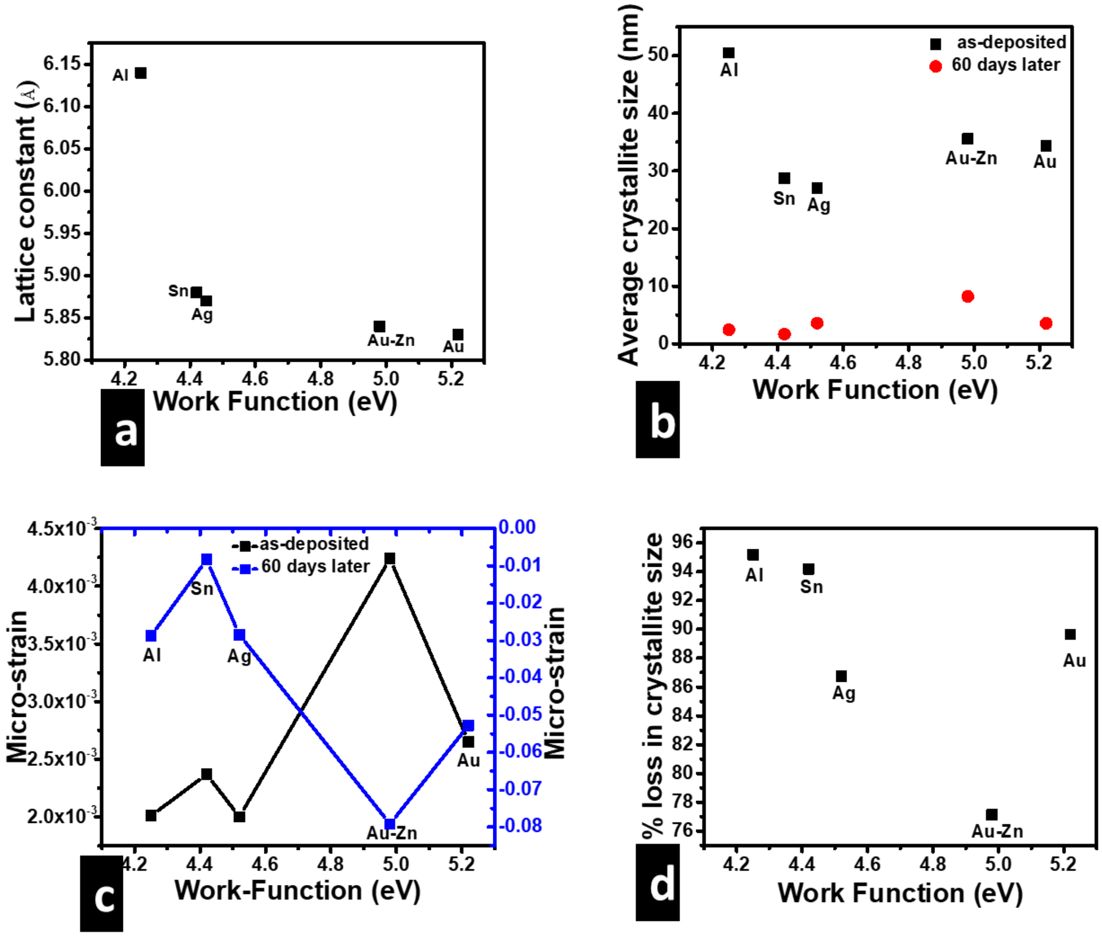

Figure 4.4.3: (a) The lattice constants of $MAPbBr_3$ on different metal surfaces vs. work function; (b) The average crystallite sizes of $MAPbBr_3$ on various metal surfaces vs. work function as-deposited and 60 days after deposition; (c) The micro-strain of $MAPbBr_3$ on different metal surfaces vs. work function as-deposited and 60 days after deposition; (d) % loss in crystallite sizes of $MAPbBr_3$ vs. work function 60 days after deposition.

4.4.3 Morphological properties

Figure 4.4.4 (a, b) shows the reference FE-SEM images of as-deposited thin $MAPbBr_3$ films on glass and FTO, respectively. Both the grains on glass and FTO have a compact morphology with variable sizes and orientations. However, the average grains size of the $MAPBBr_3$ thin film on glass is 205 nm. This is smaller than the average grain size on FTO, which is 302 nm. The variable compact morphology confirms the polycrystalline nature of the thin $MAPbBr_3$, which is also revealed by XRD as seen above.

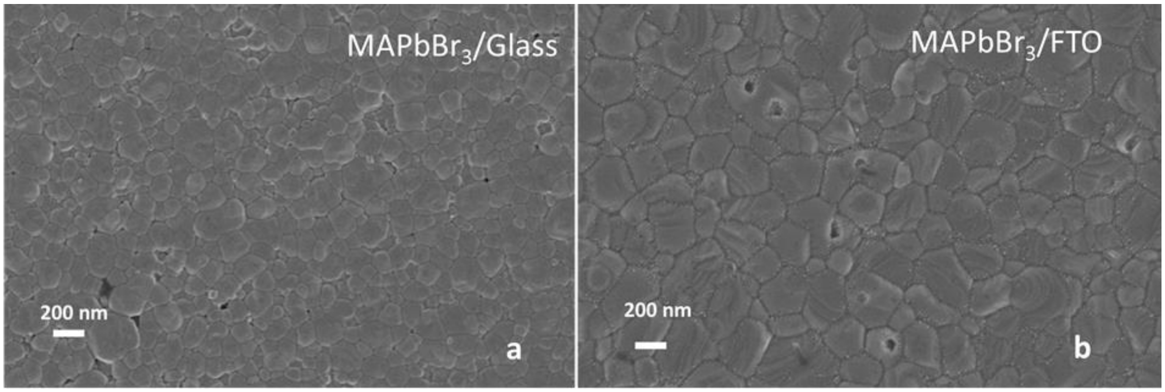

Figure 4.4.4: FE- SEM micrographs of as-deposited $MAPbBr_3$ *on glass, (b) FE- SEM micrographs of as-deposited* $MAPbBr_3$ *on FTO.*

Figure 4.4.5(a-e) show the FE-SEM photographs of as-deposited thin $MAPbBr_3$ films prepared on Al, Sn, Ag, Au-Zn and Au substrates, respectively. The micrographs displayed bimodal distributed and densely packed pinhole-free grains, with full surface coverage. The bimodal distribution originates from a discontinuous grain growth, where some few grains grow at a rapid rate than their surrounding grains, resulting in a microstructure having a few large grains. This abnormal grain growth occurs due to some grains having higher grain boundary energies, greater local grain boundary mobility and favoured texture compared to their neighbours. *Figure 4.4.5 (f)* shows the variation of the average grain size of the thin $MAPbBr_3$ films of various substrates. The average grain size was observed to increase linearly from Al through Sn, Ag and Au-Zn, to Au substrates as the metal work-function increased. The increase in average grain size of halide perovskites has been shown to cause a decrease in bandgap and increase in carrier lifetime [48,95]. To sum up, we observed that the nature of the metal substrate determines the morphology of the $MAPbBr_3$, which is consistent with results for methylammonium lead tri-iodide ($MAPbI_3$) in the literature [103].

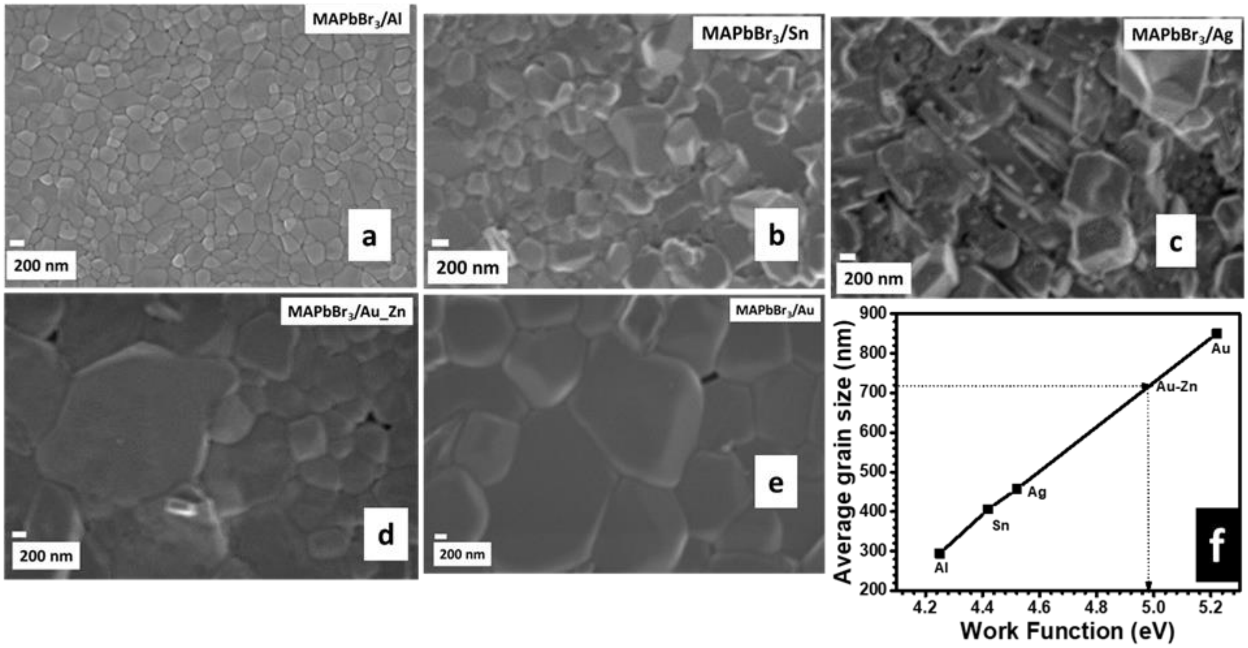

Figure 4.4.5: (a-e) FE-SEM micrographs of as-deposited $MAPbBr_3$ on metal surfaces, (f) Average grain size of as-deposited $MAPbBr_3$ vs. work functions metal surfaces.

Figure 4.4.6 (a-c) shows FE-SEM micrographs of thin $MAPbBr_3$ films on Al substrate measured at once, after ageing for one, and after 60 days, respectively. Similarly, *Figure 4.4.6 (d-o)* shows the FE-SEM micrographs of the thin $MAPbBr_3$ films on Sn, Ag, Au-Zn and Au, checked over the same period of 60 days. The $MAPbBr_3$ grains on Al started to delaminate only a day after deposition, as shown in *Figure 4.4.6 (b)*, and the rate of delamination increased over time. After ageing for 60 days, almost all the grains detached from the substrate and cracks became visible on the surface of the substrate, as shown in *Figure 4.4.6 (c)*. As previously discussed, the diffractograms of the 60 days aged film revealed the presence of Al_2O_3, from the reaction of Al with air. We think that the delamination of the grains could be due to the intrinsic tensile stresses which caused cracks seen in *Figure 4.4.6 (c)* [104], which could quickly propagate on Al_2O_3 thin layer because of its brittle nature. The failure of HaP thin films by delamination has also been seen on other ceramic substrates. In a similar study, Al quickly reduced Pb^{2+} to Pb while being oxidized to Al^{3+} in the presence of air and water, leading to the conversion $CH_3NH_3PbI_3$

to $(CH_3NH_3)_4PbI_6.2H_2O$ and subsequently to CH_3NH_3I [105]. *Soufiani and co-workers* [106] reported that the accelerated degradation of their solar cells after illumination was due to delamination of $MAPbI_3$ on a titanium dioxide (TiO_2) layer. *Han and co-workers* [107] reported the detachment of $MAPbI_3$ from TiO_2 for encapsulated solar cells that were subjected to temperatures of 55°C and 50% moisture. On the other hand, $MAPbBr_3$ grain remained attached to Sn, Ag, Au-Zn and Au substrates as shown in *Figure 4.4.6 (d-o)*, even though XRD results showed that degradation was occurring at different rates. The delaminated grain in *Figure 4.4.6 (b)* indeed revealed the 3D nature of sequential physical vapour deposited $MAPbBr_3$, consisting of nano-cuboids.

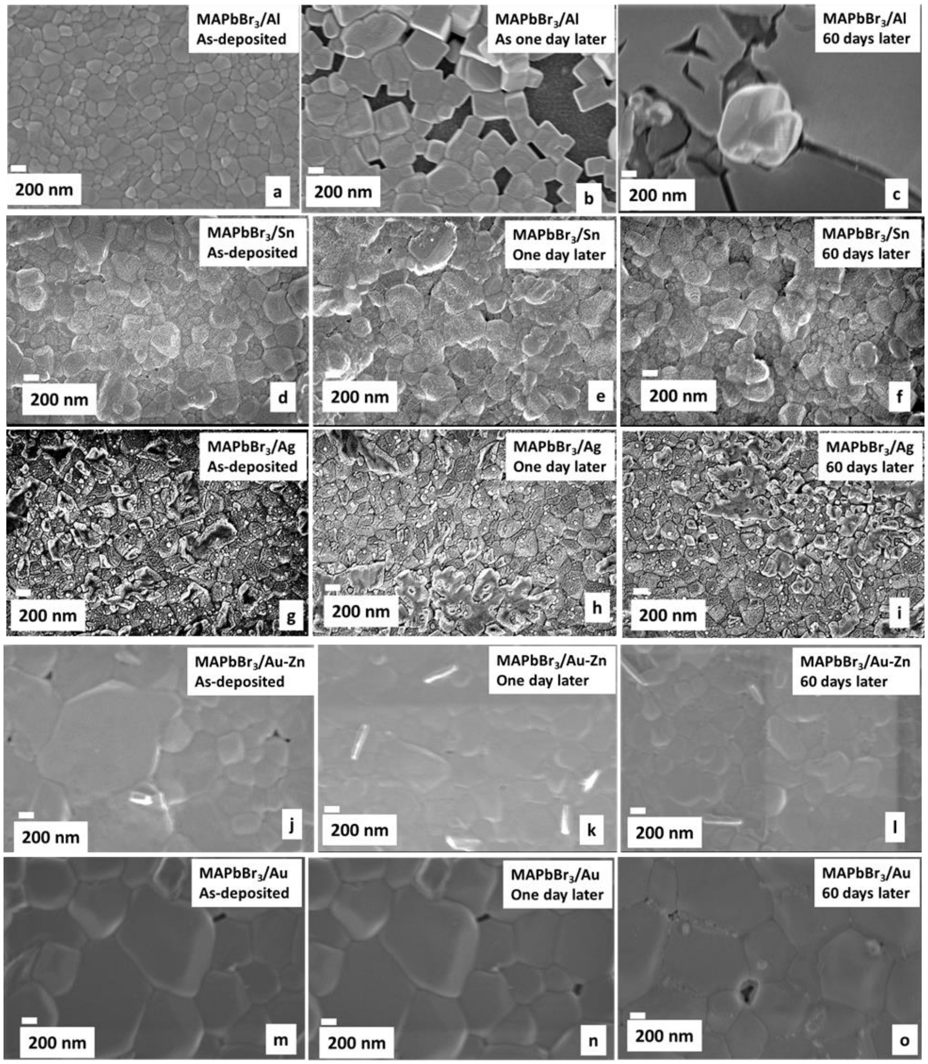

Figure 4.4.6: SEM micrographs of $MAPbBr_3$ on Al, Sn, Ag, Au-Zn and Au substrates over an ageing period of 60 days (a, d, g, j and m) SEM for as-deposited samples, (b, e, h, k and n) SEM for samples one day after deposition. (c, f, i, l, and o) SEM for samples 60 days after deposition.

References

[1] K.H. Wang, L.C. Li, M. Shellaiah, K.W. Sun, Structural and Photophysical Properties of Methylammonium Lead Tribromide ($MAPbBr_3$) Single Crystals, Sci. Rep. 7 (2017) 1–14. doi:10.1038/s41598-017-13571-1.

[2] W. Peng, L. Wang, B. Murali, K. Ho, A. Bera, N. Cho, C. Kang, V.M. Burlakov, J. Pan, L. Sinatra, C. Ma, W. Xu, D. Shi, E. Alarousu, A. Goriely, J. He, O.F. Mohammed, T. Wu, O.M. Bakr, Solution-Grown Monocrystalline Hybrid Perovskite Films for Hole-Transporter-Free Solar Cells, Adv. Mater. 28 (2016) 3383–3390. doi:10.1002/adma.201506292.

[3] J.T. Tisdale, T. Smith, J.R. Salasin, M. Ahmadi, N. Johnson, A. V. Ievlev, M. Koehler, C.J. Rawn, E. Lukosi, B. Hu, Precursor purity effects on solution-based growth of MAPbBr 3 single crystals towards efficient radiation sensing, CrystEngComm. 20 (2018) 7818–7825. doi:10.1039/c8ce01498a.

[4] M. Jäckle, H. Linnenbank, M. Hentschel, M. Saliba, S.G. Tikhodeev, H. Giessen, Tunable green lasing from circular grating distributed feedback based on CH 3 NH 3 PbBr 3 perovskite , Opt. Mater. Express. 9 (2019) 2006. doi:10.1364/ome.9.002006.

[5] G.K. Williamson, W.H. Hall, X-ray line broadening from filed aluminium and wolframL'elargissement des raies de rayons x obtenues des limailles d'aluminium et de tungsteneDie verbreiterung der roentgeninterferenzlinien von aluminium- und wolframspaenen, Acta Metall. 1 (1953) 22–31. doi:https://doi.org/10.1016/0001-6160(53)90006-6.

[6] A.R. Bushroa, R.G. Rahbari, H.H. Masjuki, M.R. Muhamad, Approximation of crystallite size and microstrain via XRD line broadening analysis in TiSiN thin films, Vaccum. 86 (2012) 1107–1112. doi:10.1016/j.vacuum.2011.10.011.

[7] S.B. Hyder, M.A. Wilkov, Effect of dislocation density on the epitaxial growth of silver, J. Appl. Phys. 38 (1967) 2386–2387. doi:10.1063/1.1709890.

[8] A. Mhamdi, H. Mehdi, A. Bouazizi, G. Garcia-Belmonte, One-step methylammonium lead bromide films: Effect of annealing treatment, J. Mol. Struct. 1192 (2019) 1–6. doi:10.1016/j.molstruc.2019.04.113.

[9] N.M. Gosavi, A.R. Shelke, N.G. Deshpande, S.R. Gosavi, A.M. Patil, C.P. Sawant, A.D. Dhondge, Influence of thickness on the photo sensing properties of chemically synthesized copper sulfide Thin Films, World J. Condens. Matter Phys. 05 (2015) 1–9. doi:10.4236/wjcmp.2015.51001.

[10] M. Singh, M. Goyal, K. Devlal, Size and shape effects on the band gap of semiconductor compound nanomaterials, J. Taibah Univ. Sci. 12 (2018) 470–475. doi:10.1080/16583655.2018.1473946.

[11] L. Kong, G. Liu, J. Gong, Q. Hu, R.D. Schaller, P. Dera, D. Zhang, Z. Liu, W. Yang, K. Zhu, Y. Tang, C. Wang, S.-H. Wei, T. Xu, H. Mao, Simultaneous band-gap narrowing and carrier-lifetime prolongation of organic-inorganic tri-halide perovskites, Proc. Natl. Acad. Sci. 113 (2016) 8910–8915. doi:10.1073/pnas.1609030113.

[12] R. Dalven, Empirical relation between energy gap and lattice constant in cubic semiconductors, Phys. Rev. B. 8 (1973) 6033–6034. doi:10.1103/PhysRevB.8.6033.

[13] C. Bi, Y. Shao, Y. Yuan, Z. Xiao, C. Wang, Understanding the formation and evolution of interdi ffusion grown organolead HaP thin films by thermal annealing, J. Mater. Chem. A, 2 (2014) 18508-18514. doi:10.1039/c4ta04007d.

[14] Giles E. Eperon, Victor M. Burlakov, Pablo Docampo, Alain Goriely, Henry J. Snaith, Morphological control for high performance, solution-processed planar heterojunction perovskite

solar cells, Adv. Funct. Mater. (2013) 151–157. doi:10.1002/adfm.201302090.

[15] M. Liu, M.B. Johnston, H.J. Snaith, Efficient planar heterojunction perovskite solar cells by vapour deposition., Nature. 501 (2013) 395–8. doi:10.1038/nature12509.

[16] C. V. Thompson, Grain growth in polycrystalline thin films of semiconductors, Interface Sci. 6 (1998) 85–93. doi.org/10.1023/A:1008616620663.

[17] D.N. Lee, H.Y.O.J. Lee, Effect of stresses on the evolution of annealing textures in Cu and Al Interconnects, J. Electron. Mater. 32 (2003) 1012-1022. doi.org/10.1007/s11664-003-0083-5.

[18] A.J. Dammers, S. Radelaar, Two-dimensional computer modeling of polycrystalline film growth, textures microstruct. 14 (1991) 757–762. doi:10.1155/tsm.14-18.757.

[19] P. Garg, R. Rai, B.K. Singh, Nuclear Instruments and Methods in Physics Research A Structural characterization of “ as-deposited ” cesium iodide films studied by X-ray diffraction and transmission electron microscopy techniques, Nucl. Inst. Methods Phys. Res. A. 736 (2014) 128–134. doi:10.1016/j.nima.2013.10.075.

[20] J.L. Hesler, T.W. Crowe, V. Diodes, Responsivity and noise measurements of zero-bias Schottky diode detectors, Proc. ISSTT (2007) 89-92

[21] P.A. Shaikh, D. Shi, J.R.D. Retamal, A.D. Sheikh, M.A. Haque, C.F. Kang, J.H. He, O.M. Bakr, T. Wu, Schottky junctions on perovskite single crystals: Light-modulated dielectric constant and self-biased photodetection, J. Mater. Chem. C. 4 (2016) 8304–8312. doi:10.1039/c6tc02828d.

[22] A. Hajibadali, M.B. Nejad, G. Farzi, Schottky Diodes Based on Polyaniline / Multi-Walled Carbon Nanotube Composites Braz. J. Phys. 45 (2015) 394-398. doi.org/10.1007/s13538-015-0334-y.

[23] M. DeJarld, P.M. Campbell, A.L. Friedman, M. Currie, R.L. Myers-Ward, A.K. Boyd, S.G. Rosenberg, S.P. Pavunny, K.M. Daniels, D.K. Gaskill, Surface potential and thin-film quality of low work function metals on epitaxial graphene, Sci. Rep. 8 (2018) 1–11. doi:10.1038/s41598-018-34595-1.

[24] M.R. Leyden, L. Meng, Y. Jiang, L.K. Ono, L. Qiu, E.J. Juarez-perez, C. Qin, C. Adachi, Y. Qi, Methylammonium lead bromide perovskite light-emitting diodes by chemical vapor deposition, J. Phys. Chem. Lett. 8 (2017) 3193-3198. doi:10.1021/acs.jpclett.7b01093.

[25] S. Gupta, P. Paramahans Manik, R. Kesh Mishra, A. Nainani, M.C. Abraham, S. Lodha, Contact resistivity reduction through interfacial layer doping in metal-interfacial layer-semiconductor contacts, J. Appl. Phys. 113 (2013) 073707. doi:10.1063/1.4811340.

[26] B. Wenger, P.K. Nayak, X. Wen, S. V. Kesava, N.K. Noel, H.J. Snaith, Consolidation of the optoelectronic properties of CH3NH3PbBr3 perovskite single crystals, Nat. Commun. 8 (2017) 1-10. doi:10.1038/s41467-017-00567-8.

[27] D. Yang, X. Zhou, R. Yang, Z. Yang, W. Yu, X. Wang, C. Li, S. Liu, R.P.H. Chang, Surface optimization to eliminate hysteresis for record efficiency planar perovskite solar cells, Energy Environ. Sci. 9 (2016) 3071–3078. doi:10.1039/c6ee02139e.

[28] S.A. Moiz, M.M. Ahmed, K.S. Karimov, Estimation of electrical parameters of OD organic semiconductor diode from measured I-V characteristics, ETRI J. 27 (2005) 319–324. doi:10.4218/etrij.05.0104.0100.

[29] G.F. Yu, M. Yu, W. Pan, W.P. Han, X. Yan, J.C. Zhang, H. Di Zhang, Y.Z. Long, Electrical transport properties of an isolated CdS micro rope composed of twisted nanowires, Nanoscale Res. Lett. 10 (2015) 1–7. doi:10.1186/s11671-015-0734-5.

[30] M.I. Saidaminov, A.L. Abdelhady, B. Murali, E. Alarousu, V.M. Burlakov, W. Peng, I. Dursun, L. Wang, Y. He, G. MacUlan, A. Goriely, T. Wu, O.F. Mohammed, O.M. Bakr, High-quality bulk hybrid perovskite single crystals within minutes by inverse temperature crystallization, Nat. Commun. 6 (2015) 1–6. doi:10.1038/ncomms8586.

[31] L.C. Chen, K.L. Lee, S.E. Lin, Observation of hybrid MAPBBr$_3$ perovskite bulk crystals grown by repeated crystallizations, Crystals. 8 (2018) 260. doi:10.3390/cryst8070260.

[32] D. Shi, V. Adinolfi, R. Comin, M. Yuan, E. Alarousu, A. Buin, Y. Chen, S. Hoogland, A. Rothenberger, K. Katsiev, Y. Losovyj, X. Zhang, P.A. Dowben, O.F. Mohammed, E.H. Sargent, O.M. Bakr, Low trap-state density and long carrier diffusion in organolead trihalide perovskite single crystals, Science, 347 (2015) 519–522. doi: 10.1126/science.aaa2725.

[33] N.J. Jeon, J.H. Noh, Y.C. Kim, W.S. Yang, S. Ryu, S. Il Seok, inorganic-organic hybrid perovskite solar cells, Nat. Mater. 13 (2014) 897-903. doi:10.1038/NMAT4014.

[34] K. Frohna, T. Deshpande, J. Harter, W. Peng, B.A. Barker, J.B. Neaton, S.G. Louie, O.M. Bakr, D. Hsieh, M. Bernardi, crystals, Nat. Commun. 9 (2018) 1-9. doi:10.1038/s41467-018-04212-w.

[35] M. Á Reinoso, C. A Otálora, G. Gordillo, Improvement properties of hybrid halide perovskite thin films prepared by sequential evaporation for planar solar cells, Mater. 12 (2019) 1394. doi: 10.3390/ma12091394

[36] J. Zhao, Strained hybrid perovskite thin films and their impact on the intrinsic stability of perovskite solar cells, Sci. Adv. 3 (2017) eaao5616. doi: 10.1126/sciadv.aao5616.

[37] T.W. Jones, A. Osherov, M. Alsari, M. Sponseller, B.C. Duck, Y.K. Jung, C. Settens, F. Niroui, R. Brenes, C. V. Stan, Y. Li, M. Abdi-Jalebi, N. Tamura, J.E. MacDonald, M. Burghammer, R.H. Friend, V. Bulović, A. Walsh, G.J. Wilson, S. Lilliu, S.D. Stranks, Lattice strain causes non-radiative losses in halide perovskites, Energy Environ. Sci. 12 (2019) 596–606. doi:10.1039/c8ee02751j.

[38] F. Haque, M. Wright, A. Mahmud, H. Yi, D. Wang, L. Duan, C. Xu, A. Uddin, Effects of hydroiodic acid concentration on the properties of CsPbI$_3$ perovskite solar cells, ACS Omega, 3 (2018) 11937-11944.doi:10.1021/acsomega.8b01589.

[39] P. Fan, D. Gu, G. Liang, J. Luo, J. Chen, Z. Zheng, High-performance perovskite CH$_3$NH$_3$PbI$_3$ thin films for solar cells prepared by single-source physical vapour deposition, Nat. Publ. Gr. 6 (2016) 1–9. doi:10.1038/srep29910.

[40] J.B. Patel, R.L. Milot, A.D. Wright, L.M. Herz, M.B. Johnston, Formation dynamics of CH$_3$NH $_3$PbI$_3$ perovskite following two-step layer deposition, J. Phys. Chem. Lett. 7 (2016) 96-102. doi:10.1021/acs.jpclett.5b02495.

[41] Q. Chen, H. Zhou, T. Bin Song, S. Luo, Z. Hong, H.S. Duan, L. Dou, Y. Liu, Y. Yang, Controllable self-induced passivation of hybrid lead iodide perovskite toward high-performance solar cells, Nano Lett. 14 (2014) 4158–4163. doi:10.1021/nl501838y.

[42] B. Park, N. Kedem, M. Kulbak, D.Y. Lee, W.S. Yang, N.J. Jeon, J. Seo, G. Kim, K.J. Kim, T.J. Shin, G. Hodes, D. Cahen, S. Il Seok, Understanding how excess lead iodide precursor improves halide perovskite solar cell performance, Nat. Commun., 9 (2018) 1–8. doi:10.1038/s41467-018-05583-w.

[43] T.J. Jacobsson, J.P. Correa-Baena, E. Halvani Anaraki, B. Philippe, S.D. Stranks, M.E.F. Bouduban, W. Tress, K. Schenk, J. Teuscher, J.E. Moser, H. Rensmo, A. Hagfeldt, Unreacted PbI$_2$ as a double-edged sword for enhancing the performance of perovskite solar cells, J. Am. Chem. Soc. 138 (2016) 10331–10343. doi:10.1021/jacs.6b06320.

[44] U. Kwon, M.M. Hasan, W. Yin, D. Kim, N.Y. Ha, S. Lee, T.K. Ahn, H.J. Park, Investigation into the advantages of pure perovskite film without PbI$_2$ for high-performance solar cell, Sci. Rep. 6 (2016) 1–8. doi:10.1038/srep35994.

[45] T.J. Jacobsson, L.J. Schwan, M. Ottosson, A. Hagfeldt, T. Edvinsson, Determination of thermal expansion coefficients and locating the temperature-induced phase transition in methylammonium lead perovskite using X-ray diffraction, Inorg. Chem. 54 (2015) 10678–10685.

doi:10.1021/acs.inorgchem.5b01481.

[46] H. Zhang, M. Tao, B. Gao, W. Chen, Q. Li, Q. Xu, S. Dong, Preparation of $CH_3NH_3PbI_3$ thin films with tens of micrometer-scale at high temperature, Scientific Rep., 7 (2017) 1-9. doi:10.1038/s41598-017-09109-0.

[47] M. Ozta, Influence of grain size on electrical and optical properties of InP films, Chinese Phys. Lett. 25 (2008) 4090–4092. doi:10.1088/0256-307X/25/11/069.

[48] V. D'Innocenzo, A.R. Srimath Kandada, M. De Bastiani, M. Gandini, A. Petrozza, Tuning the light emission properties by bandgap engineering in hybrid lead HaP, J. Am. Chem. Soc. 136 (2014) 17730–17733. doi:10.1021/ja511198f.

[49] W. Shockley, H.J. Queisser, Detailed balance limit of efficiency of p-n junction solar cells, J. Appl. Phys 32 (1961) 510-519. doi:10.1063/1.1736034.

[50] W.E.I. Sha, X. Ren, L. Chen, W.C.H. Choy, The efficiency limit of $CH_3NH_3PbI_3$ perovskite solar cells, Appl. Phys. Lett. 106 (2015) 221104. doi:10.1063/1.4922150.

[51] R. Robles, C. Katan, D. Sapori, L. Pedesseau, J. Even, S. Chimiques, C. Université, D.R. Rennes, I.C.N. Institut, C. De Nanociencia, Rashba and Dresselhaus effects in hybrid organic À inorganic perovskites : from basics to devices, ACS nano, 9 (2015) 11557-11567. doi.org/10.1021/acsnano.5b04409

[52] T. Etienne, E. Mosconi, F. De Angelis, Dynamical Origin of the Rashba Effect in Organohalide Lead Perovskites: A Key to Suppressed Carrier Recombination in Perovskite Solar Cells?, J. Phys. Chem. Lett. 7 (2016) 1638–1645. doi:10.1021/acs.jpclett.6b00564.

[53] F. Zheng, L.Z. Tan, S. Liu, A.M. Rappe, Rashba spin-orbit coupling enhanced carrier lifetime in organometal halide perovskites, Nano Lett. 15 (2015) 7794-7800. doi.org/10.1021/acs.nanolett.5b01854

[54] C. V. Ramana, R.J. Smith, O.M. Hussain, Grain size effects on the optical characteristics of pulsed-laser deposited vanadium oxide thin films, Phys. Status Solidi Appl. Res. 199 (2003) 5–7. doi:10.1002/pssa.200309009.

[55] S.M. Jain, B. Philippe, E.M.J. Johansson, B.W. Park, H. Rensmo, T. Edvinsson, G. Boschloo, Vapor phase conversion of PbI_2 to $CH_3NH_3PbI_3$: Spectroscopic evidence for the formation of an intermediate phase, J. Mater. Chem. A., 4 (2016) 2630–2642. doi:10.1039/c5ta08745g.

[56] G. Abdelmageed, L. Jewell, K. Hellier, L. Seymour, B. Luo, F. Bridges, J.Z. Zhang, S. Carter, Mechanisms for light-induced degradation in MAPbI3 perovskite thin films and solar cells, Appl. Phys. Lett., 109 (2016) 0–5. doi:10.1063/1.4967840.

[57] B. Dunn, Y. Yang, M. Wang, L. Zuo, H. Guo, N. De Marco, D.S. Ginger, S. Dong, S. Jariwala, D.W. deQuilettes, R. DeBlock, Polymer-modified halide perovskite films for efficient and stable planar heterojunction solar cells, Sci. Adv. 3 (2017) e1700106. doi:10.1126/sciadv.1700106.

[58] K.H. Hendriks, J.J. Van Franeker, B.J. Bruijnaers, J.A. Anta, M.M. Wienk, R.A.J. Janssen, 2-Methoxyethanol as a new solvent for processing methylammonium lead halide perovskite solar cells, J. Mater. Chem. A. 5 (2017) 2346–2354. doi:10.1039/C6TA09125C.

[59] W. Zhao, D. Yang, Z. Yang, S. (Frank) Liu, Zn-doping for reduced hysteresis and improved performance of methylammonium lead iodide perovskite hybrid solar cells, Mater. Today Energy. 5 (2017) 205–213. doi:10.1016/j.mtener.2017.06.009.

[60] N. Liu, Q. Du, G. Yin, P. Liu, L. Li, H. Xie, C. Zhu, Y. Li, H. Zhou, W. Bin Zhang, Q. Chen, Extremely low trap-state energy level perovskite solar cells passivated using NH_2-POSS with improved efficiency and stability, J. Mater. Chem. A. 6 (2018) 6806–6814. doi:10.1039/c7ta11345e.

[61] K. Meerholz, S. Van Smaalen, F. Panzer, Impact of excess PbI_2 on the structure and the

methylammonium lead iodide perovskite, J. Mater. Chem. C, 6 (2018) 7512-7519. doi:10.1039/c8tc02237b.

[62] Y. Liu, F. Li, Z. Chen, T. Guo, C. Wu, T. Whan, Resistive switching memory based on organic/ inorganic hybrid perovskite materials, Vaccum. 130 (2016) 109–112. doi:10.1016/j.vacuum.2016.05.010.

[63] M.A. Lampert, Simplified theory of space-charge-limited currents in an insulator with traps, Phys. Rev. 103 (1956) 1648–1656. doi:10.1103/PhysRev.103.1648.

[64] L. Zhou, W. Lanford, A.T. Ping, I. Adesida, J.W. Yang, A. Khan, Low resistance Ti/Pt/Au ohmic contacts to p-type GaN, Appl. Phys. Lett. 76 (2000) 3451–3453. doi:10.1063/1.126674.

[65] L. Gil-escrig, A.M. Sempere, M. Sessolo, H.J. Bolink, Mixed iodide-bromide methylammonium lead perovskite-based diodes for light-emission and photovoltaics mixed iodide-bromide methylammonium lead perovskite-based diodes for light-emission and photovoltaics, J. Phys. Chem. Lett. 6 (2015) 3743-3748. doi:10.1021/acs.jpclett.5b01716.

[66] J.H. Noh, S.H. Im, J.H. Heo, T.N. Mandal, S. Il Seok, Chemical management for colourful, efficient, and stable inorganic-organic hybrid nanostructured solar cells, Nano Lett. 13 (2013) 1764-1769. doi.org/10.1021/nl400349b

[67] P. Pistor, T. Burwig, Thermal stability and miscibility of co-evaporated, J. Mater. Chem. A, 6 (2018) 11496-11506. doi:10.1039/c8ta02775g.

[68] Y. Zhang, Y. Liu, Y. Li, Towards optimised optoelectronic applications, J. Mater. Chem. C. 4 (2016) 9172-9178. doi:10.1039/C6TC03592B.

[69] R.K. Misra, L. Ciammaruchi, S. Aharon, D. Mogilyansky, L. Etgar, Effect of halide composition on the photochemical stability of perovskite photovoltaic materials, arXiv preprint arXiv:1603.08683 (2016).

[70] D.M. Jang, K. Park, D.H. Kim, J. Park, F. Shojaei, H.S. Kang, J. Ahn, J.W. Lee, J.K. Song, Reversible halide exchange reaction of organometal tri-halide perovskite colloidal nanocrystals for full-range band gap tuning, Nano Lett. 15 (2015) 5191-5199. doi:10.1021/acs.nanolett.5b01430.

[71] F. Lehmann, A. Franz, M.T. Daniel, S. Levcenco, T. Unold, A. Taubert, S. Schorr, RSC Advances The phase diagram of a mixed halide (Br, I) hybrid perovskite obtained by synchrotron X-ray, (2019) 11151–11159. doi:10.1039/c8ra09398a.

[72] C.R. Dong, Y. Wang, K. Zhang, H. Zeng, halide perovskite materials as light harvesters for solar energy conversion, EnergyChem 2 (2020)100026. doi:10.1016/j.enchem.2020.100026.

[73] S.D. Stranks, R.L.Z. Hoye, D. Di, R.H. Friend, F. Deschler, The Physics of Light Emission in HaP Devices, Adv. Mater. 31 (2019) 1803336. doi:10.1002/adma.201803336.

[74] J.N. Fru, N. Nombona, M. Diale, Synthesis and characterisation of methylammonium lead tri-bromide perovskite thin films by sequential physical vapour deposition, Phys. B Phys. Condens. Matter. 578 (2020) 411884. doi:10.1016/j.physb.2019.411884.

[75] S.A. Kulkarni, T. Baikie, P.P. Boix, N. Yantara, N. Mathews, S. Mhaisalkar, Band-gap tuning of lead halide perovskite using a sequential deposition process, J. Mater. Chem. A., 2 (2014) 9221–9225. doi:10.1039/c4ta00435c.

[76] N.J. Röhr JA, Kirchartz T, On the correct interpretation of the low voltage regime in intrinsic single-carrier devices., J. Phys Condens Matter. 29 (2017) 205901. doi.org/10.1088/1361-648X/aa66cc.

[77] J.A. Röhr, X. Shi, S.A. Haque, T. Kirchartz, J. Nelson, Charge transport in spiro-OMeTAD investigated through space-charge-limited current measurements, Phys. Rev. Appl. 9 (2018) 44017. doi:10.1103/PhysRevApplied.9.044017.

[78] S.A. Moiz, M.M. Ahmed, K.S. Karimov, Estimation of electrical parameters of OD organic semiconductor diode from measured I-V characteristics, 27 (2005) 319–325. doi:10.4218/etrij.05.0104.0100.

[79] J.A.R. Thomas Kirchartz and Jenny Nelson, Journal of Physics: Condensed Matter, J. Phys. Condens. Matter. 29 (2017) 205901. doi:org/10.1088/1361-648X/aa66cc.

[80] U. Rau, T. Kirchartz, Charge carrier collection and contact selectivity in solar cells, Adv. Mater. Interfaces 6 (2019) 1900252. doi:10.1002/admi.201900252.

[81] H. Lee, C. Lee, Influence of electrical traps on the current density degradation of inverted perovskite solar cells, Mater. 12 (2019) 1644. doi.org/10.3390/ma12101644.

[82] M. Fischer, K. Tvingstedt, A. Baumann, V. Dyakonov, Doping profile in planar hybrid perovskite solar cells identifying mobile ions, ACS Appl. Energy Mater. 1 (2018) 5129-5134. doi:10.1021/acsaem.8b01119.

[83] W. SHOCKLEY, The theory of p-n junctions in Semiconductors and p-n junction transistors, Bell Syst. Tech. J. 28 (1948) 435–489. doi.org/10.1002/j.1538-7305.1949.tb03645.x.

[84] B. Bera, A. Chakraborty, T. Kar, P. Leuaa, M. Neergat, Density of States, Carrier concentration, and flat band potential derived from electrochemical impedance measurements of N-doped carbon and their influence on electrocatalysis of oxygen reduction reaction, J. Phys. Chem. C. 121 (2017) 20850–20856. doi:10.1021/acs.jpcc.7b06735.

[85] P. Yadav, D. Prochowicz, M. Saliba, P.P. Boix, S.M. Zakeeruddin, M. Grätzel, Interfacial kinetics of efficient perovskite solar cells, Crystals, 7 (2017) 252. doi:10.3390/cryst7080252.

[86] O. Almora, C. Aranda, E. Mas-marzá, G. Garcia-belmonte, On Mott-Schottky analysis interpretation of capacitance measurements in organometal perovskite solar cells On Mott-Schottky analysis interpretation of capacitance measurements in organometal perovskite solar cells, Appl. Phys. Lett. 109 (2016) 173903. doi:10.1063/1.4966127.

[87] W.N.S. Steven S. Hegedus, Thin-film solar cells: device measurements and analysis, 176 (2004) 155–176. doi:10.1002/pip.518.

[88] D. Priante, I. Dursun, M.S. Alias, D. Shi, V.A. Melnikov, T.K. Ng, O.F. Mohammed, O.M. Bakr, B.S. Ooi, The recombination mechanisms leading to amplified spontaneous emission at the true-green wavelength in $CH_3NH_3PbBr_3$ perovskites, Appl. Phys. Lett. 106 (2015) 2–6. doi:10.1063/1.4913463.

[89] J.N. Fru, N. Nombona, M. Diale, Characterization of sequential physical vapour deposited methylammonium lead tri-iodide perovskite thin films, Vacuum. 182 (2020) 109727. doi:10.1016/j.vacuum.2020.109727.

[90] N. Giesbrecht, J. Schlipf, L. Oesinghaus, A. Binek, T. Bein, P. Müller-Buschbaum, P. Docampo, Synthesis of Perfectly Oriented and Micrometer-Sized MAPbBr3 Perovskite Crystals for Thin-Film Photovoltaic Applications, ACS Energy Lett. 1 (2016) 150–154. doi:10.1021/acsenergylett.6b00050.

[91] M. Saitou, Phase diagram and tin whisker growth during electrodeposition, Int. J. Electrochem. Sci. 13 (2018) 1869–1878. doi:10.20964/2018.02.24.

[92] F.X. Bock, T.M. Christensen, S.B. Rivers, L.D. Doucette, R.J. Lad, Growth and structure of silver and silver oxide thin films on sapphire, Thin Solid Films. 468 (2004) 57–64. doi:10.1016/j.tsf.2004.04.009.

[93] I. Dutta, C.B. Munns, G. Dutta, An X-ray diffraction (XRD) study of vapour-deposited gold thin films on aluminum nitride (AlN) substrates, Thin Solid Films. 304 (1997) 229–238. doi:10.1016/S0040-6090(97)00220-4.

[94] X. Sun, K. Gao, X. Pang, Q. Sun, J. Li, Thermodynamic energy variation diagram to speculate

preferred growth orientation of magnetron sputtered PbSe thin films on monocrystalline silicon substrates, Appl. Surf. Sci. 452 (2018) 1–10. doi:10.1016/j.apsusc.2018.04.200.

[95] W. Zhu, J. Chang, C. Zhang, J. Zhang, Y. Hao, Microstructure Engineering of Metal-HaP Films for Efficient Solar Cells, Emerg. Sol. Energy Mater. (2018). doi:10.5772/intechopen.74225.

[96] C. Jiang, Y. Xie, R.R. Lunt, T.W. Hamann, P. Zhang, Elucidating the impact of thin-film texture on charge transport and collection in perovskite Solar Cells, ACS Omega, 3 (2018) 3522-3529. doi:10.1021/acsomega.8b00026.

[97] A. Begum, A. Hussain, A. Rahman, Effect of deposition temperature on the structural and optical properties of chemically prepared nanocrystalline lead selenide thin films, Beilstein J. Nanotechnol. 3 (2012) 438–443. doi:10.3762/bjnano.3.50.

[98] P.M. Shafi, A.C. Bose, Impact of crystalline defects and size on X-ray line broadening : A phenomenological approach for tetragonal SnO_2 nanocrystals Impact of crystalline defects and size on X-ray line broadening : A phenomenological approach for tetragonal, AIP Adv. 5 (2015) 057137. doi:10.1063/1.4921452.

[99] K. Reimann, R. Würschum, Distribution of internal strains in nanocrystalline Pd studied by x-ray diffraction, J. Appl. Phys. 81 (1997) 7186–7192. doi:10.1063/1.365307.

[100] C. Zhu, X. Niu, Y. Fu, N. Li, C. Hu, Y. Chen, X. He, G. Na, P. Liu, H. Zai, Y. Ge, Y. Lu, X. Ke, Y. Bai, S. Yang, P. Chen, Y. Li, M. Sui, L. Zhang, H. Zhou, Q. Chen, Strain engineering in perovskite solar cells and its impacts on carrier dynamics, Nat. Commun. 10 (2019) 815. doi:10.1038/s41467-019-08507-4.

[101] S.C. Seel, C. V Thompson, S.J. Hearne, J.A. Floro, S.C. Seel, C. V Thompson, Tensile stress evolution during deposition of Volmer–Weber thin films tensile stress evolution during deposition of Volmer – Weber thin films, J. Appl. Phys. 88 (2000) 7079-7088. doi:10.1063/1.1325379.

[102] C.W. Mays, J.S. Vermaak, W. Company, F. Avenue, On surface stress and surface, Surface Sci., 12 (1968) 134-140. doi.org/10.1016/0039-6028(68)90119-2.

[103] S. Olthof, K. Meerholz, Substrate-dependent electronic structure and film formation of $MAPbI_3$ perovskites, Nat. Publ. Gr. 7 (2017) 1–10. doi:10.1038/srep40267.

[104] H. Chai, J. Fox, On delamination growth from channel cracks in thin-film coatings, Int. J. Solids Struct. 49 (2012) 3142–3147. doi:10.1016/j.ijsolstr.2012.06.012.

[105] L. Zhao, R.A. Kerner, Z. Xiao, Y. Lisa, K.M. Lee, J. Schwartz, B.P. Rand, B.P. Rand, Redox Chemistry dominates the degradation and decomposition of metal halide perovskite optoelectronic devices, ACS Energy Lett. 1 (2016) 595-602. doi:10.1021/acsenergylett.6b00320.

[106] A.M. Soufiani, Z. Hameiri, S. Meyer, S. Lim, M.J.Y. Tayebjee, J.S. Yun, A. Ho-Baillie, G.J. Conibeer, L. Spiccia, M.A. Green, Lessons learned from spatially resolved electro-and photoluminescence imaging: interfacial delamination in $CH_3NH_3PbI_3$ planar perovskite solar cells upon illumination, Adv. Energy Mater. 7 (2017) 1–12. doi:10.1002/aenm.201602111.

[107] Y. Han, S. Meyer, Y. Dkhissi, K. Weber, J.M. Pringle, U. Bach, L. Spiccia, Y.-B. Cheng, Degradation observations of encapsulated planar $CH_3NH_3PbI_3$ perovskite solar cells at high temperatures and humidity, J. Mater. Chem. A. 3 (2015) 8139–8147. doi:10.1039/C5TA00358J.

5 Conclusions and future work

5.1 Conclusions

This study has developed a simplified and reproducible sequential thermal vapour deposition (STVD) method for growing quality 3D HaP thin films for solar cells. The STVD method was applied in preparing pure and mixed HaP including $MAPbI_3$, $MAPbBr_3$ and $MAPb(I_{1-x}Br_x)_3$ thin films. The structure, morphology, UV-Vis absorption, trap density and charge carrier mobility of the HaP thin films were optimised by varying the thickness of the organic cation from 300 to 500 nm and post-annealing time from 0 to 60 min. Also, the STVD method was used to grow $MAPbBr_3$ thin films on various metal substrates, and the interfacial properties of the metal/$MAPbBr_3$ interface were monitored over 60 days, and the rate degradation of the $MAPbBr_3$ thin films on different metal substrates predicted.

Section 4.1 reports on the growth of the thin $MAPbBr_3$ films on FTO by STVD of $PbBr_2$ and MABr single layers for the first-time. The variation of structural, morphological, optical, electrical, and photoelectrical characteristics of the $MAPbBr_3$ with the thickness of MABr and annealing time were presented and discussed. XRD results revealed the cubic polycrystalline structure of $MAPbBr_3$ having a $Pm\overline{3}m$ space group when the $PbBr_2$ thickness was kept at 100 nm and MABr thickness increased from 300 to 500 nm. The crystallinity, lattice constant, and average crystallite size of the $MAPbBr_3$ thin film was observed to correlate positively with MABr thickness but negatively with post-annealing time. The increase in the lattice constant and average crystallite size was attributed to the decrease in the magnitude of the compressive micro-strain. The lattice constant of the 500 nm MABr thick film was comparable to those $MAPbBr_3$ single crystals synthesized from high purity precursor, showing minimal distortion of the unit cell of the thin film. The as-deposited films also showed the cubic polycrystalline structure of $MAPbBr_3$ having a $Pm\overline{3}m$ space group, pointing to the fact that recrystallization of $MAPbBr_3$ thin film starts during the deposition of the MABr on $PbBr_2$. This heat energy generated during the thermal evaporation of MABr raised the temperature of the substrate to 95℃, which was sufficient to cause the diffusion of MABr into the voids in the $PbBr_6$ octahedral framework to form $MAPbBr_3$. FE-SEM images showed pin-hole-free and densely packed grains with an average grain size that increased from 217 to 302 nm as the MABr was increased from 300 to 500 nm. The increase in average grain size generally leads to a decrease in grain boundaries, with active sites for the accumulation of electron and hole traps that reduce charge carrier lifetime. The polycrystalline nature of the thin film was also confirmed by the fact that the average grain sizes were about ten times larger than the average crystallite sizes, showing that a grain consisted of many crystallites. UV-Vis absorbance showed broadband in the 400 to 500 nm wavelength, typical of $MAPbBr_3$. The bandgap stayed at a constant value (2.28 eV) as the annealing time was increased from 0 to 60 min. This confirmed that crystallization of the $MAPbBr_3$ started within the deposition chamber and pointed to the fact that post-deposition annealing does not significantly change the optical properties of the sequential physical vapour deposited $MAPbBr_3$. Au/$MAPbBr_3$/FTO devices were fabricated and *J-V* characteristics under dark and illumination determined. SCLC analysis of the *J-V* curves revealed an increase in carrier mobility from 1.89×10^{-2} to 1.08×10^{-1} $cm^2 V^{-1} s^{-1}$ and a decrease in trap density from 1.89×10^{16} to 1.40×10^{16} cm^{-3} as MABr thickness increased. The specific contact resistivity of the Au/$MAPbBr_3$/FTO devices increased with an increase in the thickness of MABr indicating that $MAPbBr_3$ is self-doped and the level of doping decreased with an increase in MABr thickness. The devices having the 500 nm MABr thick films generated the highest photocurrent under 100 mW/cm^2 and AM1.5 illumination conditions. This could be due to its high absorbance, small bandgap and low defect density. Therefore, the best properties for solar cell applications were achieved at 100 nm $PbBr_2$ and 500 nm of MABr, corresponding to resultant $MAPbBr_3$ film thickness of 373 nm. This method is repeatable since the same absorption onset (bandgap) was obtained for three different experiments.

In section 4.2, we demonstrated the preparation of thin $MAPbI_3$ films by STVD of PbI_2 and MAI single layers. The structural, optical, morphological, and electrical properties were optimised by changing the thickness of the MAI film and post-deposition annealing time. All the XRD diffractograms showed the tetragonal $MAPbI_3$ phase having the I4/mcm space group. The crystallinity was observed to increase with an increase in MAI film thickness and prolonged post-deposition annealing resulted in the transformation of $MAPbI_3$ to PbI_2. Notably, the un-annealed films showed the pure $MAPbI_3$ phase, indicating crystallization started in situ during the deposition of MAI on PbI_2 at a substrate temperature of 95°C. The micro-strain and crystallite size increased, and dislocation density decreased with an increase in MAI thickness while the changes in these properties with annealing time showed no regular pattern. FE-SEM results showed compact grains of variable sizes and orientations and with average grain size that increases with the thickness MAI but decreased with increased in post-annealing time. The reason for the decrease in average grain size with increasing post-annealing time, however, needs further investigation. Direct and indirect Tauc-plots of the UV-Vis absorption spectra showed a small Rashba effect, with optimum direct and indirect bandgaps of 1.60 and 1.59 eV, respectively. Also, the bandgap increased, and absorption intensity decreased with an increase in annealing time. We observed that films containing PbI_2 produced during post-annealing showed lower absorption intensity. The trap density was observed to decrease with an increase in annealing time, and the maximum charge carrier mobility of 1.29 $cm^2\ V^{-1}\ s^{-1}$ was obtained for the unannealed film. The *J-V* characteristics under illumination also revealed that the unannealed film had the highest photogenerated current. Based on our findings, we recommend the optimal thickness of 100 nm PbI_2 and 500 nm MAI and no post-annealing for low trap density, high charge carrier mobility, and pure thin $MAPbI_3$ films by SVPD.

In section 4.3, we reported the growth of PbI_2-rich $MAPb(I_{1-x}Br_x)_3$ thin films with $x = 0.89$, 0.94 and 0.95 by stacking different $MAPbBr_3$ thin films on $MAPbI_3$ bottom layer that were both prepared by STVD. The value of x was varied by increasing the thickness of MABr from 300 to 500 nm. Optical, electrical, morphological, and structural properties were found to depend significantly on x. The optical and structural properties were of the $MAPb(I_{1-x}Br_x)_3$ were compared with those of pure $MAPbI_3$ ($x = 0$) and $MAPbBr_3$ ($x = 1$). X-ray diffractograms revealed the transformation of the tetragonal phase of $MAPbI_3$ to the cubic phase of $MAPbBr_3$ as the $MAPb(I_{1-x}Br_x)_3$ and PbI_2 were formed. The PbI_2 phase that was formed with the $MAPb(I_{1-x}Br_x)_3$ film was observed to decrease in intensity as the thickness of MABr increased from 400 to 500 nm. The exact origin of the PbI_2 phase is not fully understood but may include the reversible transformation of $MAPbI_3$ to PbI_2 due to prolonged annealing of the $MAPbI_3$ under-layer during the synthesis of the $MAPbBr_3$ top layer. This transformation may be due to the high temperature (140°C) of the substrate as the $PbBr_2$ was being deposited. The decrease in micro-strain of $MAPb(I_{1-x}Br_x)_3$ as the thickness of MABr increased could be attributed to a reduction in Br to I ratio. UV-Vis absorption spectra showed that the bandgap of the thin $MAPb(I_{1-x}Br_x)_3$ film alloy decreased from 2.21 to 2.14 eV as the thickness of MABr was increased from 300 to 500 nm. The bandgap was observed to be directly proportional to the bromine mole ratio, x, and inversely related to the lattice constant, consistent with results obtained using other solution deposition techniques. The lower the Br ratio in thin $MAPb(I_{1-x}Br_x)_3$ films, the higher the absorbance. FE-SEM micrographs depicted densely packed grains that covered the substrate. The morphology of the $MAPb(I_{1-x}Br_x)_3$ evolved from a mixture of cuboidal grains and gel-like structures at 300 nm MABr thickness to one with only faceted bimodal distributed grains when thickness reached 500 nm. This faceted cuboidal grain is a typical characteristic of the cubic $MAPbBr_3$. The average grain size increased from 150 to 320 nm as the thickness of MABr rose from 300 to 500 nm. The increase in average grain size may be due to a rise in the number and size of $MAPbBr_3$-like grains in the alloy. SCLC analysis of the dark *J-V* characteristics of FTO/TiO_2/ $MAPb(I_{1-x}Br_x)_3$/Au devices showed relatively high charge carrier mobilities that increased linearly with MABr thickness. The SCLC analysis also revealed that the trap density decreased with an increase in the thickness of MABr. Investigation of dark *J-V* and C-V characteristics of FTO/c-TiO_2/m-TiO_2/$MAPb(I_{0.11}Br_{0.89})_3$/Au solar cells revealed a sizeable built-in voltage (V_{bi}) of 1.6 V, and an accumulation of charge at interfaces for voltages were more significant than 0.2 V. The charge accumulation could be due to ion migration. A similar analysis for FTO/TiO_2/$MAPbI_3$/Au device showed a small V_{bi} of 0.7 V and no charge carriers at interfaces. Therefore, the high V_{bi} of the FTO/c-TiO_2/m-TiO_2/$MAPb(I_{0.11}Br_{0.89})_3$/Au solar cells may be due to the electric field resulting from the accumulation of charges at the m-TiO_2/$MAPb(I_{0.11}Br_{0.89})_3$ interface. Also, the presence of charge accumulation in FTO/c-TiO_2/m-TiO_2/$MAPb(I_{0.11}Br_{0.89})_3$/Au solar and charge accumulation in the FTO/TiO_2/$MAPbI_3$/Au device confirms that ion migration is greater in mixed halide perovskites than in pure halide perovskites.

In section 4.4, we synthesized thin $MAPbBr_3$ films on glass and FTO, and on Al, Sn, Ag, Au-Zn and Au metal substrates using the SPVD and the samples on the metals allowed to age for 60 days. The optical absorption of the film on glass and FTO showed a sharp edge at 540 nm, corresponding to a bandgap of 2.25 eV confirming the growth of $MAPbBr_3$. The cubic $Pm\overline{3}m$ crystal structure on glass and FTO substrates further confirmed the preparation of $MAPbBr_3$ thin films. The as-deposited thin $MAPbBr_3$ films prepared by the same approach on the various metals had a similar cubic structure but with different crystallographic textures. The intensity of the prominent peaks decreased considerably after 60 days of ageing, with the films on Al experiencing the most significant loss in intensity and crystallite size while those on Au-Zn experienced the smallest loss. This pointed to the fact the thin $MAPbBr_3$ film decayed at the fastest rate at the Al/$MAPbBr_3$ interface and the slowest rate at Au-Zn/$MAPbBr_3$ interface. Besides, both $PbBr_2$ and MABr were observed as decay products of $MAPbBr_3$ on all metal substrates. Further analysis of the XRD spectra of the different metal substrates revealed that the lattice constants and crystallite sizes were negatively correlated with the work function of the metals. There was a significant drop in average crystallite sizes of thin $MAPbBr_3$ films after 60 days of decay. The most significant percentage loss occurred on Al and the least significant loss on Au-Zn. This again confirms that the thin film was most stable on Au-Zn and least stable on Al. At the same time, there was a change in micro-strain from tensile to compressive as the thin films decayed on the metals. The grains were compact, randomly distributed, and the average grain size increased linearly with work function from 294 nm on Al through Sn, Ag and Au-Zn, to 850 nm on Au. Remarkably, the $MAPbBr_3$ grains delaminated rapidly on Al because of the oxidation of Al to Al^{3+} and the intrinsic stresses that caused cracks on the surface of the substrate. On the other hand, the $MAPbBr_3$ grains remained adhered to the Sn, Ag, Au-Zn and Au substrates during degradation. Therefore, the choice of metal electrode determines the degradation of the $MAPbBr_{3.}$ The degradation most at the Al/$MAPbBr_3$ and least at Au-Zn/$MAPbBr_3$ interfaces.

Generally, we recommend 100 nm thick PbI_2 and 500 nm thick MAI and post-annealing times shorter than 10 min for the growth of quality $MAPbI_3$ thin films by STVD for solar cell applications. Similarly, 100 nm thick $PbBr_2$ thin film and 500 nm think MABr thin film and post-annealing times shorter than 10 min are recommended for the growth of quality $MAPbBr_3$ thin films by STVD for solar cell applications. Growing the optimum sequential thermal vapour deposited $MAPbBr_3$ on optimum sequential thermal vapour deposited $MAPbI_3$ gives optimum $MAPb(I_{0.11}Br_{0.89})_3$ with optimum properties. The nature of the metal determines the stability and properties of $MAPbBr_{3.}$ $MAPbBr_3$ decays at a fast rate when in contact with Al metal and at a very slow rate when in contact with Au-Zn. Thus, Al is not recommended for applications involving the direct contact of HaP with a metal.

5.2 Future work

In the future, we will study the quality of the thin films by Photoluminescence spectroscopy to predict and compare the carrier lifetimes of the synthesized $MAPbI_3$, $MAPbBr_3$ and $MAPb(I_{0.11}Br_{0.89})_3$. Besides, we will determine and compare the efficiencies of solar cells applying the optimised $MAPbI_3$, $MAPbBr_3$ and $MAPb(I_{0.11}Br_{0.89})_3$ and compare charge transfer at the TiO_2/perovskite interfaces using transient absorption spectroscopy to confirm the charge accumulation. For the synthesis of the mixed HaP, we will investigate the possibility of using $MAPbBr_3$ as a seed layer instead of $MAPbI_3$. The stability of $MAPbI_3$ and $MAPb(I_{0.11}Br_{0.89})_3$ thin films on various metal surfaces will also be investigated.

Appendix

List of articles in scientific journals

1. **J.N. Fru,** N. Nombona, M. Diale, "Synthesis and Characterization of Methylammonium Lead Tri-Bromide Perovskite by Sequential Physical Vapor Deposition", Phys. B Phys. Condense. Matter, 578 (2020) 411884. doi: 10.1016/j.physb.2019.411884
2. **J.N. Fru**, N. Nombona, M. Diale, "Characterization of Sequential Physical Vapor Deposited Methylammonium Lead Tri-iodide Perovskite thin films", Vacuum, 182 (2020). 109727 doi.org/10.1016/j.vacuum.2020.109727
3. **J.N. Fru**, N. Nombona, M. Diale, "Growth and Degradation of Methylammonium Lead Tri-Bromide Perovskite Thin Film at Metal/Perovskite Interfaces", Thin Solid Films. (2021). 138568. doi.org/10.1016/j.tsf.2021.138568.
4. **J.N. Fru**, N. Nombona, M. Diale, "Characterization of Thin MAPb($I_{1-x}Br_x$)$_3$ Alloy Films Prepared by Sequential Physical Vapour Deposition" Mater. Res. Bull. (Submitted)

List of conference presentations

1. **J.N. Fru,** N. Nombona, M. Diale, "Synthesis and Characterization of Halide Hybrid Perovskite Thin Films by Sequential Physical Vapor Deposition", International Conference on Perovskite Solar Cells, Photonics and Optoelectronics (NIPHO20), Seville, Spain, (2020, February).
2. **J.N. Fru,** N. Nombona, M. Diale, "Using Self-Doping to Study the Effect of Interfaces on Performance of Hybrid Organic-Inorganic Perovskite Solar Cells", International Conference on Surfaces, Coatings and Nanostructured Materials (NANOSMAT-AFRICA), Cape Town, South Africa, (2018, November).
3. **J.N. Fru,** N. Nombona, M. Diale, "Synthesis and Characterization of Methylammonium Lead Tri-Bromide Perovskite by Sequential Physical Vapor Deposition", The 8th South African Conference on Photonic Materials (SACPM2019), Kariega Game Reserve, Eastern Cape Province, South Africa, (2019, May).